# TECHNISCHE UNIVERSITÄT CHEMNITZ

# Neuartige Charakterisierungsmethoden für moderne Thermische Interface-Materialien einschließlich deren Struktur-Eigenschafts-Korrelation

## Novel Characterization Methods for Advanced Thermal Interface Materials Including their Structure-Property Correlation

Von der Fakultät für Elektrotechnik und Informationstechnik der
Technischen Universität Chemnitz

genehmigte

Dissertation

zur Erlangung des akademischen Grades

Doktoringenieur
(Dr.-Ing.)

vorgelegt

von Mohamad Abo Ras
geboren am 05.05.1978 in Aleppo, Syrien
Tag der Einreichung am 23.08.2019

Gutachter:
Prof. Dr. Bernhard Wunderle
Prof. Dr. Clivia Sotomayor Torres

Tag der Verteidigung 26.02.2020

# Bibliographic Description

*Novel Characterization Methods for Advanced Thermal Interface Materials Including their Structure-Property Correlation*

Mohamad Abo Ras

Technische Universität Chemnitz, Faculty of Electrical Engineering and Information Technology

## Abstract

The continuous miniaturization of electronic systems accompanied by increasing performance and functionality leads to an increase in power density. In order to comply this trend, new heat dissipation concepts are needed which demand new materials and material composites. An important aspect of this work is therefore the concentration on the materials that are decisive for the heat flow. This thesis deals with the development of methods for comprehensive thermal characterization of the different materials and material classes used in the electronics industry. The measuring systems have been designed and developed in such a way that they enable to take into account specific application conditions, no costly sample preparation is necessary and at the same time high measuring accuracy is ensured. Four different measuring systems were developed and realized within this work, which, in their entirety, enable the characterization of almost all package materials under desired boundary conditions. Based on this, numerous materials and effects were investigated and discussed in the context of this work with the developed measurement systems.

## Keywords

Thermal interface materials, die attach materials, thermal characterization, thermal conductivity, thermal diffusivity, thermal interface resistance, sintered silver, process-structure-property correlation.

# Bibliografische Beschreibung

*Neuartige Charakterisierungsmethoden für moderne Thermische Interface-Materialien einschließlich deren Struktur-Eigenschafts-Korrelation*

Mohamad Abo Ras

Technische Universität Chemnitz, Fakultät für Elektrotechnik und Informationstechnik

# Kurzreferat

Die fortschreitende Miniaturisierung von elektronischen Systemen begleitet von steigender Leistung und Funktionalität führt zur Erhöhung der Leistungsdichte. Um diesem Trend zu entsprechen, werden neue Entwärmungskonzepte benötigt, die wiederum neuartige Materialien und Materialverbünde fordern. Ein wichtiger Aspekt dieser Arbeit ist deshalb die Konzentration auf die für den Wärmetransport entscheidenden Materialien. Diese Arbeit befasst sich mit der Entwicklung von Methoden für die umfassende thermische Charakterisierung von den verschiedenen Materialien und Materialklassen, die in der Elektronikindustrie verwendet werden. Die Messsysteme wurden so entworfen und entwickelt, dass spezifische Anwendungsbedingungen berücksicht werden können, keine aufwändige Probenherstellung notwendig ist und gleichzeitig eine hohe Messgenauigkeit gewährleistet ist. Es wurden vier verschiedene Messsysteme innerhalb dieser Arbeit entwickelt und realisiert, die in ihrer Gesamtheit die Charakterisierung von fast allen Package-Materialien unter gewünschten Randbedingungen ermöglichen. Zahlreiche Materialien und Effekte wurden daraufhin im Rahmen dieser Arbeit mit den entwickelten Messsystemen untersucht und diskutiert.

# Stichworte

Thermische Interface-Materialien, Die-attach-Materialien, thermische Charakterisierung, Wärmeleitfähigkeit, Temperaturleitfähigkeit, thermischer Grenzflächenwiderstand, gesintertes Silber, Prozess-Struktur-Eigenschafts-Korrelation.

# CONTENTS

# Acronyms

| | |
|---|---|
| ADC | Analog-Digital-Converter |
| ASIC | Application-Specific Integrated Circuit |
| BGA | Ball Grid Array |
| BLT | Bond Line Thickness |
| CNT | Carbon Nanotube |
| COB | Chip on Board |
| CTE | Coefficient of Thermal Expansion |
| CVD | Chemical Vapor Deposition |
| DA | Die Attach |
| DCB | Direct Bonded Copper |
| FC | Flip Chip |
| FE | Finite Elements |
| FIB | Focused Ion Beam |
| HACNT | Horizontally Aligned Carbon Nanotube |
| HPA | High-Power Amplifier |
| HTCC | High Temperature Co-fired Ceramic |
| IGBT | Insulated-Gate Bipolar Transistor |
| IMC | Intermetallic Compound |
| IMP | Intermetallic Phase |
| IMS | Insulated Metal Substrate |
| IR | Infrared |
| LED | Light-Emitting Diode |
| LMA | Low melting point Metal Alloy |
| LTCC | Low Temperature Co-fired Ceramic |
| MMIC | Monolithic Microwave Integrated Circuit |
| MOSFET | Metal-Oxide-Semiconductor Field-Effect Transistor |
| NTC | Negative Temperature Coefficient Thermistor |
| PCB | Printed Circuit Board |
| PCM | Phase Change Material |
| QFN | Quad Flat No Leads Package |

| | |
|---|---|
| QFP | Quad Flat Package |
| RB | Reference Body |
| RF | Radio Frequency |
| SEM | Scanning Electron Microscope |
| SiP | System in Package |
| SoA | State of the Art |
| SPM | Smart Power Module |
| TC | Thermal Couple |
| TCA | Thermally Conductive Adhesives |
| TIM | Thermal Interface Material |
| TLPB | Transient Liquid Phase Bonding |
| TTC | Thermal Test Chip |
| TTV | Thermal Test Vehicle |
| VACNT | Vertically Aligned Carbon Nanotube |
| Via | Vertical Interconnect Access |
| VOG | Vertically Oriented Graphite |
| WB | Wire-Bond |
| WBG | Wide-Band Gap |

# Acknowledgement

First of all I would like to thank my doctoral supervisor, Prof. Dr. Bernhard Wunderle from the Technical University of Chemnitz, for his continuous support, valuable inspiration, encouragement and appreciation. The work with him has strongly influenced my scientific and professional development. And it always brought me a huge pleasure, especially the inspiration by discussion of unconventional ideas has made the work very fascinating.

I would also like to thank Prof. Dr. Clivia Sotomayor Torres from Catalan Institute of Nanoscience and Nanotechnology (Barcelona, Spain) for the valuable scientific advice and for her willingness to review the dissertation.

I wish to express my sincere thanks to Dr. Afshin Ziaei from Thales Research and Technology (Palaiseau, France) and Dr. Hermann Oppermann from Fraunhofer Institute for Reliability and Microintegration (Berlin, Germany) for their readiness to be part of the doctoral committee and for their support and cooperation over the past years.

A special thanks goes to my former department head, the retied Prof. Dr. Bernd Michel for his constant motivation and generous support, which had a great impact on my career.

I would like to express my gratitude to my colleague and companion Dr. Daniel May for the unrestricted technical support during my research work, especially for the support in the FE simulation, which provided an important contribution to the development of the measurement systems.

My warm thanks go to Prof. Dr. Ralph Schacht for his constant availability for discussion and for the helpful hints and tips for the structuring of the work.

I would like to thank all the proofreaders, Dr. Corinna Grosse, Mrs. Ilona Soremski, Dr. Daniel May, Mr. Torsten Nowak, Mr. Tobias von Essen, and especially Dr. Thomas Winkler for his patience and the time he has spent for the correction and discussion, as

well as for the support I have received from him over the last twelve years.

Many thanks to all the research project and industrial cooperation partners for the challenging problems and valuable suggestions. In particular, I would like to thank Mr. Markus Bast from FH-Kiel (Germany) for providing the numerous sintered silver samples and Mr. Helge Kristiansen and Mrs. Nina Høglund from Conpart Technology (Norway) for supplying the adhesives filled with silver-coated polymer spheres. I would also like to thank Dr. Ana Borta-Boyon, Dr. Laurent Divay and Mr. Julien Fortel from Thales (France) for their contribution to the design and manufacture of the VACNT modules.

Heartfelt thanks to all my colleagues at the Berliner Nanotest und Design GmbH and the JointLab Berlin for the Technical Safety for their support and the pleasant working atmosphere.
I sincerely thank Mr. Dan Wargulski for the exciting discussions and for his thought-provoking impulses to improve the measuring accuracy of the TIMAwave test stand. I am also grateful to Mr. Pranav Panchal for his help with the thermal impedance measurement.

My thanks also go to all employees of the Micro Material Center of Fraunhofer ENAS under the guidance of Prof. Dr. Sven Rzepka as well as to the staff of the Chair for Materials and Reliability of Microsystems at Chemnitz University of Technology. In particular, I acknowledge the contribution of Mr. Jens Heilmann for performing the FIB and SEM investigations on sintered silver samples.

I am indebted to thank my parents for giving me the opportunity to study in Germany and for supporting me mentally and financially in my first years despite difficult times.

Last but not least, special thanks to my wife Ligita Cipaite, who took over most of the education and care of our wonderful children Celine, Diana, Emilia and Adam during my endless working hours. Without her backing, support and love, this work would not have been possible.

# Chapter 1

# Introduction

## 1.1 Background and Motivation

Electronic devices are indispensable in our lives. Whether in our communication, mobility, healthcare, security or in any other field of our everyday life, we are simply dependent on electronics. Due to this dependency, our expectations and demands on reliability of these devices are very high.

Fact is that everything becomes electrified from car to toothbrush and every electrical system becomes electronic and every electronic device becomes more capable, smaller and faster by each generation. Continuous miniaturization of electronic devices accompanied by higher integration density demands more efficient heat removal techniques to handle the increasing power density and rising temperature of hot spots. For this reason, it is important to investigate thermal properties of all materials used in these devices. Nowadays, the electronics industry is using elaborate simulations from the early development phase to the design of electronic devices, packages and components. Fundamentally important for this are sufficiently accurate material data. The quality of the simulation results greatly depends on the quality of the material data used.

Electronic packages consist of several components (i.e. die, die attach, heat spreader, heat sink, different layers of thermal interface material, substrate, encapsulation etc.). These components are made of different materials such as:

- metals, which can be bulk, thin film, mono metal or metal alloy,
- semiconductors, which can be highly, low or non-doped silicon, silicon carbide, gallium nitride or gallium arsenide,
- glass as substrate or as dielectric thin layer,
- ceramics as substrate or as filler of TIMs,

- polymers for encapsulation or as matrix of TIMs,
- carbons as heats spreader, TIMs or filler in TIMs.

The range of thermal conductivity of these materials varies from some $mW/(m \cdot K)$ to some $kW/(m \cdot K)$. To provide reliable material data within this huge range of thermal conductivity, specific characterization methods are needed, as there is no method available, which can handle this range of materials with the required accuracy for reliable simulation results.

One of the major bottlenecks in advanced thermal packaging solutions is represented by the thermal resistance of thermal interface materials (TIMs). Part of the thermal resistance is governed by the bulk thermal conductivity, another is determined by the interface resistance [1], [2]. So, development for advanced thermal technology has to focus on an understanding of heat transfer across bulk and interfaces of thermal interface materials (TIMs), the influences of processing conditions and – as a necessary requirement for progress – their accurate characterization [3], [4]. Thermal characterization methods for TIMs narrate a long story of confusion, as results from different characterization methods often disagree formidably. Even worse, thermal conductivity values will be different when applied to the real device, likely to cause over-, or more often, fatally under-designed thermal heat paths. The reason for this misjudgment is often that TIM characterization is done under much too favorable conditions (e.g. polished surfaces, excessive pressure conditions) or disregarding technological influences (e.g. cure regime for adhesives, dissimilar surfaces). It is therefore of importance to assure characterization under real technological boundary conditions.

There are many methods available for thermal characterization of thermal interface materials. The most commonly used method is the steady-state based on ASTM D5470 [5]. Many market available devices were built according to this method. The main disadvantage of these instruments is that they do not take application-specific conditions into account, but were developed to measure the material properties of the bulk material conductivity. The method tries to eliminate interface resistances by using smooth and flat surfaces. This approach simply tends to underestimate the contact resistance component in each specific application [6].

Further methods and measurement techniques for material characterization with their advantages and disadvantages are described in section 2.2.

One of the challenges of this work is to develop characterization systems that enable the

characterization of materials with regard to adjustable process and operating conditions. In addition, it should be a feature that the measurement systems can be adapted to the commonly available industrial samples and do not require complicated and specially fabricated samples.

The test system for the characterization of thermal interface materials to be developed in the context of this work is intended to have a significant improvement in resolution compared to commercial steady-state measurement techniques with the same or even better measurement accuracy. This will be achieved by understanding error sources and using innovative approaches.

Not only TIM can be characterized with this measuring technique, but also substrates or multilayer structures. A special feature of the system, which distinguishes it from commercial techniques, is the computer-controlled mode for long-term in-situ investigation of the ageing behaviour of TIM due to mechanical alternating loads.

The thermal community is constantly on the quest for new thermal interface technologies. Materials scientists and technologists are constantly developing new classes of materials that are becoming thinner and thinner and more thermally performing. For example, silicone based thermal pads are being replaced by indium or VACNT based pads. Also die attach materials like solder or glue are more and more replaced by new technologies like sintering. For the characterization of these novel technologies and materials, whose thermal properties are strongly process dependent, novel measurement techniques will be developed and implemented within this work, which will be used, among others, to investigate the process-structure-property correlation (PSPC) of sintered silver in such a way that has never been done before.

## 1.2 Objectives and Outlines

This work deals with the development of different characterization techniques for thermal characterization of almost all materials used in an electronic package. However, due to the fact that materials getting better and thinner, the bulk values of these materials play less and less role, instead the influence of the process becomes more and more important. The main focus will be therefore on characterization of thermal interface materials and their process-structure-property correlation.

In chapter 2, the state of the art (SoA) of commonly used thermal materials and technologies will be discussed which will be followed by the description of different characterization

techniques that nowadays are used for thermal characterization of TIMs and other components of electronic packages.

Chapter 3 describes the theoretical basics necessary for understanding the test methods developed, realized in test stands and applied to representative characterization tasks within this thesis. Two steady-state test stands and two transient test stands have been developed and realized.

Chapter 4 will explore a steady-state test stand, the so-called *TIMA*, which conforms with the established ASTM standard D5470 [5], but has many remarkable ameliorations to allow characterization of advanced thermal interfaces materials under real or specific conditions, as well as characterization of different types of substrates (bulk, multi-layer or heterogeneous). To maximize the measurement accuracy of the characterization system, the system will be analyzed to understand the error sources and their influence on the measured values. Within this work, the resolution and limitation of the developed test stand will be figured out by systematically studying of measurement error. Furthermore, several actions and improvements will be developed to overcome the limitation of the ASTM standard technique.

Since not only the bulk thermal conductivity of TIM is decisive for its thermal performance, but also the thermal interface resistance is playing an important role, especially for thin and highly thermal conductive TIMs. The thermal interface resistance is mainly determined by the surface properties of the contact media, so it is necessary to characterize the TIMs between similar surfaces as they occur in real applications. TIMA will offer the possibility to select the surfaces quality of the contact media (material type, roughness, metallization etc.). Furthermore, TIMA will also allow to investigate TIMs between silicon and metal surfaces. For this purpose a thermal test chip will be developed, designed and manufactured.

Results of several materials characterized by the test stand *TIMA* will be discussed within this work. Among others, following questions will be answered:

- How does the thermal performance of a TIM change when using silver coated polymer particles instead of bulk silver particles as fillers?
- What bulk thermal conductivity can be achieved by using vertically oriented graphite (VOG) as filler in thermal pads?
- Is thermal conductivity of VOG dependent on the applied pressure?
- How does the thermal conductivity of thermal grease behave when its bond line

thickness approaches the particle size?

- What influence does the particle volume fraction have on the thermal conductivity of adhesives?
- What influence does the operation temperature have on the thermal conductivity of adhesives?
- What influence does mechanical cycle loading have on the thermal conductivity of thermal compounds (grease and gap filler)?

Materials with high thermal conductivity constitute an important part within the thermal interface materials. However, they cannot be measured with high accuracy by the common ASTM procedure due to the low temperature gradient and because the thermal properties of these materials are mostly dependent on the assembly process. For example, vertically-aligned carbon nanotubes (VACNTs) as a TIM is a promising technology due to the excellent thermal conductivity of CNTs. However, it has been shown that the effective thermal conductivity of VACNTs is highly dependent on the assembling process due to the non-uniform length of the VACNTs [7], [8]. The open question is whether and how the assembly process influences the thermal conductivity of VACNTs based TIMs. In order to be able to investigate the VACNT based TIM on package level, a new approach will be applied for the first time and presented in chapter 5. This approach will provide the possibility to characterize the VACNT based TIM in the package by replacing the chip by the thermal test chip, which is also developed and manufactured within this work. For the characterization the thermal impedance technique is used.

Chapter 6 deals with characterization of highly thermal conductive materials. Common steady-state systems, which are already on the market, following ASTM standard D5470 [5] or JEDEC standard JESD51-3 [9] are limited to low and medium thermally conductive materials, due to the small temperature gradients over the tested materials. The ASTM standard E1225 [10] is a modification of the ASTM standard D5470 to be used for thermal conductivity measurement of high thermally conductive samples. However, it works only for solid samples with a certain geometry that allows integration of minimum two temperature sensors to measure the temperature gradient across the sample. For high thermally conductive materials such as metals, semiconductors or ceramics, transient flash technique is usually used [11]. This technique provides thermal diffusivity, from which the thermal conductivity can be calculated if knowing the density and the specific heat capacity of the tested material. Within this work, an innovative steady-state test stand will be presented (chapter 6), which can be used for direct thermal conductivity measurement of package components such as metallic heat sinks, dies, high thermally conductive substrates, die attach materials (solder alloys or sintered mono metals). A systematic study of sintered

silver regarding the correlation between process, structure and property is an important part of this work. There are several open questions regarding sintered silver die attach. Some of these questions will be answered within this thesis:

- Can the thermal conductivity of high thermally conductive materials such as sintered silver be measured by a steady-state method?
- Which influence do the sintering parameters have on thermal and electrical conductivity of sintered silver?
- Is there a correlation between porosity and thermal and electrical properties of sintered silver?
- Is the Wiedemann-Franz law valid for sintered silver?

Chapter 7 deals with the development of a transient test stand for thermal diffusivity measurements based on Ångström's method. The theoretical background of the method will be explained in detail followed by a study of the effect of heat losses on the results and ways to overcome them. Furthermore, the implementation of the method in a test stand will be shown. Finally, results of thermal diffusivity measurements of several materials will be shown and discussed.

# Chapter 2

# State of the Art

Chip innovation led in less than a decade to an increase in current density by a factor of three. In addition, the packaging must be capable to handle switching power in the range of 500 W/cm$^2$. For this reason, the package needs to be enhanced: New die attach materials, new thermal interface materials and new interconnect technologies on chip topside must be developed. New and cost-effective packaging materials and production concepts are also needed for competitiveness reasons. A new requirement follows the trend of improved cooling concepts for multi-chip modules, sometimes even resorting to 3D packaging architectures for the smallest form factor. This means that the packaging must follow a further system miniaturization (trend towards embedding technologies, heterogeneous integration and power SiP).

There are several technologies of electronic packages. The selection of packaging technologies as well as the materials and components used for, depends on the application fields of this packages. Figure 2.1 shows exemplary schematics of different packages where different types of TIMs and die attach materials are used in.

Automotive applications for power electronics is increasing rapidly due to hybrid and full-electric vehicles. The automotive industry has specific requirements for its power electronic systems such as compact design, high reliability and extremely low cost to power ratio. A typical automotive power electronics package consists of a power SiP connected to heat sink using grease, pads or gap filler as TIM.

Some RF applications such as global navigation satellite systems are facing heat removal challenges of several $100\,\mathrm{W/cm}^2$ hot spots. For such application the only option is the selection of high performance TIM to cool this RF modules under weight, size and reliability (harsh environment) boundary conditions typical for avionics systems. In RF application, wide-band gap (WBG) semiconductors (e.g. GaN, SiGe, GaAs) are used, which provide higher frequency, higher power, higher operation temperature, lower losses
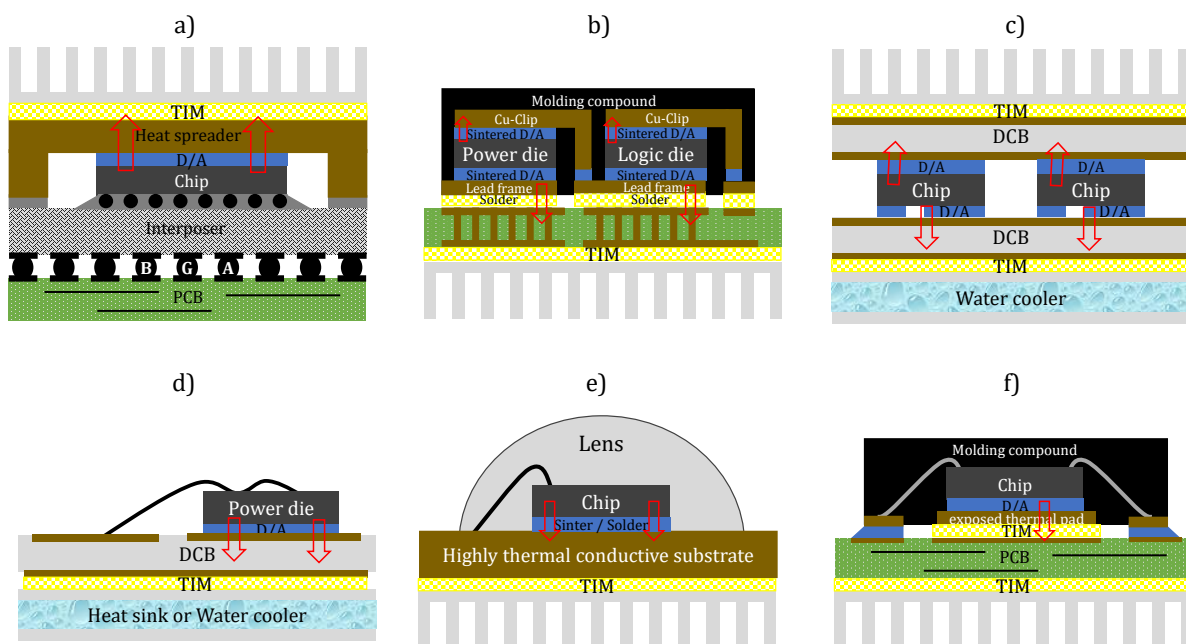
**Figure 2.1:** Schematic illustration of different electronic packages. a) Flip chip and BGA package with topside cooling, typical for micro processor application. b): Power SiP for automotive and industrial application. c) Power module with double side cooling (air and water cooling) for high power application. d) MOSFET sintered or soldered on DCB, typical power module for automotive application. e) Power LED package, direct chip attach by Chip-on-Board technology. f) QFN package with exposed thermal pad, typical package for consumer electronic application

and smaller system size than Silicon. WBG semiconductors exist as bulk materials but usually are grown as thin layers on Si or SiC substrate. As die attach materials, sintered silver, high temperature solders or VACNTs are typically used.

In the solid state lighting (LED) sector, the LED chip is normally mounted on a heat spreader using an eutectic solder or adhesive as die attach material and the heat spreader placed onto thermally enhanced organic substrate. According to the OIDA roadmap[1], it is expected that the power density on die level for high power LED increases to levels of 500 to 1000 W/cm$^2$ by 2020. For such high power density, it is clear that the thermal path from die to heat transferring surface must be efficient with minimum thermal resistance and maximum heat spreading. This can be achieved by reducing the layers between die and heat sink using Chip-on-Board (COB) technology, where the LED chip is directly attached to a highly thermal conductive substrate (e.g. IMS, AlN-DCB) using highly thermal conductive die attach materials.

---

[1]An OIDA technology roadmap update 2002, November 2002, Optoelectronics Industry Development Association, Washington, USA

A summary of these and other applications of electronics is given in table 2.1.

**Table 2.1:** Overview of application fields for electronics devices with their typical requirements and properties

| **Application** | Avionics | Traction | Auto-motive | Energy conver-sion | Industrial | Consumer electro-nics | Solid State Lighting |
|---|---|---|---|---|---|---|---|
| |  |  |  |  |  |  |  |
| **Category** | RF | Power | Power SiP | High Power | Power ASIC | ASIC, µP | LED |
| **Packaging technology** | GaN on Si/SiC | Si/SiC on DCB | Si on PCB | SiC on DCB | SPM, BGA, QFN | QFN, BGA, QFP | LED on sub-mount, COB |
| **Typical power dissipation** | few hundred watt | few kilo watt | few hundred watt | few mega watt | few ten watt | few ten watt | few hundred watt |
| **Typical power density** | 100-200 $W/cm^2$ | 1-10 $kW/cm^2$ | 200-300 $W/cm^2$ | 10-100 $kW/cm^2$ | 30-300 $W/cm^2$ | 50-200 $W/cm^2$ | 500-1000 $W/cm^2$ |
| **Typical TIM1 (DA)** | sintered silver, CuSn/eutectic solders, TLPB | | | | eutectic solders, adhesives | | |
| **Typical TIM2** | grease, pads, gap filler, adhesive, sintered silver adhesive, Pads, PCM | | | | | | |
| **Lifetime demands** | 30 years | 25 years | 20 years | 20 years | 15 years | 3-5 years | 5-8 years |

## 2.1 SoA of thermal interface materials

Thermal Interface Materials (TIMs) play a key role in the thermal management of various electronics packages. All interfaces between different components in an electronic package (e.g. chip, heat spreader, substrate, heat sink etc.) exhibit a finite roughness, they may increase the Kapitza resistance when joining two surfaces. TIMs serve to fill the gap between the two adjoining surfaces.

Figure 2.2 (left) illustrates the contact of two surfaces with and without TIM. The right-hand diagram in figure 2.2 presents measurement results of the interface resistance of two surfaces as a function of the pressure with and without TIM. The pressure is applied perpendicularly to the interface. The contact media had a surface roughness $R_z = 2$ µm. It can be seen, that the thermal resistance decreases by a factor of 10 when filling the gap with a TIM.
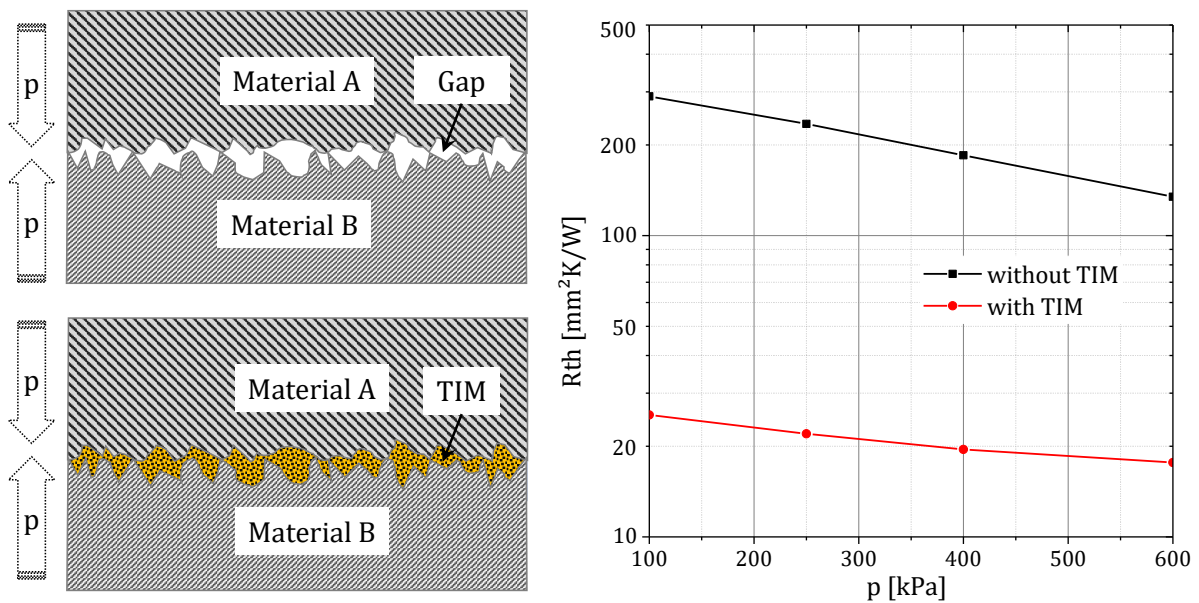
**Figure 2.2:** Schematic illustration of joining two rough surfaces with and without TIM (left); owner measurement of thermal interface resistance with and without TIM (right).

TIMs are the bottleneck of the heat path in an electronic package as the thermal conductivity of the TIM is one to two orders of magnitude lower than the thermal conductivity of most of the package components (e.g silicon chip, copper heat spreader, aluminium heat sink, gold or silver metallization etc.).
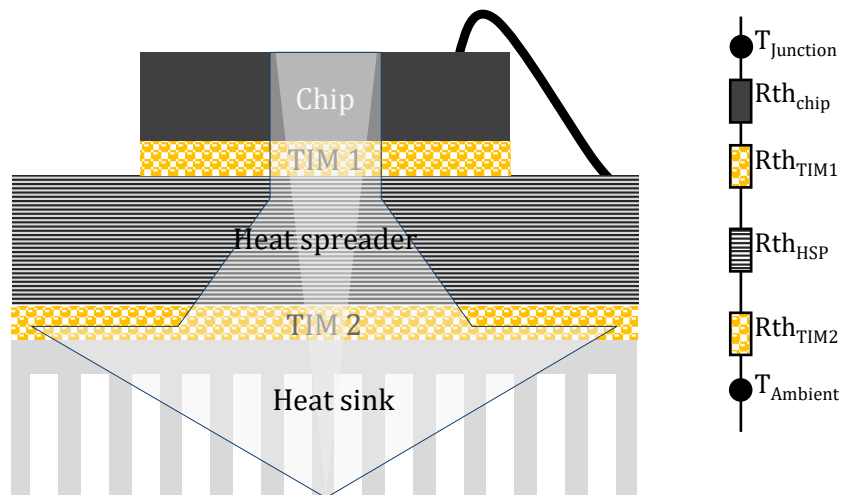


**Figure 2.3:** Schematic illustration of heat flow path in an electronic package.

In table 2.2 the thermal resistances of the package components and their thermal budget has been calculated using typical materials and geometry. To visualize the importance of the TIM for the thermal management, the thermal budget (portion of the total thermal resistance) of the different package components has been calculated. Figure 2.3 shows

a schematic of an electronic package consisting of a silicon chip soldered (TIM1) onto a copper heat spreader, which is mounted onto an aluminium heat sink using a thermal grease (TIM2). The total thermal resistance between junction and ambient is the sum of the thermal resistances of chip, TIM1, heat spreader, TIM2 and heat sink.

**Table 2.2:** Thermal resistance of electronic package components and their proportions of the total thermal resistance of the package.

| Layer | Material | Thermal conductivity $[W/(m \cdot K)]$ | Thickness $[\mu m]$ | Thermal resistance $[mm^2 \cdot K/W]$ | Thermal budget $[\%]$ |
|---|---|---|---|---|---|
| Chip | Si | 149 | 300 | 2.01 | 16 |
| **TIM1** | **Solder** | **50** | **20** | **0.40** | **3** |
| Heat spreader | Cu | 380 | 200 | 0.53 | 4 |
| **TIM2** | **Grease** | **5** | **50** | **10.0** | **77** |
| Package | | | 570 | 12.9 | 100 |

It can be seen in table 2.2 that the thermal resistance of the TIMs is around 80% of the total thermal resistance of the package.

It has to be mentioned that the criteria for the selection of TIMs are not limited to the thermal performance. There is a large number of factors to be taken into account for both fabrication and application of TIMs. The following list shows the most important criteria for selection of TIMs:

| | |
|---|---|
| Thermal properties: | Thermal diffusivity and conductivity <br> Thermal contact resistance <br> Lowest thermal resistance <br> Heat capacity <br> Coefficient of thermal expansion <br> Phase change temperature |
| Electrical properties: | Electrical conductivity <br> Electrical contact resistance <br> Insulation strength <br> Shielding of electromagnetic interference |
| Mechanical properties: | Modulus of elasticity <br> Hardness and stiffness <br> Viscosity <br> Density <br> Adhesive strength |

| | Shrinkage |
|---|---|
| Reliability issues: | Long-term stability |
| | Out-gassing and out-pumping |
| | Temperature and moisture resistance |
| Processability issues: | Rheological behaviour |
| | Curing conditions |
| | Reusability and reworkability |
| | Pot life |
| Safety issues: | Flammability |
| | Toxicity |
| | Environmental and recycling process |
| | Contaminant |

In general, TIMs consist of highly conductive fillers, e.g. CNTs, graphite/graphene or other nano or mirco particles, which are added to mechanically conforming and much poorer thermal conductivity polymers, phase change materials or epoxy matrix. The mixing ratio between particles, particle size, particle shape and matrix determines the material properties. The compromise is that sufficient filler must be introduced to achieve adequate thermal conductivity by reaching the percolation threshold without making the material so stiff that it does not form a thin bond line or displace the air trapped in the grooves and imperfections of the mating surfaces. For example, mixing larger and smaller particle as filler materials leads to reducing the interface resistance between the particles and the mating surfaces, as the particles can produce a conforming surface, when they are smaller than the roughness of the mating surface. On the other hand the bulk thermal conductivity of the material decreases due to the high number of interface between the particles.

Figure 2.4 presents schematically the important rules to be taken into account by designing and applying TIMs.

1. Percolation: heat flows mainly through the filler, as the thermal conductivity of the filler is two or three order of magnitude higher than the thermal conductivity of the matrix. The packing density of the filler particle can be enormously improved with increasing modality. A simple rule describing the order of magnitude of the increase or even the value of the packing density cannot be established, since a small variation of the width or the proportion of a fraction can have enormous effects on the overall structure of the particle size distribution. It is therefore necessary to know the actual distribution functions of the individual fractions and to recalculate
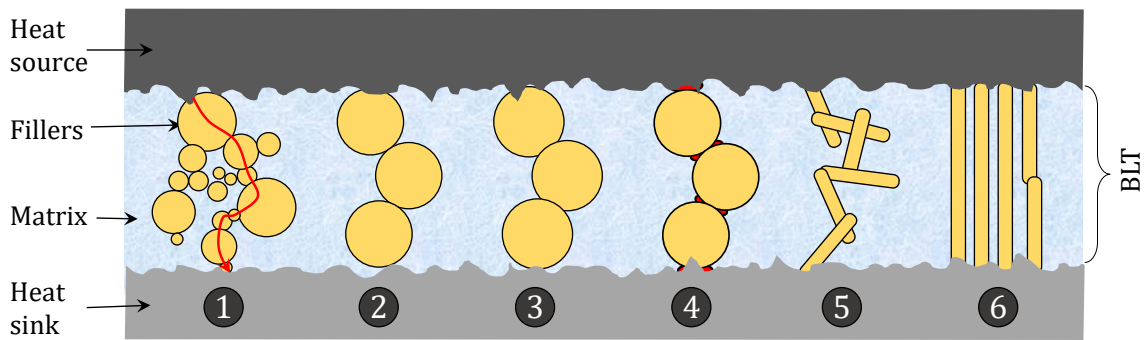
**Figure 2.4:** Schematic TIM Golden Rules

the packing coefficient in each case for comparison purposes and trend statements [12]. The packing density of the filler has not only impact on thermal conductivity but also on the processability and and reliability of the material.

2. Filler size: the diameter of filler particle has a significant influence on the overall thermal resistance and the thickness of the bond line. Larger particles increase the bulk thermal conductivity but it cannot be applied in thin bond line.

3. Matrix densification: Matrix normally have chemical and/or thermal shrinkage. This has the positive effect that particles have more contact with each other, but also the negative effect that stress can occur in the TIM layer, which affects the reliability.

4. Contact resistance (incl. Kapitza): The particle-to-particle contact and the particle-to-surface contact are point contacts due to the shape of the particles. This contact is the major heat removal bottleneck. To improve this contact, innovative technologies are used, such as surface functionalization or by building necks between the particles. This can be achieved by means of hierarchical self-assembly of micro-nano-sized particles using centrifugation and capillary-bridging [13].

5. Aspect ratio: The filler's aspect ratio is another factor for the conductivity of a composite, since the large aspect ratio fillers easily form the bridges between them, known as conductive networks. The formation of random bridges or networks of conductive particles facilitates electron and phonon transfer and leads to high conductivities. In addition, there are practical limits to the loading of the maximum packaging fraction, which often leads to problems in terms of processability and mechanical performance. This means that a hybrid filler system with large network formation is necessary for the preparation of next generation heat dissipation materials [14].

6. Alignment: alignment of filler in a TIM as a bridge between the two mating surfaces is the most effective way to achieve excellent heat transfer. The challenge herewith is the bonding between the filler and mating surface.

The following chapter will review the current status and future trends of commercial and advanced TIMs, including polymers, carbon and metal based TIMs.

## 2.1.1  Thermal greases

Thermal greases are usually comprised of two primary components, i.e. matrix polymer and filler. Silicone is commonly used as matrix for its good thermal stability, wetting characteristics and low modulus of elasticity [15].
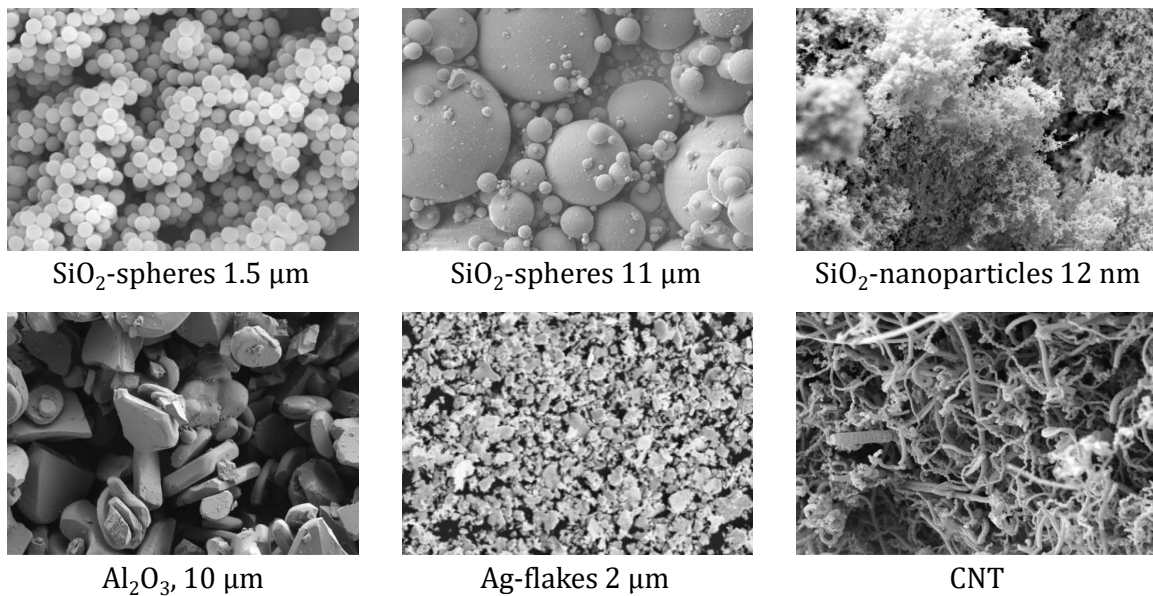


| $SiO_2$-spheres 1.5 µm | $SiO_2$-spheres 11 µm | $SiO_2$-nanoparticles 12 nm |
| --- | --- | --- |
| $Al_2O_3$, 10 µm | Ag-flakes 2 µm | CNT |

**Figure 2.5:** SEM images of different fillers of thermal grease [16].

Ceramics such as $Al_2O_3$, AlN, ZnO, $SiO_2$ and BeO are used as fillers due to their moderate cost and good dielectric properties. For electrically conductive thermal greases, metallic fillers such as Ag are usually used. The proportion of the filler affects the thermal performance and the rheological properties of the grease. The higher the filler percentage, the greater the thermal conductivity and the higher the viscosity of the grease. The SEM images in figure 2.5 show different types of fillers ($SiO_2$, $Al_2O_3$, Ag, CNT) which are commonly used to improve the thermal conductivity of TIMs with polymer matrix.

The main advantages of thermal grease are: excellent wetting, relatively high bulk thermal conductivity, thin bond line with minimum attach pressure and reworkability [15].

The main disadvantage of thermal grease is its susceptibility to the so-called "pump-out"

effect, which occurs due to movement of contact surfaces driven by the mismatch of their coefficient of thermal expansion (CTE) [17]. The grease, which may be forced out of the interface, can lose the thermal contact and contaminate neighbouring components [18]. Thermal grease can also dry out over time due to the separation of the fillers from the polymer matrix at elevated temperatures [19].

### 2.1.2 Thermally conductive adhesives (TCA)

An adhesive as thermal interface material has the advantage compared to thermal grease that it creates both a thermal and mechanical connection without the requirement of mechanical clamping. Thermally conductive adhesives comprise a thermosetting polymer matrix and fillers and can be found as one- or two-component system. Different types of thermosetting polymers are usually used, which mainly differ in curing properties and operation temperatures. Adhesives are cured to allow for cross linking of the polymer which provides the adhesive property. A thermal adhesive can be electrically insulating by using non electrically conductive fillers such as $Al_2O_3$ or AlN, or electrically conducting by using electrically conductive fillers such as Ag.

### 2.1.3 Gap fillers

Gap fillers are one of the largest segments of the thermal interface market [20], they are normally used to fill large gaps up to several millimetres, for example, to connect components with high topography and/or stack-up tolerances to a universal heat sink or housing. Gap fillers are existing either as soft pads in different thicknesses or as liquid filling material, which can be one- or two-component. Gap fillers are not designed to be a structural adhesive. After the curing, they are normally softer than typical adhesives and harder than thermal greases. This makes the gap fillers resistant against the so-called pump-out effect.

### 2.1.4 Phase change materials (PCM)

Phase change materials comprise low temperature thermoplastic polymers that typically melt at $50\,°C - 80\,°C$ [18] and appear in a variety of configurations with fillers to enhance their thermal conductivity. Phase change materials can also be based on alloys melting at low temperatures. Generally, phase change materials are designed to have a melting temperature below the maximal operation temperature of the electronic component [21]. Polymeric phase change materials usually exist as thermal pads which are solid at room temperature and easy to handle. As the electronic component reaches its operation temperature, the pads become softer and start to flow like a fluid into the gaps in the interfaces.

Phase change materials have the advantage over thermal grease that they generally do not suffer from pump-out effects and dry-out problems [15].
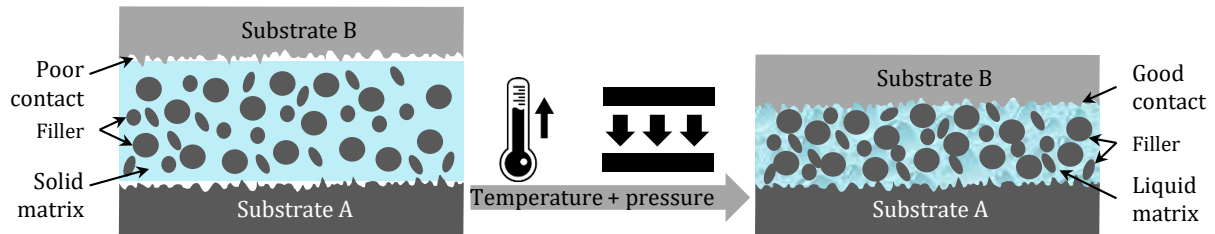


**Figure 2.6:** Schematic of PCM structures; left: initial state (solid matrix); right: at operation temperature (liquid matrix).

Metallic phase change materials consist of low melting point metal alloys (LMAs), which are usually alloys of gallium, indium, bismuth and tin [22], [23]. Several studies of low melting point metal alloys as TIM have been reported in [24], [25] and [26]. The studies showed that LMAs have a thermal conductivity an order of magnitude higher than traditional TIMs and extremely low thermal resistances at small contact pressure and at thin bond line.

### 2.1.5 Carbon based TIMs

Carbon based materials such as graphene and carbon nanotubes (CNTs) are directly used as TIMs or as filler in composites due to their extremely high thermal conductivity. For graphene a thermal conductivity of 2000 W/(m·K) [27], for single-walled CNTs of 6000 W/(m·K) [28] and for multi-walled CNTs of 3000 W/(m·K), respectively [29] have been reported. Different types of carbon based materials including graphite, amorphous carbon, and carbon nanotubes have been used as fillers to improve the thermal conductivity of the TIMs [30], [31], [32]. However, when carbon based materials such as CNTs are added to a polymer matrix, the enhancements of thermal properties are less than expected [33]. The CNT dispersion in the matrix or the defects of the CNTs may be responsible for these poor properties. Figure 2.7 shows a schematic of CNTs in a polymer matrix. The heat path through the highly conductive CNTs between heat source and heat sink is partially interrupted, which leads to an increase of the effective thermal resistance of the TIM layer.

To overcome this limitation and take advantage of the excellent thermal conductivity of the CNTs, several research groups are working in different technological processes such as arc discharge, laser ablation or chemical vapor deposition (CVD) to grow CNTs on flat substrates, in which all the nanotubes have a similar orientation. These results are called
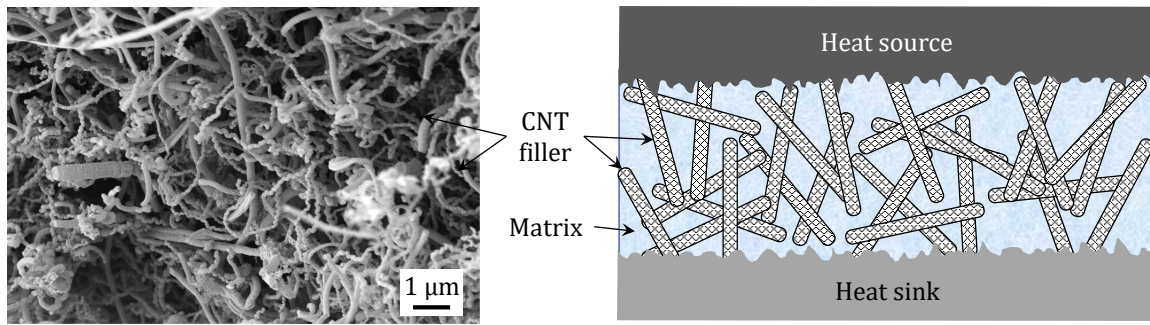
**Figure 2.7:** Randomly distributed carbon nanotubes in polymer matrix (left: SEM image, right: schematic).

vertically aligned carbon nanotube (VACNT) and horizontally aligned carbon nanotube (HACNT) [34].
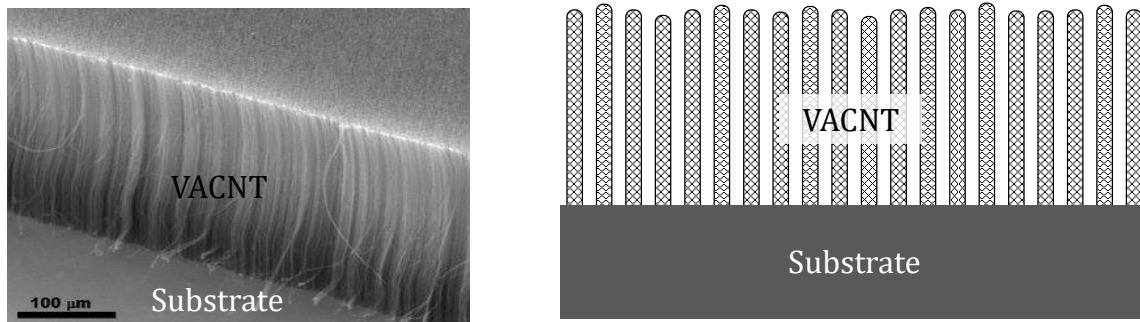


**Figure 2.8:** Vertically aligned carbon nanotube (left: SEM image (Source: Van Hooijdonk et al; licensee Beilstein-Institut), right: schematic).

The effective thermal conductivity of the VACNT depends on density, quality of the tubes (defects), poor interaction with CNTs and metals or polymers . However, the bottleneck of the heat path is the contact resistance between the free end of the VACNTs and the target surface due to the non uniform length of the VACNT and the rough surface of the substrate. Several methods have been proposed to deal with this issue, such as the application of pressure on the interface [8] or the thermocompression bonding, which uses a metal as an interface material between the CNT and the substrate [35], [36]. However, the industrial approach yielding the best results is the use of a heated polymer thin film as an adhesive layer at the CNT-substrate interface [7].

Several studies about the effective thermal resistance of VACNTs between two substrates have been reported. Xu and Fisher [37] found the thermal resistance of dry contact of CNT arrays (Cu-VACNT-Si) to be about 19.8 mm$^2 \cdot$K/W at 445 kPa. However, they found that the addition of a PCM to the free end of CNT array (Cu-PCM-VACNT-Si) substantially reduces the thermal resistance. At 350 kPa, the lowest resistance recorded
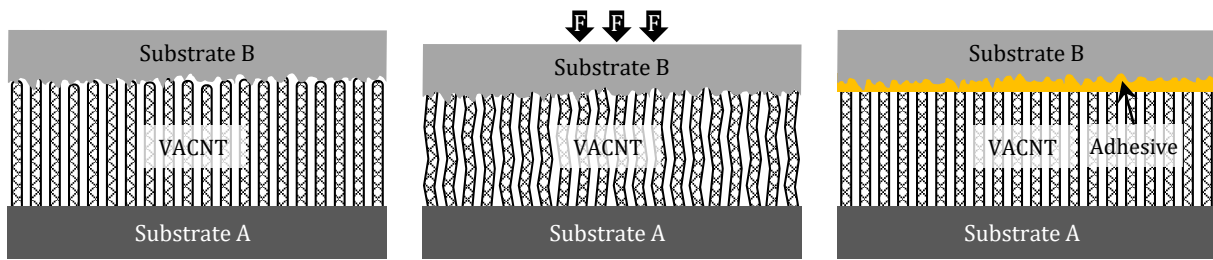
**Figure 2.9:** Different methods for assembly of VACNT; left: dry contact; middle: by applying pressure; right: gluing by thin polymer layer.

was 5.2 mm$^2 \cdot$ K/W, while the lowest resistance recorded for the PCM compound without CNTs was 16.2 mm$^2 \cdot$ K/W. In [38], an effective thermal resistance of 1 mm$^2 \cdot$ K/W has been reported where a thin indium layer has been used to connect the VACNT to a Cu substrate.

One of the disadvantages concerning the use of VACNT as TIM is the extremely high temperature of over 600 °C needed to grow the CNTs, which does not allow direct synthesis on electronic packages. Another concern is the weak adhesion between the CNTs and the substrate, on which the CNTs grew [39].

## 2.1.6  Die attach materials

Die attach materials (also called TIM1) are used to connect the chip to a substrate or lead frame. In addition to the thermal conductivity requirements, die attaches should also be electrically conductive. Therefore, solder, metallic and metal filled polymers are dominating the sector of die attach materials. Soldering is the established technology for die attach. A solder material should have a reasonably low melting point not to cause damage to electronics but not too low not to melt during the operation. Solder should be electrically and thermally conductive as well as environmentally friendly. Until the end of the 1990s, lead-based solders were typically used in the electronics industry due to their relatively low melting temperature. In recent years, efforts to develop alternatives to lead-based solders have increased dramatically. These efforts began as a response to potential legislation and regulations restricting lead usage in the electronics industry. Lead is extremely toxic when inhaled or ingested. As researchers began to focus on lead-free solders, they recognized their value in high temperature applications (e.g. automotive) where Sn/Pb solders do not meet the requirements. There are many factors to consider when developing lead-free alloys. These include manufacturability, availability, reliability, cost and environmental safety. Of these, the most challenging and time consuming is the reliability of alternative solders [40]. In table 2.4, melting temperature and thermal conductivities of some common solder alloys are shown.

**Table 2.4:** Melting temperature and thermal conductivity of selected solder alloys.

| Solder | Melting temperature [°C] | Thermal conductivity [W / (m · K)] | Ref. |
|---|---|---|---|
| AuSi (97/3) | 363 | 27 | [41] |
| AuSn (80/20) | 280 | 57 | [41] |
| SnCu (99.3/0.7) | 227 | 65 | [42] |
| SnAg (96.5/3.5) | 221 | 78 | [41] |
| SnAgCu (95.6/3.5/0.9) | 217 | 60 | [42] |
| SnAgCu (95.5/3.5/0.7) | 215-217 | 60 | [42] |
| SnPb (63/37) | 183 | 50 | [41] |

One of the most important reactions in the solder process is the intermetallic phase (IMP) between solder alloy and surface finish of substrate. Intermetallic phase or intermetallic compound (IMC) is defined as solid phase containing two or more metallic elements, whose crystal structure differs from that of the other constituents. For intermetallic phases the bonding between solder alloy and metallization of substrate is important. For example for SnAg solder alloy, Cu surface is best suited as Sn and Cu form the intermetallic compound $Cu_6Sn_5$ and $Cu_3Sn$. IMP is hard and brittle, i.e. it has high yield stress, high melting temperature and high stiffness. The intermetallic compound is responsible for the mechanical contact after soldering. It is a time and temperature dependent process, however the temperature has a higher influence on the growth rate of the IMP.
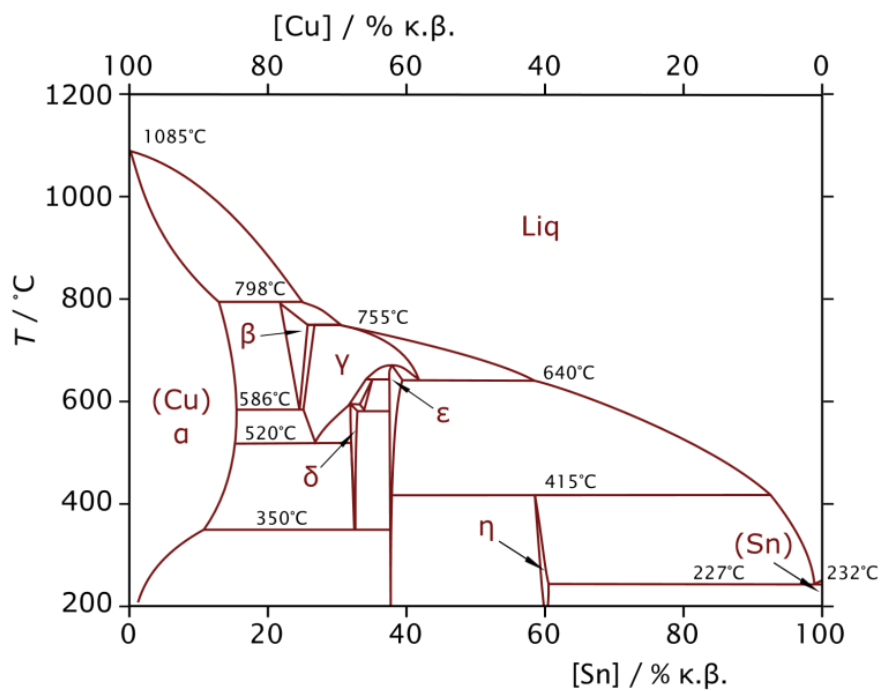


**Figure 2.10:** Cu-Sn phase diagram (*Source: H. Baker et al., Alloy Phase Diagrams*)

The effect of intermetallic phase (IMP) is used to create a solder process for high temperature application. By the so-called transient liquid phase bonding (TLPB) the whole solder layer is converted into intermetallics to obtain the compound with a higher melting temperature.

For example, when tin-based solder with the melting temperature of $217\,°C$ is plated between two Cu substrates and bonded under pressure and higher temperature than the eutectic temperature of the Sn, the Sn and the Cu will form the intermetallic compounds $Cu_6Sn_5$ and $Cu_3Sn$ with the melting temperature of $415\,°C$ (see figure 2.11).
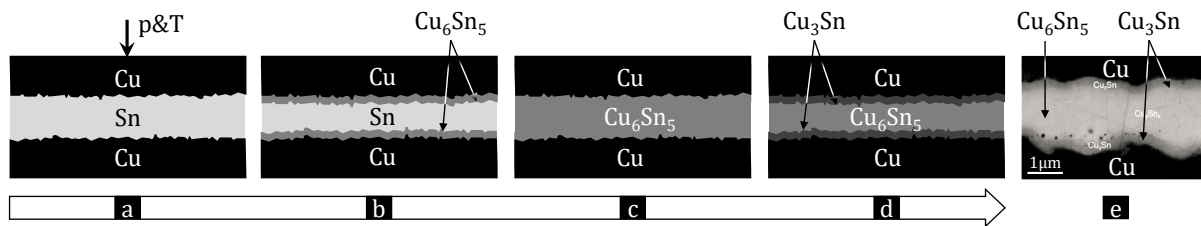


**Figure 2.11:** Process flow of transient liquid phase bonding. a: Sn bonded between Cu-substrates. b: Growth of $Cu_6Sn_5$ due to repaid diffusion of Cu into Sn to form liquid phase. c: Interdiffusion under temperature, $Cu_6Sn_5$ form until all Sn is consumed. d: Further interdiffusion under temperature, $Cu_3Sn$ form at interfaces. e: Cross section image, all Sn has been transformed and results in solder joint with melting temperature of $415\,°C$ [43].

Another promising die attach technology is sintering. Sintering is a method to compact and form a solid mass of materials from powder by heat and/or pressure without melting it to the point of liquefaction. Compared to soldering, sintering does not require a phase change. The link between the particles are governed by diffusion mechanisms to form first a porous material and then to reduce the porosity [44]. Silver sintering as die attach concept attracts increasing interest for technology fields like power electronics. The main advantages of sintered silver layer are the high thermal conductivity and the high temperature stability of the bond. The bonding temperature is similar to the bonding temperature of solders ($300\,°C$). However, the sintered silver bond withstands much higher working temperature in comparison to solder, due to the high melting temperature of silver of $961\,°C$ [4].

Physical properties (thermal, electrical and mechanical) of sintered silver depend on the porosity of the sintered joint, which on the other hand depends on the sintering parameters (pressure and temperature). Fully dense sintered silver interconnects are difficult to achieve. Up to a few tens of percent of porosity seem typical as reported in [45] and [46]. Additionally, lower applied pressures for sintering are continually being aimed, so resulting porosity in these sintered joints are likely to be higher. For example, it has been reported in [47] that porosity ranges between 5-20% when the pressure used in sintering was varied. These results have been also confirmed within this work (see section 6.5.2).

## 2.2 SoA of thermal characterization methods

Several experimental techniques exist for thermal characterization of materials and components used in electronics industry. Due to the fact, that the different material classes and their properties cannot be characterized by one method, different types of techniques are needed, which enable characterization of the different material classes having different mechanical properties as well as different thermal properties which are mainly bulk thermal conductivity, effective thermal conductivity, thermal resistance, thermal interface resistance, thermal diffusivity, heat capacity, and all these properties as function of temperature, pressure, surface finishes etc. In the following, the most important characterization techniques will be elucidated.
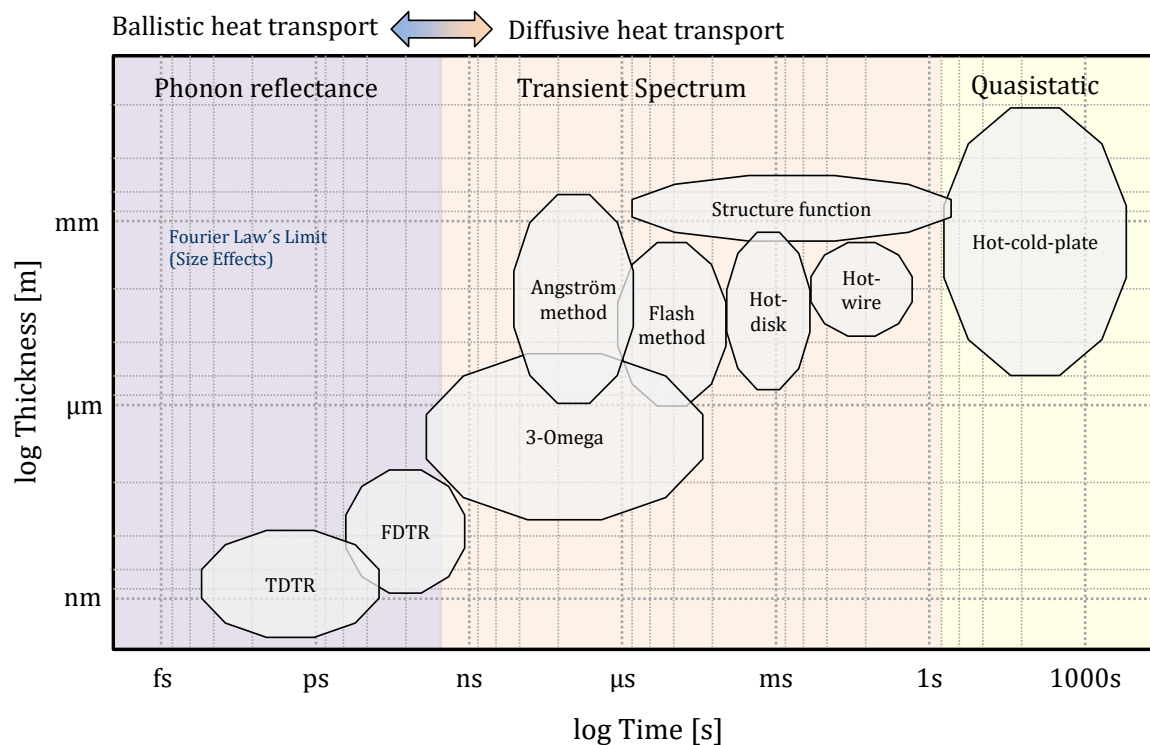
**Figure 2.12:** Overview of thermal characterization methods.

As illustrated in figure 2.12, macroscopic layers underlie quasi-static process and can be typically characterized by steady state methods such as hot-cold-plate method. For materials with higher thermal diffusivity with temperature changes between a few $\mu s$ up to a few seconds, transient techniques are used, this transient techniques can be pulse based methods such as flash method or modulated methods such as $3\omega$ method or Ångström's method. For even more rapid thermal processes, as can be expected for nanoscale layers and geometries below the Fourier Law's limit size effects (e.g. phonon confinement or ballistic heat transport) phonon-based methods such as time-domain thermoreflectance

(TDTR) or Frequency domain thermoreflectance (FDTR) are expected to be applied.

## 2.2.1 Steady-state techniques

The steady-state method is commonly used and in principle the simplest way to measure thermal resistance and conductivity of thermal interface materials (TIMs). The sample has to be positioned between a hot and a cold plate with constant temperatures, whereby a temperature gradient arises across the sample and heat flows through the sample. To determine the thermal resistance of the sample the heat flow and the temperature gradient have to be measured. The steady-state method for TIM characterization has been defined in several standards. The mostly used, well known and often imitated method is the standard ASTM D5470 [5], which is a testing method with almost one-dimensional heat flow, in which the sample is placed between two metal cylinders with co-planar surfaces. One cylinder is heated while the other one is fixed on a cooler. Uniform heat flow is established through the two cylinders and the sample. Heat flow and temperature gradient over the sample are measured by thermocouples, which are integrated in the cylinder sockets.
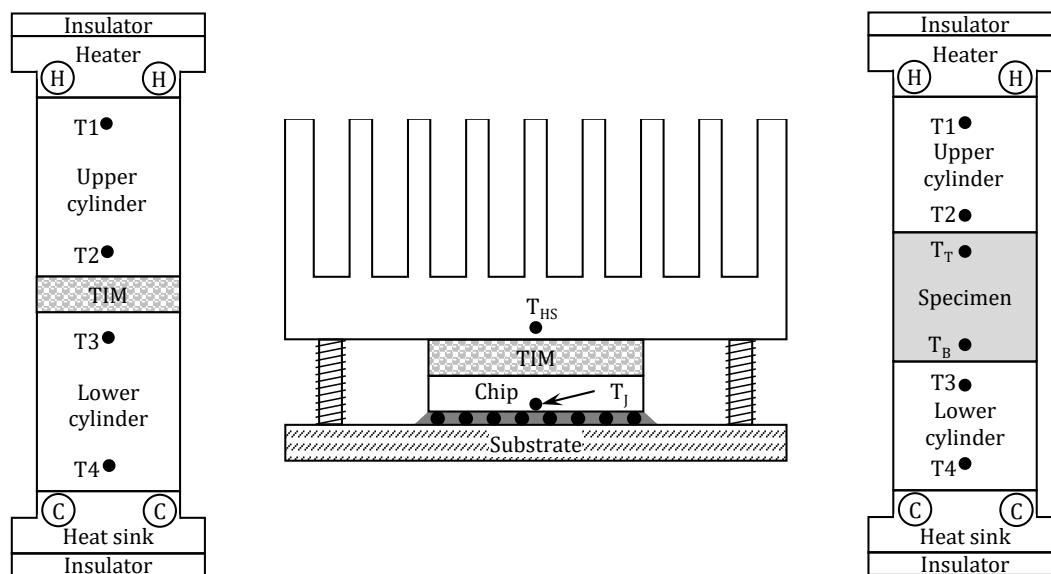


**Figure 2.13:** Schematic of steady-state methods for thermal characterization of TIM and solid materials. Left: ASTM standard D5470. Middle:JEDEC standard JESD51-3. Right: ASTM standard E1225.

A further steady-state method used for TIM characterization is based on the JEDEC standard JESD51-3 [9]. In this method, the TIM is tested between a thermal test chip (TTC) and a heat sink. The thermal test chip consists of heater and temperature sensor and is assembled onto the substrate by flip chip technology. Such type of device is also called thermal test vehicle (TTV). By measuring the junction temperature of the chip and

temperature of the heat sink, the thermal resistance of the TIM including the thermal interface resistances to chip and heat sink can be calculated.

In chapter 4, the newly developed measurement techniques will be presented which overcame different insufficiencies of the above mentioned standard methods with respect to several technical applications.

The steady-state method can be also used for thermal conductivity measurement of solid samples based on the ASTM standard E1225. The measurement principle of this method is similar to the ASTM standard D5470, which is described above. However, the temperature gradient of the sample is measured direct in the sample using temperature sensors integrated in defined distance in the sample. This technique is limited to homogeneous and solid samples with certain geometry that allow integration of temperature sensors. For thermal characterization of thin samples such as metal foil or ceramic plate, in which temperature sensors cannot be integrated, an innovative steady state technique has been developed and realized within this work. This will be presented in chapter 6.

### 2.2.2 Transient flash method

The flash method (also known as laser flash method) is a transient and contactless method for measurement of thermal diffusivity of solid uniform materials. The method was developed by Parker et al. in 1961 [11]. One side of the sample is irradiated by a short energy pulse from a laser or a flash lamp. The time-dependent temperature rise at the sample backside is measured by an IR detector. Figure 2.14 shows a schematic of the laser flash set up.
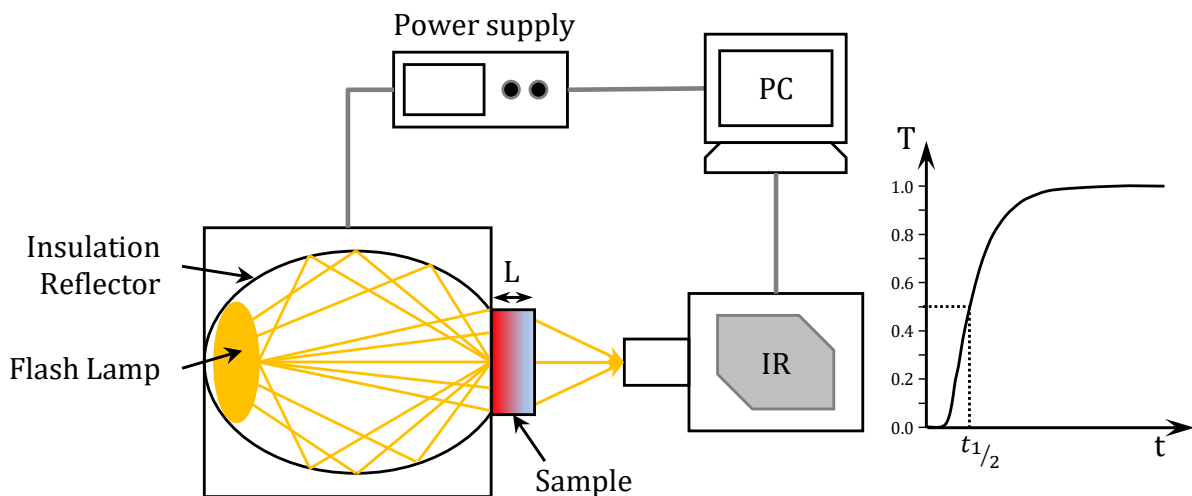


**Figure 2.14:** Schematic of laser flash set up for thermal diffusivity measurement of solid samples

The thermal diffusivity ($\alpha$) of the sample is calculated from the temperature rise of the backside of the sample by following equation:

$$\alpha = 0.1388 \cdot \frac{L^2}{t_{1/2}} \tag{2.1}$$

where, $L$ is the thickness of the sample and $t_{1/2}$ is the time to the half of the maximum.

Using equation 2.1 the thermal conductivity $\lambda$ can be obtained through the expression of equation 2.2

$$\lambda = \alpha \cdot \rho \cdot c_p \tag{2.2}$$

where $\rho$ is the density and $c_p$ is the specific heat capacity of the sample. The work of Parker et al. [11] has been further developed by Cowan in 1963 by introducing corrections for non-adiabatic measurement conditions [48].

The laser flash technique can also be used for characterization of heterogeneous and multilayer samples. In [49] and [50] methodology for this investigation was derived. The technique is based on measuring the effective thermal diffusivity of the heterogeneous structure or multilayer samples, which are treated as homogeneous material. Using an iterative algorithm, the total thermal resistance $R_{th}$ of a multilayer can be extracted. The multilayer may also consist of TIM layer sandwiched between two substrates with known thermophysical properties (thermal diffusivity, density and specific heat capacity). The total thermal resistance $R_{th}$ includes the thermal resistance of the TIM $R_{th,TIM}$ and two interface resistance $R_{th,int}$ (TIM to substrates).

$$R_{th} = R_{th,TIM} + 2 \cdot R_{th,int} = \frac{BLT}{A \cdot \lambda_{TIM}} + 2 \cdot R_{th,int} \tag{2.3}$$

Hence, by variation of the bond line thickness (BLT) of the TIM its bulk thermal conductivity $\lambda_{TIM}$ and the interface resistance $R_{th,int}$ can be extracted by linear regression of $R_{th}$ versus the $BLT$ [51], [52].

### 2.2.3   Thermal impedance techniques

Thermal impedance $Z_{th}$ is defined as the difference in temperature between two isothermal surfaces divided by the heat flow entering the hotter of the two surfaces. Thermal impedance at thermal equilibrium is synonymous with thermal resistance. When determining the thermal impedance, the powering condition and duration must be specified, whereas thermal resistance is only defined at thermal equilibrium. Defining $T_j$ and $T_x$ as

the hot and cold isothermal surface temperatures respectively and the total heat flow rate entering the isothermal surface at temperature $T_j$ as $P$, the thermal impedance between these surfaces is:

$$Z_{th} = \frac{T_j - T_x}{P} \tag{2.4}$$

Thermal impedance is simply thermal resistance without the condition of equal heat flux across both isotherms. This inequality occurs when heat capacitances between the isothermal surfaces are storing heat energy prior to thermal equilibrium [53].

The thermal impedance concept is analogous to electrical impedance. Electrical impedance includes resistances, capacitances and inductances. However, capacity and inductance occur only in transitional periods. For direct currents only the presence of resistance is apparent. This situation is precisely analogous to thermal impedance although electrical inductors have no thermal analogy.

Measurement of thermal impedance is widely used for thermal characterization of electronic packages. One of the important values for package characteristic is the junction-to-case thermal resistance $Rth_{JC}$, which comprises the thermal resistance of all layers between the chip and the case of the package that is normally mounted onto the heat sink.
The junction-to-case thermal resistance $Rth_{JC}$ can be determined by measuring the junction temperature of the chip $T_j$, the case temperature $T_c$ and the heating power dissipation $P$ at steady-state condition. $Rth_{JC}$ can be determined according to equation 2.4. Another method to determine the junction-to-case thermal resistance is by measuring $Z_{th}$ as a function of time during cooling or heating of the device [54]
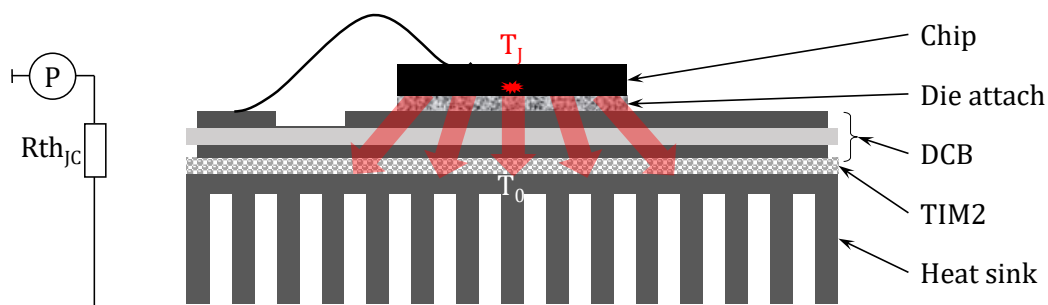


**Figure 2.15:** Schematic of electronic package showing the package layers from chip to heat sink

To record the heating curve, the heating of the device should be done simultaneously with the sensing of the temperature at the junction level of the chip. For the cooling curve, the device is heated to steady-state and then switched off while the junction temperature is recorded (see figure 2.16).
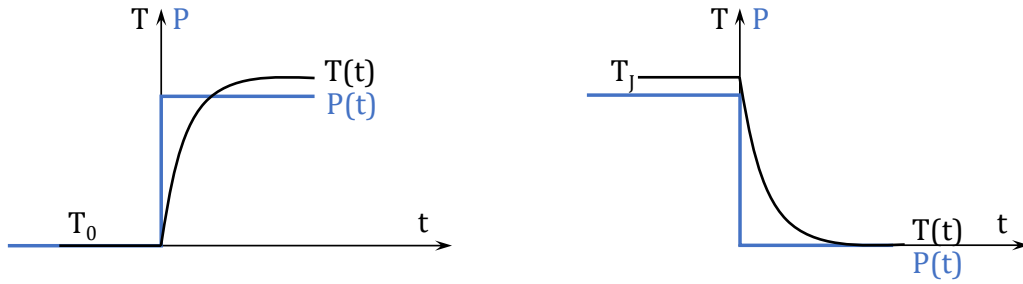
**Figure 2.16:** Transient temperature curve. Left: heating curve. Right: cooling curve

From the heating or cooling curves the thermal impedance curve over the time can be generated by equation 2.5 for cooling curve or equation 2.6 for the heating curve.

$$Z_{th}(t) = \frac{T_0 - T_j(t)}{P} \tag{2.5}$$

$$Z_{th}(t) = \frac{T_j(t) - T_0}{P} \tag{2.6}$$

Due to the fact that the temperature sensitive element of some semiconductor devices (e.g. MOSFET, IGBT) cannot be used during the operation, the recording of the cooling curve is often more convenient.

The thermal impedance curve ($Z_{th}(t)$) provides valuable insights into the cross sectional disposition of thermal resistances and capacitances within the component.
There are several methods to determinate the junction-to-case thermal resistance from the thermal impedance curve. The simplest and mostly used method is the so called "Dual Interface Method", which is covered by the JEDEC Standard JESD 51-14 [54].
The thermal impedance of the package is measured under different conditions e.g. with and without TIM2 (TIM between substrate and heat sink) and plotted over the log time scale, the junction-to-case thermal resistance is the point of the separation of the curves (figure 2.17).
This approach can also be used to measure bulk thermal conductivity ($\lambda_{bulk}$) of the TIM. Through variation of the TIM thickness, the increase of the total thermal resistance ($R_{th}$) represents the thermal resistance of the additional TIM thickness. Plotting the total thermal resistance of the package over the TIM thickness results in a linear function, the bulk thermal conductivity of the TIM can be determined from its slope ($a$).

$$\lambda_{Bulk} = \frac{1}{a \cdot A} \tag{2.7}$$

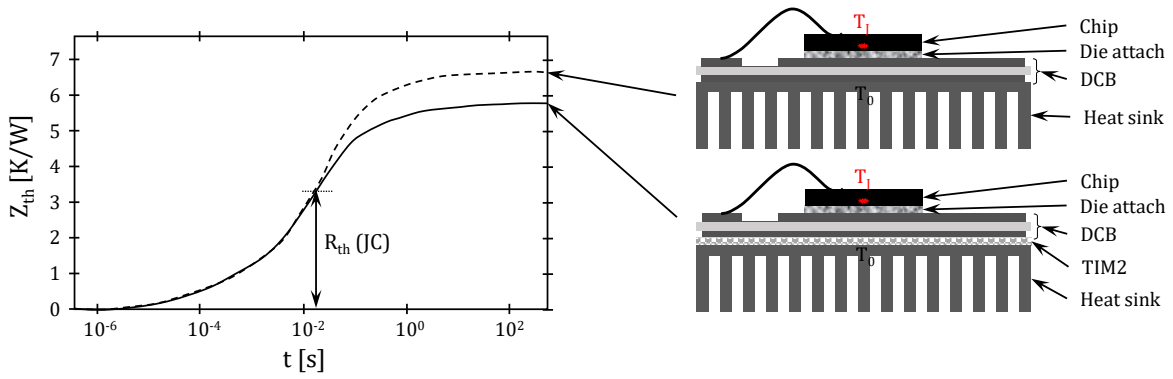where $A$ is the cross sectional area of the contact.

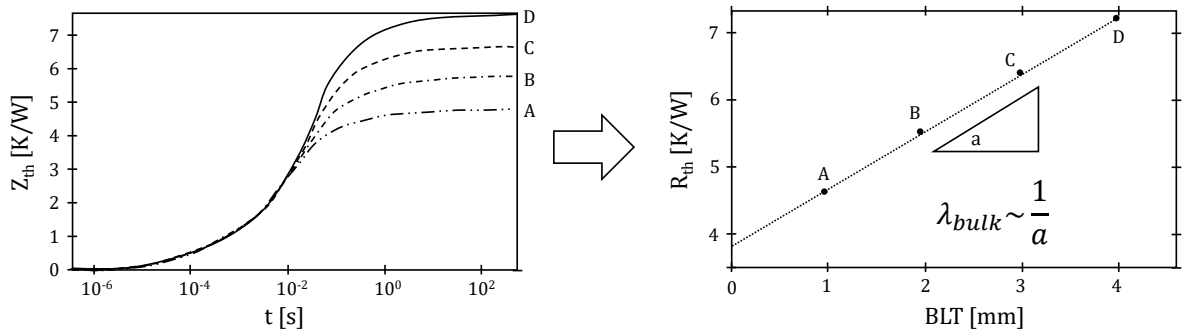**Figure 2.17:** Thermal impedance curves of electronic package with and without TIM



**Figure 2.18:** Left: thermal impedance curves of electronic package with TIM in different thicknesses. Right: total thermal resistance of the package ($R_{th}$) as function of the TIM bond line thickness (BLT), the bulk thermal conductivity of the TIM ($\lambda_{bulk}$) results from the slop

Another well-known method to extract the thermal resistance of each layer between the heat source and heat sink of the package is the so-called structure function analysis method, which transforms the thermal transient measurement result into a thermal capacitance vs. thermal resistance profile, providing detailed thermal information of each layer from junction to ambient [55], [56].

Structure function is direct model of one-dimensional heat flow. It is an interpretation of the thermal impedance of a Cauer network, which is transferred from Foster network. Foster model is accessible from mathematical point of view as it does not contain any complicated calculation, however carrying no physical signification. In contrast, Cauer model corresponds to physical structure. However, they are challenging to interpret. Structure functions are a graphical representation of hard to interpret Cauer model. Considering a electronic package mounted on a heat sink and consists of four layers, i.e. chip, die attach, substrate and TIM (figure 2.19 (a)). First the package is modelled in its equivalent Cauer network. If the layer stack is divided into numerous slices with a thickness of $\Delta x$ each along the heat flow, i.e. from the junction to the heat sink, each

slice can be modelled as resistance and shunt capacitance in a Cauer network (figure 2.19 (b)). The cumulative structure function defines this infinite Cauer ladder directly. As $\Delta x \to 0$ number of stages in the Cauer network tends to infinity. The cumulative structure function starts with the junction at the top most end, which is the source of heat and ends at the point of singularity, i.e. an ideal heat sink on the bottom most end. The y-axis i.e $C_\Sigma = \sum_{i=1}^{n} C_i$ with units [J/K] is sum of Cauer capacitances and is in logarithmic scale. The x-axis, i.e $R_\Sigma = \sum_{i=1}^{n} R_i$ with units [K/W] is the sum of Cauer resistances and in linear scale. Typically, cumulative structure functions are plotted in lin-log scale (figure 2.19 (c)) [54].
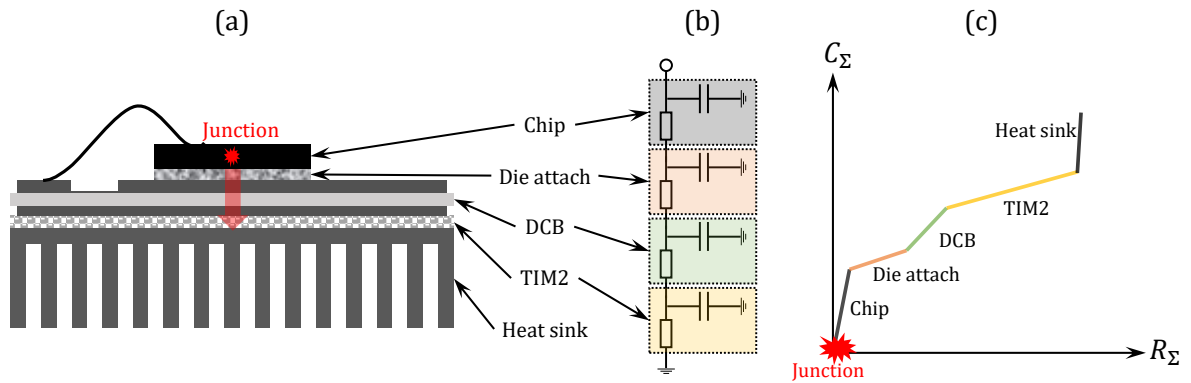


**Figure 2.19:** (a): Schematic of package layers, (b): network representing the layer, (c): graphical representation of the network, i.e. cumulative structure function

## 2.2.4 Three-omega method

The $3\omega$ method is an alternating electrical current technique to measure the thermal conductivity of bulk materials as well as thin films in micro- to nanoscale [57], [58], [59], [60]. The method was developed in the beginning of the $20^{th}$ century. However, it became popular in the Nineties of the $20^{th}$ century thanks to David Cahill, who derived the analytical solution of the temperature amplitude for a heater substrate system to determine the thermal conductivity of the substrate [61], [62]. Contemporary literature dealing with the $3\omega$ method refers mostly to Cahill's prominent work.

The $3\omega$ method uses a thin wire of metal with a preferably high temperature coefficient of resistance. The metallic wire is deposited onto an electrically insulated substrate with four contacts for electrical measurement.

Figure 2.20 shows a typical set-up, where the metal strip, which acts as heater and thermometer, is driven by an alternating current $I(t)$ with angular frequency $\omega$
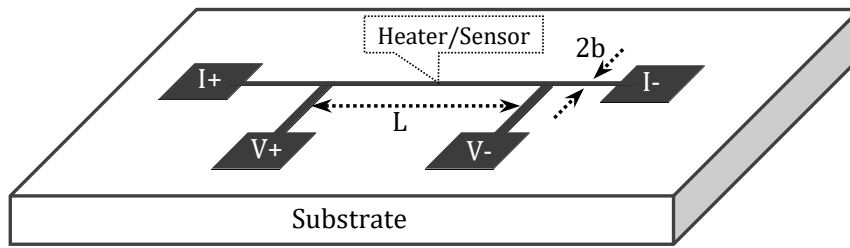
$$I(t) = I_0 \cdot \cos(\omega t) \tag{2.8}$$

**Figure 2.20:** Typical layout of a $3\omega$ structure as used in many applications for measurement of thermal conductivity

where $I_0$ is the current amplitude passing through the heater. Due to the Joule heating, the electrical resistance of the metallic strip is changing. The power $P$ is defined as

$$P(t) = R(t) \cdot I^2(t) \tag{2.9}$$

$$\Rightarrow P(t) = R_0 \cdot I_0^2 \cdot \cos^2(\omega t) \tag{2.10}$$

$$\Rightarrow P = \frac{1}{2} \cdot R_0 \cdot I_0^2 \cdot (1 + \cos(2\omega t)) \tag{2.11}$$

By the reason, that the resistance of the heater is linearly proportional to the temperature rise of the heater, the general temperature rise of the heater and the surrounding materials is also composed of two components, a steady-state part $T_0$ and an alternating part $\Delta T$. The general temperature rise can be written as:

$$T(t) = T_0 + \Delta T \cdot \cos(2\omega t + \varphi_{2\omega}) \tag{2.12}$$

where:

- $T_0$ is the steady-state temperature, increasing due to time independent component of power $P_0$

- $\Delta T$ is the temperature oscillation by the time dependent components of power $P(t)$

- $\varphi_{2\omega}$ is a phase shift.

Figure 2.21 shows exemplarily the heating power and the general temperature behavior of the heater as function of the time.

The general temperature profile and the phase shift in the heater depends on the thermal diffusivity of the sample, on which the heater is deposited.
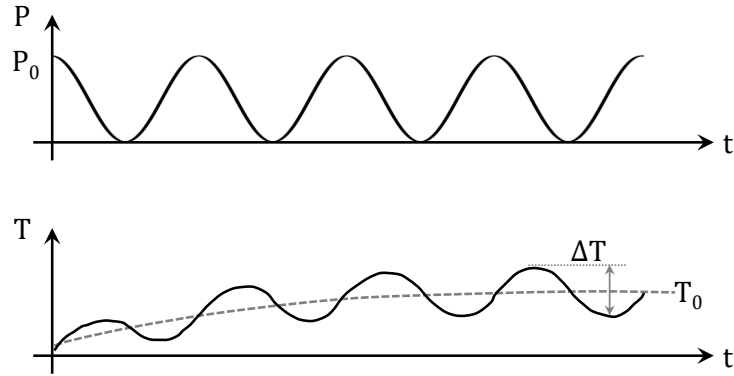
**Figure 2.21:** Heating power and temperature behavior of the heater as function of the time.

Due to its temperature dependency, the resistance of the heater $R$ increases by the steady-state temperature $T_0$ to $R_0$ and oscillates with the amplitude $\Delta R$ around this resistance at the modulated frequency $2\omega$.

$$R(t) = R_0 + \Delta R \cdot \cos\left(2\omega t + \varphi_{2\omega}\right) \tag{2.13}$$

Substitution of equation 2.8 and 2.13 into Ohm's law leads to the voltage signal $V(t)$.

$$
\begin{aligned}
V(t) &= I(t) \cdot R(t) & (2.14)\\
&= I_0 \cdot \cos\left(\omega t\right) \cdot R_0 + \Delta R \cdot \cos\left(2\omega t + \varphi_{2\omega}\right) & (2.15)\\
&= I_0 \cdot R_0 \cdot \cos\left(\omega t\right) + \frac{I_0 \cdot \Delta R}{2}\left(\cos\left(2\omega t + \varphi_{2\omega} + \omega t\right) + \cos\left(2\omega t + \varphi_{2\omega} - \omega t\right)\right) & (2.16)\\
&= I_0 \cdot R_0 \cdot \cos\left(\omega t\right) + \frac{I_0 \cdot \Delta R}{2}\left(\cos\left(3\omega t + \varphi_{2\omega}\right) + \cos\left(\omega t + \varphi_{2\omega}\right)\right) & (2.17)
\end{aligned}
$$

The modulated voltage $V(t)$ measured at the inner pads of the $3\omega$ structure (figure 2.20) contains information at $1\omega$ and $3\omega$.

The amplitude of the third harmonic component of the voltage is

$$V_{3\omega} = \frac{I_0 \cdot \Delta R}{2} \tag{2.18}$$

The oscillated resistance $\Delta R$ is given as

$$\Delta R = \frac{dR}{dT} \cdot \Delta T \tag{2.19}$$

where $dR/(dT \cdot R)$ is the specific temperature coefficient of the heater and $\Delta T$ is the amplitude of the temperature oscillation of the heater [62].

$$\Rightarrow \Delta T = \frac{dT}{dR} \cdot \Delta R \;=\; 2 \cdot \frac{dT}{dR} \cdot \frac{V_{3\omega}}{I_0} \;=\; 2 \cdot \frac{dT}{dR} \cdot \frac{R_0}{V_{1\omega}} \cdot V_{3\omega} \tag{2.20}$$

The thermal conductivity of the sample is identified by the relation between the voltage measured in experiments and the analytically described temperature amplitude. The mostly used analytical model to extract the thermal conductivity of the substrate is the so-called slope method, which states that using the $3\omega$ voltage measured at two frequencies $\omega_1$ and $\omega_2$, and the thermal conductivity $\lambda$ is calculated from [61]

$$\lambda = \frac{V_{1\omega}^3 \cdot \ln(\omega_2/\omega_1)}{4\pi \cdot L \cdot R_0^2 \, (V_{3\omega,1} - V_{3\omega,2})} \cdot \frac{dR}{dT} \tag{2.21}$$

where $L$ is heater length, $V_{3\omega,1}$ is the in-phase $3\omega$ voltage at frequency $\omega_1$ and $V_{3\omega,2}$ is the in-phase $3\omega$ voltage at frequency $\omega_2$. This equation is however only valid for a sufficiently narrow (ca. 10 µm or less) and long heater (ca. 1000 µm or more).

Due to the fact that the conventional $3\omega$ method requires equipment for the deposition of a narrow, thin metal heater line on top of the sample, the method did not find widespread use at industrial level. Furthermore, deposition of a metal heater line, which is usually done by lithography, is impossible for many materials, such as liquids or pastes. For the characterization of such samples, an innovative approach uses an extension of the $3\omega$ method, the so-called bidirectional $3\omega$ method [63], [64], [65], [66]. For this method, the sensor is first fabricated on a substrate and then covered by a thin passivation layer to allow characterization of electrically conductive materials. The sample is placed on top of this platform. Therefore, no fabrication steps are needed after the application of the sample. Furthermore, this concept does not set requirements on the sample material as it does not need to withstand the sensor fabrication processes. The bidirectional $3\omega$ approach has been used, for example, for the investigation of liquids [66], [67], solids [68], gases [69], biological tissues [70] and single cells [71].
Own developments of procedure and test stand have been undertaken in cooperation with other colleagues but is not iuncluded in this thesis (see [72])

### 2.2.5 Hot-wire method

The hot-wire method is a transient method for thermal conductivity measurement of isotropic samples. The method uses a thin and long wire as heat source embedded in the sample. The thermal conductivity of the samples can be deducted from the resulting temperature rise in a defined distance from the hot wire over a specified time interval [73]. The theory behind this method was developed by Carslaw and Jaeger [74].

To determinate the thermal conductivity $\lambda$, it is presupposed that the heat source has a continuous and uniform heat flow along the medium where the wire is embedded. Also the medium itself should be isotropic with constant initial temperature. The thermal conductivity of the sample is given by equation 2.22

$$\lambda = \frac{q}{4\pi} \frac{\ln t_2 - \ln t_1}{T_2 - T_1} \tag{2.22}$$

where $q$ is heat input per unit length of wire, $T_1$ is the temperature of the line at the time $t_1$ and $T_2$ is the temperature of the line at $t_2$.

The hot-wire method is commonly used to measure low thermal conductivity materials, such as soils [75], ice cores [76], and powdered materials. This method has also been commonly used for measuring the thermal conductivity of fluids with high degree of accuracy [77], [78], [79] and [80]. ASTM C1113 and ISO 8894 specify more details on apparatus and test procedure for the measuring of refractories using the hot-wire method.

### 2.2.6 Hot-disk method

The hot-disk method or transient plane source method uses a metal strip or disk, which acts as both, heat source and temperature sensor. The metal disk is usually electrically insulated to allow characterization of electrically conductive samples. The method typically employs two sample halves, in-between the metal is sandwiched. All other surfaces of the test samples are thermally insulated.
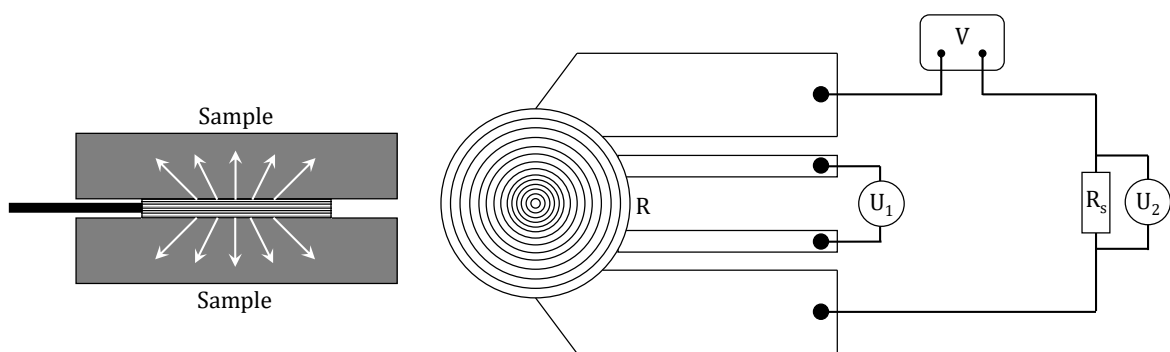


**Figure 2.22:** Top and cross-sectional views of hot-disk method

The sensor operates as heat source and simultaneously as resistance thermometer. A small constant current is applied to the metal disk to heat it up. The mean temperature $T$ of the sensor can be calculated from the mean resistance $R(T)$ using the equation

$$R(T) = R_0[1 + \beta(T - T_0)] \tag{2.23}$$

where $T_0$ is the initial temperature, $R_0$ the initial resistance of the hot-disk sensor at the temperature $T_0$ and $\beta$ is the temperature coefficient of resistance (TCR) [81].

Since the temperature increase of the metal disk is highly dependent on the two testing samples attached to it, thermal properties of the testing samples can be determined by monitoring this temperature increase for a short time period. The measured $\Delta T$ renders the inverse of thermal conductivity:

$$\Delta T(\tau) = \frac{P_0}{\pi^{3/2} \cdot r \cdot \lambda} \cdot D(\tau) \tag{2.24}$$

Where $P_0$ is the heat liberation from the sensor, $\lambda$ is the thermal conductivity of the sample, r is the radius of the disk and $\tau$ is given by:

$$\tau = \frac{\sqrt{\alpha \cdot t}}{r} = \sqrt{\frac{\alpha \cdot t}{r^2}} \tag{2.25}$$

where $\alpha$ is the thermal diffusivity of the sample, $t$ is the measurement time. $D(\tau)$ is a dimensionless theoretical expression of time-dependent increase that describes heat conduction of the sensor [82].

It has been reported that the hot-disk method has the capability to measure thermal conductivity ranging from 0.005 to 500 W/m·K including liquids, aerogels and solids [83], [84]. The hot-disk method has been specified by ASTM D7984 and ISO 22007-2 standards.

### 2.2.7 Conclusion

This chapter reviewed the measurement techniques for thermal characterization of materials used in electronic packages with mean focus on thermal interface materials. There are many characterization methods for determination of thermal properties. When selecting a measurement technique, various aspects should be considered, e.g:

- Geometry and size, surface roughness and preparation procedure of the sample, whose thermal properties is to be determined.
- Limitation of the measurement technique to a specific range of thermal properties.
- Potential error sources and their effect of the final results

Table 2.5 gives an overview about the most important characterization methods, their measurement range, advantages and disadvantages.

**Table 2.5:** Overview of thermal characterization techniques

| Measurement method | Material type | Thermal conductivity range [W/(m·K)] | Measurement of thermal interface resistance | Advantages | disadvantages |
|---|---|---|---|---|---|
| Steady-state based on ASTM D5470 | Paste, adhesive, pads, gals, | 0.01 - 50 | yes | Determination of bulk thermal conductivity and thermal interface resistance, measurement under different pressure and temperatures | Not suitable for highly thermal conductive and thin samples |
| Steady-state based on ASTM E1225 | Metals, metallic alloys, cylindrical shape | 10 - 1000 | no | High accuracy, direct measurement of thermal conductivity | Temperature sensors must be inserted into the sample, heat losses at higher temperature |
| Thermal impedance techniques | Package, TIMs and Die attach within a package | 0.01 - 50 | (yes) | TIM measurement under real application within a package | Requires active device with temperature sensitive element |
| Traditional $3\omega$ Method | Solid bulk and thin film | 0.01 - 1000 | no | High accuracy, negligible environmental effects, capable for thermal diffusivity measurement | requires lithographic structures ($3\omega$ sensor) on the sample |
| Bidirectional $3\omega$ Method | Liquids, gels, pastes, gases, biological tissues | 0.1 - 500 | no | High accuracy, negligible environmental effects, drop in specimen, capable for thermal diffusivity measurement | Requires lithographic structures ($3\omega$ sensor) on a low thermally conductive substrate |
| Transient flash method | Solid metals, metallic alloys, polymers, ceramics. | 1 - 1500 | yes | Measurement of mono and multilayer samples | Specific heat capacity and density needed for calculation of thermal conductivity |
| Hot-wire | Isotropic and refractory materials, liquid, powder | 0.02 - 2 | no | Small size probe, drop in specimen | Apply to low conductivitymaterials |
| Hot-Disk | Liquids, aerogels, solids | 0.005 - 500 | no | Apply to wide range of materials | Requires two samples with minimum one entirely planar side, interface between sensor and samples effects the accuracy |

# Chapter 3

# Theoretical Background

This chapter describes the basic theoretical principles necessary for understanding the test methods developed and realized in test stands within this thesis. However, more specific details are described in the respective chapter.

## 3.1 Mechanisms of heat transfer

Heat is transferred as result of a temperature gradient. It flows from regions of higher temperature to regions of lower temperature. Heat transfer occurs by three basic mechanisms: conduction, convection and radiation. In the following sections, these mechanisms will be discussed, however, the focus will be on the conduction due to its importance for this work.

### 3.1.1 Conduction

Conduction is transfer of heat from regions of higher temperature to lower temperature. The conduction process takes place at the molecular level and involves the transfer of energy from the more energetic molecules to those with a lower energy level [85]. In non-electrically conductive solids heat is transferred by lattice vibrations caused by atomic motion (phonons), while in electrically conductive solids, heat transfer happens due to both, the motion of free electrons, which move from high temperature region to low temperature region with smaller kinetic energy of molecules and due to phonons [86]. The lattice vibrations have the smaller contribution to the heat transfer process in electrically conductive solids [87].

At the microscopic level the heat flux $q$ $\left[\mathrm{W/m^2}\right]$, which is the heat rate per unit area along the direction x, is proportional to the temperature gradient:

$$q = -\lambda \frac{dT}{dx}, \tag{3.1}$$

where the proportionality constant $\lambda$ $[\mathrm{W/(m \cdot K)}]$ is the thermal conductivity, which is a material property. The minus sign indicates that heat is transferred in the direction of decreasing temperature. The equation 3.1 is the one-dimensional form of Fourier's law of heat conduction. The general form of Fourier's law, where the heat flux $q$ is recognized as vector quantity $\vec{q}$, can be written as:

$$\vec{J}_{th} = \vec{q} = -\lambda \cdot \vec{\nabla} T \tag{3.2}$$

where $\nabla$ the three-dimensional gradient operator and $T$ the scalar temperature field.

Considering a one-dimensional heat flow along the $x$ direction in the planar wall as shown in figure 3.1, a direct application of equation 3.1 can be made, and then the integration results in

$$q = \frac{\lambda}{L} \ (T_1 - T_2) \tag{3.3}$$
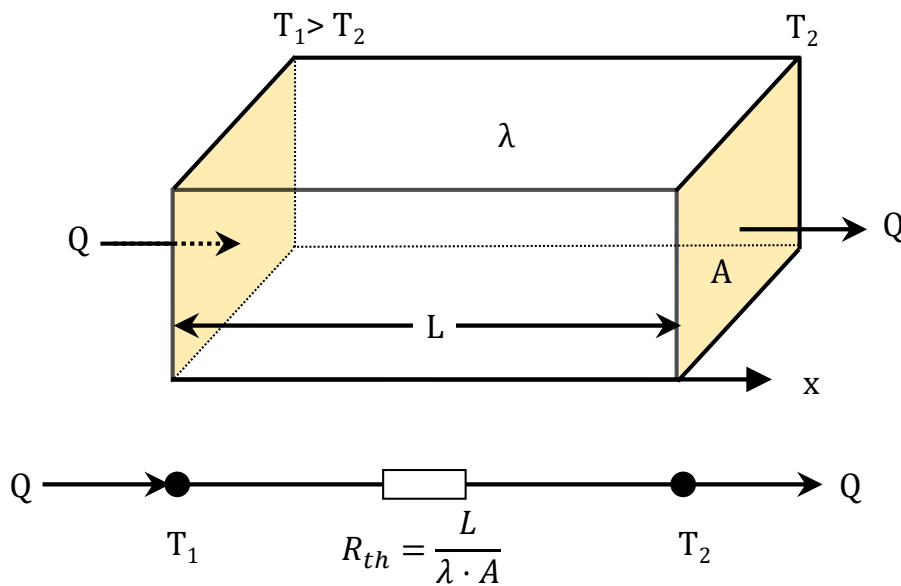


**Figure 3.1:** One-dimensional heat conduction through a plane wall.

The heat flow $Q$ [W], which is the heat energy transferred through the area, is the product of heat flux $q$ $[\mathrm{W/m^2}]$ and the area $A$ $[\mathrm{m^2}]$.

$$Q = q \cdot A = \frac{\lambda \cdot A}{L} \ (T_1 - T_2) \tag{3.4}$$

The thermal resistance $R_{th}$ of the planar wall with the area $A$, the thickness $L$ and the

thermal conductivity $\lambda$ is given by following equation:

$$R_{th} = \frac{L}{\lambda \cdot A} \tag{3.5}$$

By inserting equation 3.5 into equation 3.4 the following equation results for heat flow:

$$P = Q = \frac{\Delta T}{R_{th}} \tag{3.6}$$

It can be seen that an analogy exists between equation 3.6 and the equation of Ohm's law, where heat flow $Q$, thermal resistance $R_{th}$ and temperature gradient $\Delta T$ are equivalent to electrical current $I$, electrical resistance $R$ and electric potential $V$.

Therefore, equivalent thermal circuits may also be used for more complex systems, such as a multi-layer system. Such systems may involve any number of series and parallel thermal resistances. For example see the series composite wall of figure 3.2.
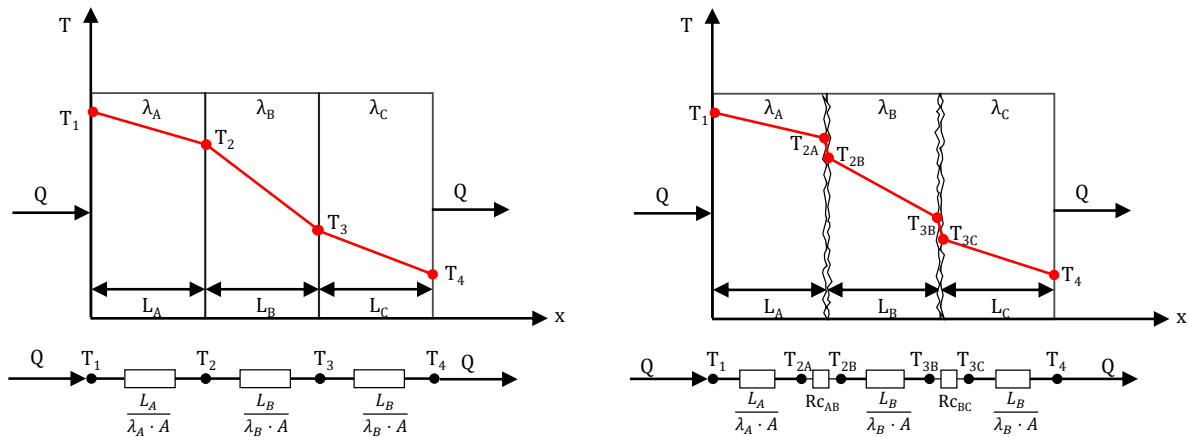


**Figure 3.2:** One-dimensional heat conduction through a three-layer system. Left: ideal interfaces with perfect match between the surface. Right: real interfaces with microscopical viods between the surfaces due to surface roughness.

The left diagram of figure 3.2 represents perfect interfaces between the layers of the system, while the right diagram takes into account real interfaces between the layers, which may be appreciable in the temperature drop across the interfaces.
The one-dimensional heat transfer rate for this system may be expressed as:

$$Q = \frac{T_1 - T_4}{\Sigma R_{th}} \tag{3.7}$$

where $T_1 - T_4$ is the overall temperature difference and the summation includes all thermal resistances. The total resistance of the ideal system in figure 3.2 is the summation of the thermal resistance of layers A, B and C

$$R_{th(tot)} = R_{th(A)} + R_{th(B)} + R_{th(C)} \tag{3.8}$$

$$\Rightarrow R_{th(tot)} = \frac{L_A}{\lambda_A \cdot A} + \frac{L_B}{\lambda_B \cdot A} + \frac{L_C}{\lambda_C \cdot A} \tag{3.9}$$

In the case of the system with real interfaces the total thermal resistance is given as following:

$$R_{th(tot)} = R_{th(A)} + Rc_{(AB)} + R_{th(B)} + Rc_{(BC)} + R_{th(C)} \tag{3.10}$$

$Rc_{AB}$ is the thermal contact resistance between layer A and layer B and $Rc_{BC}$ is the thermal contact resistance between layer B and layer C. They are defined as:

$$Rc_{(AB)} = \frac{T_{2A} - T_{2B}}{Q} \; ; \quad Rc_{(BC)} = \frac{T_{3B} - T_{3C}}{Q} \tag{3.11}$$

Besides the thermal conductivity, there is another important property related to the thermal conductivity, namely, the thermal diffusivity $\alpha \; [\mathrm{m^2/s}]$, which is also a material-specific property for characterizing transient heat conduction. This value describes the rate of heat transfer of a material from the hot side to the cold side.

$$\alpha = \frac{\lambda}{\rho \cdot c_p} \tag{3.12}$$

where $\lambda \; [\mathrm{W/(m \cdot K)}]$ is the thermal conductivity, $\rho \; [\mathrm{kg/m^3}]$ is the density and $c_p$ $[\mathrm{J/kg \cdot K}]$ is the specific heat capacity at constant pressure.

The thermal diffusivity indicates how quickly an input heat can cause rise in temperature with a material rather than it is stored in it. As it is observed in equation 3.12, the thermal diffusivity is directly proportional to the value of thermal conductivity and has a reverse dependency to specific heat capacity of the materials.

## 3.1.2 Convection

Convection is a transfer of heat from solid to fluid and within a fluid (gas or liquid). Heat transfer by convection includes two mechanisms. In addition to energy transfer by diffusion due to random molecular motion, energy is also transferred by bulk motion of fluid. This fluid motion is associated with the fact that a large number of molecules move together or as aggregates. Such a movement in the presence of a temperature gradient contributes to heat transfer.

In this work, the convective heat transfer between a fluid and solid is particularly interesting and must be considered, due to its influence on the measurement results of the

developed characterization methods. This type of heat transfer occurs when a fluid moving a long a solid surface and the solid surface are at different temperatures.

There are two types of convection, the so-called natural or free convection and the forced convection (figure 3.3).

Heat transfer by free convection occurs due to density difference in the fluid, which results from local volumetric expansion caused by temperature differences. Due to the pressure gradient induced by gravity, the fluid becomes buoyant, displaces and transfers the heat [20]. Heat transfer by forced convection generally makes use of a fan, blower, or pump to provide a high velocity to the fluid. The high velocity fluid results in a decreased thermal resistance across the boundary layer from the fluid to the heated surface. This, in turn, increases the amount of heat that is carried away by the fluid.
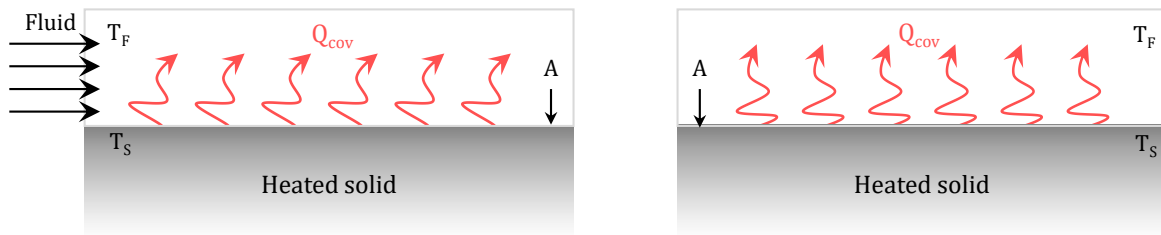
**Figure 3.3:** Schematic of heat transfer from heated solid to fluid by convection. Left: forced convection. Right: free convection.

The heat exchange between solid surface and fluid is described by Newton's law of cooling:

$$Q_c = h \cdot A \cdot (T_S - T_F) \tag{3.13}$$

where $Q_c$ [W] is heat flow by convection, $h \left[\mathrm{W}/\left(\mathrm{m}^2 \cdot \mathrm{K}\right)\right]$ is convection heat transfer coefficient, $A \left[\mathrm{m}^2\right]$ is contact area between solid and fluid, $T_S$ [°C] is surface temperature and $T_F$ [°C] is fluid temperature.

Unlike thermal conductivity $\lambda$, the convection heat transfer coefficient $h$ is not a material property. Rather it depends on geometry, fluid properties, motion and temperature difference $\Delta T = (T_S - T_F)$ [88].

### 3.1.3 Radiation

All objects with a temperature above $0\,\mathrm{K}$ emit thermal radiation. The emission of thermal radiation can occur from solids, liquids or gases, although the focus within this work will

be on radiation from solid surfaces. The energy of the radiation field is transported by electromagnetic waves. Unlike heat conduction that requires a medium in order to transport energy, electromagnetic waves are capable of transporting energy through vacuum. In fact, heat transfer by radiation occurs most efficiently in a vacuum.

The heat transfer rate by radiation $Q_R$ [W] is described by the Stefan-Boltzmann law

$$Q_R = \varepsilon \cdot \sigma \cdot A \cdot \left(T_s^4 - T_0^4\right) \tag{3.14}$$

where $T_s$ [K] is the absolute temperature of the surface and $T_0$ [K] is the ambient temperature, $A \left[\mathrm{m}^2\right]$ is the surface area, $\sigma$ is Stefan-Boltzmann constant ($\sigma = 5.67 \cdot 10^{-8} \left[\mathrm{W}/\left(\mathrm{m}^2 \cdot \mathrm{K}^4\right)\right]$ and $\varepsilon$ is the emissivity. Its value is in the range $0 \leq \varepsilon \leq 1$. This property measures the effectiveness of a surface to emits energy relative to a black-body. The emissivity is depending on surface material and finish [87].

## 3.2 Thermal conductivity of solids

A fundamental property of solids is their ability to transport heat, this ability is quantified by thermal conductivity $\lambda$.
Thermal conductivity is an intensive physical property of a material that relates the heat flow through the material per unit area to temperature gradient across the material. It is given by the Fourier's Law of heat conduction as:

$$\lambda = -\frac{\vec{q}}{\vec{\nabla}T} \tag{3.15}$$

where $\vec{q}$ is the heat flow rate vector across a unit cross section perpendicular to $\vec{q}$, $T$ is the scalar temperature field and $\vec{\nabla}$ is the three-dimensional gradient operator.

Heat energy can be transmitted through solids via electrical carriers (electrons or holes), lattice waves (phonons), electromagnetic waves, spin waves, or other excitations. In metals electrical carriers transmit the majority of heat, while in insulators lattice wave the dominant heat carriers. Theoretically the total thermal conductivity $\lambda$ can be written as a sum of all the components representing various excitations [89]:

$$\lambda = \sum_i \lambda_i, \tag{3.16}$$

where $i$ designates an excitation. However, in solid materials electrons and phonons are certainly the main heat carrying entities. Therefore, the other excitations such as

electromagnetic waves or spin waves will be not consider here due to their small and often conjectured contribution to thermal conductivity. Thus, the total thermal conductivity can be written as

$$\lambda = \lambda_e + \lambda_p \tag{3.17}$$

where $\lambda_e$ is the thermal conductivity component due to electrical charge carriers and $\lambda_p$ is the thermal conductivity component due to the phonons (lattice vibrations) [90].

### 3.2.1 Thermal conductivity of metals

The heat transport in metals is dominated by electrons, whereas phonons have a small contribution to bulk thermal conductivity in metals. However, phonos play a critical role if the electron transport is limited by *e-p* scattering at intermediate and high temperatures [91], [92]. Furthermore, *e-p* interactions are important in superconductivity [93], the response of a material abruptly heated by ion bombardment or laser irradiation [94], and thermal transport across metal-dielectric interfaces in thermoelectric devices [95]. In [86] A. Jain et al. studied numerically the separation and quantification of the phonon contribution to thermal conductivity in aluminum (Al), silver (Ag), and gold (Au) by considering *p-p* and *e-p* interactions at a temperature of 300 K. It has been shown, that the phonon contribution to thermal conductivity is around 2.4% in aluminum, 1.1% in silver and only 0.7% in gold.

The fundamental expression of electron contribution to the thermal conductivity $\lambda_e$ is

$$\lambda_e = \frac{1}{3} \cdot n \cdot c_e \cdot v_e \cdot \Lambda_e \tag{3.18}$$

where $n$ is the number of conduction electron per volume, $c_e$ is the electronic heat capacity per electron, $v_e$ is the electron velocity and $\Lambda_e$ is the electron mean free path [91]. Assuming that the electron velocity $v_e$ of quasi-free electrons equals the Fermi velocity $v_f$ and the electron heat capacity $c_e$ is

$$c_e = \left( \frac{\pi \cdot K_b}{v_f} \right)^2 \cdot \frac{T}{m} \tag{3.19}$$

the equation 3.18 can be rewritten to

$$\lambda_e = \frac{\pi^2 \cdot n \cdot K_b^2 \cdot T \cdot \tau}{3 \cdot m} \tag{3.20}$$

where $K_b$ is Boltzmann Constant, $m$ is electron mass and $\tau$ is relaxation time (collision time) of electron $\tau = \Lambda_e / v_e$.

Electrons are not only transferring heat by colliding with atoms and other electronics but also carry electrical current [96]. The electrical conductivity $\sigma$ is defined as

$$\sigma = \frac{n \cdot e^2 \cdot \tau}{m} \tag{3.21}$$

The relation between equation 3.20 and equation 3.21 leads to the Wiedemann-Franz law

$$\frac{\lambda_e}{\sigma} = L \cdot T \tag{3.22}$$

with

$$L = \frac{\lambda_e}{\sigma \cdot T} = \frac{\pi^2 \cdot K_b^2}{3 \cdot e^2} = 2.44 \times 10^{-8} \frac{W \cdot \Omega}{K^2} \tag{3.23}$$

$L$ is the so-called Lorenz number. Its theoretical value of $2.44 \times 10^{-8}\,(W \cdot \Omega)/K^2$ is valid for all metals by assuming that the thermal transport happens only by electrons, however the heat transport via lattice vibration (or phonons) plays a small role in the total heat transfer in metals. This leads to a variation of the Lorenz number of the metals to the theoretical value. Thus the Lorenz number for gold is $2.35 \times 10^{-8}$, for silver is $2.31 \times 10^{-8}$ and for aluminum is $2.18 \times 10^{-8}\,(W \cdot \Omega)/K^2$ [91]. This good agreement with the theoretical value of the Lorenz number given the fact that equation 3.23 is independent of the mass and density of the particles. Moreover, this underlines the electronic nature of thermal transport in metals.

### 3.2.2 Thermal conductivity of dielectrics and semiconductors

In insulator and semiconductors the thermal transport is dominated by lattice vibrations (phonons). Phonons are the quanta of lattice vibrations analogous to the photons, which are the quanta of light. The vibrations of atoms in a crystal can be described by means of the collective vibrational modes of the lattice, which can be calculated from the classical equations of motion of the atoms as soon as the interatomic potential is known [97].
The quantization of the lattice vibration field results in quantized vibration amplitudes and the quantization of the mode energies so that the energy excitation levels of each mode can occur only in discrete multiples of the vibration frequency.

$$E = n \cdot \hbar \cdot \omega \tag{3.24}$$

where $E$ is the mode energy, $n$ is the mode occupation number, $\hbar$ is Planck's constant divided by $2\pi$ and $\omega$ is the mode vibration frequency. The quantization of these vibrational modes, called phonons, gives the crystal excitations wave and particle behavior. Thus,

energy transport by phonons involves both particle-like behavior, such as the collision (scattering) of phonons with other phonons or interfaces, and wave-like behavior, such as interference and diffraction of phonon modes. In a finite temperature system, phonon scattering drives the system toward a thermal equilibrium in which the number of phonons in each mode, $n$, is related to temperature by the Planck distribution.

$$n = \frac{1}{\exp\left(\hbar \cdot \omega / K_b \cdot T\right) - 1} \tag{3.25}$$

where $K_b$ is Boltzmann's constant.

Thermal conductivity in dielectric materials is the result of phonons moving from a hotter to a colder region and undergoing collisions with one another or against material imperfections (defects, boundaries, etc.) so that their energy can be transferred in space. The kinetic theory of gases is commonly used in form of a mathematical model, considering that each phonon is modeled as a free-moving particle in space with a momentum and an energy, collision with other particles is an immediate event, the probability that a collision occurs during a time interval $dt$ is proportional to $dt$ and the particles reach thermal equilibrium only through these collisions [90]. The lattice contribution can be regarded as the thermal conductivity of a phonon gas and can be derived using kinetic theory of gases:

$$\lambda_p = \frac{1}{3} \cdot \frac{c_v^p}{V} \cdot v_p \cdot \Lambda_p \tag{3.26}$$

where $c_v^p / V$ is the heat capacity per unit volume, $v_p$ is the average phonon velocity and $\Lambda_p$ is the mean free path of a phonon between cwo consecutive collisions.

### 3.2.3 Thermal conductivity of composite systems

The thermal conductivity of composite systems combines the thermal conductivity of the polymer matrix with the thermal conductivity of the crystalline ceramic powder. Another parameter is the interface between the polymer matrix and the filler particles. Here thermal resistances occur due to poor wetting, voids, inclusions and impurities. They prevent a real chemical bond between the polymer matrix and the particle surface. Even with ideal wetting and bonding, the interface represents a barrier to energy transfer. The large difference in the acoustic impedances forces the scattering and reflection of the phonons at the interface [12].

Many models have been reported in the literature to determine thermal conductivity of composite systems based on the composition of continuous matrix material and discrete filler material. These models have a relatively simple structure and only use the thermal

conductivity of the matrix $\lambda_M$, the filler $\lambda_F$ and its volume filling degree $\phi$ as influencing variables. The starting point for the development of the individual models are the three possibilities for the sequence of two different material components. These can either be connected in parallel or in series or averaged (mixed). In the corresponding parallel model, the filler and matrix are connected in parallel, while in the serial model, the filler and matrix are connected in series. The third model is based on a mean property, which is calculated using the geometric mean. The thermal conductivity of the composite $\lambda_C$ can be calculated for the different modules as following:

- Parallel model: $\lambda_C = \phi \cdot \lambda_F + (1 - \phi) \cdot \lambda_M$

- Serial model: $\frac{1}{\lambda_C} = \frac{\phi}{\lambda_F} + \frac{1-\phi}{\lambda_M}$

- Geometric mean: $\lambda_C = \lambda_F^{\phi} \cdot \lambda_M^{(1-\phi)}$

With these basic models only an upper limit or a lower limit can be calculated, whereby the accuracies of these values are not sufficient for a satisfactory calculation. For more precise statements, a large number of analytical model descriptions have been developed that take into account realistic influencing factors. The model basis can be theoretical, semi-theoretical or empirical [98].

In 1870, Maxwell described the theoretical model

$$\lambda_C = \lambda_M \cdot \frac{\lambda_F + 2\lambda_M + 2\phi\left(\lambda_F - \lambda_M\right)}{\lambda_F + 2\lambda_M - \phi\left(\lambda_F - \lambda_M\right)}, \tag{3.27}$$

which is valid for calculation of thermal conductivity of composites with spherical filler.

Lewis-Nielsen developed 1970 the semi-theoretical model [99], [100]

$$\lambda_C = \lambda_M \cdot \frac{1 + (A-1) \cdot B \cdot \phi}{1 - \Psi \cdot B \cdot \phi} \tag{3.28}$$

with

$$\Psi = 1 + \frac{(1 - \phi_m) \cdot \phi}{\phi_m^2} \quad \text{and} \quad B = \frac{\lambda_F / \lambda_M - 1}{\lambda_F / \lambda_M + A - 1}$$

The Lewis-Nielsen model can be used to calculate the thermal conductivity of composite materials with spherical, fiber and flake fillers. Although the Lewis-Nielsen model provides good results for the thermal conductivity of composites, it also requires the maximum packing coefficient $\phi_m$ and the geometry factor $A$. These parameters are in most cases unknown and difficult to determine experimentally.

Many other theoretical models have also been developed to calculate the thermal conductivity of composites, among others by Bruggemann in 1935 [101], by Halpin-Tsai in 1969 [102], by Cheng-Vachon in 1970 [103] and by Hatta/Taya in 1986 [104]. All these models shows good agreement with measured values but only with volume filling degree $\phi$ up to 30 *vol*.% [105]. The reason for these deviations is that none of these models take into account the interface resistance between the fillers.

# Chapter 4

# Steady-state test system for material characterization

This chapter deals with the development and application of the test stand *TIMA*, which can be used for thermal characterization of several types of materials. The chapter starts with the theoretical background of the test method, which has been implemented in a commercial test stand as complete solution including hard- and software. Advance solutions for extending the resolution of the test method and to allow better than state of the art commercially available characterization of next generations of thermal interface materials and substrates under adjustable application-specific conditions were developed. Several measurement examples are shown in order to verify the developed test stand and also to study different thermal effects.

## 4.1 Measurement principle

*TIMA* stands for thermal interface materials analyzer. The measurement principle of *TIMA* is based on the standard ASTM D5470 [5] which describes a one-dimensional and steady-state testing method in which the specimen is placed between two reference bodies (metal cylinders) with co-planary surfaces. The upper reference body is heated while the lower one is cooled. In very good approximation, a uniform heat flow is established between hot and cold side.

To determine the effective thermal resistance $Rth_{eff}$ of a sample, the temperature gradient across the sample $\Delta T_s$ and the heat flow $Q$ through the sample have to be measured in steady-state.

$$Rth_{eff} = \frac{\Delta T_s}{Q}.$$  (4.1)
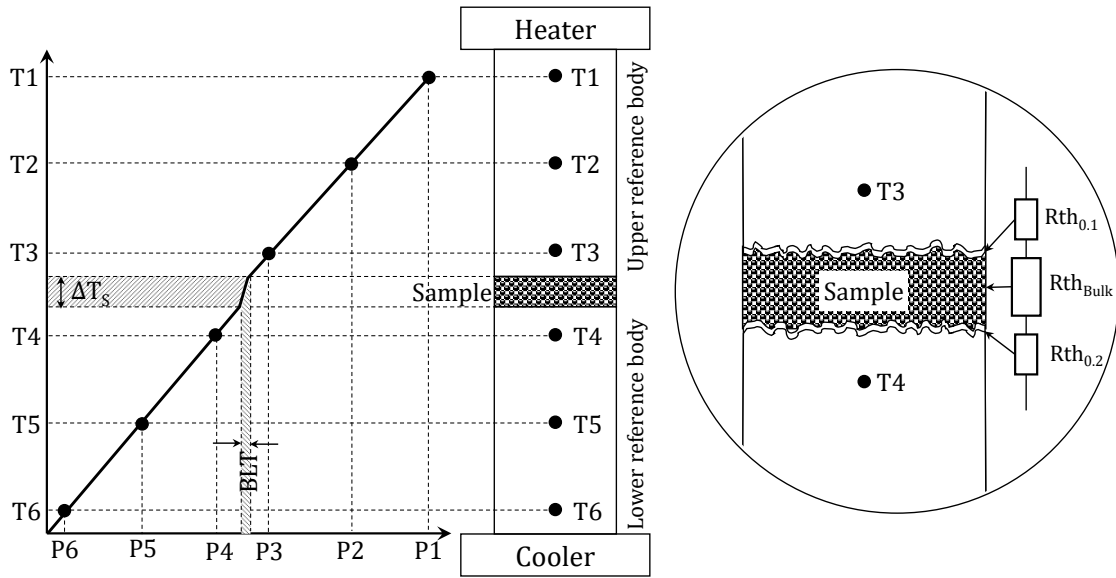
**Figure 4.1:** Schematic of the measurement module *TIMA6* which is based on the standard ASTM D5470

When using reference bodies (RB) as shown in figure 4.1, the temperature gradient across the sample ($\Delta T_s$) can be determined by the extrapolation of the linear functions of the temperatures $T1$, $T2$ and $T3$ over the temperature sensor positions $P1$, $P2$ and $P3$ as well as $T4$, $T5$ and $T6$ over the temperature sensor positions $P4$, $P5$ and $P6$ (see figure 4.1).

The heat flow through the sample is measured twice, by the upper and the lower reference bodies according equation 4.2:

$$Q = \frac{\Delta T_{RB}}{l_{RB}} \cdot A_{RB} \cdot \lambda_{RB} \tag{4.2}$$

where $\Delta T_{RB}/l_{RB}$ is the slope ($a$) of the temperature drop along the reference body as illustrated in figure 4.2

Thereby, the heat flow can be calculated as following:

$$Q = a \cdot A_{RB} \cdot \lambda_{RB} \tag{4.3}$$

Where:
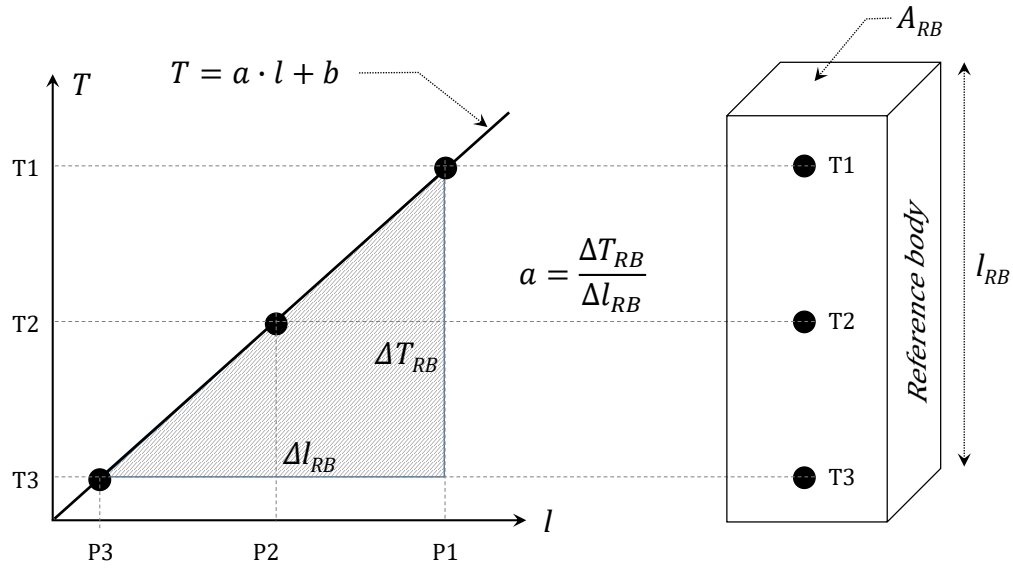
**Figure 4.2:** Principle for heat flow determination by use of a reference body

| | | |
|---|---|---|
| $a$ | The slope of the linear function of temperature drop along the reference body | $[\text{K/m}]$ |
| $\Delta T_{RB}$ | Temperature gradient across the reference body | $[\text{K}]$ |
| $l_{RB}$ | Length of reference body | $[\text{m}]$ |
| $A_{RB}$ | Cross section area of reference body | $[\text{m}^2]$ |
| $\lambda_{RB}$ | Thermal conductivity of reference body | $[\text{W}/\,(\text{m}\cdot\text{K})]$ |

The effective thermal resistance $Rth_{eff}$ is the sum of the bulk thermal resistance $Rth_{bulk}$ of the sample and the thermal interface resistance between the sample and the reference bodies $Rth_{0.1}$ and $Rth_{0.2}$ which are summarized to $Rth_0$.

$$Rth_{eff} = Rth_{bulk} + Rth_0 \tag{4.4}$$

The thermal resistance of the sample $Rth_{bulk}$ is defined by following formula:

$$Rth_{bulk} = \frac{BLT}{\lambda_{bulk} \cdot A_s} \tag{4.5}$$

Where:

| | | |
|---|---|---|
| $Rth_{bulk}$ | Bulk thermal resistance of the sample | $[\text{K/W}]$ |
| $Rth_{eff}$ | Effective thermal resistance (sample and interfaces) | $[\text{K/W}]$ |
| $Rth_0$ | Thermal interface resistance | $[\text{K/W}]$ |
| $BLT$ | Bond line thickness of the sample | $[\text{m}]$ |
| $A_s$ | Cross sectional area of the sample | $[\text{m}^2]$ |
| $\lambda_{bulk}$ | Bulk thermal conductivity of the sample | $[\text{W}/\,(\text{m}\cdot\text{K})]$ |

Inserting equation 4.5 into equation 4.4 yields in a linear dependency between effective thermal resistance $Rth_{eff}$ and bond line thickness BLT (equation 4.6).

$$Rth_{eff} = \frac{1}{\lambda_{bulk} \cdot A_s} \cdot BLT + Rth_0 \qquad (4.6)$$

Presupposing $\lambda$ as material constant, and both cross sectional area and interface resistance as constant during measurement procedure, equation 4.6 suggests that the effective thermal resistance is a linear function of the sample thickness. Its slope is $a = 1/(\lambda_{bulk} \cdot A_s)$. Thus, the bulk thermal conductivity of the sample can be calculated from the slope ($a$):

$$\lambda_{bulk} = \frac{1}{a \cdot A_s} \qquad (4.7)$$

The y-axis intercept is the thermal interface resistance $Rth_0$ (see figure 4.3).
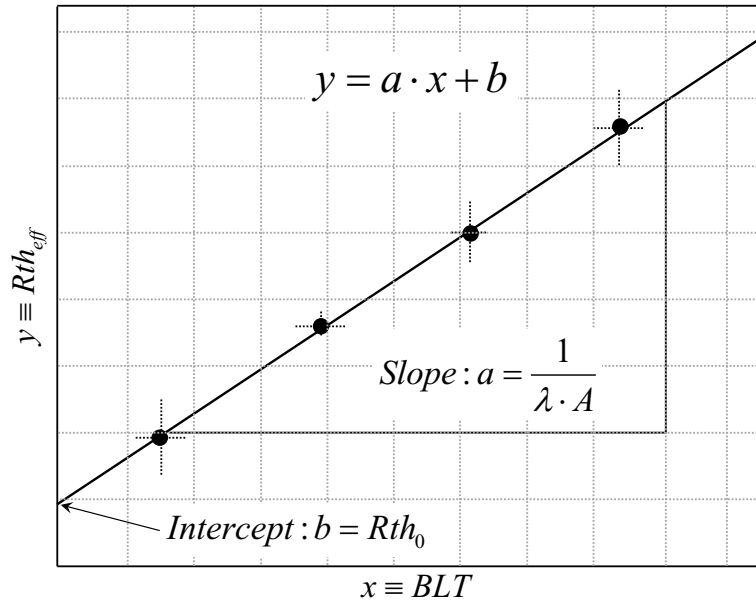


**Figure 4.3:** Effective thermal resistance as function if the bond line thickness

The thermal interface resistance strongly depends on the surface roughness at the interface of sample and reference body. Surfaces of engineering interest are never perfectly smooth and this must always be taken into account when analyzing interfacial heat transfer between contacting mediums [106].

While the bulk thermal conductivity of greases or adhesives using filler particles of different materials, size, shape and modality has been showing some improvement over the last few years, the interfaces have received much less attention, although at thin bond line thicknesses (BLT) they have a major influence on heat transfer [4], [107]. The particle density is usually lower at the interface and boundaries of dissimilar materials reduce

the heat transfer across the interface [108]. This is also due to processing conditions [109].

Firstly, thermal boundary (Kapitza) resistances have a major influence on heat transfer. Moreover, the roughness of contacting surfaces heavily influence these thermal interface resistances. Hence, thermal interface materials need to be characterized under application related conditions.

Based on the same measurement principle of the standard ASTM D5470 (see figure 4.1), the test stand *TIMA* provides the possibility to characterize the sample not only between two metals but also between a silicon and a metal surfaces by substituting the upper reference body with a silicon thermal test chip (TTC) with integrated heater and temperature sensors. This completely new approach allows characterization of TIM between metal and silicon surfaces, which is the same application condition as occurs for TIM1. This measurement module has been named *TIMA3* relating to the three temperature sensors used in the reference body instead of the former 6.
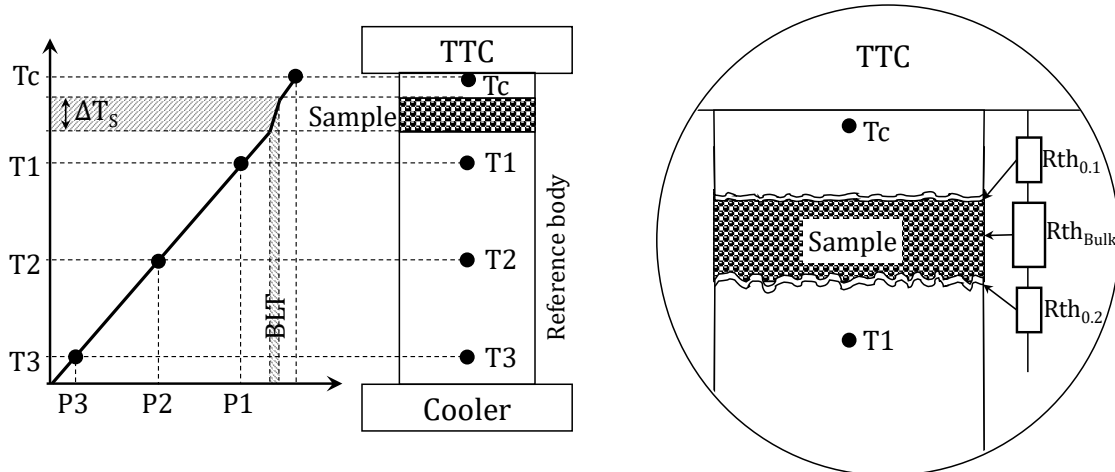


**Figure 4.4:** Schematic of the measurement module *TIMA3*

The key benefit of *TIMA3* is that the sample can be measured under adjustable conditions, as they occur in most applications of TIM1.

Design and realization of the thermal test chip used for this module is part of this work and will be discussed in section 4.4

## 4.2   Design and realization of *TIMA* hardware

The hardware of *TIMA* has been designed and realized as modular system that allows integration of different modules into a single platform. Two modules have been realized:

the *TIMA3* module, which allows the sample to be measured between a silicon and a metal surface (figure 4.4) and the *TIMA6* module, where the sample is measured between two metal surfaces (figure 4.1).
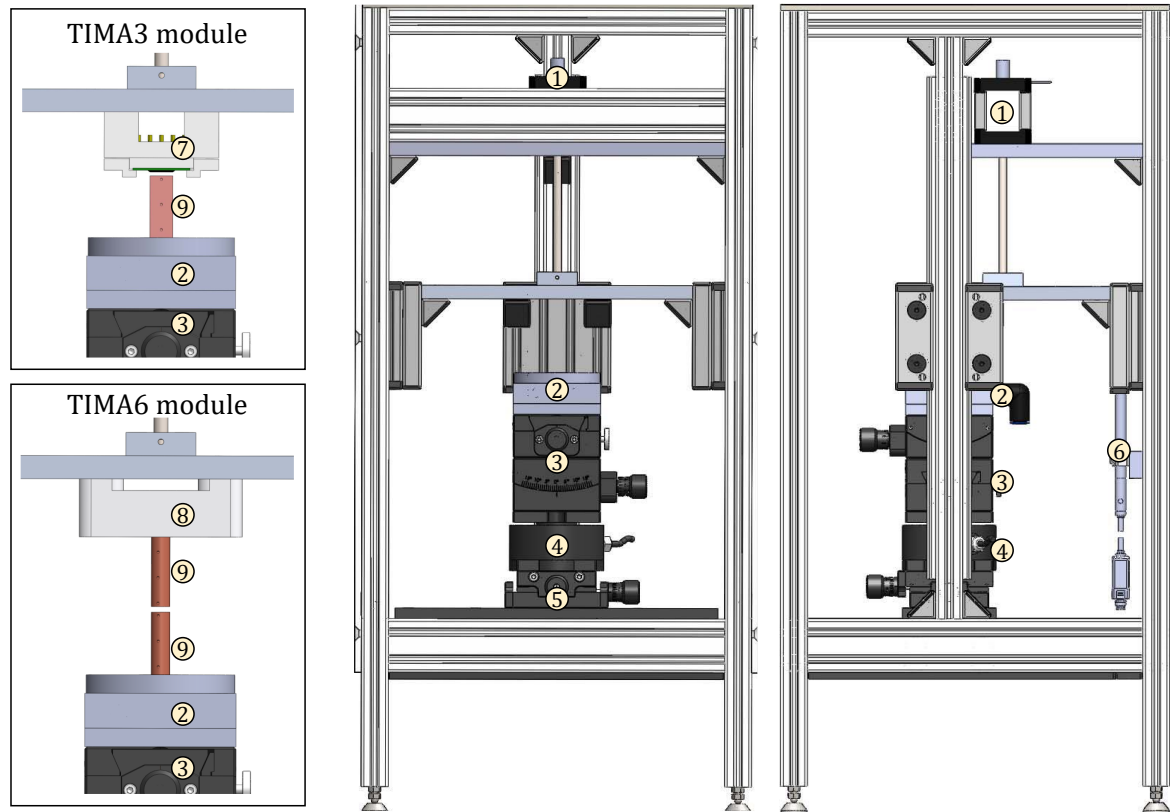


**Figure 4.5:** CAD-model of *TIMA* platform including *TIMA3* or *TIMA6* modules

Figure 4.5 shows a CAD model of the *TIMA* platform and the test modules *TIMA3* and *TIMA6*. The frame of the platform has been realized by commercially available aluminium profiles connected as building kit taking to the account the required mechanical stability.

The platform and the modules consist of following elements (figure 4.5):

1. Stepper motor including spindle for computer controlled movement of the upper part of the test stand to adjust the bond line thickness of the TIM with a resolution of 1 µm

2. Aluminium block heat sink with meander structured water channels

3. Manual Theta-Phi goniometer in the range of ±15° for co-planar contacted surfaces as well as for TIM characterization under defined tilt

4. Load cell in the range of ±200 N for in-situ measurement of the compressive or tensile load on the TIM

5. Manual XY translation stage in the range of ±3 mm to compensate for manufactu-

ring tolerances of the test stand components

6. Position sensor for in-situ measurement of the bond line thickness of the TIM

7. Thermal test chip with integrated heater and temperature sensors (see section 4.4)

8. Heater block including SiC heater for a maximum temperature up to 300°C, temperature sensor and thermal fuse.

9. Metal reference bodies with three holes for temperature sensors

For recording of temperature, force and position sensors, as well as for power supplying of heater and stepper motor, an electronic rack has been developed and realised. For setting of device parameters, reading out and processing of the data, the software LabVIEW has been used.

## 4.3   Verification and qualification of *TIMA*

In this section, the measurement accuracy and uncertainty of the test stand *TIMA* and its results will be studied. The error sources of values measured in-situ and values determined beforehand will be taken into consideration. As mentioned in section 4.1 the effective thermal resistance of a sample is measured, from which the bulk thermal conductivity, the effective thermal conductivity and the interface resistance are calculated.

### 4.3.1   Calculation of absolute error of measurement values

For the error calculation, it must be distinguished between in-situ measured values, ex-situ measured values and calculated values. In-situ measured values are temperature ($T$), sample thickness ($BLT$) and contact force ($F$). In table 4.1 the absolute and random errors for the in-situ and ex-situ measured values for the sensors and components used for the test system

Thermal conductivity ($\lambda_{RB}$) and geometry ($A_{RB}$, $l_{RB}$) of the reference bodies are ex-situ measured values.

Heat flow ($Q$), effective and interface thermal resistance ($Rth_{eff}$, $Rth_0$) and effective and bulk thermal conductivity ($\lambda_{eff}$, $\lambda_{bulk}$) are calculated values.

The effective thermal conductivity $\lambda_{eff}$ can be calculated in the following equation:

$$\lambda_{eff} = \frac{BLT}{Rth_{eff} \cdot A_S} \tag{4.8}$$

The measurement error of effective thermal conductivity $\Delta\lambda_{eff}$ regarding the laws of error propagation results in the following equation:

$$\Delta\lambda_{eff} = \lambda_{eff} \cdot \sqrt{\left(\frac{\Delta BLT}{BLT}\right)^2 + \left(\frac{\Delta Rth_{eff}}{Rth_{eff}}\right)^2 + \left(\frac{\Delta A_s}{A_s}\right)^2} \tag{4.9}$$

**Table 4.1:** In-situ and ex-situ measured values and their expected errors

| Para-meter | Absolute error | Random error[*] | Comments |
|---|---|---|---|
| $T$ | 0.2 K | 0.05 K | In-situ measured by NTCs (Negative Temperature Coefficient Thermistors). NTCs were chosen, on the one hand, due to their cylindric form which allows easy integration into the reference bodies, on the other hand, because of their high measurement accuracy |
| $BLT$ | 1 µm | 1 µm | In-situ measured by an optical position sensor integrated in the test stand |
| $F$ | 2 N | 1 N | In-situ measured by a load cell integrated in the test stand |
| $A_{RB}$ | 100 µm$^2$ | 100 µm$^2$ | Ex-situ measured, the accuracy depends on the reading errors or on the manufacturing tolerances |
| $l_{RB}$ | 10 µm | 10 µm | Ex-situ measured, the accuracy depends on the reading errors or on the manufacturing tolerances |
| $\lambda_{RB}$ | $3-6$ W/(m·K) | 5 W/(m·K) | Ex-situ measured by the *LaTIMA* test stand (section 6) or by laser flash technique |

[*] Random error means in this case, the uncertainty between the values measured by the same sensor or sensor type

$Rth_{eff}$ is measured as described in section 4.1 by the temperature gradient $\Delta T$ over the sample and the heat flow $Q$ through the sample.

$$Rth_{eff} = \frac{\Delta T_S}{Q} \tag{4.10}$$

The measurement error of the effective thermal resistance $\Delta Rth_{eff}$ can be calculated as following:

$$\Delta Rth_{eff} = Rth_{eff} \cdot \sqrt{\left(\frac{\Delta\Delta T_s}{\Delta T_s}\right)^2 + \left(\frac{\Delta Q}{Q}\right)^2} \tag{4.11}$$

$Q$ is the heat flow through the sample and measured by the reference body as calculated by the equation

$$Q = a \cdot A_{RB} \cdot \lambda_{RB} \tag{4.12}$$

The measurement error of the heat flow $\Delta Q$ is

$$\Delta Q = Q \cdot \sqrt{\left(\frac{\Delta a}{a}\right)^2 + \left(\frac{\Delta A_{RB}}{A_{RB}}\right)^2 + \left(\frac{\Delta\lambda_{RB}}{\lambda_{RB}}\right)^2} \tag{4.13}$$

The combination of equation 4.8, equation 4.10 and equation 4.12 results in the following

equation for effective thermal conductivity:

$$\lambda_{eff} = \frac{BLT \cdot a \cdot A_{RB} \cdot \lambda_{RB}}{\Delta T_s \cdot A_s} \tag{4.14}$$

Thereby, the absolute error of the effective thermal conductivity $\Delta\lambda_{eff}$ is:

$$\Delta\lambda_{eff} = \lambda_{eff} \cdot \sqrt{\left(\frac{\Delta BLT}{BLT}\right)^2 + \left(\frac{\Delta a}{a}\right)^2 + \left(\frac{\Delta A_{RB}}{A_{RB}}\right)^2 + \left(\frac{\Delta\Delta T_s}{\Delta T_s}\right)^2 + \left(\frac{\Delta A_s}{A_s}\right)^2} \tag{4.15}$$

The bulk thermal conductivity $\lambda_{bulk}$ and interface resistance are usually determined from the linear relationship between effective thermal resistance ($Rth_{eff}$) and bond line thickness BLT as shown in equation 4.6.

$$Rth_{eff} = \frac{1}{\lambda_{bulk} \cdot A_s} \cdot BLT + Rth_0 \tag{4.16}$$

$1/(\lambda_{bulk} \cdot A_s)$ is the slope ($a$) of the linear fit and results from the effective thermal resistance as function of the bond line thickness.

$$\lambda_{bulk} = \frac{1}{a \cdot A_s} \tag{4.17}$$

The error of the bulk thermal conductivity:

$$\Delta\lambda_{bulk} = \lambda_{bulk} \cdot \sqrt{\left(\frac{\Delta a}{a}\right)^2 + \left(\frac{\Delta A_s}{A_s}\right)^2} \tag{4.18}$$

The thermal interface resistance $Rth_0$ is the intercept of the linear fitted function of $Rth_{eff}$ over BLT. Thereby the error of $Rth_0$ is the error of the y-axis intercept.

## 4.3.2 Resolution and limitation of measurement techniques based on the standard ASTM D5470

To calculate the limitation of the test stand, the errors, their source and weighting should be analysed. The following calculation shows the percentage portion of the overall error of each individual error source for the measurement of a TIM with a specific thermal resistance of 10 mm$^2 \cdot$K/W. As shown in equation 4.1, the thermal resistance results from the heat flow through the sample and the temperature gradient across the sample [110].

For the temperature measurement, temperature sensors (NTC) are used with a maximum error below 0.2 K in the range from 20°C to 80°C. Thus, the maximum error of the

measured temperature gradient is 0.4 K. The measurement error of the heat flow results from the manufacturing tolerances and the thermal conductivity of the reference bodies as well as the measurement error of the temperature gradient across the reference body.

**Table 4.2:** Calculation of the relative errors of the TIM's thermal resistance and the weighting of the error sources

| Parameter | Value | Absolute error | Relative error | Error weighting |
|-----------|-------|----------------|----------------|-----------------|
| $\Delta T_s$ | 65.5 K | 0.4 K | 7.1 % | 71 % |
| $\lambda_{RB}$ | 380 W/(m·K) | 5 W/(m·K) | 1.3 % | 13 % |
| $L_{RB}$ | 25 mm | 0.1 mm | 0.3 % | 3 % |
| $A_{RB}$ | 100 mm | 0.1 mm | 0.1 % | 1 % |
| $\Delta T_{RB}$ | 37.2 K | 0.4 K | 1.1 % | 11 % |
| $Rth_s$ | 10 mm²·K/W | 1 mm²·K/W | 10 % | 100 % |

It can be seen in the calculation that over 80 % of the measurement error is caused by the temperature measurement error.

The total relative error of the thermal resistance is dependent on the value of the thermal resistance. So the relative error of highly conductive materials is high because of the low temperature gradient across the sample. Also it is high for materials with very low thermal conductivity due to low heat flow.
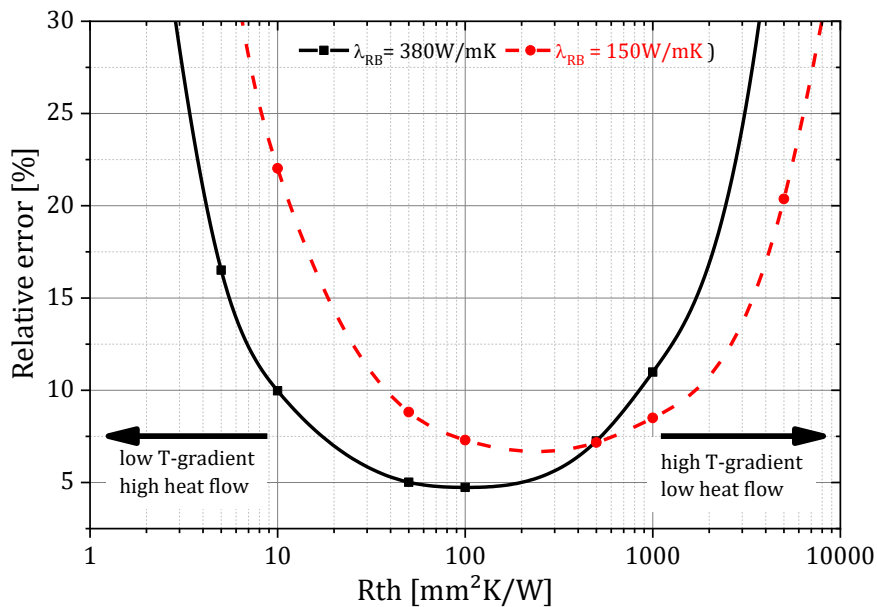


**Figure 4.6:** Relative thermal resistance error as function of the thermal resistance values

The graphs in figure 4.6 show the maximum error for different thermal resistance values. It can be seen that thermal resistances between 10 mm²·K/W and 1000 mm²·K/W can

be measured with a relative error below 10 % by using copper reference bodies[1]. By using reference bodies with lower thermal conductivity, e.g. aluminium, instate of copper, the resolution increases for samples with higher thermal resistance due to less heat flow, but it decreases for highly conductive materials.

To extend the resolution of the test method and to allow characterization of next generations of thermal interface materials and substrates, the cross section area of the sample should be kept as small as possible to generate a higher temperature gradient through the samples and the cross sectional area of the reference bodies should be kept as large as possible to allow for more heat flow. Figure 4.7 schematically shows a new approach to increase the resolution of the test method.
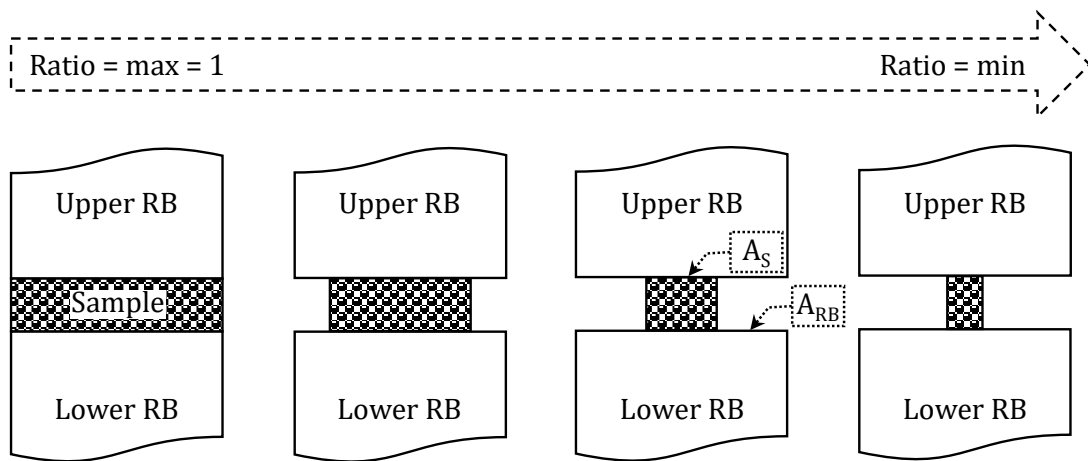


**Figure 4.7:** Schematic of ratio variation between the cross section areas of reference body and sample

To illustrate the improvement of the resolution by this approach the effective error of the thermal resistance was calculated for different ratios between the cross-sectional areas of the reference bodies $A_{RB}$ and the sample $A_S$ and for different reference body materials. Figure 4.8 shows the relative error as function of the thermal resistance values for different ratios using copper reference bodies with $380 \, \text{W}/\,(\text{m} \cdot \text{K})$ of thermal conductivity and aluminium reference bodies with $150 \, \text{W}/\,(\text{m} \cdot \text{K})$ of thermal conductivity. It can be seen that by reducing the ratio $(A_{RB}/A_S)$ to 0.1, a thermal resistance of $1 \, \text{mm}^2 \cdot \text{K/W}$ can be measured with a maximal measuring error below 10%, which is 10 times lower than the thermal resistance measured using the ratio of 1.

---

[1]Thermal resistance of $10 \, \text{mm}^2 \cdot \text{K/W}$ equates to a sample with 100 µm thickness and $10 \, \text{W}/\,(\text{m} \cdot \text{K})$ thermal conductivity
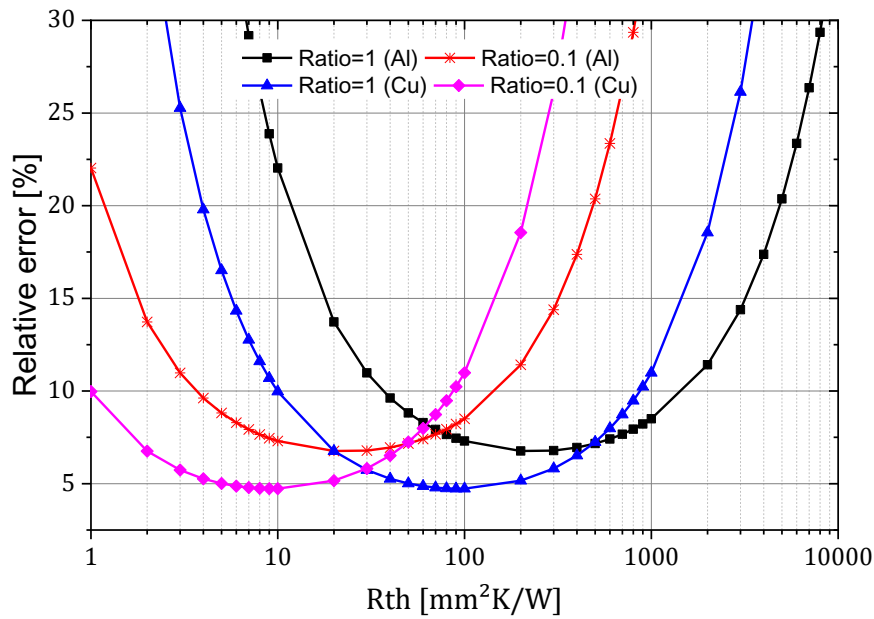
**Figure 4.8:** Maximal measuring error as function of the thermal resistance values

### 4.3.3   Influence of environment on measurement accuracy

In this section, the heat flow losses due to convection and radiation have been studied by Finite Elements (FE) simulation. Figure 4.9 shows schematic drawings of two types of reference bodies (cuboid and cylinder), and it illustrates heat inlet, heat outlet and heat losses.



$$Q_{out} = Q_{in} - Q_{loss}$$
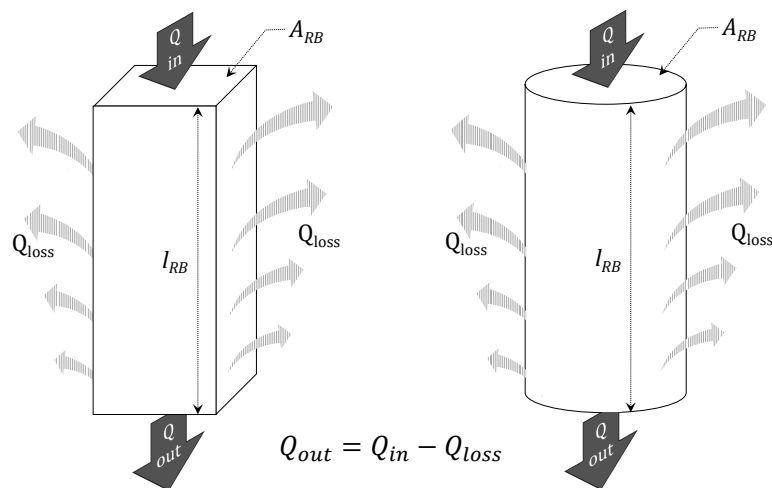
**Figure 4.9:** Schematic of reference bodies showing the heat inlet and outlet as well as the losses by convection and radiation

In order to study the heat losses by convection and radiation and their influence on the accuracy of heat flow determination, the simulation tool ANSYS Workbench has been

used. Simple parametrized 3D models of round and square reference bodies have been
generated.

The percentage heat loss as function of the heat transfer coefficient ($h$) and emissivity
coefficient ($\varepsilon$) has been studied for the following parameters:
- Constant parameters:
  - Length of reference body: $l_{RB} = 25$ mm
  - Cross sectional area of reference body: $A_{RB} = 100$ mm$^2$
  - Inlet heat flow: $Q_{in} = 20$ W
  - Environment temperature: $T = 20\,°$C
- Variable parameters:
  - Heat transfer coefficient: $h_{min} = 0$ W$/\left(\text{m}^2 \cdot \text{K}\right)$; $h_{max} = 20$ W$/\left(\text{m}^2 \cdot \text{K}\right)$
  - Emissivity: $\varepsilon_{min} = 0$; $\varepsilon_{max} = 1$

The heat loss ($Q_{loss}$) is calculated from the difference between the inlet heat ($Q_{in}$) and
the outlet heat ($Q_{out}$).

$$Q_{loss} = Q_{in} - Q_{out} \tag{4.19}$$

Figure 4.10 shows the simulation results. The maximum heat loss for a worst case scenario
is around 3.4 % at $h = 20$ W$/\left(\text{m}^2 \cdot \text{K}\right)$ and $\varepsilon = 1$, while the heat loss under real mea-
surement conditions with $h = 5$ W$/\left(\text{m}^2 \cdot \text{K}\right)$ (natural convection) and $\varepsilon = 0.1$ (standard
Aluminium surface) is below 1 %.
The heat losses are even a bit lower by using cylinder reference bodies instead of cu-
boid reference bodies, due to the ratio between volume and surface. The surface of a
cuboid reference body with the length of 25 mm and the cross-sectional area of 100 mm$^2$
is 1000 mm$^2$ while the surface of a cylinder reference body with the same length and
cross-sectional area is around 886 mm$^2$.

It could be shown in this section, that by understanding of error sources and by appro-
priate choice of geometries, materials and surfaces, the measurement accuracy can be
maximized.

## 4.4 Design and realization of the Thermal Test Chip

Thermal test chips (TTCs) usually contain heaters and temperature sensors. TTCs are
commonly used tools for thermal characterization and qualification of materials and packa-
ges. In the last two decades, many types of TTC have been developed and manufactured
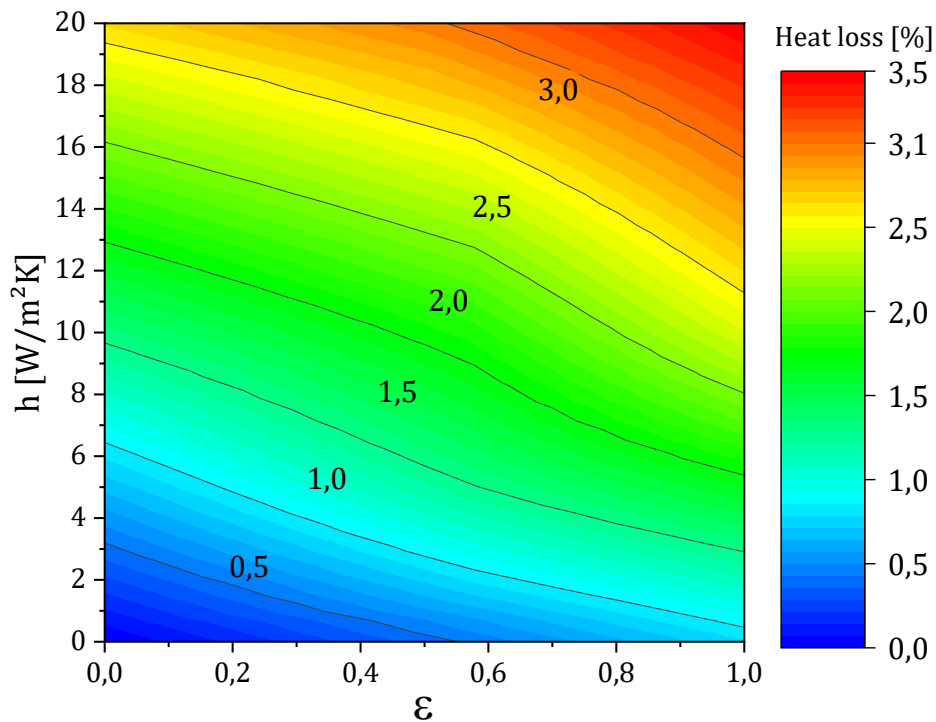
**Figure 4.10:** Heat losses as function of heat transfer coefficient ($h$) and emissivity coefficient ($\varepsilon$) for the cuboid reference body

for different applications. *Rencz et al.* compared in [111] 12 types of TTC regarding geometry, design, operation and measurement principle. All these TTCs have to generate heat power and to measure the temperature. But they differ in the types of temperature sensors, the accuracy of temperature measurement, the geometries, the maximum power dissipation or the manufacturing and assembling technologies [112], [113].
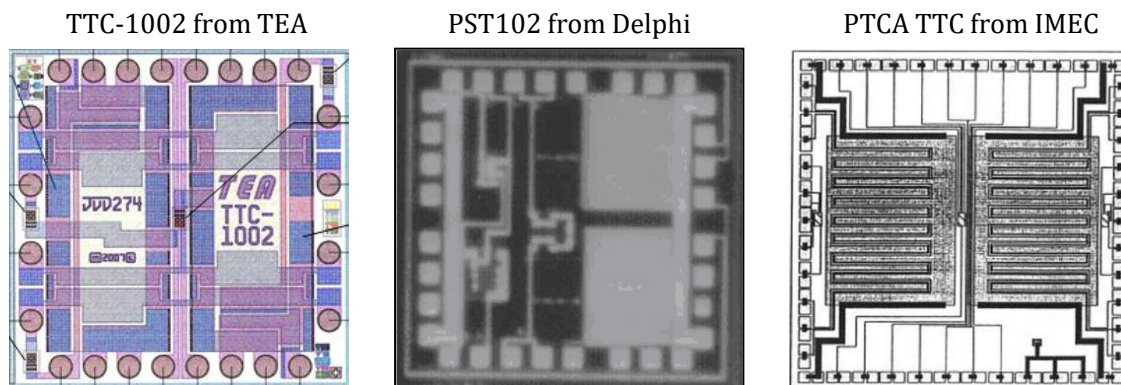


**Figure 4.11:** Images shown the structures of some market available TTCs

As described in section 4.1, for *TIMA3* module a thermal test chip is necessary for the characterization of TIM1 under real application. The key requirements for such a thermal test chip which has to be developed are:

- Maximum possible heating area relative to chip size
- Uniform temperature profile across backside area
- Temperature sensor in center of chip
- High temperature coefficient for temperature sensor
- Kelvin connections (i.e., 4-wire connections) for improved measurement accuracy
- Assembly by flip-chip technology for accessible backside area

## 4.4.1   Chip design

The TTC is designed as a modular chip with the smallest full functional chip cell of 3.2 mm x 3.2 mm which consists of ten heater lines and a temperature sensor. The challenge was to design structures of the heater and the temperature sensor using only one titanium layer as adhesion and barrier layer. The main reason of using one layer is to ensure that the temperature coefficient of the metal layer does not decrease due to possible diffusion between the adhesion and barrier layers. Figure 4.12 shows the layout of one chip cell [114].
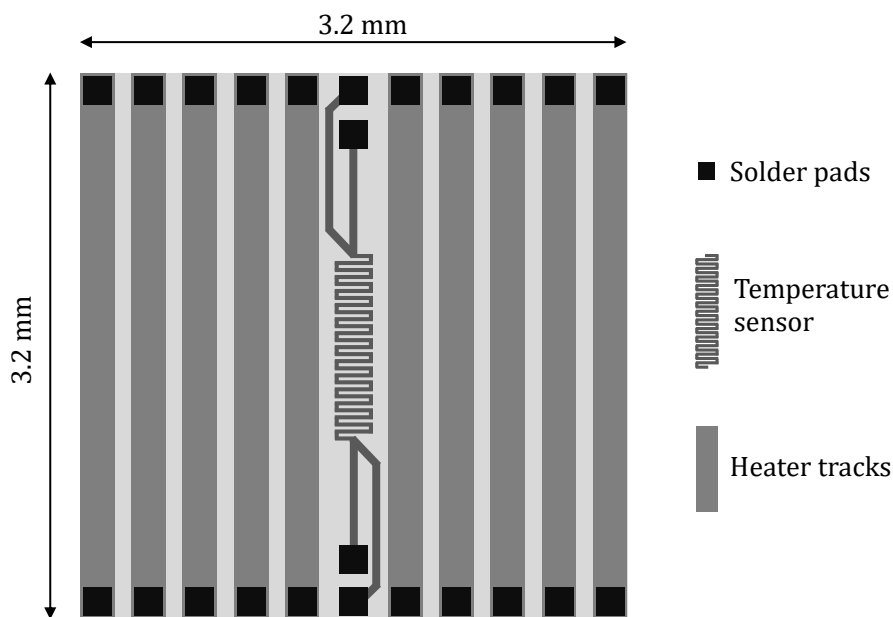


**Figure 4.12:** Layout of a single cell of the thermal test chip

### 4.4.1.1   Design of heater

The heater consists of 10 independent titanium tracks with the line/space of 200/100 µm, the length of 3.2 mm and the thickness of 70 nm. The electrical resistance of one heater track can be calculated by the equation:

$$R_{HT} = \rho \cdot \frac{L_{HT}}{W_{HT} \cdot T_{HT}} \tag{4.20}$$

Where:

| | | |
|---|---|---|
| $R_{HT}$ | Electrical resistance of one heater track | $[\Omega]$ |
| $\rho$ | Specific electrical resistance ($= 70 \cdot 10^{-8}$ for titanium) | $[\Omega \cdot m]$ |
| $L_{HT}$ | Length of one heater track ($= 3.2$) | [mm] |
| $W_{HT}$ | Width of heater track ($= 200$) | [µm] |
| $T_{HT}$ | Thickness of heater track ($= 70$) | [nm] |

The electrical resistance of one heater track is $R_{HT} = 160\ \Omega$. The 10 heater tracks can be connected individually, in serial or parallel as can be seen in Figure 4.13. To ensure a homogeneous heat dissipation in the chip, the heater tracks should be powered uniformly. Four interconnection possibilities are shown in figure 4.13.
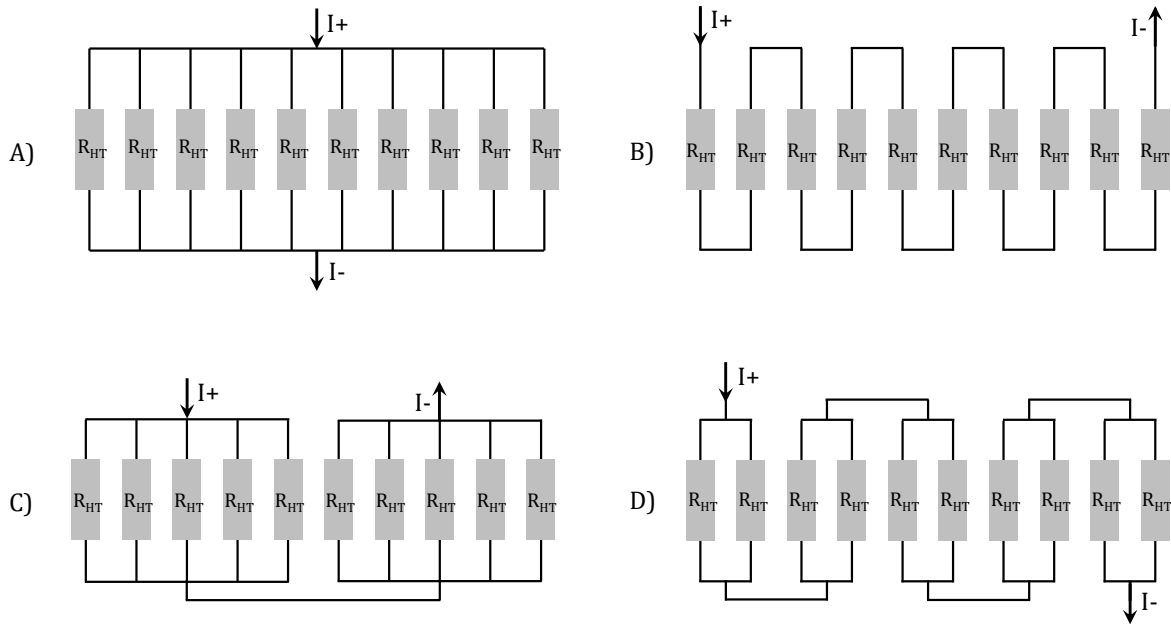


**Figure 4.13:** Equivalent circuit of heater tracks shown interconnection possibilities of heater tracks

A) All 10 heater tracks are connected parallel

$$R_{tot} = \frac{R_{HT}}{10} \Rightarrow R_{tot} = \frac{160\ \Omega}{10} = 16\ \Omega$$

B) All 10 heater tracks are connected serial

$$R_{tot} = R_{HT} \cdot 10 \Rightarrow R_{tot} = 160\ \Omega \cdot 10 = 1600\ \Omega$$

C) Five heater tracks are connected parallel and than the two groups are connected serial

$$R_{tot} = 2 \cdot \frac{R_{HT}}{5} \Rightarrow R_{tot} = 2 \cdot \frac{160 \ \Omega}{5} = 64 \ \Omega$$

D) Two heater tracks are connected parallel and than the five groups are connected serial

$$R_{tot} = 5 \cdot \frac{R_{HT}}{2} \Rightarrow R_{tot} = 5 \cdot \frac{160 \ \Omega}{2} = 400 \ \Omega$$

The different interconnection possibilities enable a wide choice of sources (power supply) with different voltage and current ranges.

#### 4.4.1.2 Design of temperature sensor

The temperature sensor is a meander structured titanium track with the thickness of 70 µm, line/space of 18 µm/ 22 µm and an overall length of 5.5 mm. The area of the temperature sensor is 0.2 mm$^2$ (1 mm x 0.2 mm). The sensor is placed in the center of the chip. The theoretically expected electrical resistance of the sensor $R_s$ can be calculated by the equation 4.21.

$$R_s = \rho \cdot \frac{L_s}{W_s \cdot T_s} \Rightarrow R_s = 3055 \ \Omega \tag{4.21}$$

Where:

| | | |
|---|---|---|
| $R_s$ | Electrical resistance of temperature sensors | $[\Omega]$ |
| $\rho$ | Specific electrical resistance ($= 70 \cdot 10^-8$ for Titanium) | $[\Omega \cdot m]$ |
| $L_s$ | Length of sensor track ($= 5.5$) | $[\text{mm}]$ |
| $W_s$ | Width of sensor track ($= 18$) | $[\text{µm}]$ |
| $T_s$ | Thickness of sensor track ($= 70$) | $[\text{nm}]$ |

The sensor is connected in four wire measurement configuration separating current carrying and sensing lines.

### 4.4.2 Fabrication, assembly and quality control of TTC

The chips were fabricated and assembled at the cleanrooms of Fraunhofer IZM based on the specification. First of all, the wafer design has been transferred into mask layouts for a set of 3 lithography masks for full wafer shadow printing [114]. After mask manufacturing, these masks serve to print the different layers of the TTC wafers. The six inch wafer provides space for around 1200 single chip cells.

For the *TIMA3* module, the chips were sawed in 3 x 3 matrix which yield nine chip

cells with the total size of 9.8 mm x 9.8 mm (3 cells, 3.2 mm each plus 2 scribe lines, 0.1 mm each). For the assembly a pick-and-place process followed by a solder reflow step was chosen. The chip has been placed on FR4 substrate. The substrate has been designed to be integrated into the *TIMA* test stand. On each substrate five temperature sensors (corner and center sensors) have been connected, which allow local temperature measurement (figure 4.14).
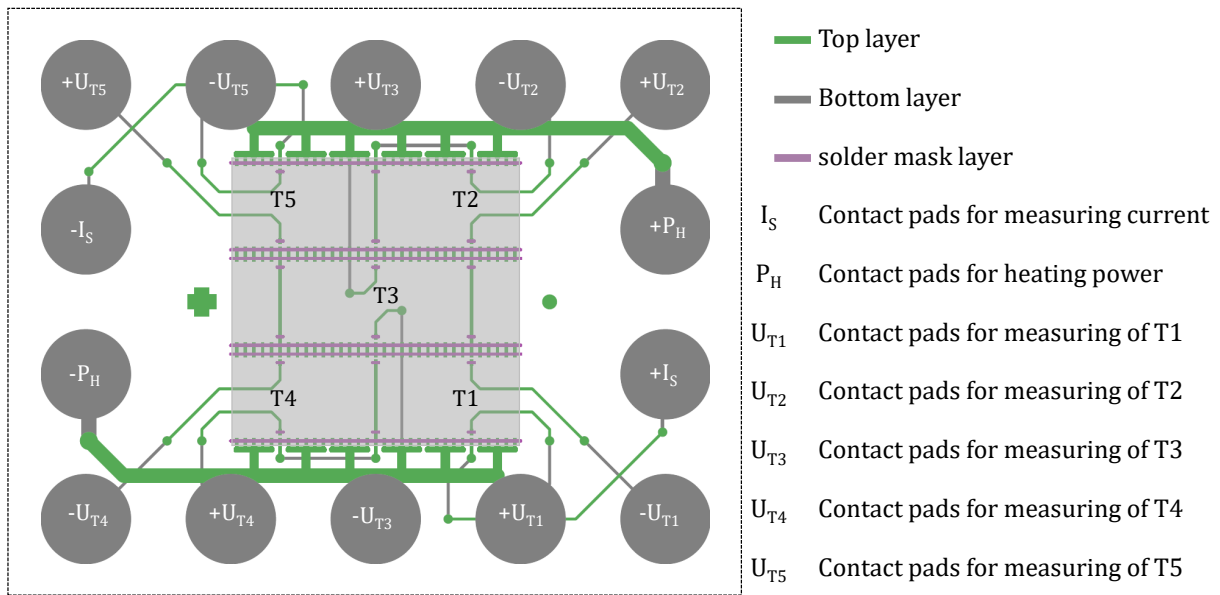


**Figure 4.14:** Layout of TTC substrate

After the reflow process, the chips have been underfilled to ensure high reliability of the chip.

Figure 4.15 shows an assembled and underfilled module. The advantage of underfilling is the enhanced reliability and temperature consistency of the module. As a decisive part for characterization of TIMs it is necessary that the modules show a high reliability [114].

### 4.4.3 Calibration and evaluation

The five temperature sensors of the assembled TTC were calibrated using an in-house built calibration chamber. Figure 4.17 shows the results of the calibration for the five temperature sensors. All sensors show very good linear behavior with a coefficient of determination $R^2 > 0.9998$ in the temperature range from $10\,°C$ to $100\,°C$.

The slopes of all sensors coincide very well with each other. The offset of the curves can be traced back to under- or over-etching of the sensor structures or by variation of the titanium thickness. Table 4.3 shows the values of the slopes and y-axis intercept (electrical resistance of the sensors at $T = 0\,°C$) for all temperature sensors. The relationship between
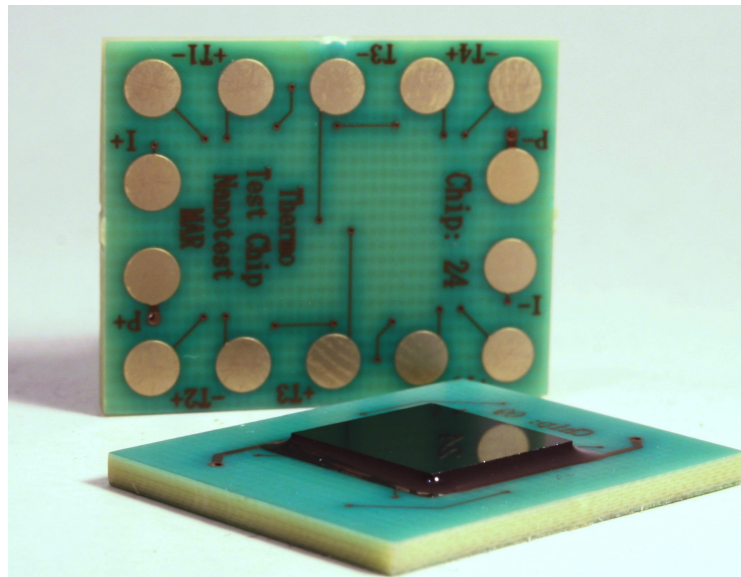
**Figure 4.15:** Photography of the soldered and underfilled TTC
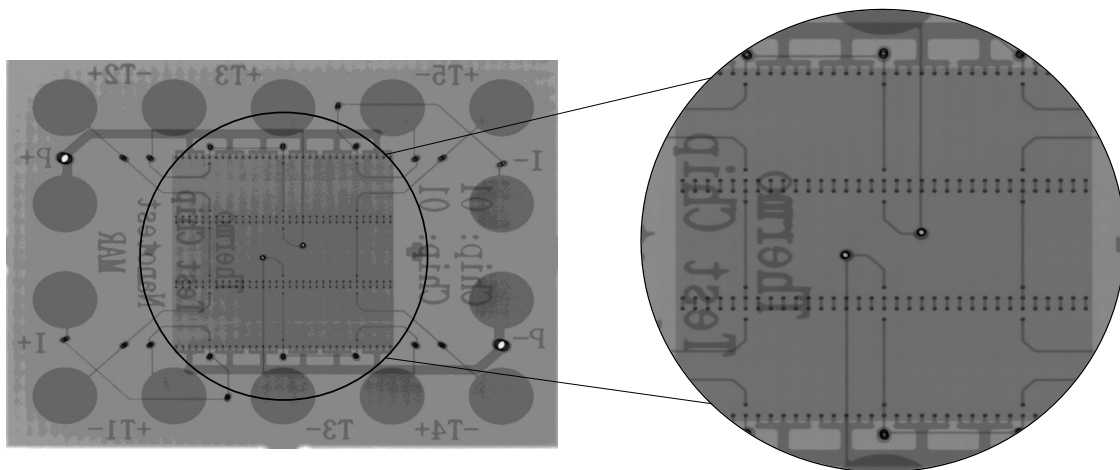


**Figure 4.16:** X-ray picture of the TTC as inspection reflow solder process *(Source: IZM)*

the resistance and the temperature is $\approx 8\ \Omega/\text{K}$, also called sensitivity.

A very important property of a TTC is the homogeneity of the generated heat. Good TTCs are characterized by a uniform heat flux over the entire contact surface of the sample. This characteristic can be determined very well with thermal simulations. Of course, this assumes that the full design and the internal structure of the relevant components are known, which is rarely given for commercial products. Alternatively, the heat flux distribution can be determined by means of contact-less thermal measurement methods such as IR thermography.

The occurring gradients in heat flow strongly depend on the absolute heat flow from the heater to the heat sink or reference body on the back side of the chip as used in *TIMA3*
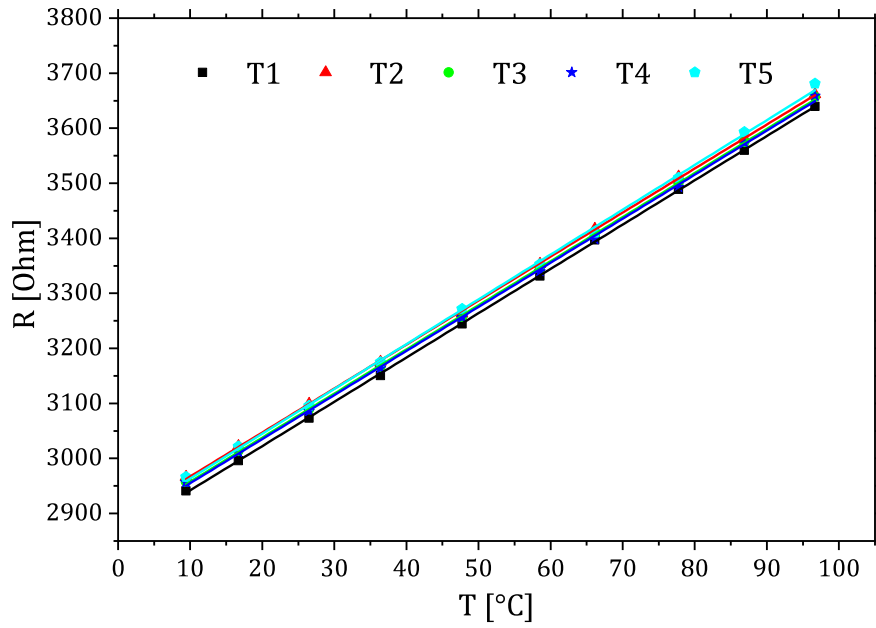
**Figure 4.17:** Calibration curves for the five temperature sensors

**Table 4.3:** Calibration values of all five temperature sensors of the chip

| Sensors | Slop [$\Omega$/K] | Offset [$\Omega$] | R-squared |
|---|---|---|---|
| T1 | 8.049 $\pm$ 0.028 | 2861 $\pm$ 1.7 | 0.99989 |
| T2 | 7.994 $\pm$ 0.033 | 2887 $\pm$ 1.9 | 0.99985 |
| T3 | 8.013 $\pm$ 0.035 | 2878 $\pm$ 2.0 | 0.99983 |
| T4 | 8.009 $\pm$ 0.060 | 2875 $\pm$ 3.6 | 0.99949 |
| T5 | 8.140 $\pm$ 0.079 | 2882 $\pm$ 4.7 | 0.99915 |
| Main value | 8.041 | 2877 | – |
| Standard deviation | 0.053 | 9 | – |

module (figure 4.4). Heated under terms of natural convection, for example, no heat flow will be derived as the whole chip would easily saturate thermally. Maximizing the heat flow a maximum temperature gradient will occur. Therefore, a high heat flow should be maintained during the investigation of the homogeneity to determine the largest gradient to occur. However, during the operation the surface of the TTC is not optically accessable and cannot be analyzed by common thermal imaging techniques such as IR thermography. As shown in figure 4.4, the TTC is in direct thermal contact with the specimen and a reference body.

But, replacing the static IR analysis method by a transient one like the Lock-in thermography it is possible to evaluate the homogeneity of heat flow without a connected thermal reference resistor and without thermally saturating the chip. This technique allows to determine buried heat sources inside the chip/package top side up with thermal resolution in µK to mK range [115].

The heater structures of a TTC are typically located on one side of the chip where thermal excitation occurs by periodically switching on and off power supply with a specified frequency. On the opposite this temperature oscillation can be measured effectively by the Lock-In thermography technique. This is shown in figure 4.18.
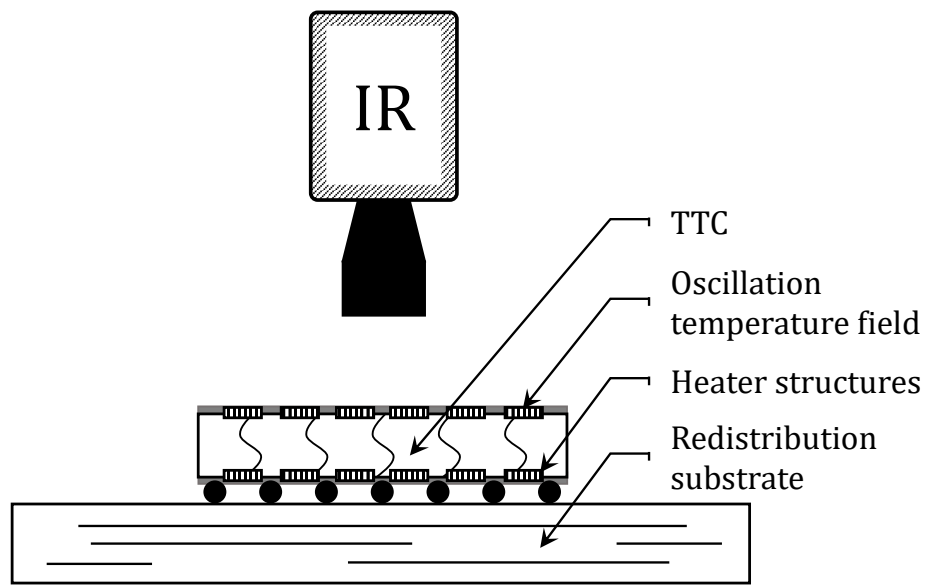


**Figure 4.18:** Schematic of experimental setup for the evaluation of temperature homogeneity of TTC surface by Lock-In thermography

The main statement of such results is how areas of the surface are heated by the corresponding heater structures on the opposite side. By choosing the Lock-In frequency $f = 25$ Hz the thermal diffusion length in silicon is about 1 mm. Thus, the thermal wave front just reaches the opposite side. At the same time a low spreading and thus a sharp imaging of the heater structures is achieved. The parameters shown in table 4.4 were chosen for the experiments.

Amplitude images overlaid with chip structures of the investigations related to two TTCs are shown in figure 4.19. On the one hand (left) the PCT102 of Delphi and on the other (right) the new NT16-3k developed within this work and described above.

In direct comparison, it can be seen that the temperature distribution at the NT16-3k-chip is homogeneously spread across the entire chip area. Also absolute numbers witness advantage. Where at the PST102 a maximum temperature gradient of 30 mK occurs, the NT16-3K only shows 7 mK of absolute temperature gradient. The difference can be explained well with the structure of the heating elements. Compared to the NT16-3K

**Table 4.4:** Parameters for the Lock-In thermography experiments of TTC

| Parameter | Symbol | Value |
|---|---|---|
| Lock-In frequency | $f_{LI}$ | 25 Hz |
| Duty cycle | $d_c$ | 50 % |
| Excitation power | $P_{exc}$ | 0.5 W |
| Excitation time | $t_{exc}$ | 20 ms |
| Sampling rate of IR camera | $f_{IR}$ | 100 Hz |
| Excitation periods took into account | $P$ | 1500 |
| Preheating for steady-state | $t_{ss}$ | 120 s |
| Mean temperature | $T_m$ | 40.5 °C |
| Overall experimental time | $t_{total}$ | 180 s |

only half of a unit cell of PST102 has heater structures. Especially at the edges this causes high differences in temperature distribution (blue stripe left edge, red stripe right edge).

For measurements using the PST102 chips these effects amount to not negligible errors. During *TIMA*-measurements a homogeneous heat flow is assumed and the contact temperature as important parameter is measured at only one point, which leads to a miscalculation of the actual heat flow. In summary, it can be stated that the improved distribution of the heating structures significantly contributes to the TTC's accuracy and, consequently to the TIMA measurement accuracy.
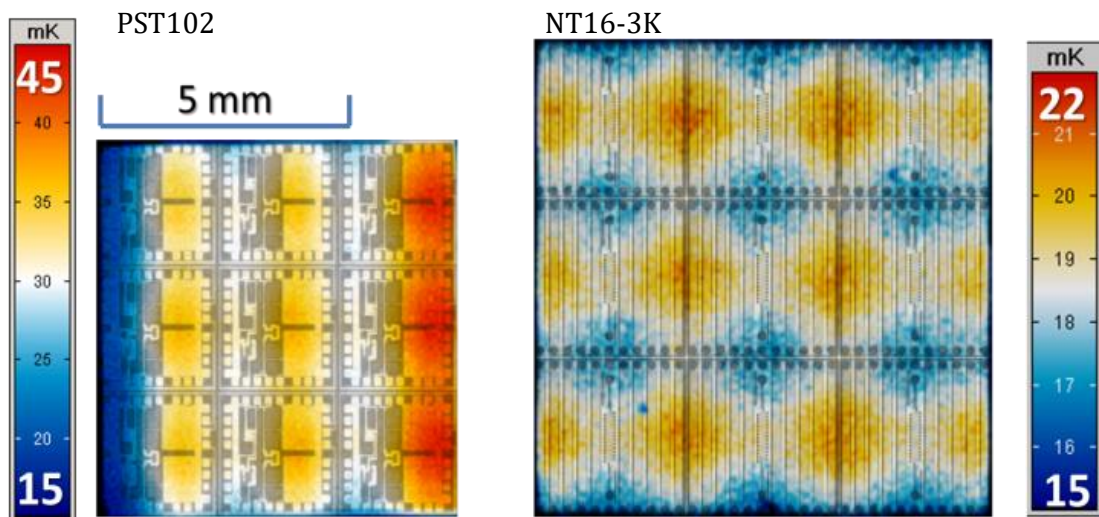


**Figure 4.19:** IR Lock-In amplitude images of two different TTCs for heater homogeneity evaluation

# 4.5 Characterization results by *TIMA*

Several thermal interface materials, substrates and multi-layer samples have been characterized by the *TIMA* test stand. In addition to the thermal properties such as bulk and effective thermal conductivity, thermal resistance, thermal interface resistance, several effects and influences such as thermal properties as function of temperature, pressure, curing condition etc. have been studied.

## 4.5.1 Thermal characterization of TIMs

As described in section 4.1, in order to determinate the bulk thermal conductivity and the thermal interface resistance, the effective thermal resistance of a material should be measured at different thicknesses under the same conditions, which have a linear relationship. The bulk thermal conductivity is calculated from the slope and the interface resistance is represented by the intercept with the thermal resistance axis (Y-axis).

The bulk thermal conductivity and the thermal interface resistance of different types of TIMs have been measured by *TIMA*. Some measurement results will be presented here. Particular attention has been paid to the process-structure-property correlation as well as the influence of boundary conditions (temperature, pressure etc.) on thermal properties.

### 4.5.1.1 Characterization of thermal pad

Thermal pads are among the simplest measured TIMs. They are easy to handle and barely require sample preparation. Several thermal pads have been characterized by the *TIMA* test stand. The characterization results of an advanced thermal pad as representative example will be shown. The selected material is a thermal conductive sheet containing vertically oriented graphite (VOG) fillers in an acrylic rubber-based matrix.
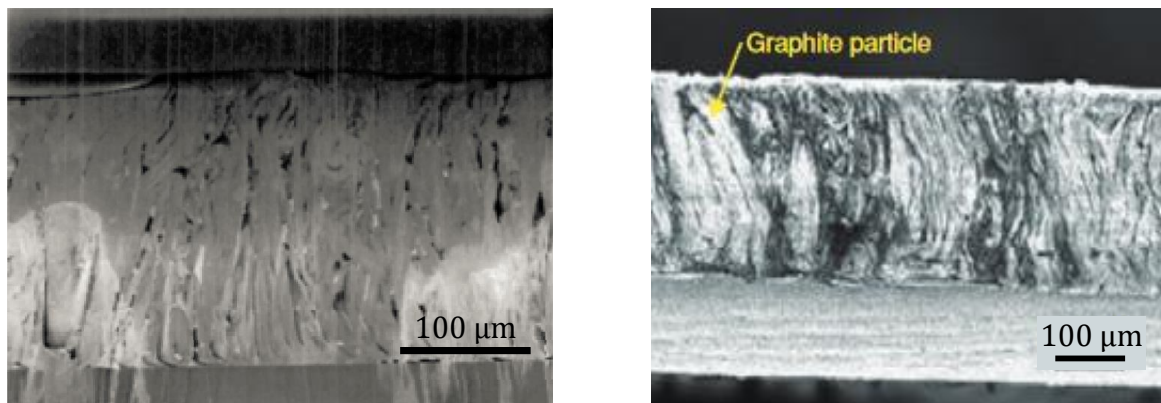


**Figure 4.20:** SEM cross-section of thermal pad with vertically oriented graphite (VOG) [116]

The TIM existed in three different thicknesses (150 µm, 250 µm and 500 µm), this allows to determine the bulk thermal conductivity ($\lambda_{bulk}$) and the thermal interface resistance ($Rth_0$). The effective thermal resistance ($Rth_{eff}$) as function of the bond line thickness ($BLT$) has been measured at different pressures ($p$) between 100 kPa and 2 MPa.

The diagram (figure 4.21) shows the linear dependency between $Rth_{eff}$ and $BLT$.
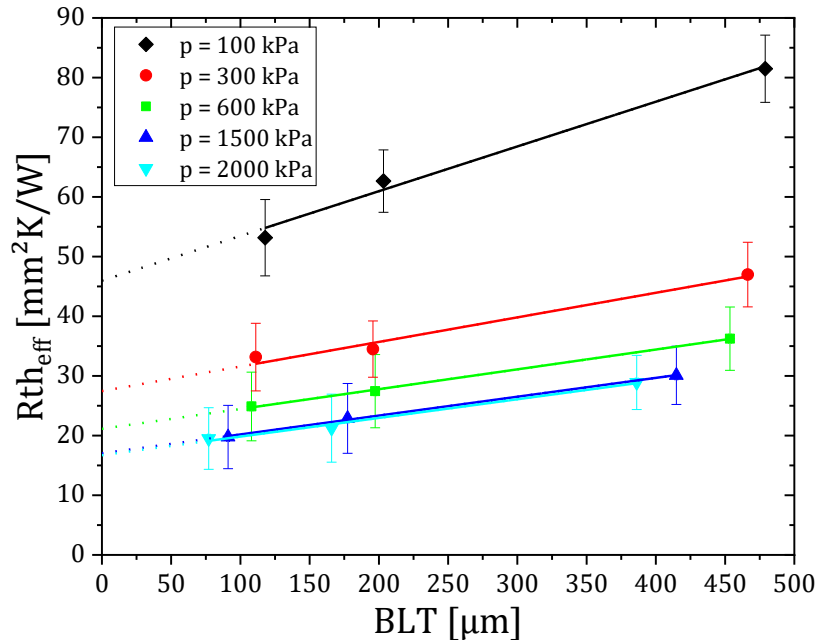


**Figure 4.21:** Effective thermal resistance as function of bond line thickness of the VOG based TIM measured under different pressures

**Table 4.5:** Bulk thermal conductivity and thermal interface resistance of the VOG based TIM

| $p$ [kPa] | $\lambda_{bulk}$ [W/(m$\cdot$K)] | $Rth_0$ [mm$^2\cdot$K/W] |
|---|---|---|
| 100 | 13.3 $\pm$ 1.6 | 46.0 $\pm$ 4.1 |
| 300 | 24.3 $\pm$ 2.4 | 27.5 $\pm$ 3.4 |
| 600 | 30.1 $\pm$ 2.7 | 21.1 $\pm$ 3.2 |
| 1500 | 31.6 $\pm$ 2.6 | 17.0 $\pm$ 2.7 |
| 2000 | 32.0 $\pm$ 2.5 | 16.7 $\pm$ 2.2 |

As can be seen in table 4.5 and figure 4.22, both the bulk thermal conductivity and the thermal interface resistance of the VOG based TIM are strongly dependent on the pressure. The bulk thermal conductivity measured at 600 kPa pressure is around 2.2 times higher than the bulk thermal conductivity measured at 100 kPa. This improvement is due to the consolidation of the VOG under pressure. Also the thermal interface resistance at 600 kPa is around 2.2 times lower than at 100 kPa because of the increasing of the contact between the surfaces and the graphite fillers. The measurement results for more

than 600 kPa showed less improvement in both bulk thermal conductivity and thermal interface resistance.
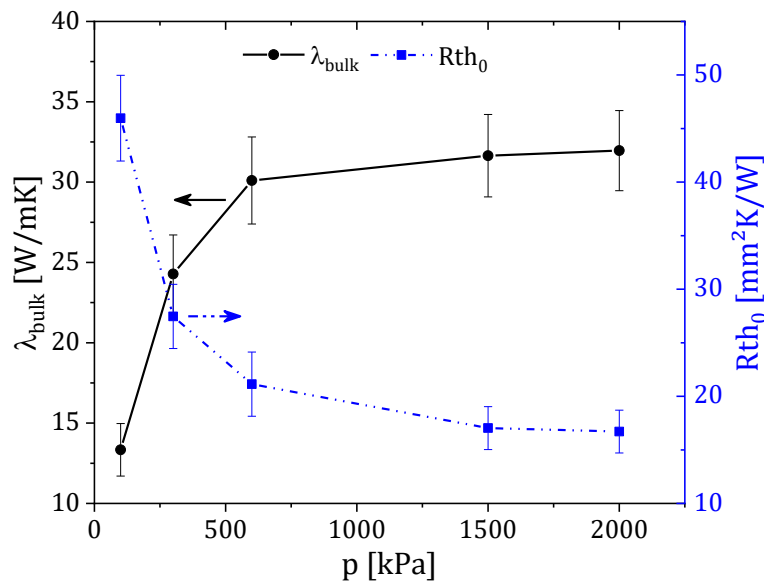


**Figure 4.22:** Bulk thermal conductivity and thermal interface resistance of VOG based TIM as function of pressure

This relatively high number of bulk thermal conductivity up to $32\,\mathrm{W/(m \cdot K)}$ is an atypical value for thermal pads [117], [21]. But the highly thermal conductive vertically oriented graphite makes it possible [116].

### 4.5.1.2  Characterization of thermal grease

To demonstrate the characterization of thermal greases, a material has been selected which consists of dicyandiamid filled with silver-coated polymer spheres with uniform diameter of 10 µm and 140 nm silver coating [118]. First of all, the bulk thermal conductivity and the interface resistance of the unfilled dicyandiamid have been determined by measuring the effective thermal resistance ($Rth_{eff}$) at different bond line thicknesses ($BLT$) by *TIMA6* using aluminium reference bodies with standard surface roughness $R_Z \approx 2$ µm.

It results for the unfilled dicyandiamid a bulk thermal conductivity $\lambda_{bulk}$ of $0.23\,\mathrm{W/(m \cdot K)}$ and a thermal interface resistance $Rth_0$ of $84\,\mathrm{mm^2 \cdot K/W}$ (figure 4.23). Due to the very low viscosity of the materiel, the measurements of thermal resistance in all thicknesses have been performed without pressure.

In a second step, the dicyandiamid has been filled by silver-coated polymer particles (diameter: 10 µm, thickness of coating: 140 nm, particle proportion: 32 vol%).
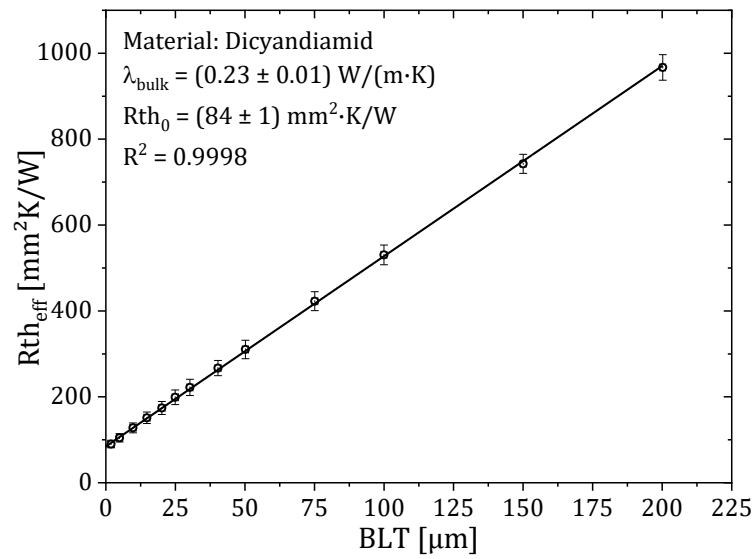
**Figure 4.23:** Effective thermal resistance of dicyandiamid as function of the bond line thickness

The effective thermal resistance of the mixture has been measured at different thicknesses by *TIMA6* using the same aluminium reference bodies.
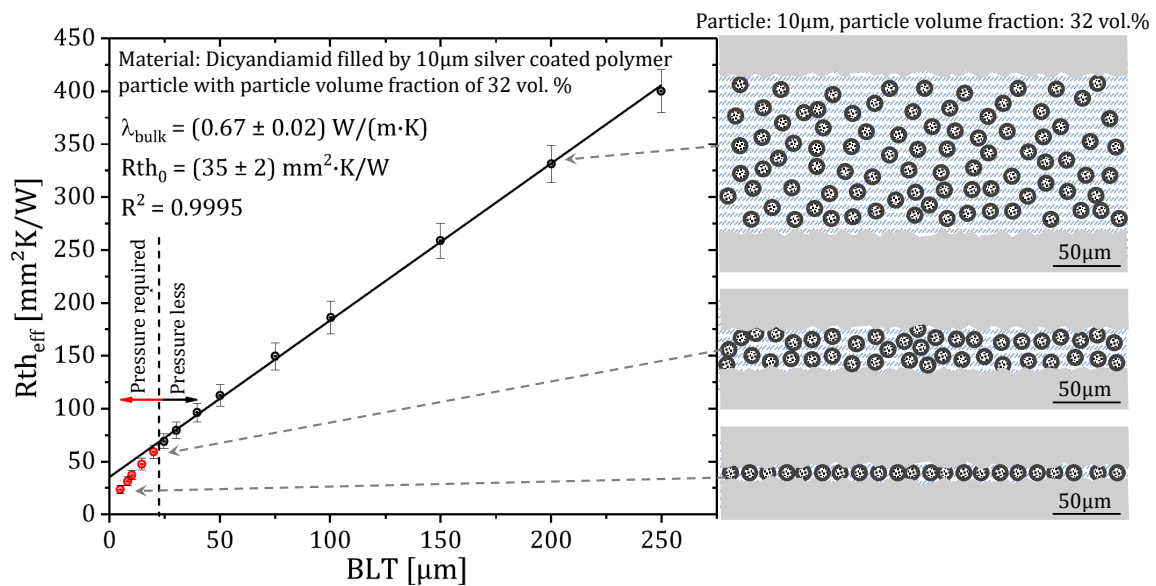


**Figure 4.24:** Left: effective thermal resistance as function of bond line thickness of filled dicyandiamid by 10 µm silver-coated polymer particles. Right: schematic illustration of particle distribution in the thermal grease layer at different bond line thicknesses

The measurements of thermal resistance in the thicknesses between 250 µm and 25 µm did not require any pressure and show a very good linearity which results in bulk thermal conductivity of 0.67 W / (m · K). To produce bond line thicknesses below 25 µm, pressure was required as particles move closer to each other and to the surfaces.

The measured effective thermal resistance at these thicknesses fall out of line, they show

lower thermal resistance as expected. This size effect can be explained by the more direct contact between particles and reference bodies.

BLTs below the diameter of the particles (10 µm) could also be achieved under pressure (around 240 kPa), their effective thermal resistance values are even lower than the thermal interface resistance results from the extrapolation of the linear fit (see figure 4.24).

The lowest thermal resistance of $(23 \pm 3)$ mm$^2 \cdot$K/W has been achieved at BLT of 5 µm, which is around 35% lower than the thermal interface resistance of $(35 \pm 2)$ mm$^2 \cdot$K/W calculated from the linear fit of thermal resistance over the BLT.

Another mixture has been prepared and measured. The mixture consisted of the dicyandiamid and larger, i.e. 30 µm silver-coated polymer particles with the same fraction (32 vol%). The measurement of the results of thermal resistance showed similar behavior as for the material with 10 µm particles (figure 4.25).
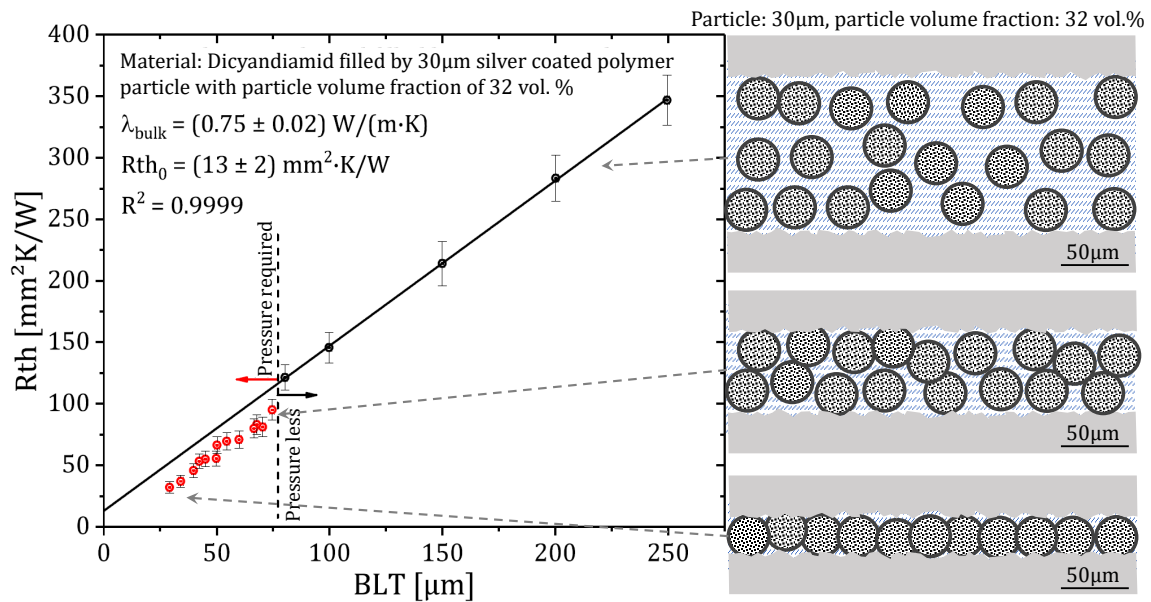


**Figure 4.25:** Left: effective thermal resistance as function of bond line thickness of filled dicyandiamid by 30 µm silver-coated polymer particles. Right: schematic illustration of particle distributions in the thermal grease layer at different bond line thicknesses

Measurement at BLT down to 75 µm did not require any pressure. The results showed a good linearity between thermal resistance and BLT, from which the bulk thermal conductivity of 0.75 W/$($m$\cdot$K$)$ and the thermal interface resistance of 13 mm$^2 \cdot$K/W have been calculated. For BLT below 75 µm pressure was required. To achieve a BLT of 25 µm, pressure up to 1.5 MPa has been applied. The thermal resistance of the layers measured under pressure showed here also lower values than expected. The lowest measured thermal resistance of this grease was around 30 mm$^2 \cdot$K/W, which matches well with the lowest value measured of the grease with the smaller 10 µm particles.

### 4.5.1.3  Characterization of adhesive

The test stand *TIMA* also provides the possibility to characterize adhesive material. This option given by the test stand *TIMA* is a considerable advantage compared to other test stands based on ASTM D-5470. To determine the bulk thermal conductivity and the thermal interface resistance of the adhesive, samples with different bond line thicknesses (BLT) are needed again. For this an assembly tool has been designed and manufactured. The tool allows assembling of the adhesive in well-defined BLT between two reference bodies and curing them at temperatures up to 500°C if needed. Figure 4.26 illustrates the assembling procedure from single reference body to cured adhesive samples with well-defined BLT ready to be measured by *TIMA*.
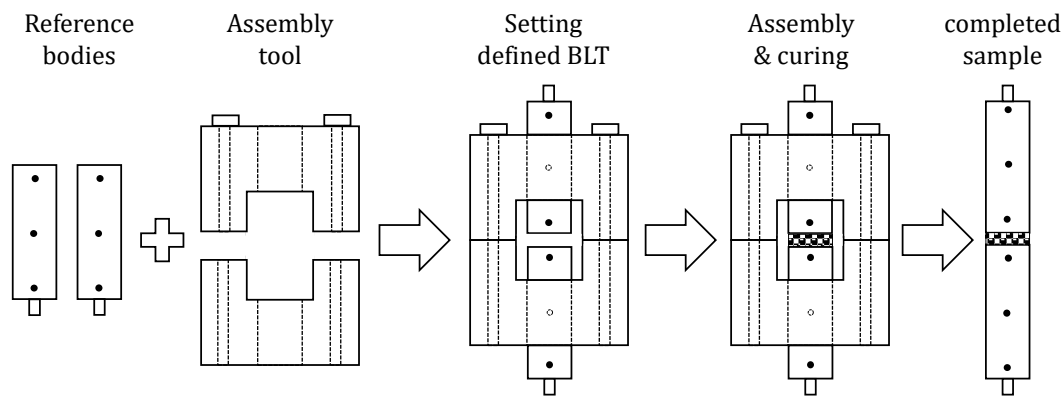


**Figure 4.26:** Preparation procedure of adhesive samples with defined BLT using the assembly tool

Within this work a novel thermal adhesive has been selected and characterized by the *TIMA* test stand. The selected adhesive consists of epoxy matrix with silver-coated polymer spheres as conductive filler instead of solid metal particles, fabricated by the company Conpart. The polymer particles have the uniform size of 10 µm with the thickness of silver coating of 140 nm.
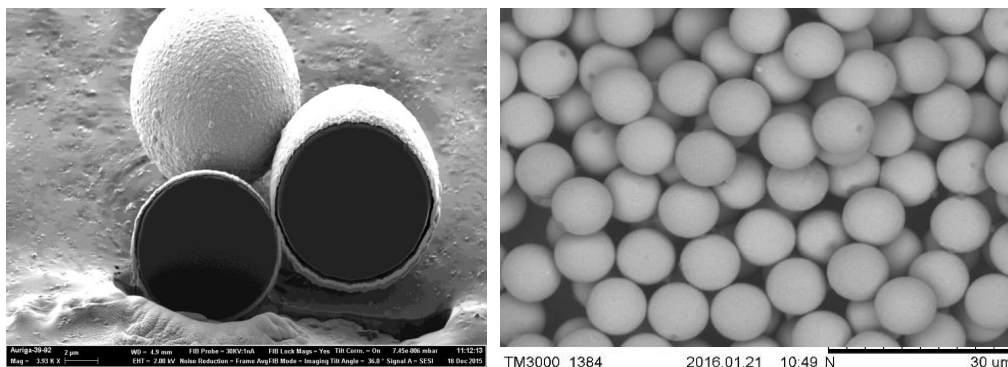


**Figure 4.27:** SEM images show 10 µm polymer spheres coated with 140 nm silver layer (*Source: Conpart Technology, Norway*)

Three different mixtures have been characterized, which varied in the volume fraction of particles (40 vol%, 45 vol% and 50 vol%).

From each mixture four samples with different BLT between 70 µm and 370 µm have been assembled by the tool shown in figure 4.26 and cured for one hour at 150°C. The effective thermal resistances of all samples have been measured by the test stand *TIMA6* under three different temperatures 40°C, 60°C and 80°C (mean temperature of TIM). Finally, the BLT of all samples have been double checked by cross section images (see figure 4.28).
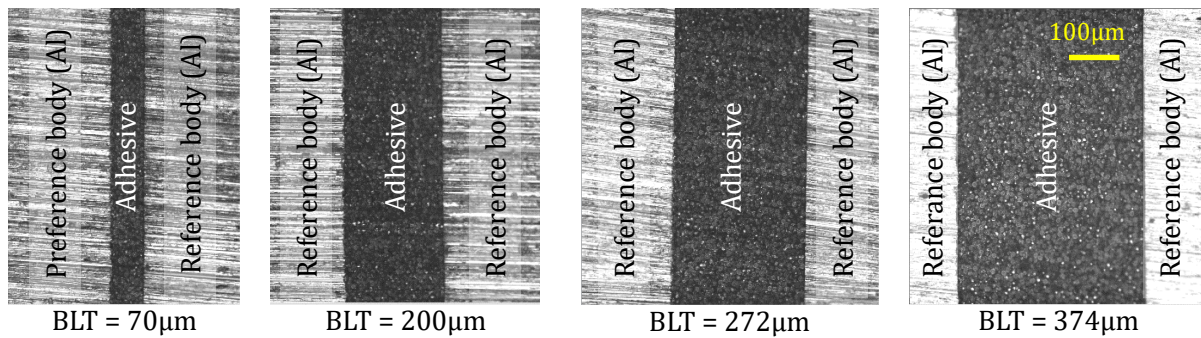


**Figure 4.28:** Cross section images of selected samples to measure the actual BLT

The results of bulk thermal conductivity as function of volume fraction and measurement temperature are shown in figure 4.29.
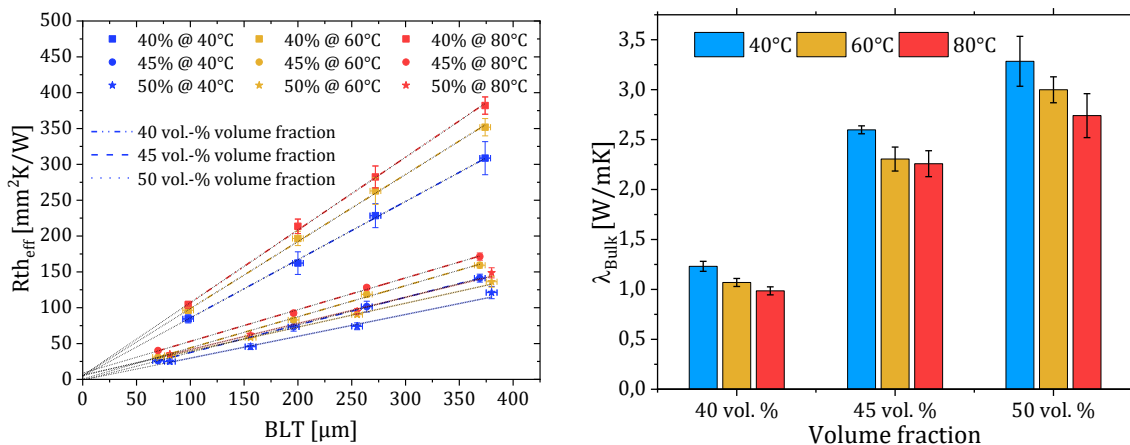


(a) Effective thermal resistance as function of the bond line thickness

(b) Bulk thermal conductivity as function of volume fraction and temperature

**Figure 4.29:** Thermal characterization results of the adhesive as function of particle volume fraction and temperature

The influence of the particle volume fraction on the thermal performance can be clearly seen. The bulk thermal conductivity is increased by 175 % by increasing the particle volume fraction from 40 vol% to 50 vol%. However, increasing the particle volume fraction from 40 vol% to 45 vol% led to 120 % higher thermal conductivity, while the increase from
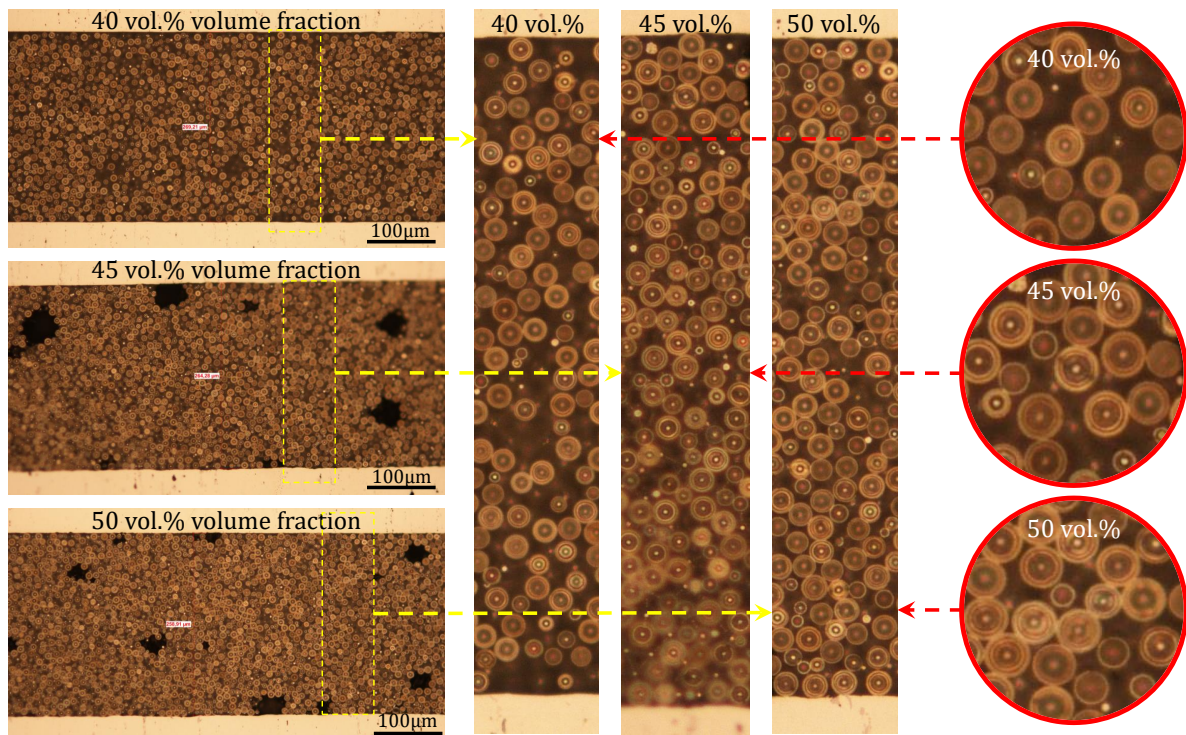
**Figure 4.30:** Microscopic images show the particle distribution for different particle volume fraction. Differences in particle density can be clearly seen.

45 vol % to 50 vol % resulted in only 25% increasing of the thermal conductivity. Also the measurement temperature shows an influence on the thermal conductivity. The higher the temperature the lower the thermal conductivity. Bulk thermal conductivity of the sample at 80°C is around 20 % lower than the value measured at 40°C.

In order to understand the influence of the particle volume fraction on the bulk thermal conductivity of the adhesive, the micro structures of the layers have been investigated using scanning electron microscopy (SEM). As can be seen in figure 4.30, increasing the particle density results in improvement in thermal path, which leads to higher thermal conductivity. It can also be seen that voids occur in the adhesive layer with higher particle volume fraction, due to the loss of viscosity, which weakness the thermal path, too.

As can be seen in figure 4.29 (a), the thermal interface resistances of all samples are relatively low (close to zero), which could be attributed to the good wetting of the surfaces, since the materials have relatively low viscosity.

This assumption has been confirmed by FIB and SEM investigation of the interface between adhesive and reference body. The images in figure 4.31 show perfect interface between adhesive and reference body, which led to very low thermal interface resistance.
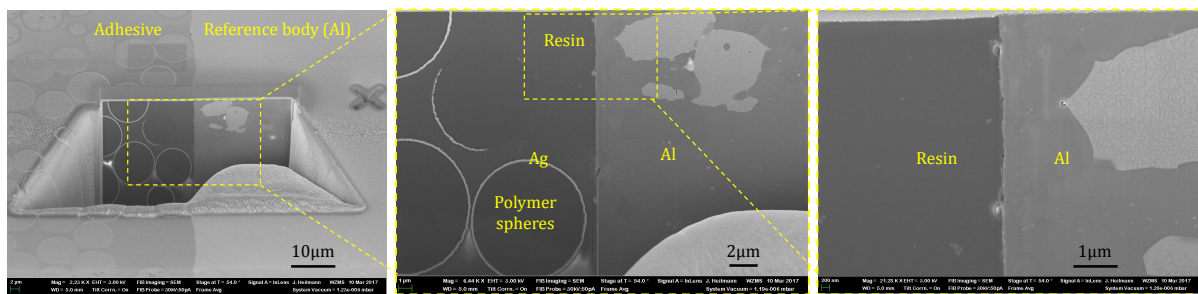
**Figure 4.31:** SEM images of the adhesive with 45 vol% particle volume fraction showing the interface between adhesive and reference body

#### 4.5.1.4   Characterization of gap filler

Three commercial gap fillers have been selected to be characterized by the test stand *TIMA*. All three gap fillers are two-component materials, which were mixed in 1 : 1 ratio and cured for one hour at 100°C.

Corresponding test samples with different BLT have been assembled between aluminium reference bodies using the assembly tool shown in figure 4.26. Due to the fact that gap fillers are usually used to bridge large gaps between hot components and cold surface, the samples have been built in relativity thick BLT between 150 µm and 900 µm. Figure 4.32 presents the effective thermal resistance of the three gap fillers plotted over the BLT. The values of the bulk thermal conductivity and the thermal interface resistance are listed in table 4.6.
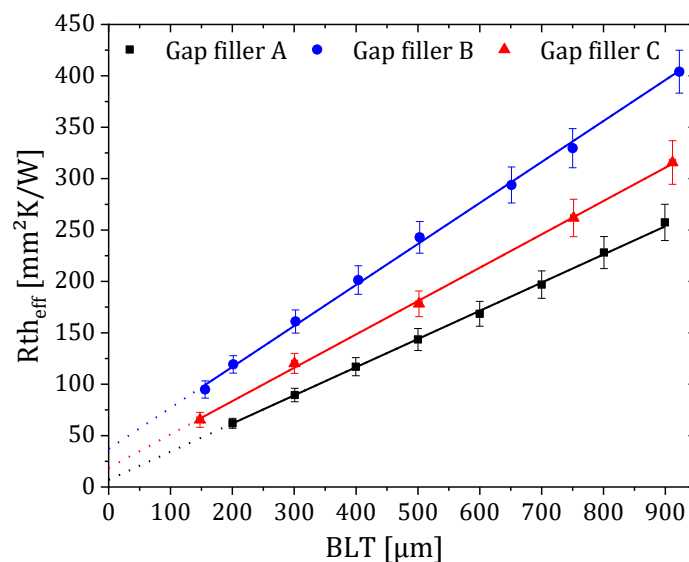


**Figure 4.32:** Effective thermal resistance as function of the bond line thickness of three different silicone based gap fillers

**Table 4.6:** Bulk thermal conductivity and thermal interface resistance of the measured gap fillers

| Material | $\lambda_{bulk}$ [W/(m·K)] | $Rth_0$ [mm$^2$·K/W] |
|---|---|---|
| Gap Filler A | 3.6 ± 0.1 | 7 ± 2 |
| Gap Filler B | 2.5 ± 0.2 | 37 ± 3 |
| Gap Filler C | 3.1 ± 0.2 | 17 ± 3 |

### 4.5.2  Thermal characterization of substrate

Usually, the thermal conductivity of substrates is determined by transient methods such as the laser-flash method [119], where the the thermal diffusivity of a bulk sample is measured. To determine the thermal conductivity, the specific heat capacity and the density are needed in addition. For the characterization of multilayer samples such as Insulated Metal Substrate (IMS) or samples with heterogeneous thermal conductivity such as substrate with electrical or thermal vias, the steady-state method could be the better choice, as this method will rather make a statement about the thermal conductivity of the whole sample. There are two challenges within the substrate characterization by steady-state techniques: On one hand, the relatively high thermal interface resistance between the sample and the matted surfaces, and on the other hand, the high thermal conductivity of the sample.

In contrast to characterization of TIMs, the thermal interface resistance heavily complicates the characterization of highly thermal conductive substrates using the steady-state techniques, due to the high surface roughness and the lack of a gap filler.
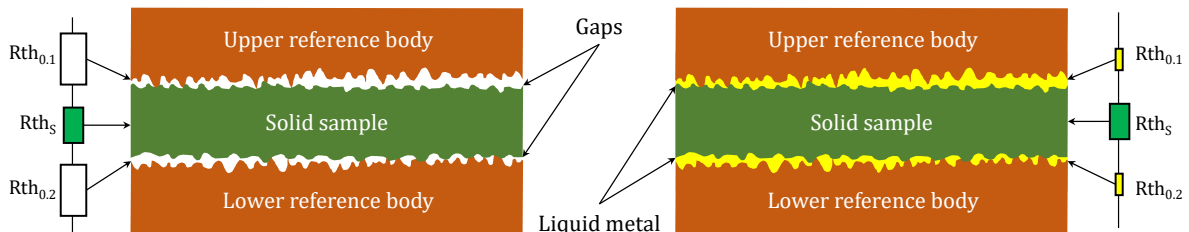


**Figure 4.33:** Schematic of the microscopic surface roughness of reference body and solid sample. Left: dry contact with gaps; right: Gap filled by liquid metal.

To reduce the thermal interface resistance, highly thermal conductive liquid metal has been used, which can perfectly fill the gap between the sample and the matted surfaces whilst only having a negligible influence on the measurement results credibility. Figure 4.33 shows schematically the contact between matted surfaces and substrate with and without liquid metal.

To demonstrate the effect of liquid metal as thermal interface material, a simple experiment has been done by using the test stand *TIMA6*, in which the thermal interface

resistance between two copper reference bodies with surface roughnesses $R_z \approx 2\,\mu m$ has been measured using two liquid metals, a standard silicone based grease and a dry contact (air). In addition, the measurements were performed using different pressures between 100 kPa and 600 kPa.

Figure 4.34 shows the results of the thermal resistance of the different materials for different pressures. It can be seen, that one liquid metal leads to extremely low thermal resistance even at low pressure. The other liquid metal also has a relatively low thermal resistance, which is at under 100 kPa pressure around 5 times lower than the standard thermal grease and it goes to zero under pressure. The thermal interface resistance of the dry contact is extremely high. This result confirms the imperative of using highly conductive material to eliminate the interface resistance.
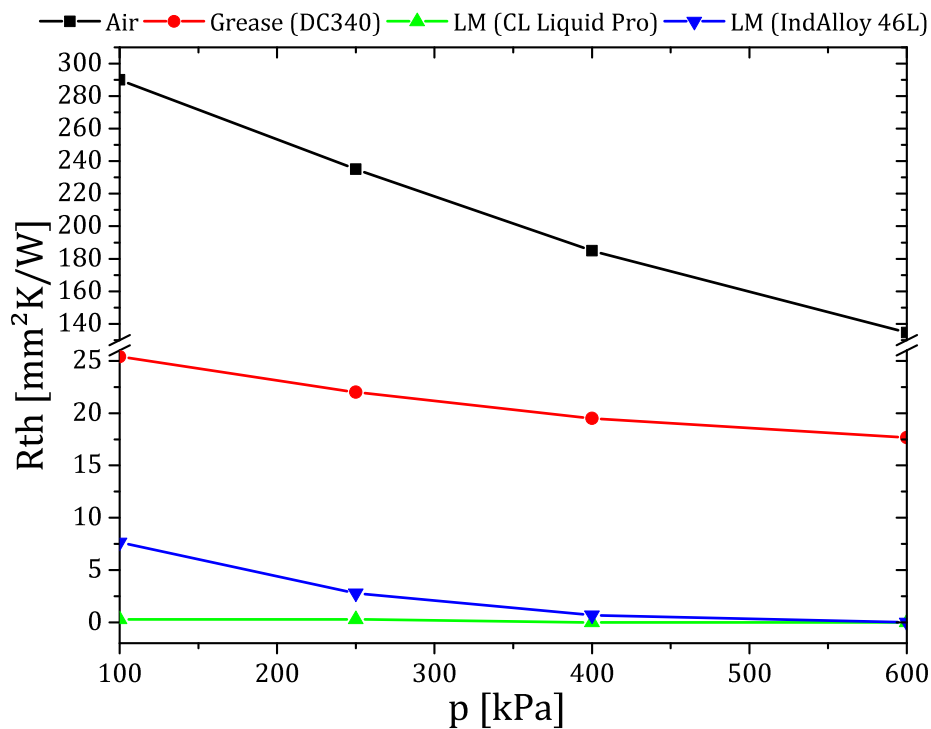


**Figure 4.34:** Thermal resistance as function of pressure. Upper curve: metal to metal contact without TIM; lower curves: metal to metal contact with two liquid metals *CL Liquid Pro and IndAlloy 45L* and one grease *DC340*

The liquid metal *CL Liquid Pro* shows better thermal performance. However, for the characterization of solid samples by *TIMA* the liquid metal *IndAlloy 45L* has been chosen, due to availability and cost. The liquid metal *IndAlloy 45L* consists of 61% Gallium, 25% Indium, 13% Tin and 1% Zinc. The melting temperature of this liquid metal is around 7°C.

In the following, thermal characterization results of different substrates, measured by the test stand *TIMA* using the approach described above will be presented and discussed.

#### 4.5.2.1 Thermal characterization of bulk substrate

Table 4.7 summarizes the results of the bulk thermal resistance and bulk thermal conductivity of different substrates measured by the *TIMA* by using the liquid metal *IndAlloy 45L* to minimize the interface resistance between the reference body and the sample:

**Table 4.7:** Thermal characterization results of bulk substrates

| Material | Thickness [µm] | $Rth_{bulk}$ $\left[\text{mm}^2 \cdot \text{K/W}\right]$ | $\lambda_{bulk}$ [W / (m·K)] | $\lambda_{bulk}$ (Literature) [W / (m·K)] |
|---|---|---|---|---|
| LTCC | 639 ± 5 | 292 ± 12 | 2.18 ± 0.12 | 1.8 ⋯ 3.3 [120] |
| FR4 | 300 ± 5 | 968 ± 32 | 0.31 ± 0.03 | 0.29 [121], 0.34 [122] |
| $Al_2O_3$ | 360 ± 5 | 17.2 ± 2 | 21 ± 3 | 17 ⋯ 28 [123] |

The results of thermal conductivity for all three bulk substrates agree with the literature values, as can be seen in the table 4.7.

#### 4.5.2.2 Thermal characterization of multi-layer substrate

Multi-layer substrates such as DCB (Direct Bonded Copper), IMS (Insulated Metal Substrate), multi-layer PCB (Printed Circuit Board) or multi-layer LTCC (Low temperature co-fired ceramic) are often used in electronics devices. The knowledge of their thermal properties is significant for the design of components and systems. As mentioned before, *TIMA* is particularly suitable for the direct measurement of the effective thermal conductivity of such substrates. Table 4.8 shows the measurement results of some multi-layer substrates measured by *TIMA* using the liquid metal *IndAlloy 45L* to minimize the interface resistance between the reference body and the sample.

**Table 4.8:** Thermal characterization results of multi-layer substrates

| Material | Thickness [µm] | $Rth_{eff}$ $\left[\text{mm}^2 \cdot \text{K/W}\right]$ | $\lambda_{eff}$ [W / (m·K)] |
|---|---|---|---|
| LTCC (incl. 5 Cu layers) | 690 ± 5 | 299 ± 15 | 2.3 ± 0.1 |
| LTCC (incl. 7 Cu layers) | 930 ± 5 | 370 ± 18 | 2.4 ± 0.1 |
| IMS (Cu/Polymer/Cu) | 3200 / 100 / 300 | 40.6 ± 2.1 | 89 ± 5 |
| IMS (Cu/Polymer/Cu) | 1000 / 100 / 200 | 23.9 ± 1.2 | 54 ± 3 |

#### 4.5.2.3 Thermal characterization of heterogeneous substrate

The term heterogeneous substrate describes substrates with regions filled with highly conductive materials such as LTCC with silver vias or FR4 substrate with copper core. Such substrates are usually used for heat dissipation of small chips e.g. for LEDs. Also for this case, *TIMA* is a suitable method for the measurement of the effective thermal conductivity of such substrates.
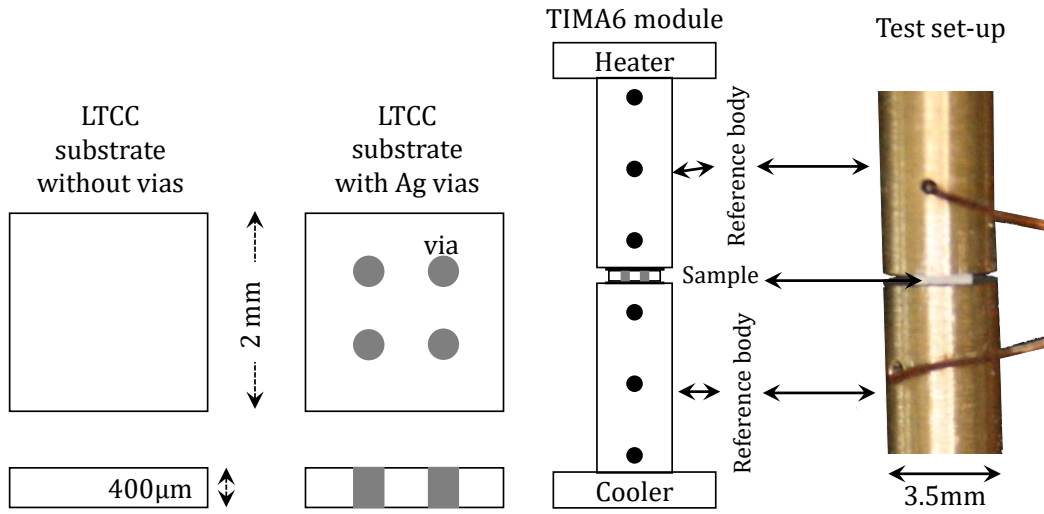
**Figure 4.35:** Test set-up and samples. Right: schematic and photography of test set-up *TIMA6* module; left: schematic of the samples (LTCC substrate with and without vias).

In the following example the characterization results of a LTCC substrate with thermal vias (sintered silver) will be presented.

To increase the resolution of the measurement, according to the investigation described in section 4.3.2, the samples were cut in 2 x 2 mm$^2$. The measurement has been done between two Cu reference bodies with the diameter of $\varnothing = 3.5$ *mm* using the *TIMA6* module. Liquid metal has been used as interface medium.

In order to demonstrate the improvement of the thermal performance by the Ag vias and to calculate the thermal conductivity of the vias, LTCC substrates with and without vias have been measured under the same conditions.

**Table 4.9:** Characterization results of LTCC substrates with and without vias

| Sample | Thickness [µm] | $Rth_{eff}$ $\left[\text{mm}^2 \cdot \text{K/W}\right]$ | $\lambda_{eff}$ $\left[\text{W}/\left(\text{m} \cdot \text{K}\right)\right]$ |
|---|---|---|---|
| LTCC with four Ag vias ($\varnothing = 300\,\mu\text{m}$) | $400 \pm 2$ | $17.3 \pm 0.6$ | $23 \pm 1$ |
| LTCC without vias | $400 \pm 2$ | $172 \pm 5$ | $2.5 \pm 0.1$ |

As can be seen in table 4.9, the thermal conductivity of the LTCC substrate with the vias is at one order of magnitude higher than the that without vias.

Figure 4.36 illustrates the equivalent circuit of the LTCC substrate with four Ag vias. The total thermal resistance is described by following equation:
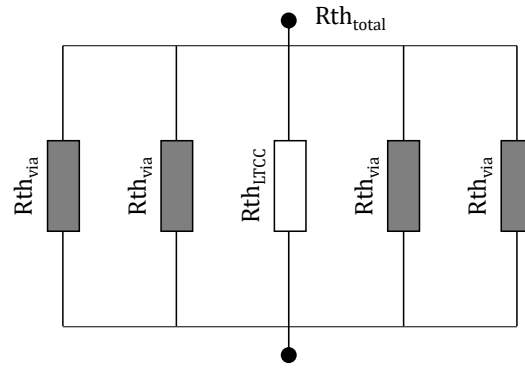
**Figure 4.36:** Equivalent circuit for LTCC substrate with four thermal vias (parallel circuit)

$$\frac{1}{Rth_{total}} = \frac{1}{Rth_{LTCC}} + \frac{4}{Rth_{via}} \tag{4.22}$$

$$\Rightarrow Rth_{via} = \frac{4}{(1/Rth_{total}) - (1/Rth_{LTCC})} \tag{4.23}$$

where $Rth_{total}$ is the thermal resistance of LTCC substrate including all four vias, $Rth_{via}$ is the thermal resistance of one via and $Rth_{LTCC}$ is the thermal resistance of bulk LTCC.

The thermal resistance of the substrate with vias as well as the bulk substrate have been measured, so the thermal resistance of the vias can be easy calculated. It results in the thermal resistance for one via of $Rth_{via} = (19.2 \pm 0.9) \cdot 10^{-6}$ K/W.

The thermal conductivity of the vias $\lambda_{via}$ can be calculated by following equation:

$$\lambda_{via} = \frac{l_{via}}{A_{via} \cdot Rth_{via}} \tag{4.24}$$

where, $l_{via}$ the length of the vias $= 400\,\mu m$, $A_{via}$ the cross section area of one via $= 70.7\,\mu m^2$ ($\varnothing = 300\,\mu m$).

This results in a thermal conductivity of $\lambda_{via} = (295 \pm 10)$ W/(m·K) for the sintered Ag via, which is in the expected range. This measurement approach has been also successfully used to detect failures in vias. Some sintered silver vias showed lower thermal conductivity due to voids or defects, which have been detect by microscopic images of cross sections.

The previous examples show that the test stand *TIMA* is also able to characterize different types of substrates. It provides the required measurement accuracy to extract parameters

of specific values in a system such as for a single layer in a multi-layer sample or a single via in a substrate.

### 4.5.3 Investigation of long-term stability of TIMs

The long-term stability of thermal interface materials (TIMs) is the most important parameter because it has an influence on the reliability of the whole system. It depends strongly on the type of the TIMs (liquid, viscous, stiff, solid, phase changed etc.) as well as on the application and operation conditions. So thermal greases show pump-out and dry-out effects. The thermal mismatch in the device causes a relative motion between the die and the heat spreader (in-plane and/or out-of-plane), which tends to squeeze the thermal grease out of the interface gap [17] or air is pumped in the gap moving the grease out of the center of the contact area [124]. This phenomenon results in increased thermal resistance due to loss of grease material from the interface.



**Figure 4.37:** Examples for degradation of thermal contact

Grease dry-out occurs due to the separation of the filler from the polymer matrix at elevated temperatures. The polymer matrix tends to flow out of the interface preferentially and results in "drying-out" of the grease. This results in degradation of thermal resistance of the TIM [19]. Exposure to high humidity levels has also been shown to induce changes in the thermal resistance of a grease layer, primarily an effect of the filler and resin system employed and their response to high levels of moisture [125].
In the case of stiff and solid TIMs such adhesives, solders or cured gap fillers, interface delamination and bulk cracks are the main initiator of reducing thermal performance and lifetime of package and devices.

In order to qualify the reliability of thermal interface materials in an electronic package cooling application, traditional temperature or power cycle tests are commonly used to detect potential thermal failures due to grease pump-out, grease dry-out, cracks, delamination etc. [126]. These traditional temperature and power cycle tests are time consuming

processes due to the long heating and cooling time.
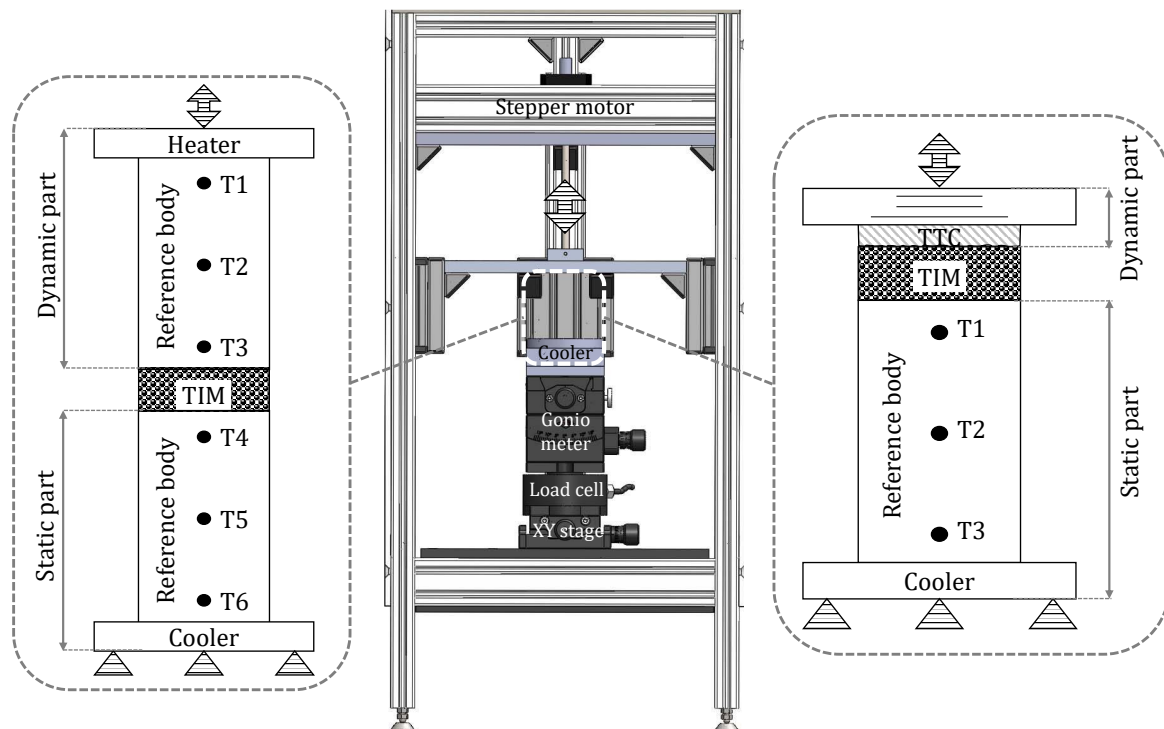


**Figure 4.38:** Schematic of *TIMA* platform and the modules for investigation of long-term stability of TIMs

In addition to the described different capabilities for characterization under different conditions, the *TIMA* test stand offers accelerated ageing investigation of TIMs. In order to accelerate the potentially applied load of TIM during the cyclic operation, the *TIMA* test stand is used to simulate the squeezing action of TIM and to measure in-situ the changing of thermal resistance of TIM (figure 4.38). Both *TIMA3* and *TIMA6* modules can be used for the accelerated ageing tests. The TIM is mounted between the static reference body and the dynamic part, which can be a thermal test chip (for *TIMA3*) or a reference body (for *TIMA6*). The dynamic part is contacted to a stepper motor which is computer controlled and moves in vertical direction to expand and compress the TIM.

Scores of TIMs under different conditions were characterized by the *TIMA* test stand with respect to their ageing behaviour. In the following investigation results of a thermal grease will be presented.

A commercially available non-solvent thermal grease (G765 from Shin-Etsu Chemical Co., Ltd.) has been dispensed in the *TIMA3* module between aluminium reference body and silicon thermal test chip in bond line thickness of 500 µm. The thermal grease has been mechanically loaded by 1000 cycles. One cycle consists of four steps:

Step 1:  BLT = 500 µm (initial)
Step 2:  BLT = 475 µm (5 % compression)
Step 3:  BLT = 500 µm (5 % expansion to the initial thickness)
Step 4:  BLT = 525 µm (5 % expansion)

Figure 4.39 illustrate schematically the procedure of one cycle.
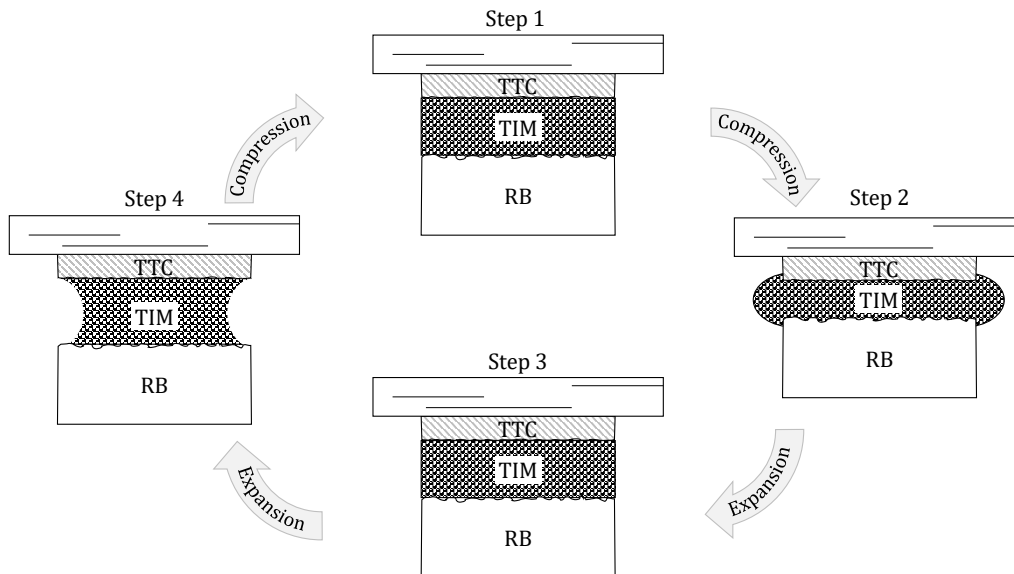


**Figure 4.39:** Schematic illustration of one cycle of mechanical loading

After each step, the effective thermal resistance has been measured in steady-state. Figure 4.40 shows the effective thermal conductivity and effective thermal resistance for the four steps over the number of cycles. As can be seen in the diagram, the tested thermal grease showed continuous increasing of thermal resistance and decreasing of thermal conductivity. The material showed around 15 % degradation after 100 cycles, however around 50 % of this degradation happened in the first 100 cycles. After the first 100 cycles the material showed slower degradation.

This behavior does not occur in the same way with all materials. In many greases, it is observed that the thermal resistance decreases during the first cycles, remains constant for a while and then increases. The improvement in thermal performance at the beginning of the test is due to the fact that the material adapts to the surface through mechanical movement, which leads to a reduction in thermal interface resistance.

In the case of pre-cured gap fillers or adhesives, it has been observed that the thermal resistance does not change until a certain number of cycles and then increases abruptly,
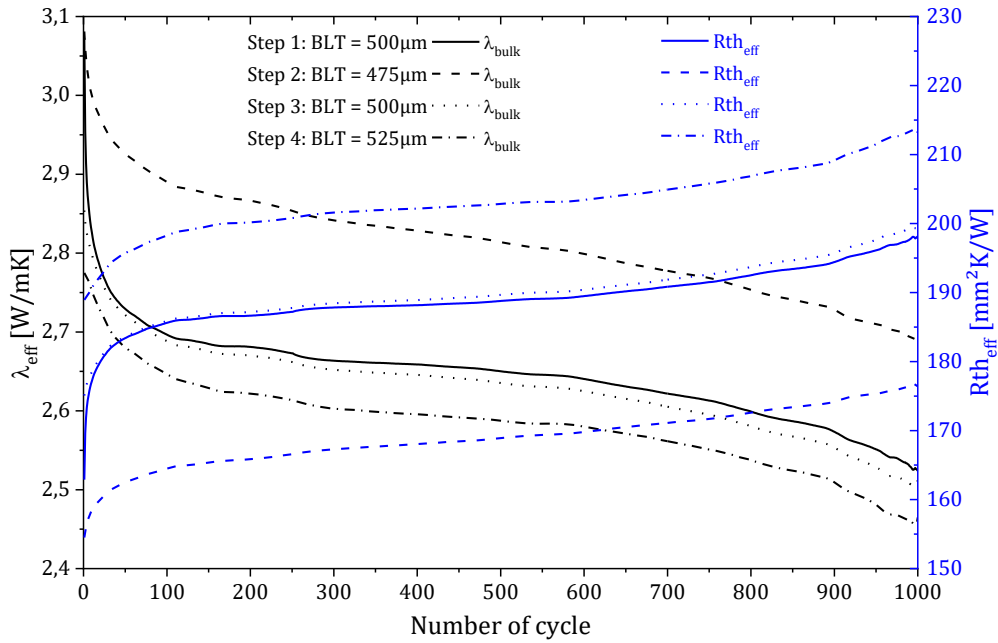
**Figure 4.40:** Results of thermal conductivity and thermal resistance as function of the cycle number showing the degradation of thermal grease due to mechanical loading caused by thermal mismatch of the package

due to delamination in the interface. In such tests, the speed of movement plays an important role and should not be neglected.

### 4.5.4 Measurement of the heat transfer coefficient

The goal of this investigation is to determine the heat transfer coefficient ($h$) of different combinations of aluminium plates and aluminium sheets with different surface roughness as function of the pressure. The solid to solid heat transfer coefficient ($h$) is the inverse of the thermal interface resistance ($Rth_{int}$). To determine the heat transfer coefficient between the plate and sheets, four measurements were needed. Figure 4.41 shows schematically the four measurements performed to determine the heat transfer coefficient between aluminium plate and aluminium sheet.

In the fist measurement the plate P and the sheet S were stacked on each other and connected by thermal grease to the silicon thermal test chip and the aluminium reference body. The total thermal resistance of the first measurement is:

$$Rth_1 = Rth_G + Rth_S + Rth_{int} + Rth_P + Rth_G \tag{4.25}$$

where $Rth_G$ is thermal resistance of the grease, $Rth_S$ is the thermal resistance of the sheet, $Rth_P$ is the thermal resistance of the plate and $Rth_{int}$ is the thermal interface resistance between plate and sheet.
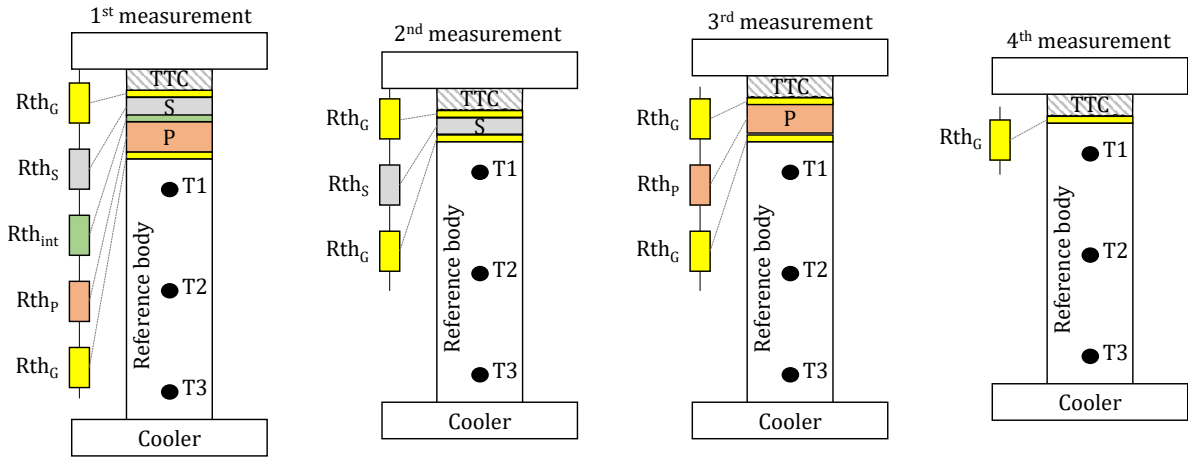
**Figure 4.41:** Schematic of measurements preformed to determinate the heat transfer coefficient between aluminium plate (P) and aluminium sheet (S)

In the second measurement the thermal resistance of the sheet S including the thermal resistance of two thermal grease layers $Rth_G$ has been measured:

$$Rth_2 = Rth_G + Rth_S + Rth_G \tag{4.26}$$

In the third measurement the thermal resistance of the plate P including the thermal resistance of two thermal grease layers has been measured:

$$Rth_3 = Rth_G + Rth_P + Rth_G \tag{4.27}$$

In the fourth measurement the thermal resistance of the thermal grease layer has been measured:

$$Rth_4 = Rth_G \tag{4.28}$$

Each these effective thermal resistances $Rth_1 \cdots Rth_4$ has been measured under pressure variation between $0.2\,\text{MPa}$ and $1.5\,\text{MPa}$.

From the equations 4.25 - 4.28, the following equation can be obtained for the the thermal interface resistance between the aluminium plate (P) and the aluminium sheet (S):

$$Rth_{int} = Rth_1 - Rth_2 - Rth_3 + 2 \cdot Rth_4 \tag{4.29}$$

The thermal interface resistance $Rth_{int}$ of two surface combinations has been determined:

Combination 1: Aluminium plate and aluminium sheet, both with high surface roughness $(R_Z \approx 10\,\text{µm})$

Combination 1: Aluminium plate and aluminium sheet, both with low surface roughness
$(R_Z \approx 5\,\mu m)$

The results of the thermal resistance of all measurement steps is illustrated in figure 4.41 including the interface resistance between the plate and the sheet calculated in equation 4.29 for two combinations as function of the pressure are shown in figure 4.42.



(a) Combination 1: High surface roughness     (b) Combination 2: Low surface roughness
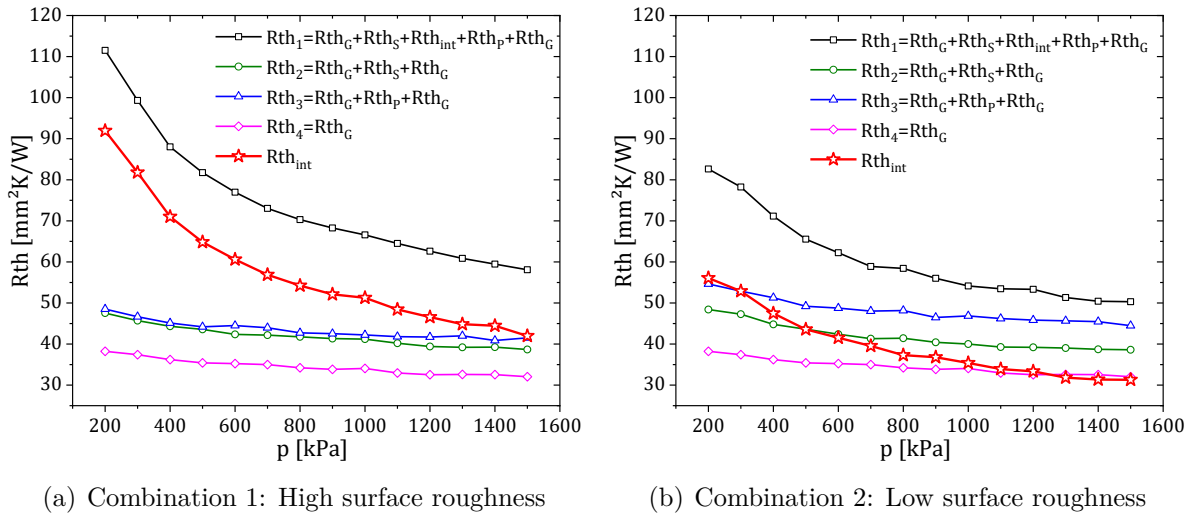
**Figure 4.42:** Thermal resistances of $Rth_1$, $Rth_2$, $Rth_3$ and $Rth_4$ as well as the calculated interface resistance $Rth_{int}$ as function of the pressure for two combinations

The heat transfer coefficient ($h$) between the aluminium plate and aluminium sheet is the inverse of the thermal interface resistance ($Rth_{int}$).

$$h = \frac{1}{Rth_{int}} \tag{4.30}$$

The results of heat transfer coefficient for both combinations are shown in figure 4.43.

It can be seen that the heat transfer coefficient between the plate and the sheet with low surface roughness is higher than between the plate and the sheet with high surface roughness. It could also be shown, that the heat transfer coefficients increase with the increasing of the pressure.

## 4.6 Conclusion

This chapter dealt with the development, evaluation and application of the steady-state test stand *TIMA*. The test stand has been designed and realized as modular platform, which enables integration of different measurement modules for characterization under
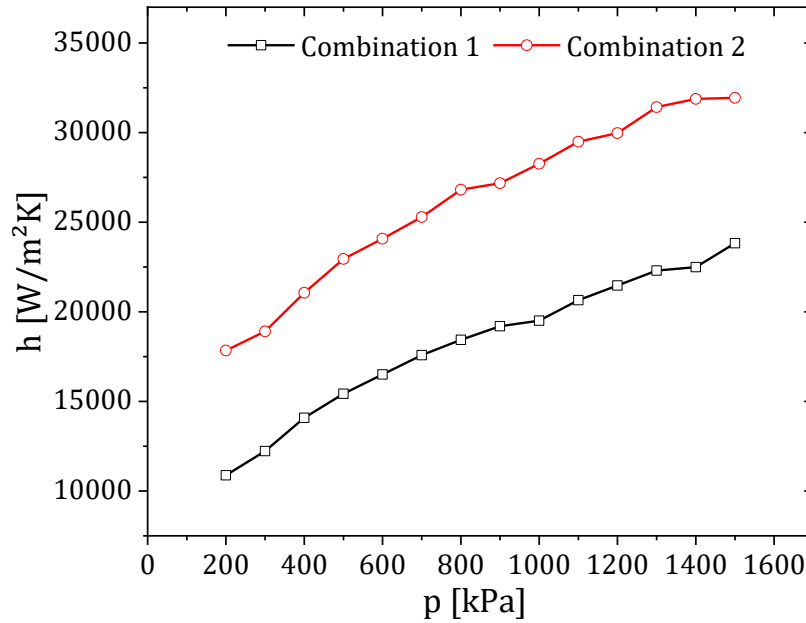
**Figure 4.43:** Heat transfer coefficient of combination 1 (high surface roughness) and combination 2 (low surface roughness) as function of the pressure

different conditions. Two modules have been realized. The accuracy and limitation of the test stand have been studied in order to identify the error sources and increase the measurement accuracy and resolution of the test stand. It turned out from the error calculation that over 80% of the measurement error is caused by the error of the temperature measurement. Therefore, a special Thermal Test Chip has been designed and fabricated, which offers a very homogeneous temperature distribution and accurate temperature measurement. It has also been shown that, through the reduction of the ratio of cross section area of sample and contact medium to 1/10, the measurement range of steady-state technique can be extended to measure thermal resistance down to $1\,\mathrm{mm^2 \cdot K/W}$, which is around 10-times lower than the thermal resistance measured by commercial equipment for the same measurement accuracy. To demonstrate the functionality and the capabilities of the developed test stand, several properties of different classes of materials (Thermal pads, thermal greases, gap fillers, adhesives, substrates) have been characterized and discussed, including specific adaptations of test setup and procedure.

# Chapter 5

# Transient test stand for material characterization

This chapter deals with the development and realization of an innovative test stand for thermal transient characterization of thermal interface materials. The chapter starts with the description of the main idea of the test stand, which is using the TTC developed within this work as active device for heating and temperature measurement. A simple test set up for characterization of TIM at material level will be presented. Finally, a specific package for thermal transient characterization of VACNT based TIMs at package level will be shown and discussed.

## 5.1 Concept and realization

The thermal impedance technique is usually used for thermal characterization of electronic packages and requires an active device with a temperature sensitive element (e.g. MOSFET, IGBT, diode). The idea here is to replace the active device by a thermal test chip (TTC) with integrated heater and temperature sensor. The TTC described in section 4.4 is used as active device. As the test stand uses the hardware of *TIMA3* module of the *TIMA* test stand (see section 4) and is based on the transient technique, it has been named *TransTIMA*.

The TTC provides a great advantage over MOSFET or IGBT. The heater and temperature sensors of TTC are independent. Thus, thermal impedance can be determined from cooling and heating curves. Furthermore, it is possible to perform thermal characterization at material, package or system levels. Thanks to the modularity concept of the TTC, it can be used as stand-alone device or integrated into a package or system. The developed TTC can be assembled by flip-chip or wire-bond technologies.

For transient thermal characterization at material level, a simple test setup has been designed and realized. It combines the setup of *TIMA3* module (see section 4.1) with the thermal impedance technique described in section 2.2.3.

The setup consists of a TTC, which is flip-chipped onto an organic PCB (see figure 4.15), and a water cooled heat sink. The heater and temperature sensor of the TTC is controlled by in-house developed electronic, which controls the heating process and records the transient temperature profile of the TTC. The water cooler and the changeable heat sink are mounted to the manual translation stage.

Figure 5.1 shows a picture and a schematic of the *TransTIMA* test setup for thermal impedance measurement at material level.
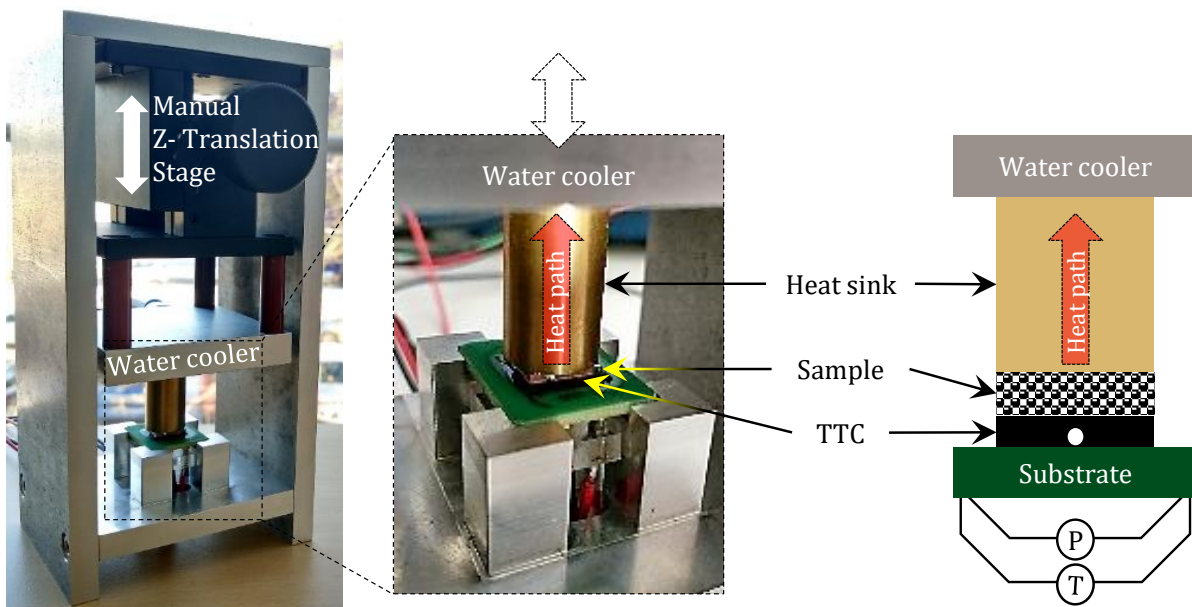


**Figure 5.1:** *TransTIMA* setup for transient thermal characterization at material level. Left: photography. Right: schematic showing the power and temperature controlled TTC, the heat sink and the TIM between them.

To benchmark the test setup, the thermal impedance of the test setup with a commercial grease at three different bond line thicknesses (BLT) has been measured (figure 5.2 left). To calculate the bulk thermal conductivity of the grease, the total thermal resistances of the setup for the three measurements were plotted over the BLT of the grease, which shows a linear dependency (figure 5.2 right). The bulk thermal conductivity results from the slope.

It was found that the bulk thermal conductivity of the grease measured by *TransTIMA* fits very well to the results of $1\,\mathrm{W/m\cdot K}$ obtained by the steady-state test stand *TIMA*.
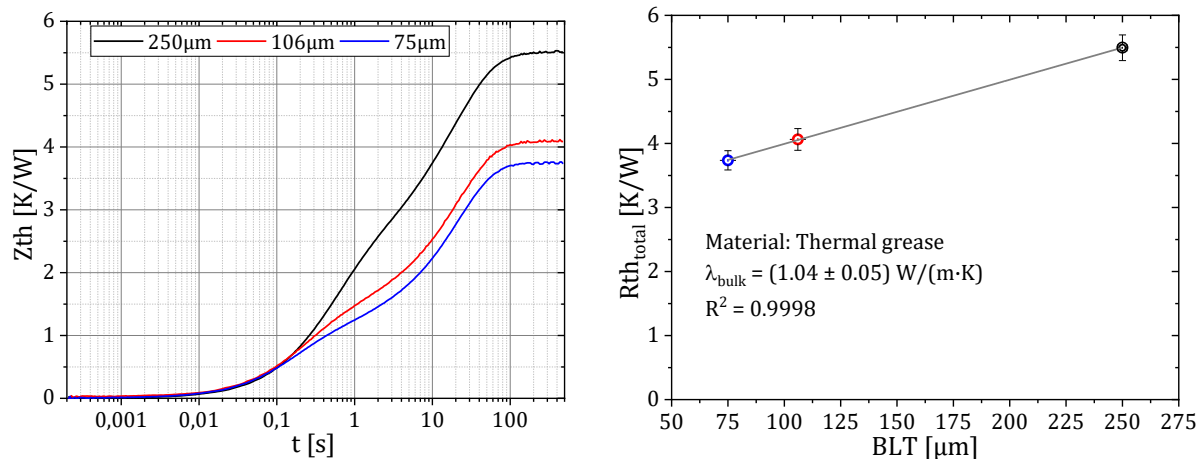
**Figure 5.2:** Thermal impedance of test setup using a commercial thermal grease at three different BLT (left); total thermal resistance over the BLT (right)

The intercept with the *Rth*-axis includes all the thermal resistances junction and cooler except the thermal resistance of the measured TIM (e.g. chip, heat sink and interfaces between chip and TIM as well as between heat sink and TIM).

## 5.2    Characterization of VACNT at module level

Vertically-aligned carbon nanotubes (VACNTs) as TIM is a promising technology not only due to the excellent thermal conductivity of CNTs which can achieve $6600\,\mathrm{W/(m\cdot K)}$ [28] for single-walled and $3000\,\mathrm{W/(m\cdot K)}$ for multi-walled CNTs [29] but also for its high electrical conductivity and outstanding mechanical properties. However, the effective thermal conductivity of VACNTs depends on several factors such as density, growth quality, uniformity of length and of course the nature of connectivity between the open ends of the CNTs and the target surface, which is the bottleneck of the heat path. Thermal properties of VACNTs are very dependent on the growing and assembling processes, therefore VACNTs should be characterized under real conditions only.

In this chapter, an industrial demonstrator for RF application using VACNT as TIM1 will be characterized. The demonstrator consists of a HPA (high-power amplifier) module using a GaN-based MMIC (Monolithic Microwave Integrated Circuit) chip which is soldered on a doped silicon substrate, on its backside VACNT is grown by thermal CVD process. The free end of VACNT is mounted onto copper substrate using few nm functionalized polymer layer. The schematic in figure 5.3 shows the cross section of the MMIC demonstrator [127].
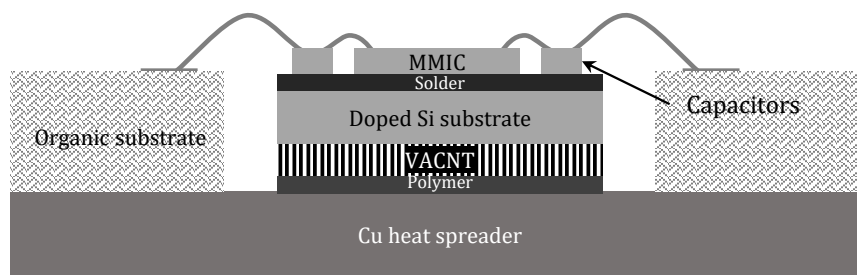
**Figure 5.3:** Cross section of RF demonstrator using VACNT as TIM1

## 5.2.1   Design and realization of VACNT characterization demonstrator

Due to the complexity of the MMIC chip while used for transient thermal characterization, it has been fallen back to the *TransTIMA* concept in this work by replacing the MMIC chip by the thermal test chip (TTC). Thanks to the variability of the TTC, it was possible to create the same size and power losses of MMIC chip by using two cells of TTC. Furthermore, the independent heater track of the TTC enables to simulate real heat concentration scenarios by powering the heater tracks individually. Figure 5.4 shows the schematic cross section of the characterization demonstrator.
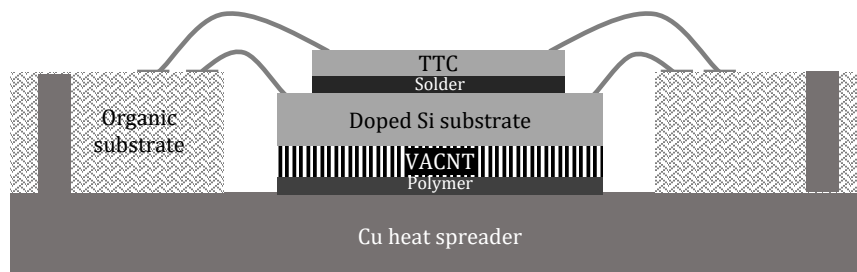


**Figure 5.4:** Cross section of characterization demonstrator using VACNT as TIM1 and TTC replacing MMIC chip

It can be seen, that only the TTC replaced the MMIC chip. All other layers including the VACNT have been assembled under the same conditions as in the target demonstrator. The characterization demonstrator consists mainly of three components, the thermal test chip for powering and sensing the demonstrator, the VACNT including growth substrate and the PCB as heat spreader and electrical connection substrate.

The VACNT were grown at the company SHT in Sweden by a thermal chemical vapour deposition process (TCVD) on a silicon substrate in wafer form. The wafer was deposited by $Al_2O_3$ and Fe catalyst. During the growth process, the wafer was annealed at high

temperature (around 800 °C) under $H_2$ gas to transform the Fe catalyst layer into spheres which later act as nucleation site of the carbon atoms. The VACNTs then grew using $C_2H_2$ as carbon precursor until they reached the desired height of around 10 to 20 µm.

The assembly of the characterization demonstrator was performed at the company Thales. The assembly started with soldering the TTC onto the doped silicon substrate on which the VACNT layer was grown. As die attach material the AuSn alloy has been used. In the next step, the PCB substrate was spin-coated with a few hundred nm functionalized polymer layer [128] on the area where the VACNT layer is going to be placed. The role of this polymer layer is to enhance the heat transfer between the VACNT layer and the receiving substrate by both increasing the number of participating nanotubes and facilitating phonon transfer by a covalent bonding between VACNT and functionalized polymer [129]. The coated substrate was then brought in contact with the VACNT tab. The assembly has been then exposed to heat and pressure to allow the bonding of the VACNTs with the functionalized polymer. Figure 5.5 (a) shows schematically a cross section of the characterization demonstrator.

Finally, the TTC has been wire bonded to the substrate pads using thermosonic gold ball bonding (25 µm). All heater tracks have been bonded in parallel. The current pads of the temperature sensors have been bonded in series while the sense pads have been bonded separately to allow 4-terminal sensing of each temperature sensor. The assembled characterization demonstrator can be seen in figure 5.5 (b) and (c).
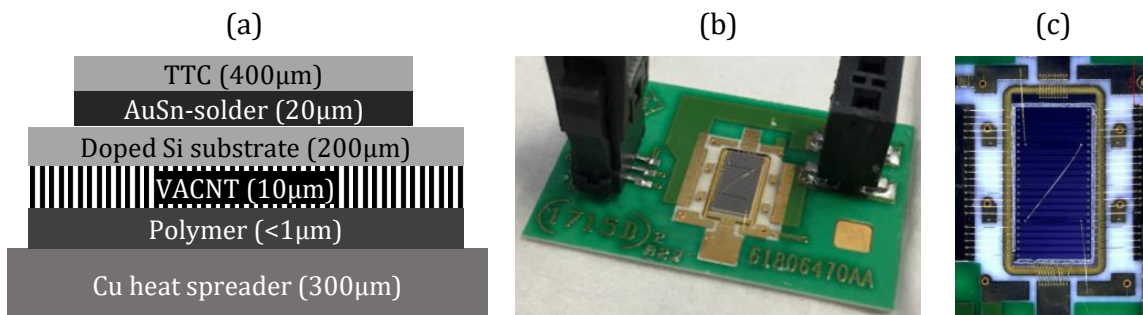


**Figure 5.5:** (a) Cross-sectional layer by layer view of the module; (b) Photo of an assembled module; (c) Top view of the module shows the wire bonded TTC.

In order to investigate the overall improvement of the thermal properties of the module with VACNT as TIM1, reference modules have been assembled in which the VACNT based TIM1 was replaced by two commercial silver filled adhesives. One adhesive has a relatively high thermal conductivity of 12 W/(m·K) (here adhesive 1) and the other has a lower thermal conductivity of 2.5 W/(m·K) (here adhesive 2). For all modules, the TIM1 layer has the same thickness of 10 µm.

## 5.2.2 Characterization results

For the thermal characterization of the modules, the thermal transient spectrum analysis has been used. The aim of the characterization is to determinate the junction-to-case thermal resistance $Rth_{JC}$ of the modules with different TIM1 materials (VACNT, adhesive 1 and adhesive 2).

All three modules have been measured under the same conditions by keeping the heat sink temperature constant at 20°c and power loss at 11.0 $\pm$ 0.5 W. The test setup has been realized by mounting the module onto a water-cooled heat sink with the help of screws to apply homogeneous pressure (see figure 5.6).
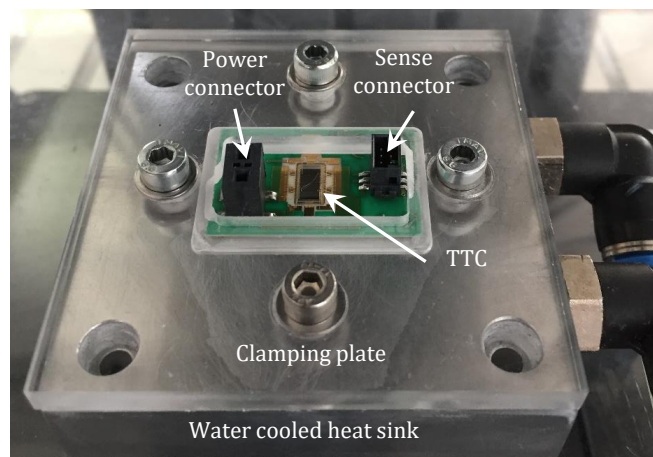


**Figure 5.6:** Picture of measurement setup showing the characterization modules assembled between a water cooled heat sink and a clamping plate

To determine the $Rth_{JC}$ and to compare the thermal performance between the module containing VACNTs and polymer adhesive, respectively, as TIM1, the transient so-called dual-interface method from JEDEC JESD51-14 standard [54] has been used. The device has been heated with a load power of 11.5 W and then the time-dependent voltage has been measured during cooling of the device. In a first step, the junction-to-ambient thermal resistance $Rth_{JA}$ of the modules has been measured with and without TIM2 between module and heat sink.

Figure 5.7 shows the thermal impedance curves $Z_{th}$ of all three modules measured with and without TIM2. The steady-state thermal resistance is the junction-to-ambient thermal resistance while the separation points of each curve pair represent the junction-to-case thermal resistance of the module, which includes the thermal resistance of thermal test chip, solder layer, silicon substrate, TIM1 (VACNT, adhesive 1 or adhesive 2) and copper heat spreader (see figure 5.5 (a)).
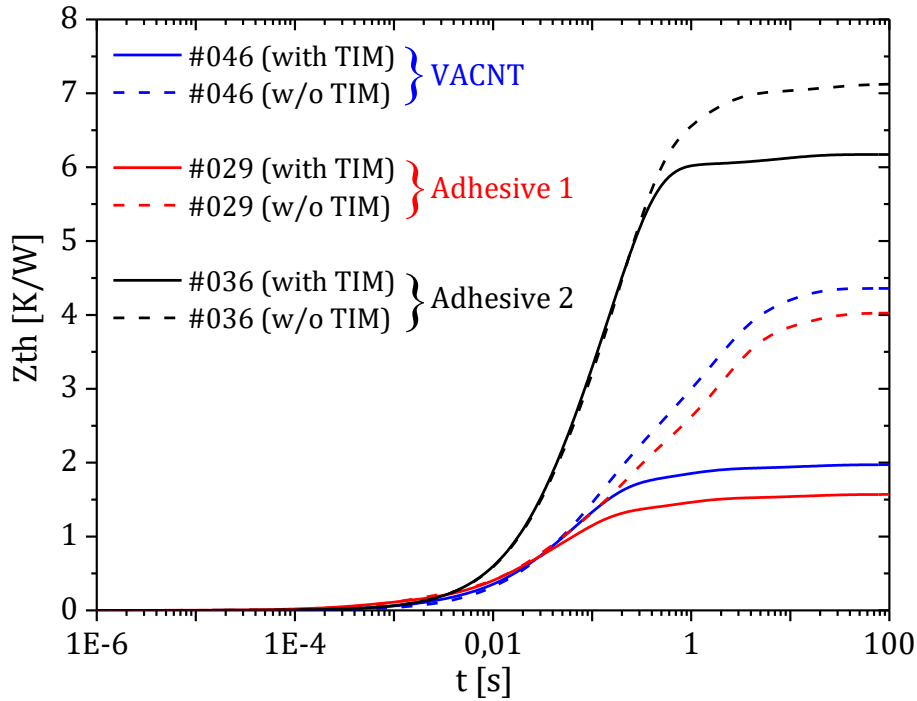
**Figure 5.7:** Comparison of Zth curves of different modules with and without TIM2

The diagrams in figure 5.8 summarize the results of the transient thermal characterization of all three modules. Diagram (a) shows the maximum temperature of the modules measured by the temperature sensors of the TTC at 11.0 W power loss and 20°C heat sink temperature. Diagram (b) shows the junction-to-ambient thermal resistance of the modules by using thermal grease as TIM2 and diagram (c) shows the junction-to-case thermal resistance, which has been calculated from the separation point using the transient dual-interface method.
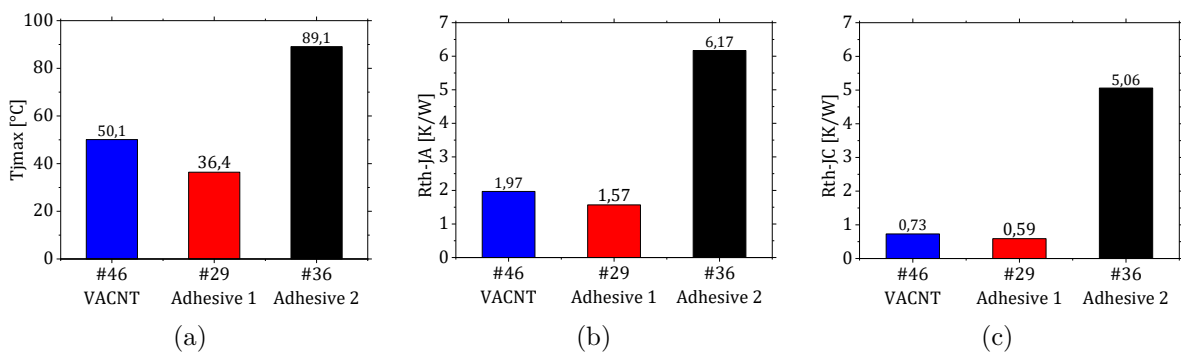


**Figure 5.8:** Comparison of transient characterization results of the modules with different TIM1. (a) maximum temperature, (b) junction-to-ambient thermal resistance, (c) junction-to-case thermal resistance

It can be seen in figure 5.8 that the performance of the module with VACNT based TIM

is slightly behind the performance of the adhesive 1 module with thermal conductivity of $12\,\mathrm{W/(m \cdot K)}$. It is also around six times better than the adhesive 2 module with thermal conductivity of $2.5\,\mathrm{W/(m \cdot K)}$. The very first module with VACNT based TIM already showed a thermal performance competitive against state-of-the-art adhesive layers. The prototypic VACNT based TIM could outperform a common adhesive in terms of thermal impedance and nearly reaches the thermal performance of the silver-filled thermally enhanced conductive adhesive.

## 5.3 Conclusion

In this chapter, a further test stand for thermal characterization of materials, packages and systems based on thermal transient technique has been described. The main advantage of the developed test stand lies in using a thermal test chip as fully controllable active device for both heating and temperature measurement. A simple test setup for thermal characterization at material level has been realized and benchmarked. Another application for the test stand has been successfully demonstrated within characterization of VACNT based TIM at module level under real assembly conditions.

# Chapter 6

# Steady-state test system for characterization of highly conductive materials

Material characterization using the *TIMA* test stand can become difficult if the thermal conductivity is high. Therefore, another test stand has been developed, which allows both thermal and electrical characterization of highly conductive materials. Moreover, in contrast to the *TIMA* system this system is also suitable for measurements of strip-shaped samples. In this chapter the methodology, concept and design of the test stand will be discussed, which have been supported by FE simulation in order to identify and minimize parasitic effects.

The test stand has been benchmarked by measuring several well-known materials. Finally, thermal and electrical conductivities of bulk sintered silver samples sintered under variation of sintering parameters (pressure and temperature) have been measured. In order to investigate the correlation between processing, structure and properties, the structure of samples has been analyzed by scanning electron microscope (SEM).

## 6.1 Measurement principle

The measurement principle of the test stand is similar to the measurement principle of the *TIMA6* module of the *TIMA* characterization system (section 4.1), where the samples are tested between a hot and a cold plate (see figure 4.1). However, this other test stand is also able to measure the thermal conductivity of samples with a high thermal conductivity and the lateral thermal conductivity of strip-shaped samples, as well. And, in contrast to the *TIMA* test stand, it is not necessary to measure samples with different geometries in order to determine the bulk thermal conductivity as the thermal interface

resistance is not included in the calculation.

To determine the thermal resistance of the sample, the temperature gradient along the sample and the heat flow through the sample have to be measured. The effective thermal resistance of the sample results from the temperature gradient across the sample and the heat flow through the sample. The higher the thermal conductivity of the sample, the lower the temperature gradient. This can be demonstrated by a simple calculation of the temperature gradient over the sample and the heat flow through the sample as a function of the thermal conductivity of the sample.

For the calculation, following parameters have been used for *TIMA*6 configurations:

- Sample thickness, $BLT = 100\,\mu m$
- Heater temperature, $T_H = 100°C$
- Cooler temperature, $T_C = 10°C$
- Thermal conductivity of reference bodies, $\lambda = 380\,W/(m \cdot K)$
- Length of reference bodies, $L_{RB} = 25\,mm$
- Cross section area of reference bodies and samples, $A = 100\,mm^2$
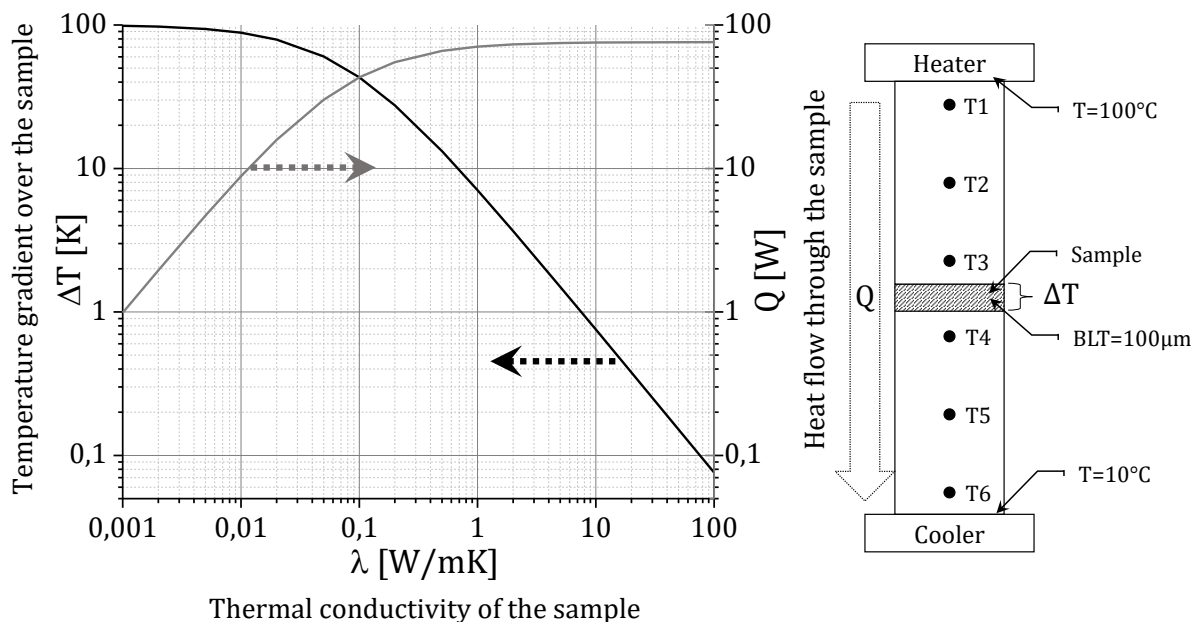


**Figure 6.1:** Temperature gradient over the sample and heat flow through the sample as function of thermal conductivity of the samples by using the *TIMA6* module

It can be seen in figure 6.1 that the temperature gradient over a sample with the thickness of $100\,\mu m$ and thermal conductivity above $40\,W/(m \cdot K)$ is below $0.2\,K$, which is in the measurement error level of the temperature sensors which are used here.
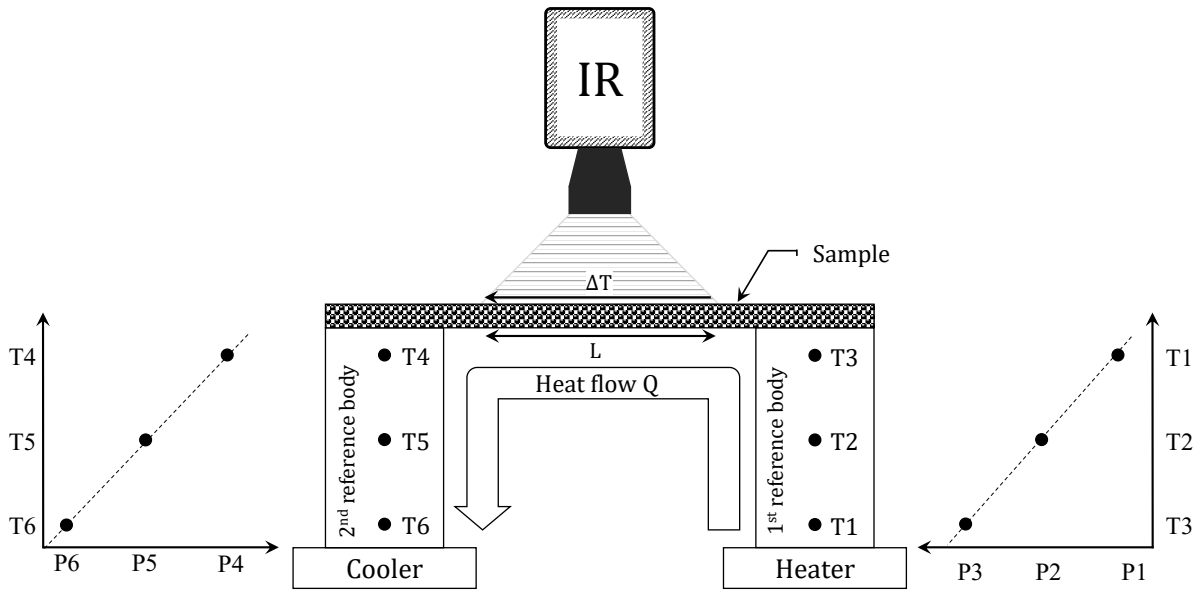
**Figure 6.2:** Schematic of the test stand *LaTIMA*

To increase the temperature gradient along the sample and consequently increase the sensitivity of the steady-state method the following approach has been developed. The method allows the characterization of the bulk thermal conductivity of highly conductive materials such as sintered silver, solders, metals and semiconductors. The sample is placed over two sockets (reference bodies), which are used for measurement of the heat flow. One socket is fixed on the heater and the other one on the cooler. The temperature gradient across the sample is measured by IR thermography. As the measurement principle of the test stand bases on the measurement principle of *TIMA* and allows lateral thermal conductivity measurement, it has been named *LaTIMA* which stands for Lateral Thermal Interface Material Analyzer. Figure 6.2 shows the schematic of the *LaTIMA* concept.

The same calculation as shown in figure 6.1 has been done with the *LaTIMA* test stand. Figure 6.3 shows the temperature gradient over the sample as function of the thermal conductivity of the sample under the same conditions for *TIMA* and *LaTIMA*. It can be seen that samples with thermal conductivity around $1000 \, \text{W}/(\text{m} \cdot \text{K})$ at the thickness of $100 \, \mu\text{m}$ can be measured by *LaTIMA*, which is over 100-times higher compared to the limitation of ASTM D5470 devices.

The thermal conductivity of the sample $\lambda_S$ is given by following equation:

$$\lambda_S = \frac{L_{IR}}{A_S} \cdot \frac{Q}{\Delta T_{IR}} \tag{6.1}$$

where:
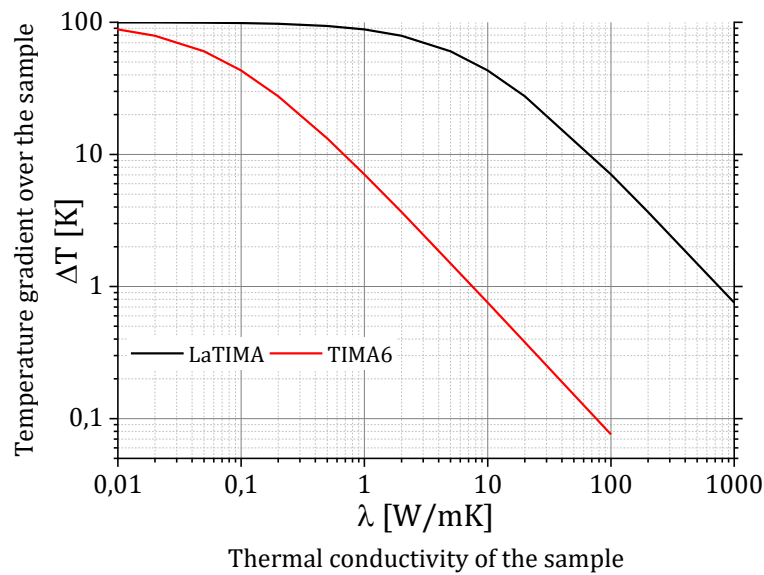
**Figure 6.3:** Comparison of the temperature gradient over the sample as function of thermal conductivity of the samples by using *TIMA* and *LaTIMA* test stand

| | | |
|---|---|---|
| $L_{IR}$: | length of the field measured by IR camera | [m] |
| $A_S$: | cross sectional area of the samples (thickness x width) | $\left[\text{m}^2\right]$ |
| $Q$: | heat flow through the sample | [W] |
| $\Delta T_{IR}$: | temperature gradient along the samples measured by IR camera | [K] |

The generated heat $Q$ flows through the first reference body, the sample and the second reference body to the cooler. The reference bodies serve exclusively as heat flow sensors to measure inlet and outlet heat flow.

## 6.2 Verification and qualification of the test stand

During the development phase significant differences between the inlet heat flow $Q_{in}$ measured by the first reference body and the outlet heat flow $Q_{out}$ measured by the second reference body were noticed. This can be explained by the heat loss on the surface to environment by radiation and convection. The knowledge of the actual heat flow $Q$ through the sample is of very high importance for the calculation of the thermal resistance of the sample. In order to study the heat loss in detail, a parametric FE model of a simplified test set-up was created (see figure 6.4). The model consists of two reference bodies (RB) and the sample. The input parameters are:

- Distance between the reference bodies
- Length of the sample
- Width of the sample

- Thickness of the sample

The temperature at the base of the first RB was kept constant at $T_H = 120°C$ while the base of the second RB was kept constant at $T_C = 10°C$. In order to study the temperature dependence of the heat loss, the temperatures of the RB bases were offset simultaneously to higher or lower temperatures.

As output of the simulation model, following parameters are derived (figure 6.4 left):

- Inlet heat flow ($Q_{in}$)
- Outlet heat flow ($Q_{out}$)
- Heat flow through the sample ($Q_{sample}$)
- Heat loss due to radiation and convection to the environment of the individual component surfaces (RB, sample).
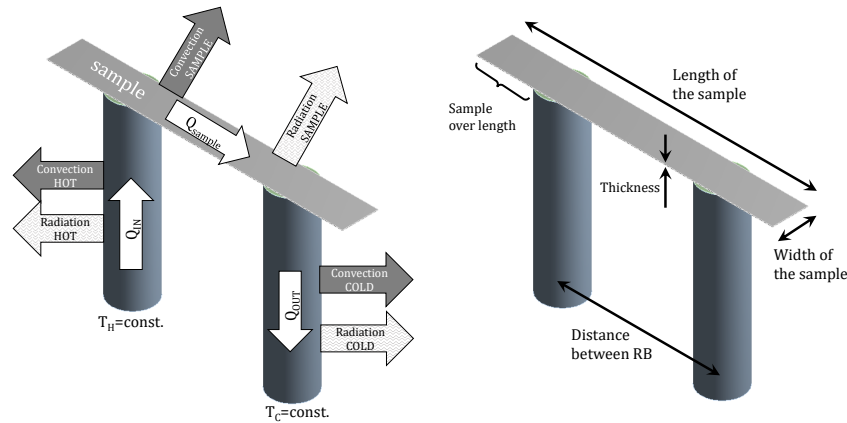


**Figure 6.4:** Simulation model, thermal boundary conditions (left), geometrical parameters (right)

Using an arbitrary sample, the simulation model was verified by adjusting its thermal boundary conditions (convection and radiation) to fit the surface temperature of the samples measured by the IR camera at the same conditions (see figure 6.5).

Using the same simulation model, a design of experiment (DoE) of the boundary conditions and geometrical conditions was performed to investigate heat loss due to radiation and convection by variation of heat convection coefficient and emissivity as well as sample geometry and thermal conductivity. An overview of the individual studies is presented in table 6.1 and the results are shown in figure 6.6.

In the following, the results of all simulation cases are discussed:

- Case 1 represents the real condition of an experiment with an arbitrary sample (thermal conductivity of the sample $\lambda_S = 150\,\text{W}/(\text{m}\cdot\text{K})$, emissivity $\varepsilon = 0.5$, convection heat transfer coefficien $h = 10\,\text{W}/(\text{m}^2\cdot\text{K})$). It can be seen, that only 45% of the inlet heat achieve the outlet. Around 55% of the heat are lost by radiation
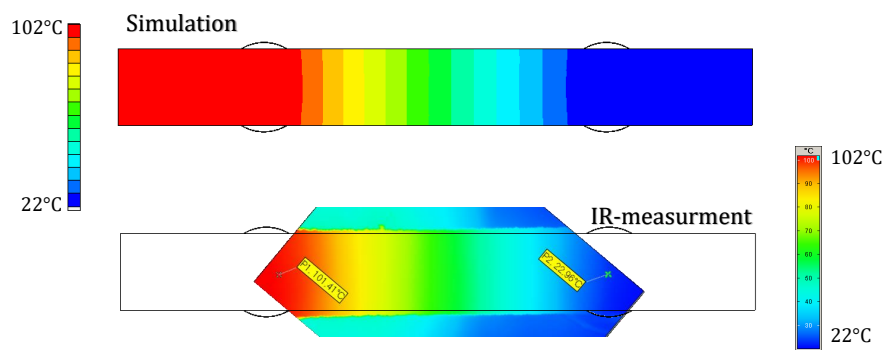
**Figure 6.5:** Top view of the sample. Temperature distribution from simulation (upper image) and IR measurement (lower image)

and convection, where 18% by radiation (13.3% at warm side reference body (RB), 0.2% at cold side RB and 4.3% at the sample) and 38% by convection (28% at warm side RB, 0.5% at cold side RB and 9% at the sample).

- The cases 2, 3 are focusing on the losses by radiation. In the real experiment (case 1), the used reference bodies (RB) are CuZn with an emissivity around 0.5[1]. In case 2 the emissivity was set to 0.1 which can be achieved by coating the RB by gold or nickel. In case 3 the emissivity was set to 1 as a worst case which can be occurred by using oxidized aluminium RB. The results show that the losses by radiation are 8% in case 2 and 28% in case 3.

- In the cases 4, 5 and 6 the losses by the convection have been studied. In case 4 the heat convection coefficient has been set to zero, which simulates measurement in vacuum. It results that the outlet heat flow is 73% of the inlet heat flow and 27% is lost by radiation (20% at the hot RB and 7% at the sample). In case 5 the heat convection coefficient was set to $5\,\mathrm{W/(m^2 \cdot K)}$ (free convection) whereby the losses by convection increase from zero to 23%. In case 6 the losses by convection increase to 28% due to increasing the heat convection coefficient to $15\,\mathrm{W/(m^2 \cdot K)}$.

- In the following three cases 7, 8 and 9 the heat loss has been investigated as function of thermal resistance of the sample. It can be seen that the samples with high thermal resistance (due to low thermal conductivity or small cross section area) cause higher heat losses by radiation and convection than samples with low thermal resistance due to the higher temperature gradient between hot and cold reference bodies.

- In the last four cases 10 - 13, the influence of the over length of the sample on the heat losses has been investigated. As it can be seen in figure 6.6, the influence of

---

[1]Mastercool, Inc., www.mastercool.com

**Table 6.1:** Overview of simulations carried out with objectives and main parameters

| Case | Objective | Parameter |
|---|---|---|
| 1 | Reference | Same conditions as used in experiment |
| 2 | Influence of radiative loss | Emissivity of RB set to 0.1 |
| 3 | | Emissivity of RB set to 1 |
| 4 | Influence of convective loss | Convective heat transfer set to zero |
| 5 | | Convective heat transfer set to $5\,\mathrm{W/(m^2 \cdot K)}$ |
| 6 | | Convective heat transfer set to $15\,\mathrm{W/(m^2 \cdot K)}$ |
| 7 | Influence of thermal resistance of the sample | Thermal conductivity of sample is changed to $50\,\mathrm{W/(m \cdot K)}$ which results in thermal resistance of $800\,\mathrm{K/W}$ |
| 8 | | Thermal conductivity of sample is changed to $250\,\mathrm{W/(m \cdot K)}$ which results in thermal resistance of $160\,\mathrm{K/W}$ |
| 9 | | Thermal conductivity of sample is changed to $400\,\mathrm{W/(m \cdot K)}$ which results in thermal resistance of $100\,\mathrm{K/W}$ |
| 10 | Influence of sample over length | Sample over length on both sides is set to 1 mm |
| 11 | | Sample over length on both sides is set to 5 mm |
| 12 | | Sample over length on both sides is set to 10 mm |
| 13 | | Sample over length on both sides is set to 0 mm |

sample over length is negligible.

The simulation study has spot out clear opportunities to minimize the disturbing heat losses and thereby increase measurement accuracy. The lowest losses occur when the experiment is performed in vacuum and the used reference body gets an additional coating e.g. gold or nickel to obtain a reduction of the emission coefficient.

Measurements under vacuum are time consuming and request costly vacuum equipment. Therefore, a further approach has been pursued. As temperature, emissivity and heat convection coefficient of reference bodies and samples are known, the losses by convection and radiation can be calculated in-situ during the measurement.

To calculate the actual heat flow through the reference body the following equation has been used:

$$Q = Q_m - Q_C - Q_R \tag{6.2}$$

where, $Q$ is the actual heat flow, $Q_m$ is the heat flow measured by RB, $Q_C$ is the heat loss by convection and $Q_R$ is the heat loss by radiation.
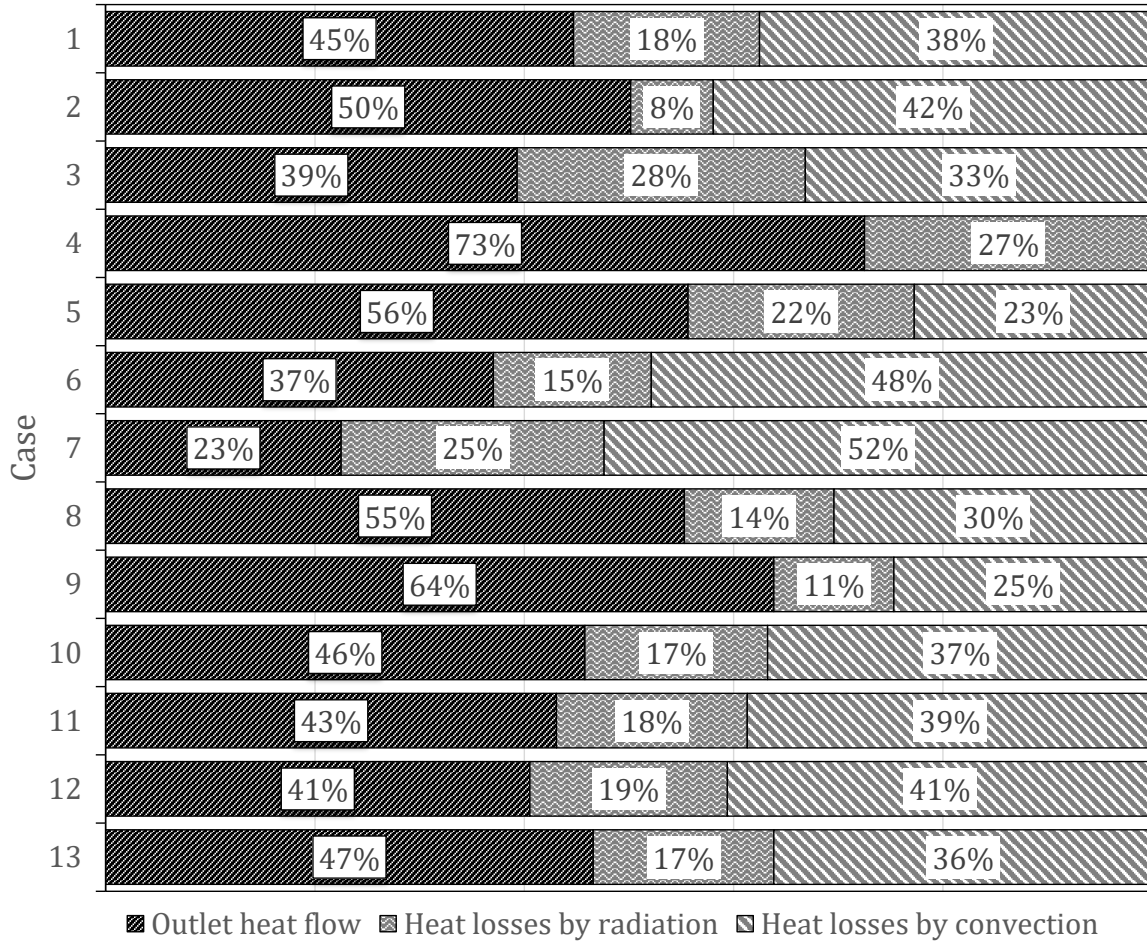
**Figure 6.6:** Simulation results show the ratios of outlet heat flow and heat losses by radiation and convection to the inlet heat flow

The heat losses by convection $Q_C$ and radiation $Q_R$ can be determined by the equations:

$$Q_C = h \cdot A \cdot (T_{RB} - T_A) \tag{6.3}$$

$$Q_R = \varepsilon \cdot \sigma \cdot A \cdot (T_{RB}{}^4 - T_A{}^4) \tag{6.4}$$

where $h$ is the convection heat transfer coefficient, $A$ is the surface area of the reference body, $\varepsilon$ is the emissivity of the reference body surface, $\sigma$ is Stefan-Boltzmann constant, $T_{RB}$ is the temperature of the reference body and $T_A$ is the ambient temperature.

Using these equations, both heat flows can be corrected, the heat flow measured by the first reference body (hot side) and by the second one (cold side), respectively. Also the actual heat flow through the sample can be determined by the same calculation, as the sample temperature is measured, the geometry is known and the emissivity can be

estimated.

## 6.3   Design and realization of the hardware

As shown in figure 6.2 the hardware of *LaTIMA* test stand consists of heater, cooler and IR camera. On the heater and the cooler, two reference bodies are fixed to measure the heat flow. The sample to be measured builds a bridge between the two reference bodies. The IR camera measures the temperature gradient along the sample.

The heater is a high power immersion heater, which allows heating power up to 80 W and operation temperatures up to 300°C. It is fixed on a ceramic plate and can be moved freely to be able to measure samples with different lengths. The cooler is a special designed TEC module, which can achieve temperatures between 0°C and 60°C.
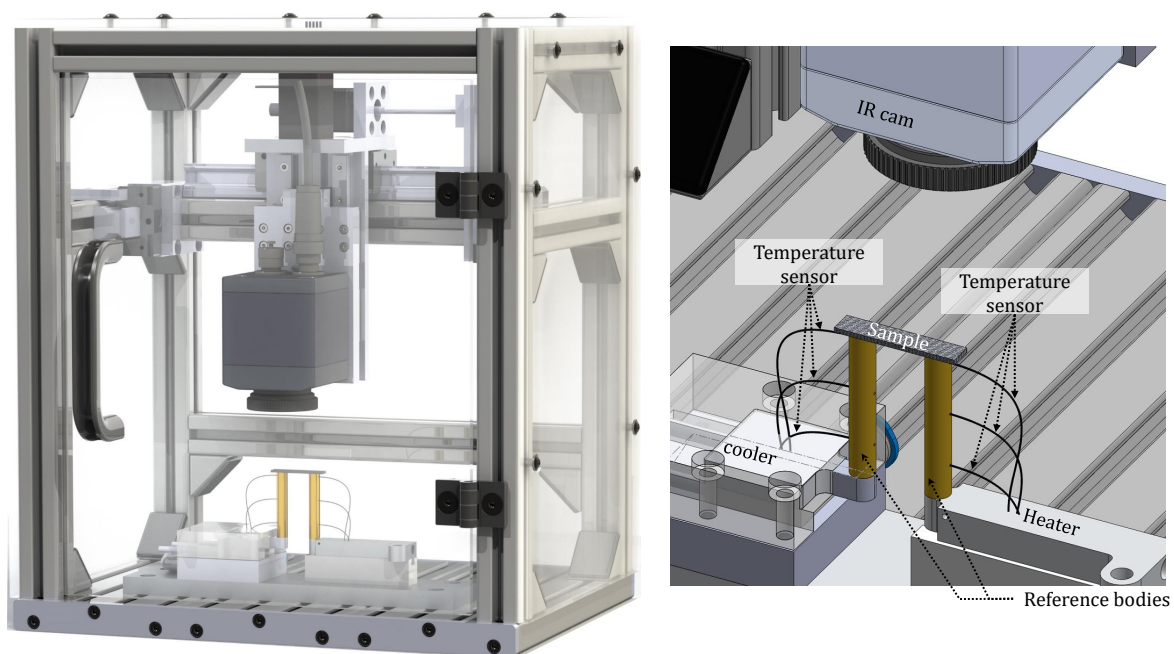
**Figure 6.7:** 3D model *LaTIMA* hardware (left), detailed measurement unit (right)

The measurement unit of the test stand is installed in a housing realized by commercially available aluminium profiles as building kit providing requested mechanical stability and shielding of forced convection. The IR camera is mounted onto three linear guides. Two of them are motorized and can be moved automatically.

In addition to the mechanical hardware, an electronics rack has been developed and realized. It contains two pulse-width modulation units for the heater and cooler, two motor-controls and a measurement board.

Measurement and controlling software has been programmed using LabVIEW for acquisition of temperature sensors and IR camera single and for controlling heater, cooler and stepper motors as well as for the calculation of the measurement value.

## 6.4 Measurement of electrical conductivity

*LaTIMA* test stand uses samples in specific geometries that also allow sophisticated electrical conductivity tests in an equivalent manner by laterally applying an electrical current and measuring the resulting voltage.

For measurement of electrical resistance in µΩ scale, four-terminal sensing with pulse delta technique is used. The method is realized by using a Keithley 6221 AC sourcemeter and a Keithley 2182 Nanovoltmeter. The method is illustrated in figure 6.8.
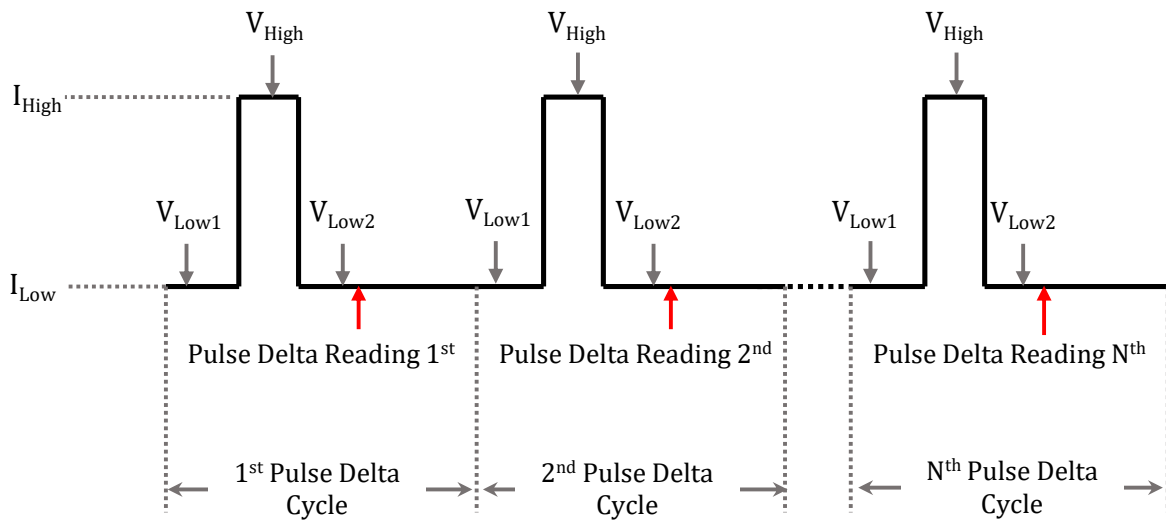


**Figure 6.8:** Measuring principle of pulse delta method

As add-on module to the *LaTIMA* test stand, a test set-up has been designed and realized. The centerpiece of the test set-up is its temperature stage with integrated computer controlled thermoelectric cooler (TEC), which allows measurement at temperatures in a range between room temperature and 120°C. The sample, which is placed on the temperature stage, is connected by six needle pins. The two outer pins have been connected to the AC sourcemeter. The four center pins are used for voltage (sense pins) measurement. They have been arranged in different distances to detect possible failures and inhomogeneities in the sample. The sense pins have been connected to a computer controlled multiplexer, which allows automatized measurement. Figure 6.9 shows the set-up of the

electrical characterization module.
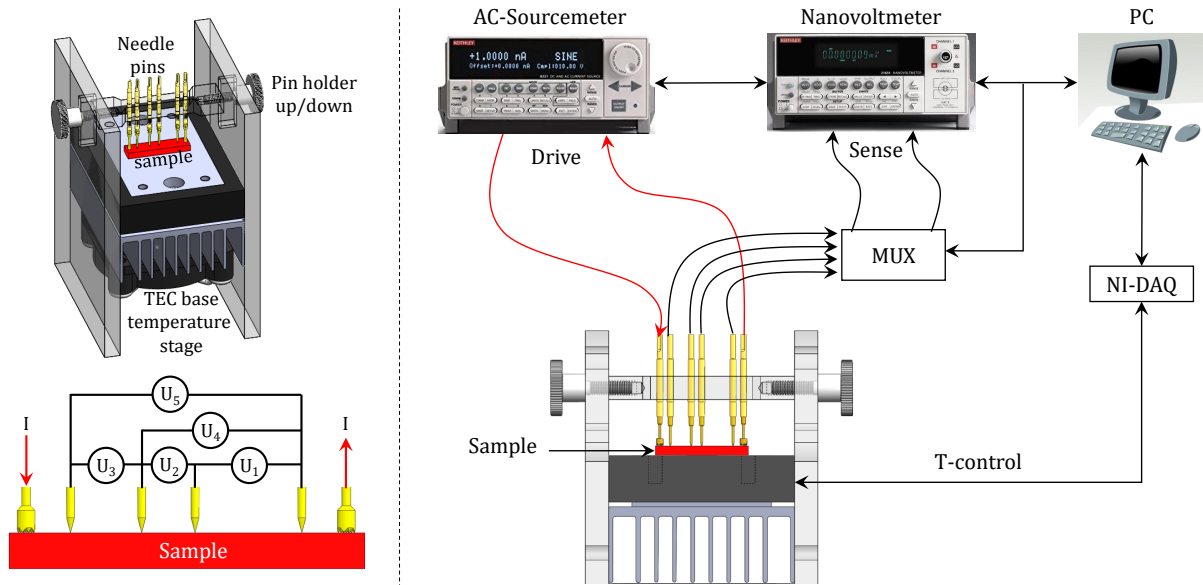


**Figure 6.9:** Set-up of electrical conductivity measurement module

## 6.5 Characterization results by *LaTIMA*

### 6.5.1 Characterization of bulk metals

To verify the functionality of the test stand, different materials with well-known thermal and electrical conductivity have been characterized by the *LaTIMA* test stand. The samples, which are aluminium $(Al\,99.5-F8)$, copper $(Cu-HCP)$, brass $(CuZn\,37)$ and silver $(Ag\,99.9)$ have been cut from market available plates with the geometries shown in table 6.2.

**Table 6.2:** Selected samples and their geometries for benchmark measurement

| Material | Length [mm] | Width [mm] | Thickness [µm] |
|---|---|---|---|
| Aluminium $(Al\,99.5-F8)$ | 20 | 5 | 500 |
| Copper $(Cu-HCP)$ | 20 | 5 | 40 |
| Brass $(CuZn\,37)$ | 20 | 5 | 300 |
| Silver $(Ag\,99.9)$ | 20 | 5 | 150 |

The samples were chosen in different thicknesses to demonstrate the capability of the test stand to measure materials with different thermal conductivities and geometries.

Table 6.3 summarizes the results of electrical and thermal conductivity measurements including their measurement error. The measurement errors result from the error propagation with respect to the inaccuracy of temperature measurement, heat flow measurement and geometry tolerances.

The Wiedemann-Franz law describes a relationship between thermal conductivity and electrical conductivity of bulk metals. The ratio of thermal conductivity and electrical conductivity measured at the same temperature is a constant number, which is known as Lorenz number $L$ [130].

$$L = \frac{\lambda}{\sigma \cdot T} \tag{6.5}$$

where:

| | | |
|---|---|---|
| $L$: | Lorenz number | $\left[\mathrm{W} \cdot \Omega / \mathrm{K}^2\right]$ |
| $\lambda$: | Thermal conductivity | $[\mathrm{W}/(\mathrm{m} \cdot \mathrm{K})]$ |
| $T$: | Measurement temperature | $[\mathrm{K}]$ |
| $\sigma$: | Electrical conductivity | $[\mathrm{MS/m}]$ |

**Table 6.3:** Thermal and electrical conductivities of the reference samples measured by *LaTIMA* and resulting Lorenz numbers

| Material | $\lambda \, [\mathrm{W}/(\mathrm{m} \cdot \mathrm{K})]$ | $\sigma \, [\mathrm{MS/m}]$ | $L \left[\mathrm{W} \cdot \Omega / \mathrm{K}^2\right]$ |
|---|---|---|---|
| Aluminium ($Al\,99.5 - F8$) | $230 \pm 11$ | $22.6 \pm 0.6$ | $(2.26 \pm 0.11) \cdot 10^{-8}$ |
| Copper ($Cu\,HCP$) | $377 \pm 20$ | $45.1 \pm 1$ | $(2.46 \pm 0.20) \cdot 10^{-8}$ |
| Brass ($CuZn\,37$) | $120 \pm 7$ | $14.4 \pm 0.5$ | $(2.47 \pm 0.15) \cdot 10^{-8}$ |
| Silver ($Ag\,99.9$) | $429 \pm 20$ | $62 \pm 1$ | $(2.27 \pm 0.20) \cdot 10^{-8}$ |

The results of the electrical and thermal conductivities as well as the calculated Lorenz number show good consistency with literature values [130].

These results demonstrate the high accuracy of the *LaTIMA* test stand and establish a benchmark for measuring the thermal and electrical conductivities of advanced die attach materials such as sintered silver, which is shown in the following section.

## 6.5.2 Characterization of sintered silver

Sintered silver is a very promising die-attach technology. Due to the expected relative high thermal conductivity, it is very difficult to determine the thermal conductivity with traditional methods. With the *LaTIMA* test stand, it could be shown that materials with such thermal conductivity and geometries can be measured.
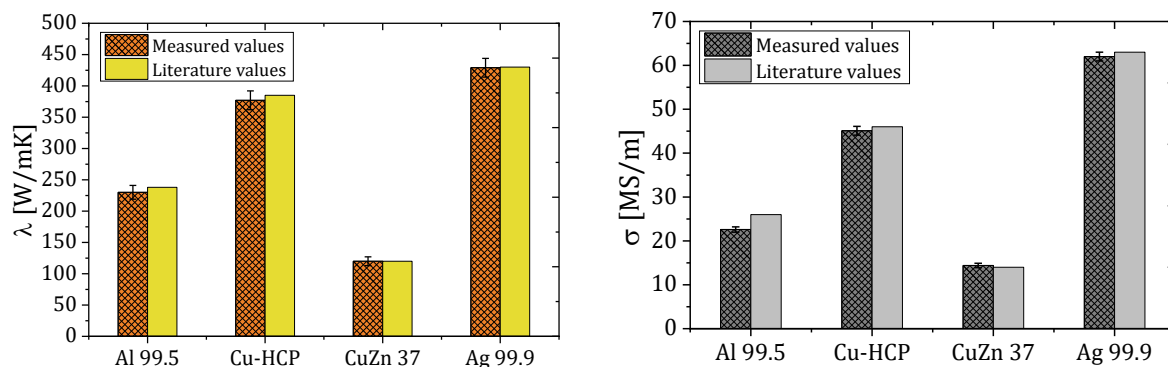
**Figure 6.10:** Thermal and electrical conductivities of the Al, Cu, CuZn and Ag samples measured by *LaTIMA* versus literature values

Thermal and electrical conductivity of sintered silver are strongly dependent on the sintering parameters [131]. To investigate these dependencies, 27 variations of sintered silver samples have been prepared. The thermal and electrical conductivities have been measured by the *LaTIMA* test stand. Finally, the microstructures of the samples have been analyzed by FIB and SEM to study the correlation between process, structure and properties.

### 6.5.2.1 Sample preparation

All samples had the same geometry (length: $l = 20\,\text{mm}$, width: $w = 5\,\text{mm}$, thickness: $t = 150\,\text{µm}$), which can be easily characterized thermally and electrically using the test stand *LaTIMA* .

For each of the 27 sample variants 3 specimens have been built and sintered simultaneously in the laboratory of FH-Kiel. These samples have been processed on a standard ceramic substrate with a certain pressure and heat resistant anti-stick layer.

The requested dimensions (length, width and thickness) have been achieved by applying a specific mask. After drying, the samples were sintered under pressure and temperature according to table 6.4.

### 6.5.2.2 Measurement of thermal conductivity

The total 54 sintered silver samples from 27 variants have been measured using *LaTIMA* at a mean temperature of 70°C. Figure 6.11 shows the results of thermal conductivity as function of the sintering parameters (pressure and temperature). The left diagram presents the results of 20 samples sintered under different pressures between 5 MPa and

**Table 6.4:** Variations of sintered silver samples

|  | $p = 5$ MPa | $p = 10$ MPa | $p = 15$ MPa | $p = 20$ MPa | $p = 25$ MPa |
|---|---|---|---|---|---|
| $T = 200°$C | x | x | x | x | x |
| $T = 225°$C | x | x | x | x | x |
| $T = 230°$C |  |  |  |  | x |
| $T = 235°$C |  |  |  |  | x |
| $T = 240°$C |  |  |  |  | x |
| $T = 245°$C |  |  |  |  | x |
| $T = 250°$C | x | x | x | x | x |
| $T = 255°$C |  |  |  |  | x |
| $T = 260°$C |  |  |  |  | x |
| $T = 265°$C |  |  |  |  | x |
| $T = 270°$C | x | x | x | x | x |

25 MPa at four different temperatures (200°C, 225°C, 250°C and 270°C).

The results show a huge dependency between thermal conductivity and sintering pressure. The thermal conductivity values vary between 65 W/(m·K) for the sample sintered under 5 MPa and 190 W/(m·K) for the one sintered under 20 MPa at 270°C, which is an increase of around 200%.



(a) $\lambda = f(p)$        (b) $\lambda = f(T)$
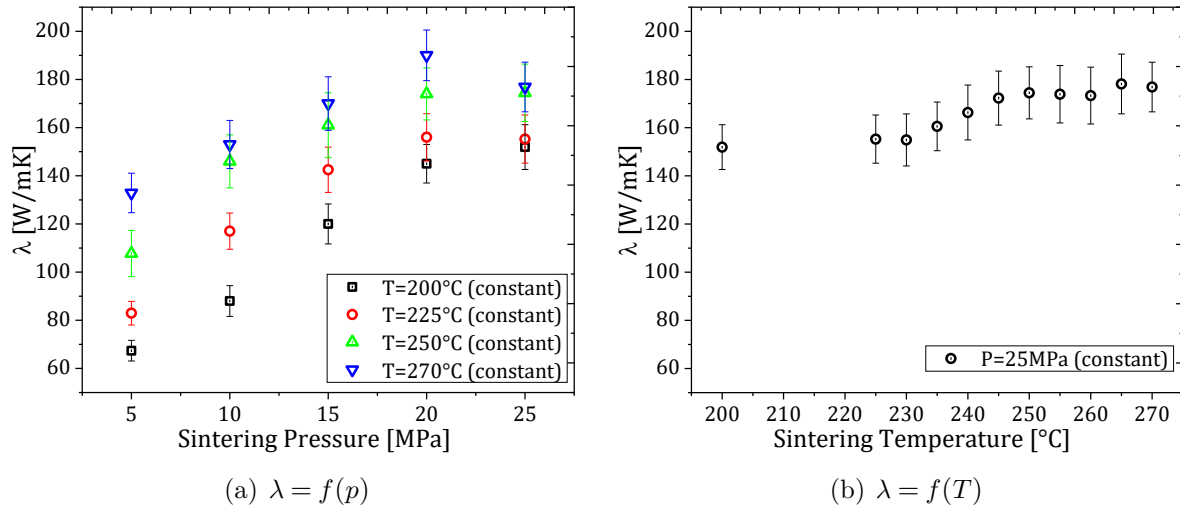
**Figure 6.11:** Thermal conductivity of sintered silver as function of sintering pressure and temperature

The influence of the sintering temperature on the thermal conductivity is shown in the right diagram of figure 6.11. The samples measured here were sintered under constant pressure of 25 MPa at 12 different temperatures between 200°C and 270°C.

The results show also a correlation between sintering temperature and thermal conducti-

vity. However, the influence of the sintering temperature on the thermal conductivity is much less than the sintering pressure. It lies at around 18% at temperatures between 200°C and 270°C.

### 6.5.2.3 Measurement of electrical conductivity

The electrical conductivity of the same samples was measured at a constant temperature of 70°C using four-terminal sensing with delta pulse technique (see section 6.4).

Figure 6.12 presents the results of electrical conductivity as function of sintering pressure and sintering temperature in analogy to the variations in thermal measurements.



(a) $\sigma = f(p)$        (b) $\sigma = f(T)$
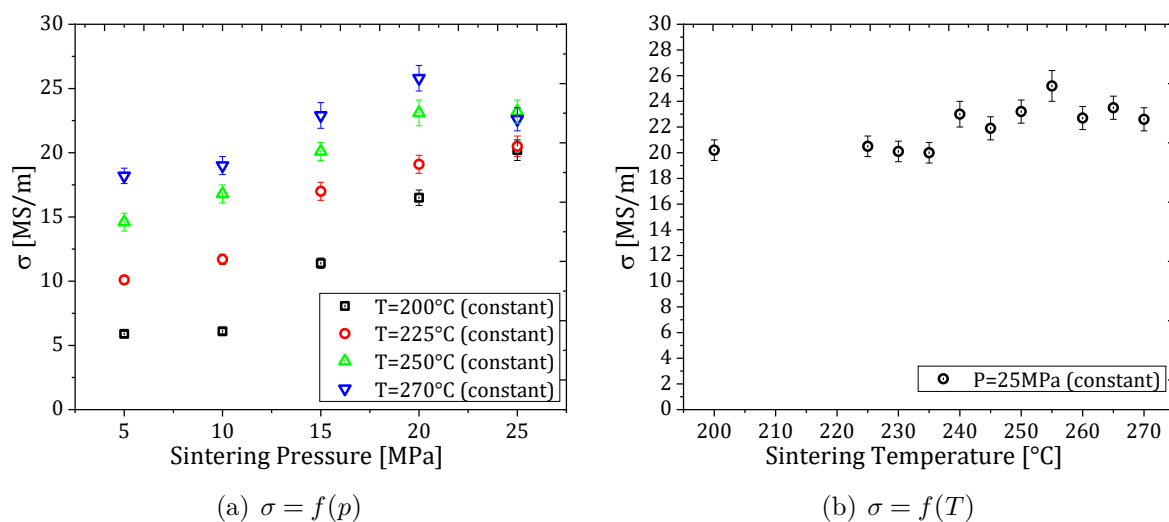
**Figure 6.12:** Electrical conductivity of sintered silver as function of sintering pressure and temperature

As one can see, both sintering temperature and pressure have an explicit influence on the electrical conductivity of the sintered silver. Indeed, the influence of the sintering pressure is much higher than the influence of the sintering temperature, which also corresponds to the results of thermal conductivity measurement.

From the results of thermal and electrical conductivity measurements, the Lorenz number L has been calculated for all samples according to equation 6.5. The results are shown in figure 6.13. It can be seen that the Lorenz number for almost all samples lies in the range of expected theoretical values for bulk metals.

### 6.5.2.4 Structure analysis of sintered silver samples

To investigate the influence of sintering parameters on the microstructure of the sintered silver and its correlation to the measured thermal and electrical properties, all samples
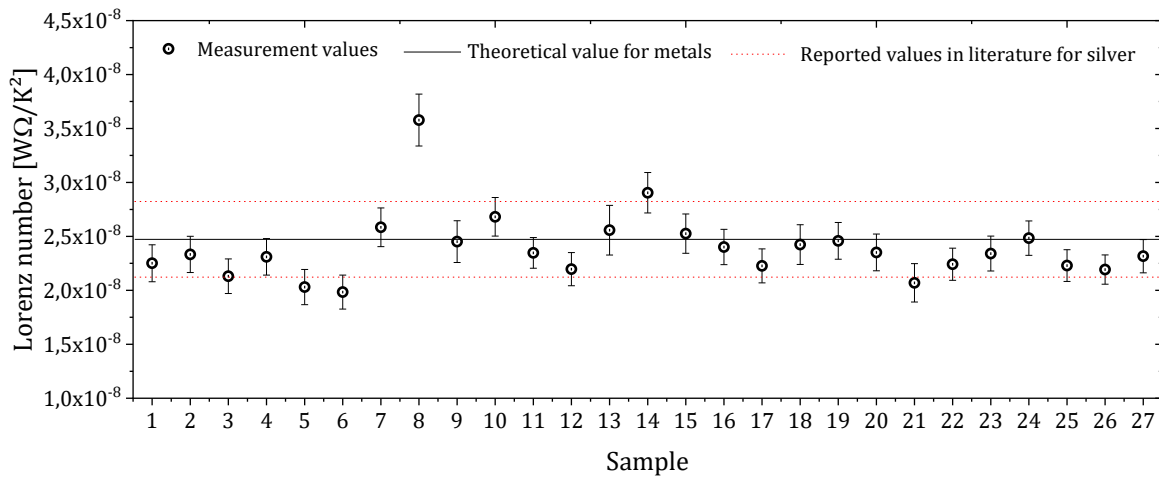
**Figure 6.13:** Lorenz number L of silver sintered samples

have been cross sectioned by FIB. Without any preparation, the samples have been cut by FIB and the microstructures have been analysed by SEM as can be seen in figure 6.14.
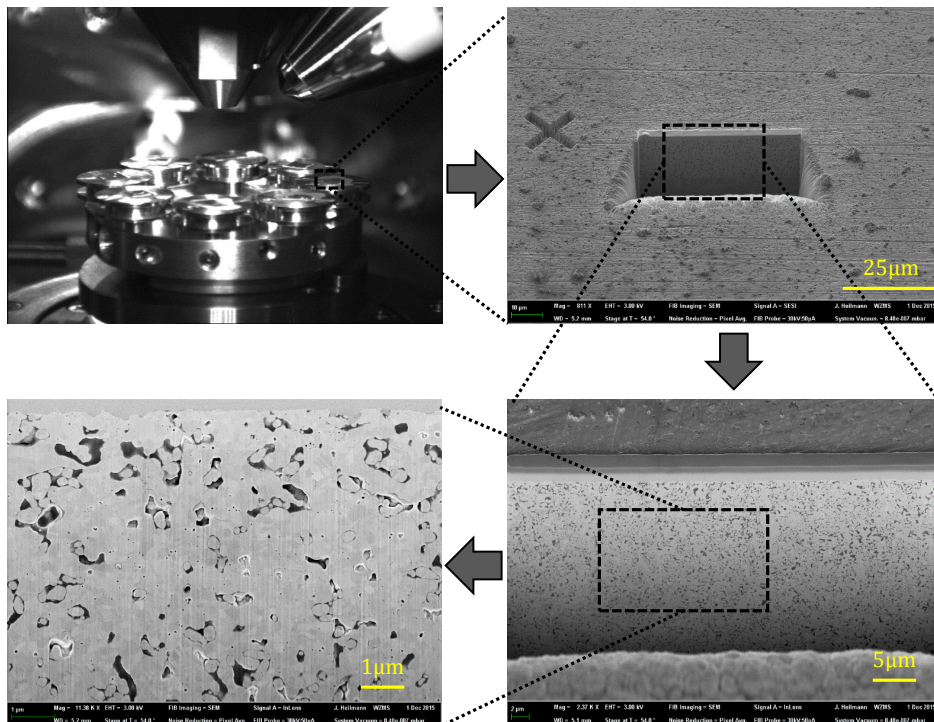


**Figure 6.14:** Process flow of FIB and SEM investigation of sintered silver samples

To derived a structure-property correlation, it has been focused on the porosity of the sintered silver layer. Since the dense/porosity is the prime parameter for thermal and electrical properties and the particle shape and grain-size can be neglected.

The porosity has been determined using an image processing by converting the images to

binary images by using a threshold value and measuring the ratio between them. This approach of porosity determination from the polished 2D-image should produce suitable results if the pores are arbitrarily orientated and the specimens are large enough for averaging. However, the accuracy of the porosity determination using this approach is also dependent on the contrast of the SEM images.

Figure 6.15 shows two exemplary SEM images, one with relatively high contrast (left) and the other with lower contrast. The calculated porosity is more accurate for the image with higher contrast. The determination errors of the porosity have been taken into account in the correlation analysis. Generally, it can be said, that the porosity of highly porose samples can be analysed easier than lower porose samples.
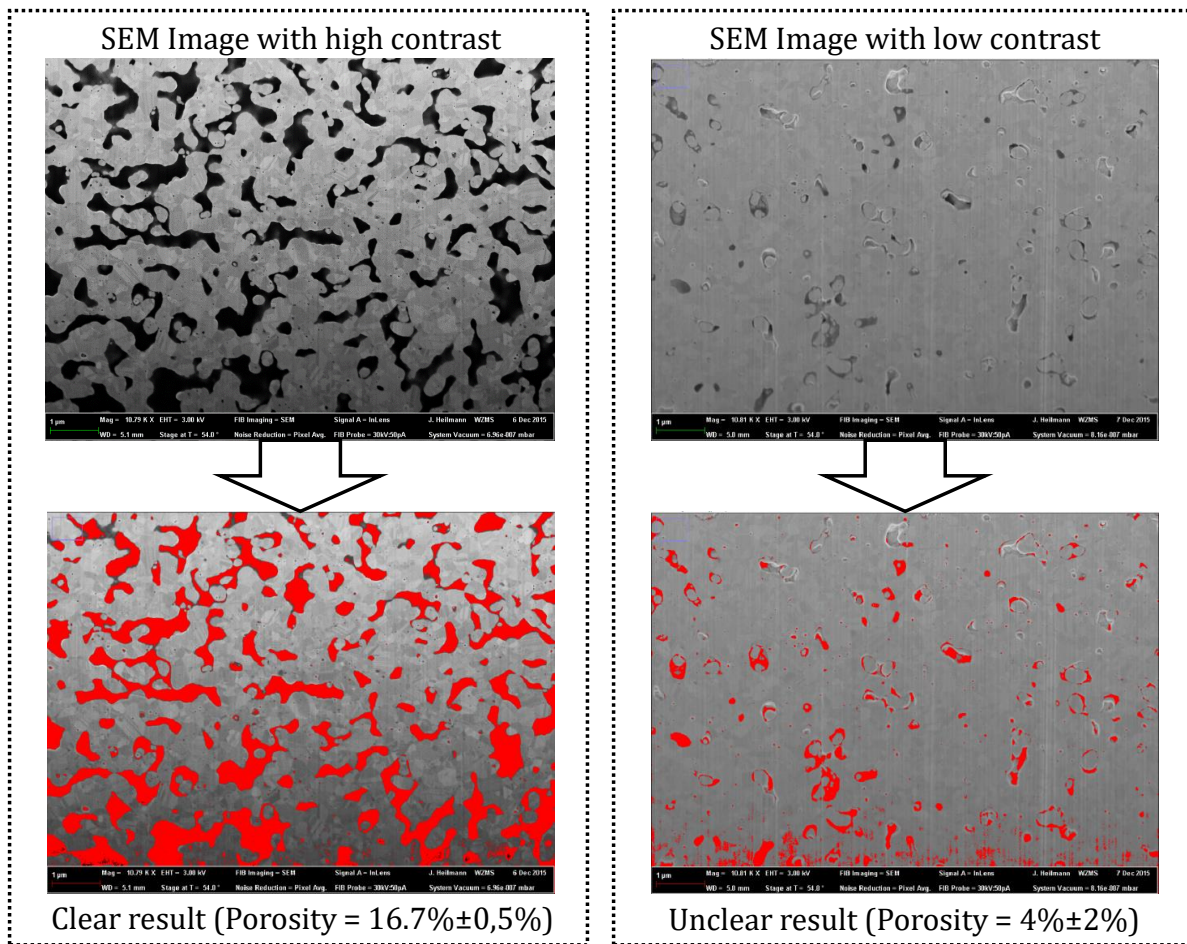


**Figure 6.15:** Determination of porosity using image processing software

Figures 6.16 - 6.19 show the microstructure of the sintered silver samples. The images are sorted in four groups. In figure 6.16, SEM images of the samples sintered under different pressures between 5 MPa and 25 MPa at constant temperature of 200°C can be seen. The porosity of these samples varies between 22% and 5%.

In the second group (figure 6.17), the SEM images of the samples sintered also under
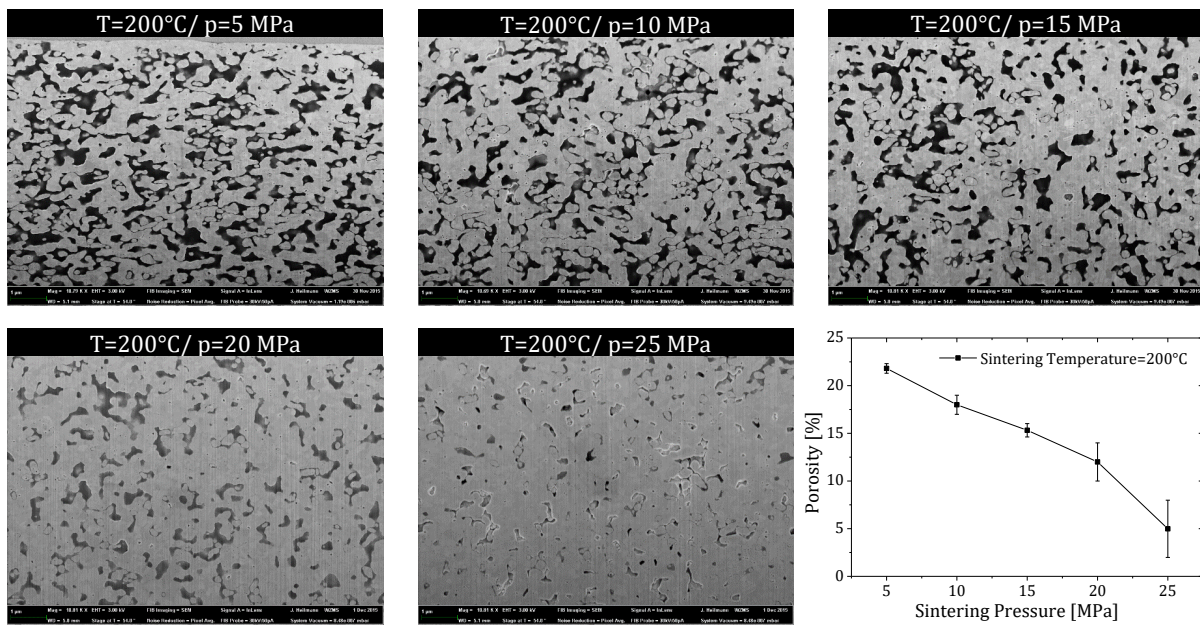
**Figure 6.16:** SEM images of sintered silver (porosity as function of sintering pressure at 200°C sintering temperature)

pressures between 5 MPa and 25 MPa but at constant temperature of 225°C can be seen. The porosity of these samples varies between 15% and 5%.
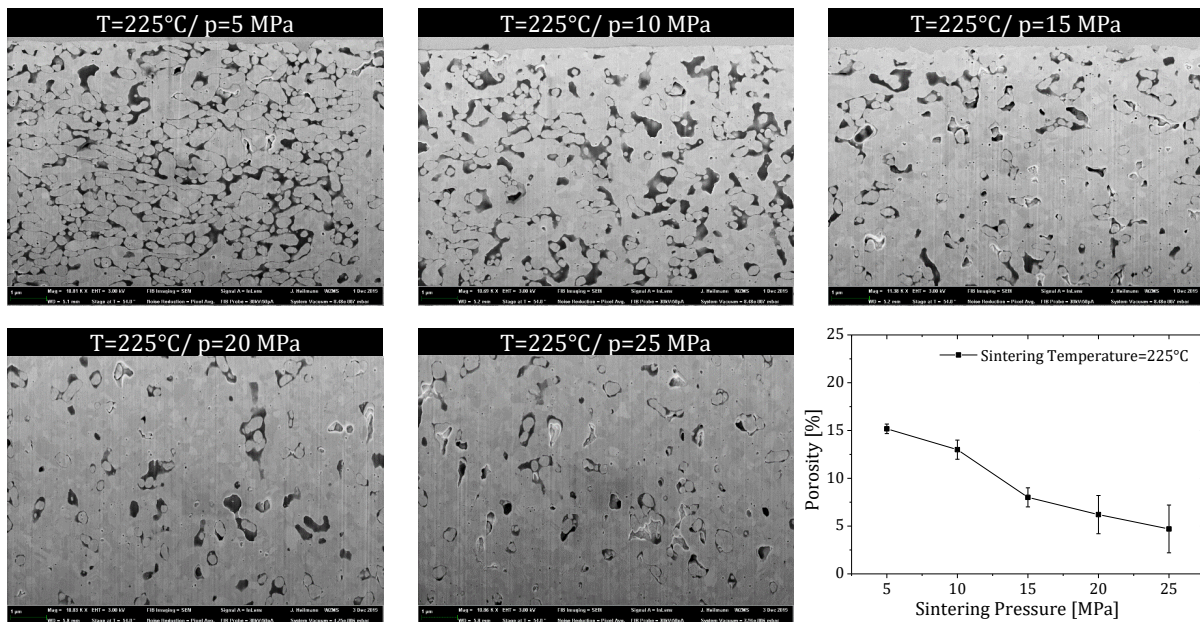


**Figure 6.17:** SEM images of sintered silver (porosity as function of sintering pressure at 225°C sintering temperature)

The porosity of the samples sintered under pressures between 5 MPa and 25 MPa but at constant temperature of 250°C (figure 6.18) and at constant temperature of 270°C (figure 6.19) varies between 14% and 4%.
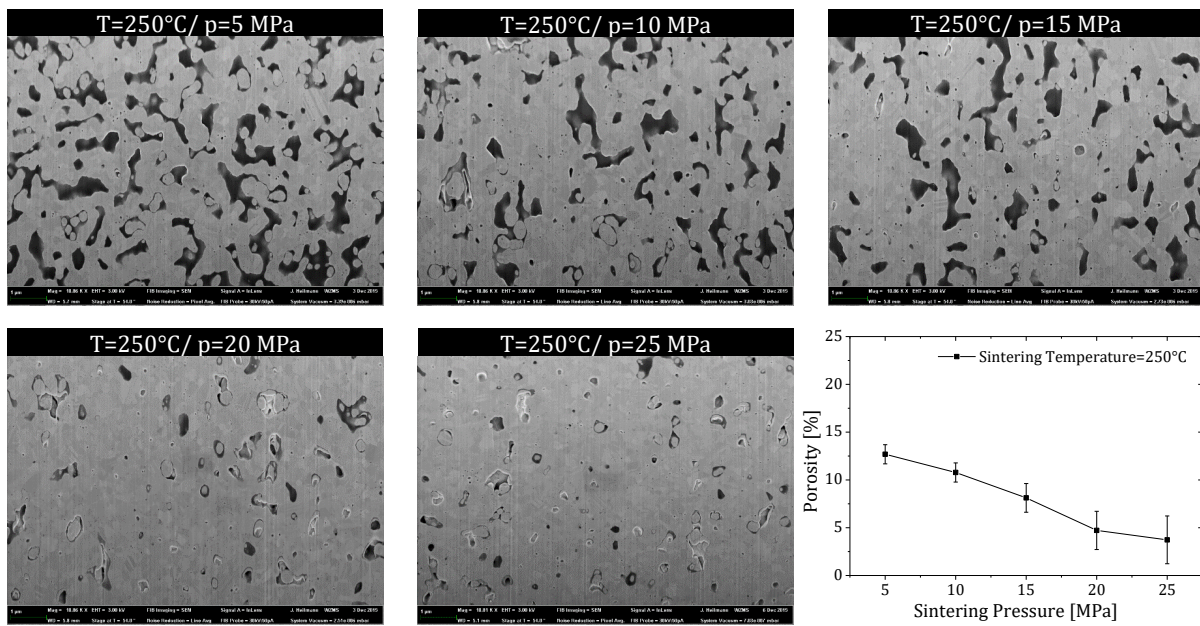
**Figure 6.18:** SEM images of sintered silver (porosity as function of sintering pressure at 250°C sintering temperature)
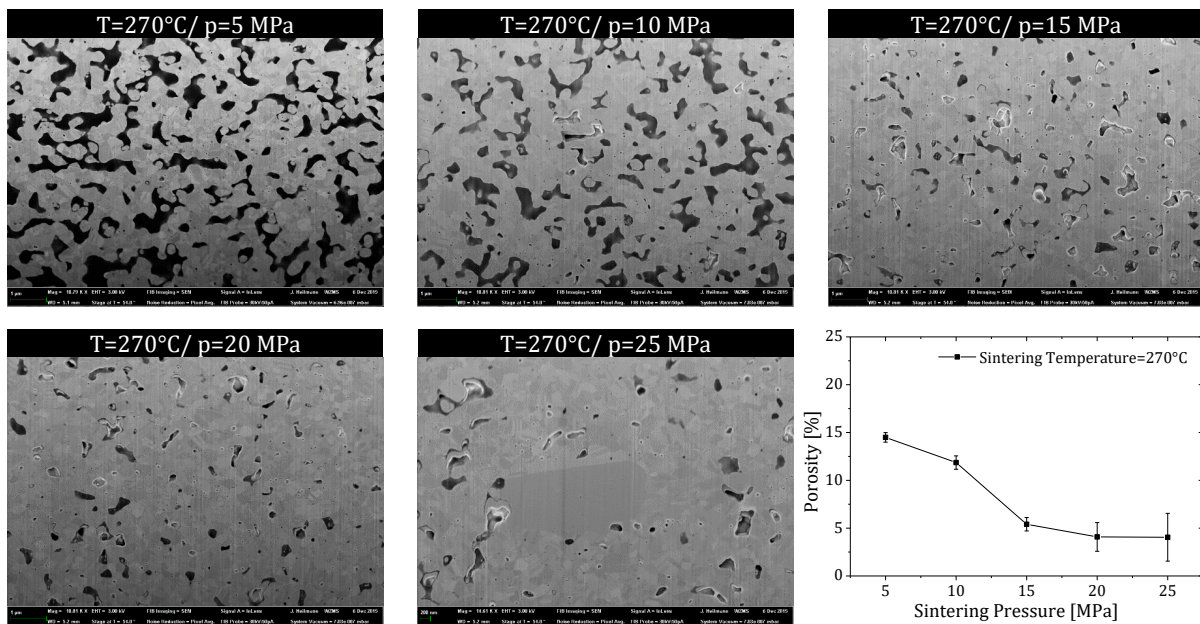


**Figure 6.19:** SEM images of sintered silver (porosity as function of sintering pressure at 270°C sintering temperature)

The diagrams in figure 6.20 summarize the porosity as function of sintering pressure and sintering temperature. It can be seen, that the sintering pressure has more influence on the micro structures of sintered silver than the sintering temperature. This knowledge confirms the results of the thermal and electrical conductivities of the same samples, which have been shown in figure 6.12.
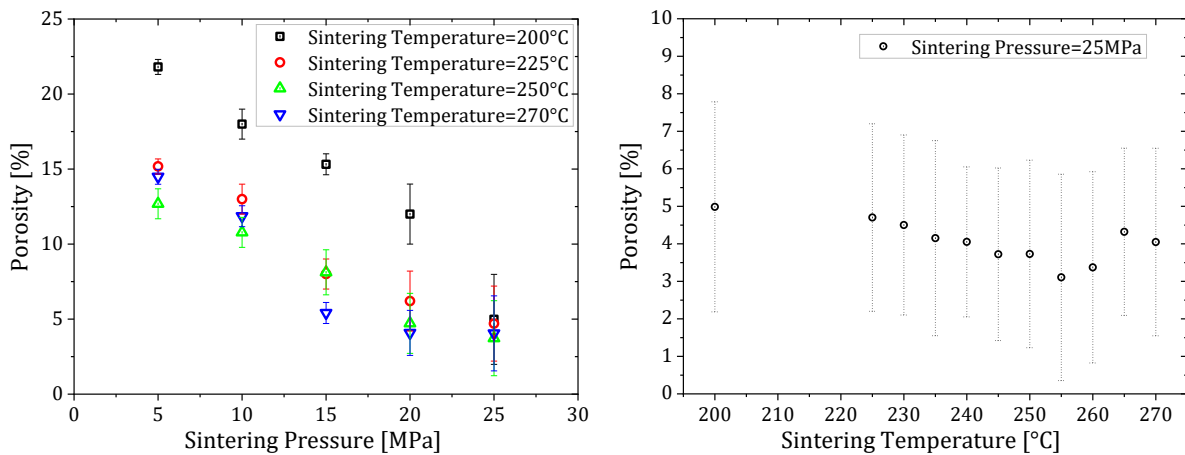
**Figure 6.20:** Porosity as function of sintering pressure and sintering temperature

#### 6.5.2.5 Process-structure-properties correlation of sintered silver

The results of thermal and electrical characterization of sintered silver samples performed by the test stand *LaTIMA* showed dependency between thermal and electrical conductivity and sintering parameters (see figures 6.11 and 6.12).
The structure analysis of the sintered silver shows also correlation between sintering parameters and porosity (figure 6.20).

From both investigations, a correlation between process, structures and properties can be established. In figure 6.21, the results of the electrical and thermal conductivities for all sintered silver samples are plotted over the corresponding porosity. Unambiguous correlation can be found between material properties and structures, which result from processing parameters.
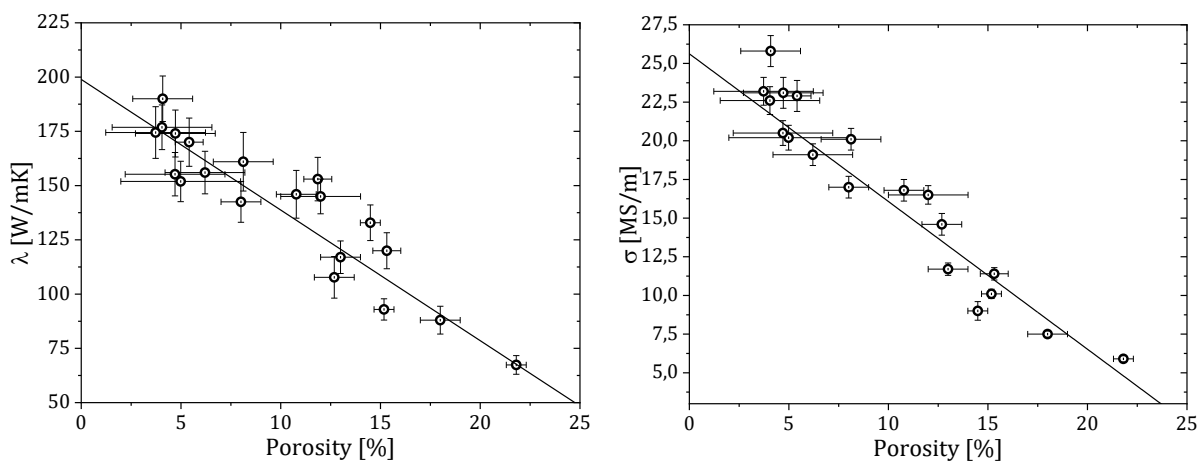


**Figure 6.21:** Thermal and electrical conductivity as function of porosity of sintered silver

However, the results show unexpected values for thermal and electrical conductivity if extrapolating to porosity of 0%. For thermal conductivity there results a value of around $200\,\mathrm{W/(m\cdot K)}$, while the expected value for bulk silver is $429\,\mathrm{W/(m\cdot K)}$. The method and its accuracy could seem doubtful by these results, however this doubt can be eliminated by the following arguments:

- The test stand has been benchmarked by measuring well known reference samples

- Bulk silver sample has been measured thermally and electrically by *LaTIMA*, the obtained results agreed very well with the literature values

- The extrapolated electrical conductivity of the sintered silver to 0% porosity is $26\,\mathrm{MS/m}$ instead of the expected $62\,\mathrm{MS/m}$ for bulk silver.

- The calculated Lorenz number from the thermal and electrical conductivity extrapolated to 0% porosity is $2.28 \cdot 10^{-8}\,\mathrm{W\cdot \Omega/K^2}$, which fits very well to the Lorenz number of bulk silver (see table 6.3)

There are two explanations for these unexpected results. The less probable one is that the way of porosity measurement is incorrect, as the used approach analyzed 2D images but the porosity is a 3D effect.

The more probable explanation is based on the fact, that the used sinter paste consists of nano silver particles. These nano silver particles are covered by organic layer, which is normally decomposed during the sintering process but for those samples the organic materials did not fully decompose.

## 6.6 Conclusion

In this section, an innovative test stand for thermal and electrical conductivity measurement of highly conductive materials has been presented. The idea, concept and realization of the test stand have been discussed. The design of the test stand and possible error sources have been analysed and studied both analytically and by FE simulation. As benchmark for the developed test stand, several well known samples have been characterized electrically and thermally by the test stand. The results show very high agreement with the literature values of these materials.

Finally, to investigate the influences of processing parameters on thermal and electrical properties of sintered silver, an extensive systematic study of sintered silver has been performed. Several sintered silver samples have been prepared under different sintering

conditions. Sintering temperature was varied between 200°C and 270°C and the sintering pressure between 5 MPa and 25 MPa. The obtained results for thermal conductivity are between $65\,\mathrm{W/(m\cdot K)}$ and $190\,\mathrm{W/(m\cdot K)}$ and between $5\,\mathrm{MS/m}$ and $25\,\mathrm{MS/m}$ for electrical conductivity. To complete the story of the processing-structure-property correlation, the microstructure of the sintered silver samples has been analyzed by FIB and SEM. They show a clear dependency between the sintering parameter and the porosity of the structures, which is also in correlation with the thermal and electrical conductivities.

# Chapter 7

# Transient test stand for thermal diffusivity measurement

This chapter deals with the development of a test stand for thermal diffusivity measurement based on Ångström's method. The theoretical background of the method will be explained in detail followed by a study of the effect of heat losses of the results and ways to overcome them. Further, the implantation of the method in a test stand will be shown. The test stand can be integrated into the hardware of the test stand *LaTIMA*, which has been developed for the measurement of thermal conductivity of highly conductive materials (see chapter 6). Finally, results of thermal diffusivity measurement for several materials will be shown and discussed.

## 7.1 Methodology

The measuring principle of the test stand is based on the thermal wave theory. Therefore the test stand has been named *TIMAwave*.
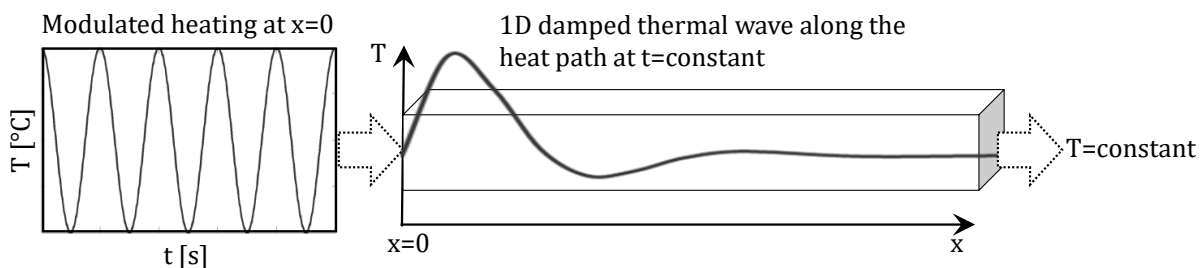


**Figure 7.1:** Damped Thermal wave

By heating a surface, damped and dispersive waves arise inside the material. These waves are called thermal waves. The Swedish physicist A. J. Ångström (1814-1874) investigated

among others thermal waves in semi-infinite samples and described a method for determination of thermal conductivity [132]. Periodically modulated heat with a modulation frequency $\omega$ is applied onto one end of a semi-infinite sample, while the other end is kept in a constant temperature (figure 7.1).

The modulated heat flow through the sample results in the form of a one-dimensional damped thermal wave, which is described by the solution of diffusion equation 7.1:

$$\frac{\partial T(x,t)}{\partial t} = \alpha \frac{\partial^2 T(x,t)}{\partial x^2} \tag{7.1}$$

The equation 7.1 can be reduced by the substitution

$$T(x,t) = u(x) \cdot e^{i\omega t} \tag{7.2}$$

to

$$\frac{\partial^2 u(x)}{\partial x^2} = \frac{i\omega}{\alpha} \cdot u(x). \tag{7.3}$$

Using the exponential substitution

$$u(x) = A \cdot e^{-Bx}, \tag{7.4}$$

in equation 7.3 leads to

$$\frac{\partial^2 u}{\partial x^2} = A \cdot B^2 \cdot e^{-Bx}, \tag{7.5}$$

Substituting equations 7.4 and 7.5 in equation 7.3 results in

$$A \cdot B^2 \cdot e^{-Bx} = \frac{i\omega}{\alpha} \cdot A \cdot e^{-Bx} \tag{7.6}$$

$$\Rightarrow B = \sqrt{\frac{i\omega}{\alpha}} \tag{7.7}$$

Integration of term $B$ from equation 7.7 in the exponential substitution (equation 7.4) leads in

$$u(x) = A \cdot e^{-x\sqrt{\frac{i\omega}{\alpha}}}, \tag{7.8}$$

or

$$u(x) = A \cdot e^{-x(1+i)\sqrt{\frac{\omega}{2\alpha}}}, \tag{7.9}$$

Through the back substitution of $u(x)$, which results in equation 7.9, in equation 7.2 we get:

$$T(x,t) = A \cdot e^{-x(1+i)\sqrt{\frac{\omega}{2\alpha}}} \cdot e^{i\omega t} \tag{7.10}$$

$$= A \cdot e^{-x\sqrt{\frac{\omega}{2\alpha}}} \cdot e^{i\left(\omega t - x\sqrt{\frac{\omega}{2\alpha}}\right)} \tag{7.11}$$

with

$$\sqrt{\frac{\omega}{2\alpha}} = k, \tag{7.12}$$

which is the wave number. Substituting equation 7.12 in equation 7.11 results in:

$$T(x,t) = A \cdot e^{-kx} \cdot e^{i(\omega t - kx)} \tag{7.13}$$

$$= A \cdot e^{-kx} \cdot \left( \cos(\omega t - kx) + i \sin(\omega t - kx) \right) \tag{7.14}$$

The solution of the equation 7.14 at the heat excitation $x = 0$ must be real and given as:

$$T(t) = A \cdot \cos(\omega t) \tag{7.15}$$

Thus, the damped thermal wave along the samples is also real, so equation 7.14 can be reduced to:

$$T(x,t) = A \cdot e^{-kx} \cdot \cos(\omega t - kx) \tag{7.16}$$

The equation of the damped thermal wave (7.16) for the steady-periodic temperature has three important properties which are:

i. The amplitude of the temperature oscillation diminishes exponentially like:

$$A \cdot e^{-k \cdot x} = A \cdot e^{-x \cdot \sqrt{\frac{\omega}{2 \cdot \alpha}}} \tag{7.17}$$

Its damping rate is dependent on the modulation frequency $\omega$.

ii. The phase $\phi$ of the temperature wave lags progressively. The lag increases with the modulation frequency $\omega$

$$\phi = k \cdot x = x \cdot \sqrt{\frac{\omega}{2 \cdot \alpha}} \tag{7.18}$$

iii. The temperature fluctuations are propagating into the sample with the velocity $v$

$$v = \mu \cdot \omega = \Lambda \cdot \frac{\omega}{2\pi} = \sqrt{2 \cdot \omega \cdot \alpha} \tag{7.19}$$

Where $\mu$ is thermal diffusion length, $\Lambda$ is wave length and $\alpha$ is thermal diffusivity.

It results from equations 7.17, 7.18 and 7.19 that the thermal diffusivity $\alpha$ can be determined by the measurement of the amplitude or phase of the thermal wave field in the sample length $x$ or of the velocity of propagation $v$.

An analytical calculation of the oscillated amplitude at different positions along a semi-infinity sample will be shown here to visualize the diminishing of the amplitude and the shifting of the phase.

Following parameters have been used for the calculation:
- Oscillation frequency: $\omega = 2\,\text{Hz}$
- Oscillation amplitude: $\Delta T = 1\,\text{K}$
- Thermal diffusivity of the semi-infinity sample: $\alpha = 100\,\text{mm}^2/\text{s}$

The wave number $k$ can be calculated form the equation $k = \sqrt{\frac{\omega}{2 \cdot \alpha}} = 0.1\,\text{mm}^{-1}$. The thermal diffusion length is $\mu = 1/k = 10\,\text{mm}$.

Figure 7.2 visualizes the thermal wave field as function of time and sample length x. It can be seen that the temperature oscillates with the full amplitude at $x = 0$ and diminishes along the semi-infinity sample.
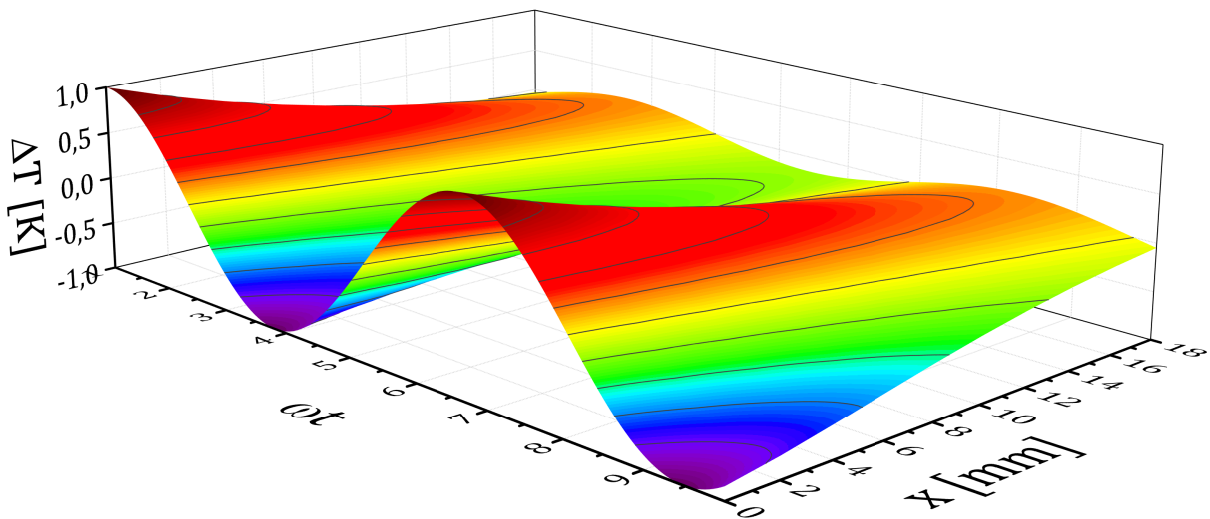


**Figure 7.2:** Thermal wave field as function of time and sample length

Figure 7.3 shows the temperature oscillation at different positions along the sample. It can be seen that:

- at x = 0 the amplitude is 100% of the start amplitude and there is no phase shift,
- at x = $\mu/2$ = 5 mm the amplitude is 61% of the start amplitude and the phase shift is 0.5 rad,
- at x = $\mu$ = 10 mm the amplitude is 37% = $1/e$ of the start amplitude and the phase shift is 1 rad and
- at $x$ = 15 mm the amplitude is 22% of the start amplitude and the phase shift is 1.5 rad.
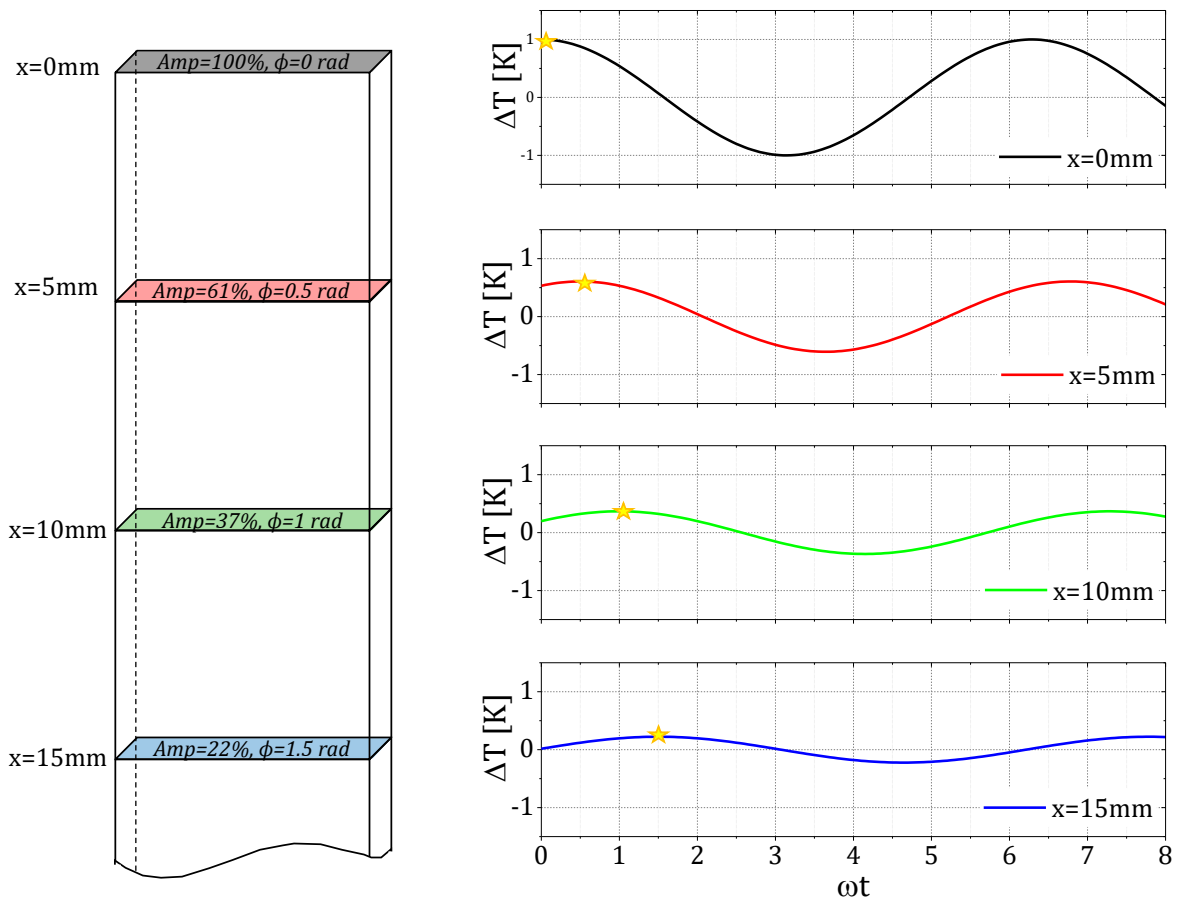


**Figure 7.3:** Left: schematic of a semi-infinity sample; right: temperature oscillation at different positions along the semi-infinity sample

Plotting the values of the oscillation amplitude and the phase shift over the sample length (figure 7.4) results in natural logarithmic dependency between the amplitude and the sample length and linear dependency between phase and sample length. The absolute values of both slopes (amplitude and phase over sample length) are the wave number $k = 0.1 \ mm^{-1}$ which is the same number used as input parameter for the calculation.
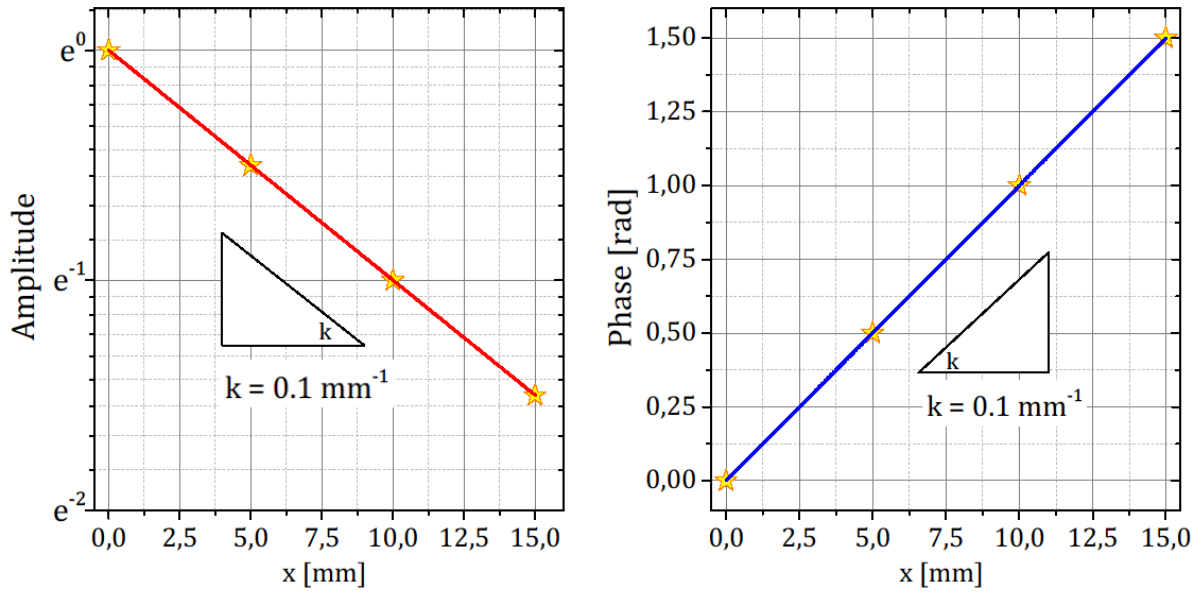
**Figure 7.4:** Left: temperature oscillation amplitude as function of the sample length $x$; right: phase shift as function of the sample length $x$

### 7.1.1 Influence of heat losses of thermal diffusivity measurement by *TIMAwave*

The calculation in the previous section shows that the wave number $k$ determined from the amplitude and phase is the same. However, this is valid only for the ideal case, where there is no heat loss along the sample. For the real case the total heat $Q_{tot}$ [W], which flows through the sample is the input heat $Q_{in}$ [W] reduced by the rate of heat losses $Q_{loss}$ [W]

$$Q_{tot} = Q_{in} - Q_{loss} \tag{7.20}$$

where:

- The rate of total heat flow in the sample $Q_{tot}$ is:

$$dQ_{tot} = A \cdot c \cdot \rho \cdot \frac{\partial T}{\partial t} \cdot dx \quad [W] \tag{7.21}$$

  where $A$ is the cross section area of the sample, $c$ is the heat capacity and $\rho$ is the density.

- The rate of the input heat through the sample $Q_{in}$ is:

$$dQ_{in} = A \cdot \lambda \cdot \frac{\partial^2 T}{\partial x^2} \cdot dx \quad [W] \tag{7.22}$$

with $\lambda$ the thermal conductivity.

- The rate of the heat loss at the sample surface $Q_{loss}$ is:

$$dQ_{loss} = h \cdot (T - T_0) \cdot G \cdot dx \quad [W] \tag{7.23}$$

where $h\ \left[\text{W/m}^2 \cdot \text{K}\right]$ is surface conductance, $T$ is the sample temperature, $T_0$ the ambient temperature and $G$ is the perimeter of the sample [74].

Putting equations 7.21, 7.22 and 7.23 in equation 7.20 we get

$$A \cdot c \cdot \rho \cdot \frac{\partial T}{\partial t} \cdot dx = A \cdot \lambda \cdot \frac{\partial^2 T}{\partial x^2} \cdot dx - H \cdot (T - T_0) \cdot G \cdot dx \tag{7.24}$$

$$\Rightarrow \frac{\partial T}{\partial t} = \frac{\lambda}{c \cdot \rho} \cdot \frac{\partial^2 T}{\partial x^2} - \frac{H \cdot G}{\rho \cdot c \cdot A} \cdot (T - T_0) \tag{7.25}$$

With:

- $\frac{\lambda}{c \cdot \rho} = \alpha$, which is the thermal diffusivity

- $\frac{H \cdot G}{\rho \cdot c \cdot A} = \nu$, heat loss factor and

- $T_0 = 0$

equation 7.25 results in

$$\frac{\partial T}{\partial t} = \alpha \cdot \frac{\partial^2 T}{\partial x^2} - \nu \cdot T \tag{7.26}$$

It can be seen that the differential equations 7.26 and 7.1 differ by the term $\nu \cdot T$. So the equation 7.1 describes the ideal case, where no heat loss occurs, while equation 7.26 covers the heat loss at the sample surface.

By solving the differential equation 7.26 using the same substitution used for equation 7.1

$$T(x,t) = u(x) \cdot e^{i\omega t} \tag{7.27}$$

we obtain

$$\frac{\partial^2 u(x)}{\partial x^2} = \frac{\nu + i\omega}{\alpha} \cdot u(x). \tag{7.28}$$

The differential equation 7.28 can be solved analog to equation 7.3. It yields for the wave number a complex number, which consists of a real and an imaginary part:

$$k = \sqrt{\frac{\nu + i\omega}{\alpha}} \tag{7.29}$$

The real part results from the amplitude $\Re(k) = k_{amp}$ and the imaginary part results from the phase $\Im(k) = k_{pha}$. With

$$k = k_{amp} + ik_{pha} \tag{7.30}$$

By equating the equations 7.29 and 7.30 and by comparison of their coefficients, it results for

$$k_{amp} = \sqrt{\frac{\sqrt{\nu^2 + \omega^2} + \nu}{2 \cdot \alpha}} = \sqrt{\frac{\sqrt{\nu^2 + \omega^2}}{2 \cdot \alpha} + \frac{\nu}{2 \cdot \alpha}} \tag{7.31}$$

and for

$$k_{pha} = \sqrt{\frac{\sqrt{\nu^2 + \omega^2} - \nu}{2 \cdot \alpha}} = \sqrt{\frac{\sqrt{\nu^2 + \omega^2}}{2 \cdot \alpha} - \frac{\nu}{2 \cdot \alpha}} \tag{7.32}$$

It can be seen in equations 7.31 and 7.32 that thermal losses influence both $k_{amp}$ and $k_{pha}$, which results in a wrong thermal diffusivity [133].

To calculate the thermal diffusivity $\alpha$, the geometric mean of the wave number of the amplitude $k_{amp}$ and of the phase $k_{pha}$ are needed which provide the great advantage of elimination of the heat loss factor $\nu$ [134].

$$k_{amp} \cdot k_{pha} = \sqrt{\frac{\sqrt{\nu^2 + \omega^2}}{2 \cdot \alpha} + \frac{\nu}{2 \cdot \alpha}} \cdot \sqrt{\frac{\sqrt{\nu^2 + \omega^2}}{2 \cdot \alpha} - \frac{\nu}{2 \cdot \alpha}} \tag{7.33}$$

$$= \sqrt{\frac{\sqrt{\nu^2 + \omega^2}}{2 \cdot \alpha} + \frac{\nu}{2 \cdot \alpha} \cdot \sqrt{\frac{\sqrt{\nu^2 + \omega^2}}{2 \cdot \alpha} - \frac{\nu}{2 \cdot \alpha}}} \tag{7.34}$$

$$= \sqrt{\frac{\omega^2}{4 \cdot \alpha^2}} \tag{7.35}$$

$$= \frac{\omega}{2 \cdot \alpha} \tag{7.36}$$

$$\Rightarrow \sqrt{k_{amp} \cdot k_{pha}} = \sqrt{\frac{\omega}{2 \cdot \alpha}} = k \tag{7.37}$$

## 7.1.2 Lock-in processing for determination of amplitude and phase information

For the determination of the amplitude and the phase of the thermal wave field in the sample, the lock-in thermography can be used. Usually the lock-in is the technique of choice, if signals have to be extracted, which are superimposed by statistical noise. Prerequisite

to using this techniques is that the primary signal can be periodically pulsed or anyhow else amplitude-modulated with a certain frequency called "lock-in frequency" $f_{li}$. The aim of the lock-in principle is to evaluate only the oscillating part of the detected signal. Mathematically, the lock-in signal process (usually called lock-in correlation procedure) can be described as multiplication of the detected signal $F(t)$ by a noise-free correlation signal $K(t)$ [135]. It results in the output signal $S$, which can be written as:

$$S = \frac{1}{t_{int}} \int_0^{t_{int}} F(t) \cdot K(t) \; dt \tag{7.38}$$

Where:

$t_{int}$:     Integration time
$F(t)$:     Detected signal
$K(t)$:     Correlation signal

Often, the input signal $F(t)$ has to be digitized to a set of numbers $F(k)$ using Analog-Digital-Converter (ADC), as the lock-in correlation procedure is performed numerically. For this reason, the correlation function $K(t)$ has to be replaced by a set of numbers $K(k)$ and the continuous singal $S$ equation 7.38 becomes a discrete function, which is the averaging of the product of the measured values $F(k)$ and a set of weighting factors $K(k)$ up to the total number of measured values $M$:

$$S = \frac{1}{M} \sum_{k=1}^{M} F(k) \cdot K(k) \tag{7.39}$$

This analysis is called one-channel lock-in process. To determine the amplitude and phase information of an oscillated signal (e.g oscillated temperature field) the so called two-channel lock-in process is required [136].

Two-channel correlation means that there are two sets of reference signals $K_j$, one approximating the sin-function, and the other one approximating the cosine one. The correlation is performed twice in parallel with these two sets. Then the first channel measures the component of the signal in-phase with the sin-function, and the other channel measures the component in-phase with the cos-function, which is 90° phase-shifted to the sin-function and usually called out-of-phase component.

Assumed are an amplitude of the detected signal $A$ and its phase $\phi$, so the detected signal $F(t)$ is given as:

$$F(t) = A \cdot \sin\left(2\pi \cdot f_{li} \cdot t + \phi\right) \tag{7.40}$$

and the two correlation signals $K_0$ and $K_{90}$ are given as:

$$K_0(t) = 2 \cdot \sin\left(2\pi \cdot f_{li} \cdot t\right) \tag{7.41}$$

$$K_{90}(t) = 2 \cdot \cos\left(2\pi \cdot f_{li} \cdot t\right) \tag{7.42}$$

Substituting equations 7.40, 7.41 and 7.42 into equation 7.38 leads to equations 7.43 and 7.44 for the lock-in signals:

$$S_0 = A \cdot \cos\left(\phi\right) \tag{7.43}$$

$$S_{90} = A \cdot \sin\left(\phi\right) \tag{7.44}$$
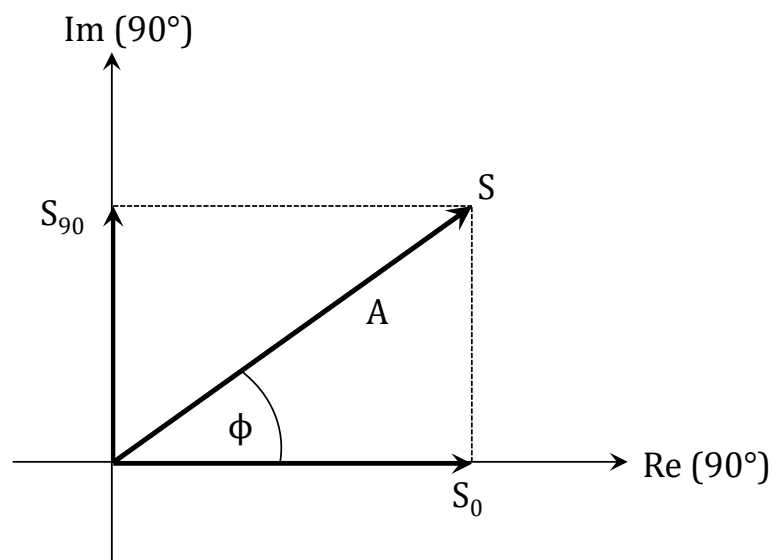


**Figure 7.5:** Visualization of the lock-in signals $S_0$ and $S_{90}$ in the complex plane where the amplitude $A$ and the phase $\phi$ can be calculated.

From equations 7.43 and 7.44 the amplitude $A$ and the phase $\phi$ result in:

$$A = \sqrt{S_0^2 + S_{90}^2} \tag{7.45}$$

$$\phi = \arctan\left(\frac{S_{90}}{S_0}\right) \tag{7.46}$$

## 7.2 Design and realization of *TIMAwave* test stand

For the realization of the *TIMAwave* test stand the following components are needed:

- Sample holder with steady state heater
- Modulated heat source
- Infrared camera to measure the surface temperature field of the sample over time
- Electronics for controlling the modulated and steady-state heaters
- Lock-in processing for the calculation of the amplitude and the phase information.

The sample holder has been designed with integrated induction heater to allow characterization at different temperatures between room temperature and 300°C. For the modulated heating a laser diode with 1.6 W optical outpot power has been selected. In contrast to contact heater, the laser does not have a thermal mass and can be modulated laser with high frequency. The heatable sample holder as stand-alone module and the laser diode can be integrated into the steady state test stand *LaTIMA* (see section 6).
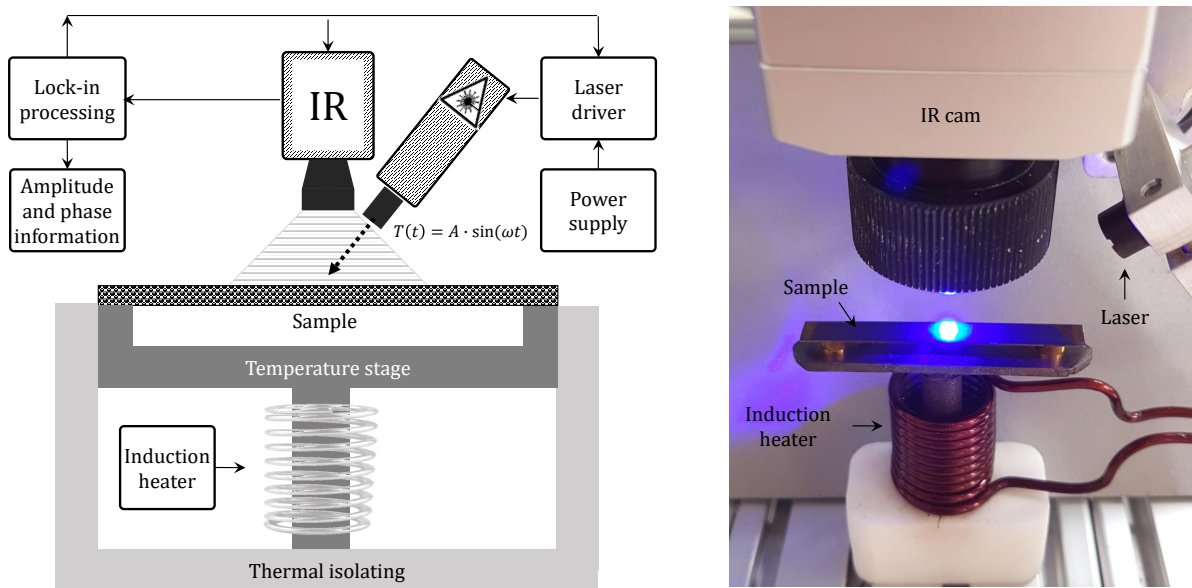


**Figure 7.6:** Left: schematic of *TIMAwave* test stand; Right: picture of the set up

Figure 7.6 shows the schematic of the *TIMAwave* setup. Both ends of the semi-infinite sample are placed on the heatable sample holder. Using the laser diode, the sample can be heated in the center by modulated power, which is controlled by lock-in process.
An IR camera which has also been connected to the lock-in process provided thermal images of the samples surface. Finally, the amplitude and the phase information of the 1D damped thermal waves from the center of the sample to both ends have been determined, whereof the thermal diffusivity of the sample has been calculated.

## 7.3 Thermal characterization by *TIMAwave*

### 7.3.1 Interaction between sample dimensions and measurement parameters for *TIMAwave* test stand

To fulfill the requirements of the one-dimensional thermal wave model, the thermal diffusion length $\mu$, which can be controlled by the modulation frequency $\omega$ and is given by:

$$\mu = \sqrt{\frac{2\alpha}{\omega}}$$

should comply with the boundary conditions related to the sample dimensions, length $l$, width $w$ and thickness $d$.

- Sample length $l$: To fulfill the requirements that the temperature oscillation $T(x)$ will be damped within the sample, the thermal diffusion length $\mu$ must be much shorter than the sample length $l$.

$$\mu << l$$

   If this is not the case, the thermal wave will reflect at the sample end. This can break the linear behavior of the phase and logarithmic amplitude along the sample and distorts the measurement results.

- Sample width $w$: The width of the sample must be less or equal to the thermal diffusion length $\mu$ to ensure the one-dimensional wave propagation

$$\mu > w$$

- Sample thickness $d$: The temperature gradient and associated heat flux over the sample thickness is negligible for thermally thin samples. A sample is considered thermally thin if its thickness is much shorter than the thermal diffusion length $\mu$ [133]

$$\mu >> d$$

The three requirements above can be consolidated to a recommendation of sample dimension relations of $10 : 1 : 0.5$ $(l : w : d)$.

### 7.3.2 Thermal diffusivity measurement by *TIMAwave*

To verify the functionality of the *TIMAwave* test stand, the thermal diffusivity of several materials has been measured. The thermal diffusivity $\alpha$ is calculated according to the

theory described above from the geometric mean of the wave number of the amplitude $k_{amp}$ and of the phase $k_{pha}$.

The selected test samples are strips of bulk materials from different material classes (metals, ceramics and semiconductors) with a wide range of thermal diffusivity. The samples are listed in table 7.1. For each of these samples, the suitable measurement frequency has been chosen based on the sample geometry and expected diffusivity.

**Table 7.1:** Selected samples for benchmark measurement with the test stand *TIMAwave*

| Material | Material class | Thickness [µm] |
|---|---|---|
| Aluminium (Al 99.5) | Metal | 500 |
| Copper bulk (Cu) | Metal | 300 |
| Copper film (Cu-HCP) | Metal | 35 |
| Silver (Ag 99.9) | Metal | 150 |
| Brass (CuZn 37) | Metal alloy | 300 |
| Silicon (Si) | Semiconductor | 300 |
| Doped silicon (D-Si)* | Semiconductor | 230 |
| Aluminium-nitride (AlN) | Ceramics | 1000 |
| Aluminium-oxide (Al$_2$O$_3$) | Ceramics | 670 |
| Silicon-nitride (Si$_4$N$_3$) | Ceramics | 320 |

\* Orientation: 100 / Dopant: phosphor / Resistivity: $\approx 5\,\Omega\cdot\text{cm}$

As shown in figure 7.7, plotting a line scan of amplitude and phase images over the sample length results in wave number $k$.
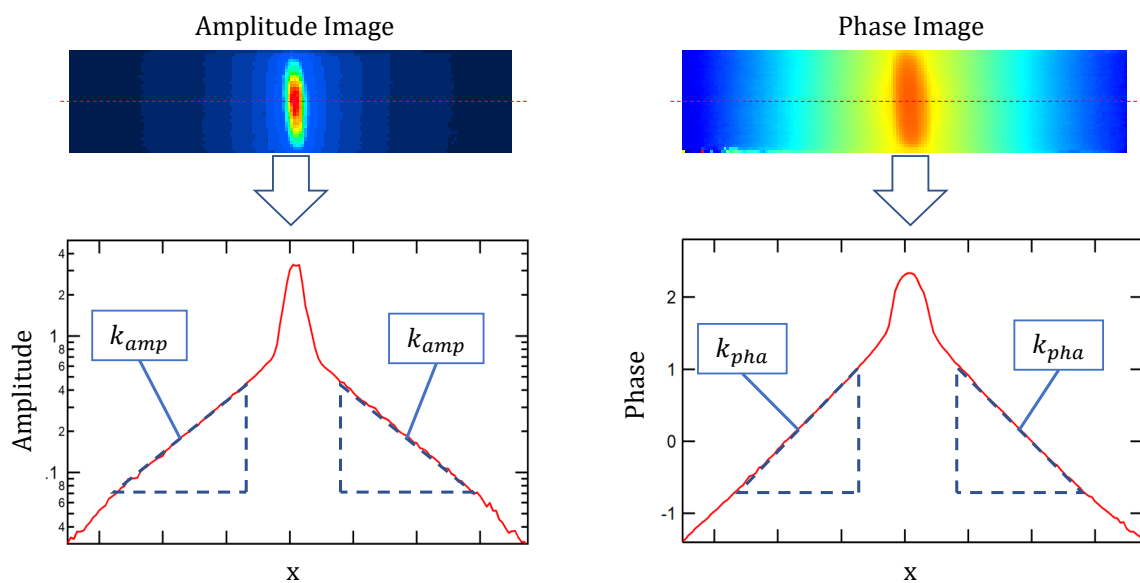


**Figure 7.7:** Top view of the sample showing amplitude and phase images. The phase and the natural logarithm of the amplitude behave linearly to the sample length

The slopes of both curves (left and right of the laser spot) are identical. However, as expected, there is a slight variation between the slopes of the amplitude and phase due to the heat losses by convection and radiation.

The results of the thermal diffusivity are shown in table 7.2. It can be seen, that the thermal diffusivity calculated from the amplitude $\alpha_A$ is lower than that calculated from the phase $\alpha_P$. This result confirms the theory described in section 7.1.1.

**Table 7.2:** Results of thermal diffusivity measurement of several materials from different classes. $\alpha_A$: thermal diffusivity calculated from the amplitude. $\alpha_P$: thermal diffusivity calculated from the phase. $\alpha$: thermal diffusivity calculated from the geometric mean of amplitude and phase.

| Material | $\alpha_A \left[\text{mm}^2/\text{s}\right]$ | $\alpha_P \left[\text{mm}^2/\text{s}\right]$ | $\alpha \left[\text{mm}^2/\text{s}\right]$ | $\alpha_{lit} \left[\text{mm}^2/\text{s}\right]$ |
|---|---|---|---|---|
| Aluminium-oxide ($Al_2O_3$) | $6.6 \pm 0.7$ | $6.7 \pm 0.7$ | $6.7 \pm 1.1$ | $8.5 \pm 1.5$ |
| Brass (CuZn 37) | $25.2 \pm 1.2$ | $29.2 \pm 1.9$ | $27.1 \pm 2.5$ | $31 \pm 8$[*] |
| Silicon-nitride ($Si_4N_3$) | $26.5 \pm 3.1$ | $35.7 \pm 1.6$ | $30.7 \pm 5.1$ | $29 \pm 4$ |
| Doped silicon (D-Si) | $39.3 \pm 1.5$ | $41.8 \pm 2.0$ | $40.6 \pm 3.0$ | $40 \pm 10$[**] |
| Aluminium-nitride (AlN) | $67.9 \pm 0.8$ | $73.6 \pm 5.4$ | $70.7 \pm 4.8$ | $75 \pm 10$ |
| Aluminium (Al 99.5) | $83.9 \pm 7.5$ | $91.3 \pm 8.3$ | $87.5 \pm 8.7$ | $88 \pm 2$ |
| Silicon (Si) | $84.6 \pm 2.0$ | $90.0 \pm 2.0$ | $87.2 \pm 3.4$ | $80 \pm 4$ |
| Copper film (Cu-HCP) | $88.4 \pm 2.5$ | $104 \pm 7.9$ | $96.0 \pm 11$ | NA |
| Copper bulk (Cu) | $105 \pm 3.2$ | $115 \pm 2.1$ | $110 \pm 5.5$ | $112 \pm 5$ |
| Silver (Ag 99.9) | $161 \pm 6.9$ | $173 \pm 7.1$ | $167 \pm 10$ | $165 \pm 5$ |

[*] Large dispersion in literature references due to the degree of alloying
[**] Large dispersion in literature references due to the degree of doping

The correct values for thermal diffusivity $\alpha$ can be calculated from the geometrical mean of $\alpha_A$ and $\alpha_P$.

$$\alpha = \sqrt{\alpha_A \cdot \alpha_P}$$

Figure 7.8 shows the results of thermal diffusivity of the samples measured at room temperature.

The thermal diffusivity of the samples has also been measured at different temperatures. The semiconductors show the strongest temperature dependency of thermal diffusivity. The thermal diffusivity of pure silicon shows a remarkable drop from $89\,\text{mm}^2/\text{s}$ at $30°C$ to $39\,\text{mm}^2/\text{s}$ at $200°C$. Also the thermal diffusivity of doped silicon declines from $40\,\text{mm}^2/\text{s}$ at $30°C$ to $22\,\text{mm}^2/\text{s}$ at $200°C$ (see figure 7.9).

In contrast to semiconductors, thermal diffusivity of metals shows a smaller dependency on the temperature. This was expected since the thermal conductivity on semiconductors is primarily due to the transmission of lattice vibrations at these temperatures while it
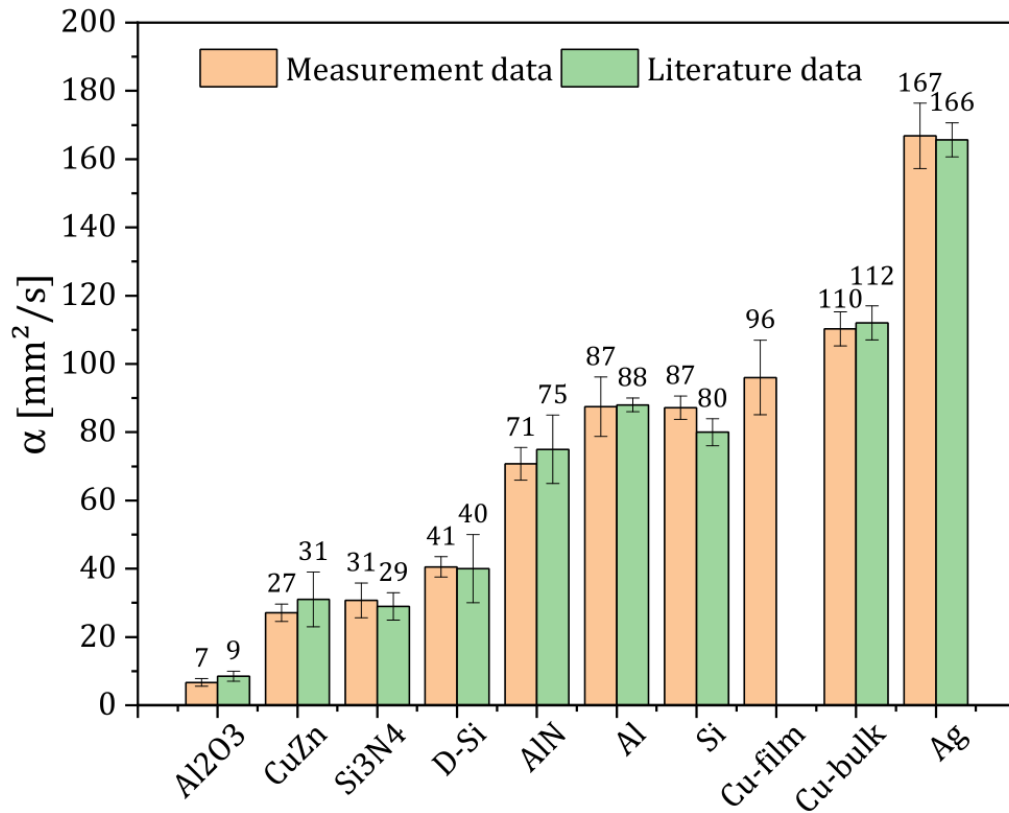
**Figure 7.8:** Results of thermal diffusivity of different samples measured by *TIMAwave* test stand

is mostly due to electrons in metal. The limiting factor of the thermal conductivity of semiconductors is therefore phonon-phonon scattering, which is strongly dependent on the temperature [137].
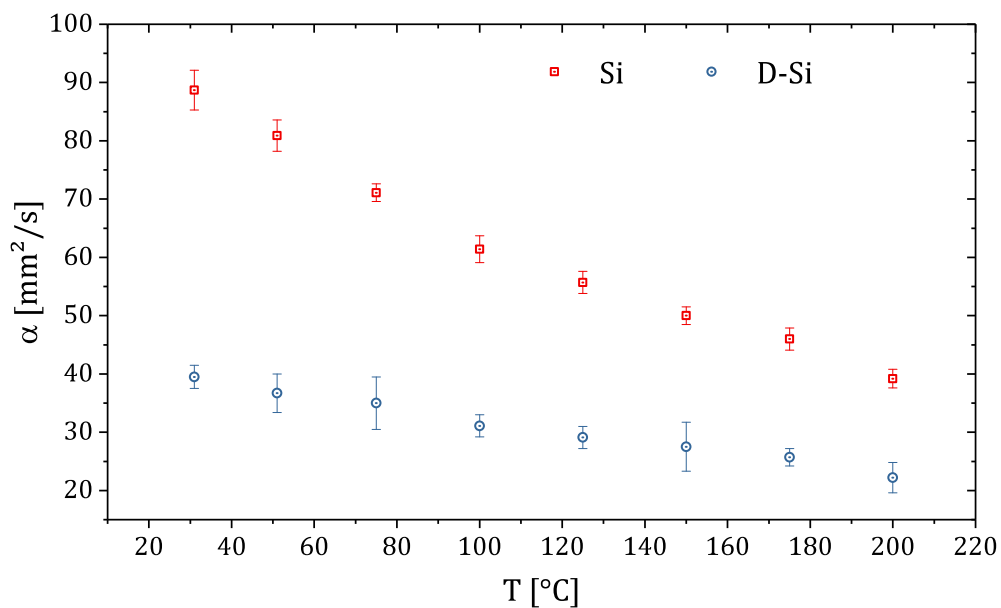


**Figure 7.9:** Thermal diffusivity of pure silicon and doped silicon as function of temperature

## 7.4 Conclusion

In this chapter, the test stand *TIMAwave* for thermal diffusivity measurement of bulk samples based on Ångström's method has been presented. At first, the theoretical background and the derivation of thermal diffusivity from the equation of a one-dimensional damped thermal wave have been discussed. Further, the influence of heat losses by convection and radiation on the measurement accuracy have been discussed. It has been shown how to overcome these influences.

As the method is based on IR thermography, from which amplitude and phase information can be extracted by lock-in processing, the lock-in principle has been briefly introduced.

Finally, the test stand with respect to the instructions of the methodology has been designed and realized. To demonstrate the functionality and accuracy of the test stand, thermal diffusivity of several samples from different material classes has been measured. In addition, the thermal diffusivity of two silicon types (low and highly doped) have been measured at different temperatures between 25°C and 200°C.

# Chapter 8

# Conclusions and outlook

This work dealt with development of innovative techniques for thermal characterization of almost all materials used in electronic packages. Based on analysis of thermal materials and thermal management techniques, two steady-state and two transient measurement techniques and corresponding test stands have been developed and realized within this work, which, in their entirety, enable the characterization of almost all package materials under desired boundary conditions. In addition to the development, realization and verification of these measurement systems, a number of material science questions were investigated, which become possible because of the improved measurement techniques. In the following the main results are summarized.

The first realized test system (named *TIMA*) is a steady-state test stand, which was developed primarily for the characterization of thermal interface materials. The test stand has been designed as modular platform, which enables integration of different measurement modules for characterization under different boundary conditions such as contact surface finish, temperature, pressure or long term stability.
To increase the measurement accuracy and resolution of the test stand, the error criteria have been identified by systematic studying of accuracy and limitation of the test stand. It turned out from the error calculation that over 80% of the measurement error is caused by the error of the temperature measurement. It could be shown that the smallest measurable thermal resistance with a measuring accuracy of 10% is $10\,\mathrm{mm^2 \cdot K/W}$. However, this limit could be exceeded by an innovative approach. Through the reduction of the ratio of cross section area of sample and contact medium to 1/10, the measurement range of steady state technique can be extended to measure thermal resistance down to $1\,\mathrm{mm^2 \cdot K/W}$, which is around 10 times lower than the thermal resistance measured by commercial equipment for the same measurement accuracy.

To demonstrate the functionality and the capability of the developed test stand, several

properties of different classes of materials have been characterized and discussed. In the following some results are listed:

- Effective thermal conductivity of filled thermal grease increases at BLT below three times of the particle size. This phenomenon is a size effect and can be explained in such a way that the particles have better contact to surfaces and to each other. Furthermore, the number of internal interfaces is smaller, which leads to an additional improvement of the thermal path. This effect does not occur in the case of unfilled greases, which was confirmed by measuring unfilled dicyandiamide. This study will help material manufacturers and users to select the appropriate size of filler particles for a specific application.

- Bulk thermal conductivity increases with increasing volume fraction of particles, however it showed a non-linear dependency. It could be shown in an example that increasing particle volume fraction from 45 vol% to 50 vol% resulted in only 25% increasing the thermal conductivity, while increasing the particle volume fraction from 40 vol% to 45 vol% led to 120% higher thermal conductivity. This investigation has shown that there is a threshold for the particle volume fraction above which there is no major improvement in the thermal property.

- Bulk thermal conductivity of a filled adhesive is temperature dependent, the higher the temperature the lower is the thermal conductivity. Bulk thermal conductivity of the measured sample at 80°C is around 20% lower than the value measured at 40°C.

- Liquid metal can eliminate the thermal interface resistance and allows measuring bulk thermal conductivity of solid samples by the *TIMA* test stand, even if the material is available in only one thickness. This has been demonstrated by characterization of FR4, LTCC and $Al_2O_3$ substrates.

- It has been shown that the test stand *TIMA* is able to measure thermal conductivity of a single via in a substrate. Thermal conductivity of $\lambda_{via} = (295 \pm 10)$ W/(m·K) for 300 µm sintered Ag via in 400 µm LTCC substrate has been measured, which is in the expected range. Such investigations are novel and have never been successfully performed with a steady-state technique before.

- The heat transfer coefficient between aluminium plate and aluminium sheet as function of the pressure and surface roughness has been measured by the *TIMA* test stand.

The second test stand developed and realized within this work has been named *Trans-TIMA*, as it can be used for characterization of TIM layers by means of a transient

technique. The main idea of the test stand lies in using a thermal test vehicle (developed and realized within this work) as fully controllable active device for both heating and temperature measurement. A simple test setup consisting of heat sink and thermal test vehicle has been realized for measurement of thermal interface materials. To benchmark the test stand, the thermal impedance of the test setup with a commercial grease at three different bond line thicknesses (BLT) has been measured. The bulk thermal conductivity of the grease measured by *TransTIMA* fits very well to that measured with the steady-state test stand *TIMA*.

The *TransTIMA* approach has been successfully used for the characterization of vertically-aligned carbon nanotube (VACNT) TIM within a package under real assembly conditions, which was never done before. The tested package has normally a MMIC chip. Due to the fact, that MMIC chip cannot be used as active device for thermal transient characterization, the MMIC chip has been replaced by the Thermal Test Chip. The thermal impedance of the package with VACNT as TIM has been measured and compared with similar packages used different adhesives as TIM. It has been shown that the prototypic VACNT TIM could outperform a common adhesive in terms of thermal impedance and nearly reaches the thermal performance of a silver-filled thermally enhanced conductive adhesive.

The investigations have shown that the thermal conductivity of VACNT still has great potential for improvement. The thermal conductivity is still at least two orders of magnitude below the thermal conductivity of CNT. This is mainly due to the interface between CNT and heat sink as well as due to the non-uniformity of the CNT length. This knowledge confirms that such materials should only be investigated in the package. The approach developed within this work makes this possible.

A third test stand (*LaTIMA*) has been developed and realized within this work for the characterization of highly thermal conductive materials such as pure metals, metals alloys, ceramic substrate, die attach materials etc. Such materials cannot be measured with the steady-state test stand *TIMA* due to the low temperature gradient at the sample. To get around this, the *LaTIMA* test stand was designed to allow heat flows in-plane the sample instead of cross-plane to have a higher temperature gradient. For this the specimens should be in a strip bar shape, which is easy to realize with metals, metal alloys and substrates.

The design of the test stand has been supported by FE-simulation in order to recognize and minimize parasitic effects, which is essential for this type of setups. The test stand

has been benchmarked with materials with well-known thermal conductivity, the results fit very well with the literature values of these materials.

The most important characterization performed by this test stand was a systematic study of sintered silver to investigate the correlation between process, structure and property of sintered silver. 27 variations of sintered silver samples have been prepared under different sintering conditions. Sintering temperature was varied between 200°C and 270°C and the sintering pressure between 5 MPa and 25 MPa. Thermal and electrical conductivities of these samples were measured. The obtained results for thermal conductivity are between $65 \, \mathrm{W/(m \cdot K)}$ and $190 \, \mathrm{W/(m \cdot K)}$ and between $5 \, \mathrm{MS/m}$ and $25 \, \mathrm{MS/m}$ for electrical conductivity. Finally, the microstructure of the sintered silver samples has been analyzed by FIB and SEM. The results showed a clear correlation between the sintering process, the porosity of the structures and the thermal and electrical conductivities.
From the results of thermal and electrical conductivities, the Lorenz number has been calculated according to the Wiedemann-Franz law, and it has been found out, that the Wiedemann-Franz law is also valid for sintered silver and not only for bulk metals. The determined Lorenz number for almost all sintered samples lay in the range of expected theoretical values for bulk metals.

Material manufacturers, users and scientists alike benefit from this type of characterization, which the *LaTIMA* test stand makes possible. With minor effort in sample preparation and without the use of complicated measurement techniques, the process property correlation of new sintered materials or new metal alloys can be studied with high accuracy ($< 5\%$).

Another test stand was developed and realized within the scope of this work by extending the hardware of the test stand *LaTIMA*. The test stand, which is based on Ångström's method, measures the thermal diffusivity of the same samples whose thermal conductivity is determined with *LaTIMA* test stand. Through this innovative application, the thermal diffusivity and thermal conductivity of the same sample can be determined simultaneously in the same hardware, from which the volumetric heat capacity of the samples can be determined.

It has been shown how the heat losses by convection and radiation can be eliminated to increase the measurement accuracy. Thermal diffusivity of several materials (pure metals, metals alloys, substrate and semiconductors) have been measured as function of the temperature to demonstrate the functionality and accuracy of the test stand.

In summary, it can be said that the thermal characterization of materials with regard to the thermal management of miniaturized and high-performance micro-systems requires thermal measurement techniques that take into account the specifics of the materials and their application conditions in an adequate way.

With the four measurement methods and the corresponding test stands developed, realized and exemplarily applied within this thesis, a substantial contribution was made. These test stands, in their entirety, allow determination of thermal material data of almost all relevant materials in electronic packages in a fast, easy and accurate way.

Numerous practice-relevant examples have shown that quite different special but decisive effects can be investigated, which is not the case with available standard methods.

A certain completion has been reached through this work in the field of steady-state and transient thermal characterization. This type of characterization methods will be used in science and industry for many years to come. Beside this, also non-contacting thermal-optical methods and especially laser-based methods (TDTR, FDTR etc.) will move more and more into the focus of research in future, as they open up many additional possibilities for material scientists.

# List of Figures

# List of Tables

# Bibliography

[1] M. Abo Ras, B. Wunderle, D. May, H. Oppermann, R. Schacht, and B. Michel, "Influences of technological processing and surface finishes on thermal behaviour of thermal interface materials," in *16th International Workshop on Thermal Investigations of ICs and Systems (THERMINIC)*, Oct. 2010. 1.1

[2] M. Rencz, "Testing Interface Thermal Resistance," in *Electronics Packaging Technology Conference, 2007. EPTC 2007. 9th*, pp. 272–277, Dec. 2007. 1.1

[3] R. Kempers, P. Kolodner, A. Lyons, and A. J. Robinson, "Development of a high-accuracy thermal interface material tester," in *2008 11th Intersociety Conference on Thermal and Thermomechanical Phenomena in Electronic Systems*, pp. 221–226, May 2008. 1.1

[4] B. Wunderle, J. Kleff, R. Mrossko, M. Abo Ras, D. May, R. Schacht, H. Oppermann, J. Keller, and B. Michel, "In-situ measurement of various thin bond-line-thickness thermal interface materials with correlation to structural features," in *14th International Workshop on Thermal Inveatigation of ICs and Systems (THERMINIC)*, pp. 112–117, IEEE, 2008. 1.1, 2.1.6, 4.1

[5] "ASTM D5470-01: Standard Test Method for Thermal Transmission Properties of Thin Thermally Conductive Solid Electrical Insulation Materials. ASTM International, 2001." 1.1, 1.2, 2.2.1, 4.1

[6] C. J. M. Lasance, C. T. Murray, D. L. Saums, and M. Rencz, "Challenges in thermal interface material testing," in *Twenty-Second Annual IEEE Semiconductor Thermal Measurement And Management Symposium*, pp. 42–49, Mar. 2006. 1.1

[7] Y. Ni, H. Han, S. Volz, and T. Dumitrica, "Nanoscale Azide Polymer Functionalization: A Robust Solution for Suppressing the Carbon Nanotube Polymer Matrix Thermal Interface Resistance," *The Journal of Physical Chemistry C*, vol. 119, pp. 12193–12198, June 2015. 1.2, 2.1.5

[8] B. A. Cola, J. Xu, and T. S. Fisher, "Contact mechanics and thermal conductance of carbon nanotube array interfaces," *International Journal of Heat and Mass Transfer*, vol. 52, no. 15, pp. 3490–3503, 2009. 1.2, 2.1.5

[9] "JEDEC standard JESD51-3: Low effective thermal conductivity test board for leaded surface mount packages." 1.2, 2.2.1

[10] "ASTM E1225 - 13 Standard Test Method for Thermal Conductivity of Solids Using the Guarded-Comparative-Longitudinal Heat Flow Technique." 1.2

[11] Parker, "Flash Method of Determining Thermal Diffusivity, Heat Capacity, and Thermal Conductivity," *Journal of Applied Physics*, vol. 32, pp. 1679–1684, Sept. 1961. 1.2, 2.2.2, 2.2.2

[12] W. Übler, *Erhöhung der thermischen Leitfähigkeit elektrisch isolierender Polymerwerkstoffe.* PhD Thesis, Universität Erlangen-Nürnberg, 2002. 1, 3.2.3

[13] T. Brunschwiler, G. Schlottig, S. Ni, Y. Liu, J. V. Goicochea, J. Zürcher, and H. Wolf, "Formulation of percolating thermal underfills using hierarchical self-assembly of microparticles and nanoparticles by centrifugal forces and capillary bridging," *Journal of Microelectronics and Electronic Packaging*, vol. 9, no. 4, pp. 149–159, 2012. 4

[14] G.-W. Lee, M. Park, J. Kim, J. I. Lee, and H. G. Yoon, "Enhanced thermal conductivity of polymer composites filled with hybrid filler," *Composites Part A: Applied Science and Manufacturing*, vol. 37, pp. 727–734, May 2006. 5

[15] G. Becker, C. Lee, and Zuchen Lin, "Thermal Conductivity in Advanced Chips," *Advanced Packaging*, vol. 14, pp. 14–16, July 2005. 2.1.1, 2.1.1, 2.1.4

[16] T. Braun, *Feuchtediffusion in partikelgefüllten Epoxidharzen für die Mikroelektronik.* Stuttgart: Fraunhofer Verlag, 2013. 2.5, 8

[17] C.-P. Chiu, B. Chandran, K. Mello, and K. Kelley, "An accelerated reliability test method to predict thermal grease pump-out in flip-chip applications," in *Electronic Components and Technology Conference, 2001. Proceedings., 51st*, pp. 91–97, 2001. 2.1.1, 4.5.3

[18] D. Blazej, "Thermal interface materials," *Electronics Cooling*, vol. 9, pp. 14–21, 2003. 2.1.1, 2.1.4

[19] R. Viswanath, V. Wakharkar, A. Watwe, V. Lebonheur, and others, "Thermal performance challenges from silicon to systems," 2000. 2.1.1, 4.5.3

[20] X. C. T. Ph.D, *Advanced Materials for Thermal Management of Electronic Packaging*. Springer Science & Business Media, Jan. 2011. 2.1.3, 3.1.2

[21] F. Sarvar, D. C. Whalley, and P. P. Conway, "Thermal interface materials-A review of the state of the art," in *Electronics Systemintegration Technology Conference, 2006. 1st*, vol. 2, pp. 1292–1302, IEEE, 2006. 2.1.4, 4.5.1.1

[22] C. G. Macris, T. R. Sanderson, R. G. Ebel, C. B. Leyerle, and E. Solutions, "Performance, reliability, and approaches using a low melt alloy as a thermal interface material," in *Proceedings IMAPS*, 2004. 2.1.4

[23] R. L. Webb and J. P. Gwinn, "Low melting point thermal interface material," in *ITherm 2002. Eighth Intersociety Conference on Thermal and Thermomechanical Phenomena in Electronic Systems (Cat. No.02CH37258)*, pp. 671–676, 2002. 2.1.4

[24] Y. Martin and T. Van Kessel, "High performance liquid metal thermal interface for large volume production," *IMAPS Thermal and Power Management, San Jose CA*, 2007. 2.1.4

[25] C. K. Roy, S. Bhavnani, M. C. Hamilton, R. W. Johnson, J. L. Nguyen, R. W. Knight, and D. K. Harris, "Investigation into the application of low melting temperature alloys as wet thermal interface materials," *International Journal of Heat and Mass Transfer*, vol. 85, pp. 996–1002, June 2015. 2.1.4

[26] C. K. Roy, S. Bhavnani, M. C. Hamilton, R. W. Johnson, R. W. Knight, and D. K. Harris, "Thermal performance of low melting temperature alloys at the interface between dissimilar materials," *Applied Thermal Engineering*, vol. 99, pp. 72–79, Apr. 2016. 2.1.4

[27] V. Goyal and A. A. Balandin, "Thermal properties of the hybrid graphene-metal nano-micro-composites: Applications in thermal interface materials," *Applied Physics Letters*, vol. 100, Feb. 2012. 2.1.5

[28] S. Berber, Y.-K. Kwon, and D. Tománek, "Unusually High Thermal Conductivity of Carbon Nanotubes," *Physical Review Letters*, vol. 84, pp. 4613–4616, May 2000. 2.1.5, 5.2

[29] T. Tong, Y. Zhao, L. Delzeit, A. Kashani, M. Meyyappan, and A. Majumdar, "Dense Vertically Aligned Multiwalled Carbon Nanotube Arrays as Thermal Interface Materials," *IEEE Transactions on Components and Packaging Technologies*, vol. 30, pp. 92–100, Mar. 2007. 2.1.5, 5.2

[30] H. Babaei, P. Keblinski, and J. M. Khodadadi, "Thermal conductivity enhancement of paraffins by increasing the alignment of molecules through adding CNT/graphene," *International Journal of Heat and Mass Transfer*, vol. 58, pp. 209–216, Mar. 2013. 2.1.5

[31] K. M. F. Shahil and A. A. Balandin, "Thermal properties of graphene and multilayer graphene: Applications in thermal interface materials," *Solid State Communications*, vol. 152, pp. 1331–1340, Aug. 2012. 2.1.5

[32] P. Bonnet, D. Sireude, B. Garnier, and O. Chauvet, "Thermal properties and percolation in carbon nanotube-polymer composites," *Applied Physics Letters*, vol. 91, Nov. 2007. 2.1.5

[33] F. H. Gojny, M. H. G. Wichmann, B. Fiedler, I. A. Kinloch, W. Bauhofer, A. H. Windle, and K. Schulte, "Evaluation and identification of electrical and thermal conduction mechanisms in carbon nanotube/epoxy composites," *Polymer*, vol. 47, pp. 2036–2045, Mar. 2006. 2.1.5

[34] J. G. Ok, J. Y. Lee, H. W. Baac, S. H. Tawfick, L. J. Guo, and A. J. Hart, "Rapid anisotropic photoconductive response of ZnO-coated aligned carbon nanotube sheets," *ACS applied materials & interfaces*, vol. 6, no. 2, pp. 874–881, 2013. 2.1.5

[35] R. D. Johnson, D. F. Bahr, C. D. Richards, R. F. Richards, D. McClain, J. Green, and J. Jiao, "Thermocompression bonding of vertically aligned carbon nanotube turfs to metalized substrates," *Nanotechnology*, vol. 20, no. 6, 2009. 2.1.5

[36] A. Hamdan, J. Cho, R. Johnson, J. Jiao, D. Bahr, R. Richards, and C. Richards, "Evaluation of a thermal interface material fabricated using thermocompression bonding of carbon nanotube turf," *Nanotechnology*, vol. 21, no. 1, 2010. 2.1.5

[37] J. Xu and T. S. Fisher, "Enhancement of thermal interface materials with carbon nanotube arrays," *International Journal of Heat and Mass Transfer*, vol. 49, pp. 1658–1666, May 2006. 2.1.5

[38] T. Tong, Y. Zhao, L. Delzeit, A. Kashani, M. Meyyappan, and A. Majumdar, "Dense Vertically Aligned Multiwalled Carbon Nanotube Arrays as Thermal Interface Materials," *IEEE Transactions on Components and Packaging Technologies*, vol. 30, pp. 92–100, Mar. 2007. 2.1.5

[39] L. Zhu, D. W. Hess, and C. P. Wong, "Assembling Carbon Nanotube Films as Thermal Interface Materials," in *2007 Proceedings 57th Electronic Components and Technology Conference*, May 2007. 2.1.5

[40] A. Zoran Miric and A. Grusd, "Lead free alloys," *Soldering & Surface Mount Technology*, vol. 10, pp. 19–25, Apr. 1998. 2.1.6

[41] J. King, "Materials handbook for hybrid microelectronics," *Artech House Inc, 685 Canton Street, Norwood, Massachusetts 02062, USA, 1988.*, 1988. 2.4

[42] J. Bilek, J. K. Atkinson, and W. A. Wakeham, "Thermal conductivity of molten lead-free solders," *International journal of thermophysics*, vol. 27, no. 1, pp. 92–102, 2006. 2.4

[43] M. Hutter, *Verbindungstechnik höchster Zuverlässigkeit für optoelektronische Komponenten.* Stuttgart: Fraunhofer Verlag, 2009. 2.11, 8

[44] A. Masson, W. Sabbah, R. Riva, C. Buttay, S. Azzopardi, H. Morel, D. Planson, and R. Meuret, "Die attach using silver sintering. Practical implementation and analysis," *European Journal of Electrical Engineering*, vol. 16, no. 3-4, pp. 293–305, 2013. 2.1.6

[45] J. G. Bai, Z. Z. Zhang, J. N. Calata, and G. Q. Lu, "Low-Temperature Sintered Nanoscale Silver as a Novel Semiconductor Device-Metallized Substrate Interconnect Material," *IEEE Transactions on Components and Packaging Technologies*, vol. 29, pp. 589–593, Sept. 2006. 2.1.6

[46] W. Schmitt and W. C. H. Gmbh, "Novel silver contact paste lead free solution for die attach," in *2010 6th International Conference on Integrated Power Electronics Systems*, Mar. 2010. 2.1.6

[47] C. Goebl and J. Faltenbacher, "Low temperature sinter technology die attachment for power electronic applications," in *2010 6th International Conference on Integrated Power Electronics Systems*, Mar. 2010. 2.1.6

[48] R. D. Cowan, "Pulse Method of Measuring Thermal Diffusivity at High Temperatures," *Journal of Applied Physics*, vol. 34, pp. 926–927, Apr. 1963. 2.2.2

[49] H. J. Lee, "THERMAL DIFFUSIVITY IN LAYERED AND DISPERSED COMPOSITES.," *MyScienceWork*, Jan. 1975. 2.2.2

[50] T.-Y. R. Lee, "THERMAL DIFFUSIVITY OF DISPERSED AND LAYERED COMPOSITES.," *MyScienceWork*, Jan. 1977. 2.2.2

[51] B. Carlberg, *Integration of Nanofibrous Materials in Microsystem Applications, Process Development and Characterization.* Doctoral thesis, Chalmers University of Technology, 2012. 2.2.2

[52] W. Lin and C. P. Wong, "Vertically aligned carbon nanotubes for thermal interface materials: Quality control, alignment improvement and laser flash measurement," in *2010 Proceedings 60th Electronic Components and Technology Conference (ECTC)*, pp. 967–972, June 2010. 2.2.2

[53] J. W. Sofia, "Fundamentals of Thermal Resistance Measurement," 1995. 2.2.3

[54] "JEDEC JESD 51-14 - Transient Dual Interface Test Method for the Measurement of the Thermal Resistance Junction to Case of Semiconductor Devices with Heat Flow Trough a Single Path | Engineering360." 2.2.3, 2.2.3, 2.2.3, 5.2.2

[55] Y. Luo, "Structure function based thermal resistance amp; thermal capacitance measurement for electronic system," in *2010 IEEE CPMT Symposium Japan*, Aug. 2010. 2.2.3

[56] V. Székely and T. Van Bien, "Fine structure of heat flow path in semiconductor devices: A measurement and identification method," *Solid-State Electronics*, vol. 31, pp. 1363–1368, Sept. 1988. 2.2.3

[57] M. K. L. Feuchter, *Investigations on Joule heating applications by multiphysical continuum simulations in nanoscale systems*, vol. 43. KIT Scientific Publishing, 2014. 2.2.4

[58] J.-Y. Duquesne, D. Fournier, and C. Frétigny, *Analytical solutions of the heat diffusion equation for 3-omega method geometry.* AIP, 2010. 2.2.4

[59] T. Yamane, N. Nagai, S.-i. Katayama, and M. Todoki, "Measurement of thermal conductivity of silicon dioxide thin films using a 3-omega method," *Journal of Applied Physics*, vol. 91, pp. 9772–9776, May 2002. 2.2.4

[60] C. E. Raudzis, F. Schatz, and D. Wharam, "Extending the 3-omega method for thin-film analysis to high frequencies," *Journal of Applied Physics*, vol. 93, pp. 6050–6055, May 2003. 2.2.4

[61] D. G. Cahill and R. O. Pohl, "Thermal conductivity of amorphous solids above the plateau," *Physical review B*, vol. 35, no. 8, p. 4067, 1987. 2.2.4, 2.2.4

[62] D. G. Cahill, "Thermal conductivity measurement from 30 to 750 K: the 3-omega method," *Review of scientific instruments*, vol. 61, no. 2, pp. 802–808, 1990. 2.2.4, 2.2.4

[63] D.-W. Oh, A. Jain, J. K. Eaton, K. E. Goodson, and J. S. Lee, "Thermal conductivity measurement and sedimentation detection of aluminum oxide nanofluids by

using the 3-Omega method," *International Journal of Heat and Fluid Flow*, vol. 29, no. 5, pp. 1456–1461, 2008. 2.2.4

[64] I. K. Moon, Y. H. Jeong, and S. I. Kwun, "The 3-Omega technique for measuring dynamic specific heat and thermal conductivity of a liquid or solid," *Review of scientific instruments*, vol. 67, no. 1, pp. 29–35, 1996. 2.2.4

[65] B. K. Park, N. Yi, J. Park, and D. Kim, "Note: Development of a microfabricated sensor to measure thermal conductivity of picoliter scale liquid samples," *Review of Scientific Instruments*, vol. 83, no. 10, 2012. 2.2.4

[66] S. D. Lubner, J. Choi, G. Wehmeyer, B. Waag, V. Mishra, H. Natesan, J. C. Bischof, and C. Dames, "Reusable bi-directional 3-Omega sensor to measure thermal conductivity of 100-um thick biological tissues," *Review of Scientific Instruments*, vol. 86, no. 1, 2015. 2.2.4

[67] S. R. Choi, J. Kim, and D. Kim, "3-Omega method to measure thermal properties of electrically conducting small-volume liquid," *Review of scientific instruments*, vol. 78, no. 8, 2007. 2.2.4

[68] M. L. Bauer and P. M. Norris, "General bidirectional thermal characterization via the 3-Omega technique," *Review of Scientific Instruments*, vol. 85, no. 6, 2014. 2.2.4

[69] S. Gauthier, A. Giani, and P. Combette, "Gas thermal conductivity measurement using the three-omega method," *Sensors and Actuators A: Physical*, vol. 195, pp. 50–55, 2013. 2.2.4

[70] H. Natesan, W. Hodges, J. Choi, S. Lubner, C. Dames, and J. Bischof, "A microthermal sensor for focal therapy applications," *Scientific reports*, vol. 6, 2016. 2.2.4

[71] B. Kyoo Park, N. Yi, J. Park, and D. Kim, "Thermal conductivity of single biological cells and relation with cell viability," *Applied Physics Letters*, vol. 102, no. 20, p. 203702, 2013. 2.2.4

[72] C. Grosse, M. Abo Ras, A. Varpula, K. Grigoras, D. May, B. Wunderle, P.-O. Chapuis, S. Gomès, and M. Prunnila, "Microfabricated sensor platform with through-glass vias for bidirectional 3-omega thermal characterization of solid and liquid samples," *Sensors and Actuators A: Physical*, vol. 278, pp. 33–42, Aug. 2018. 2.2.4

[73] F. Faghani, *Thermal conductivity measurement of PEDDOT:PSS by 3-omega technique.* PhD thesis, Linköpigs Universitet, Sweden, Oct. 2010. 2.2.5

[74] H. S. Carslaw and J. C. Jaeger, "Conduction of heat in solids," *Oxford: Clarendon Press, 1959, 2nd ed.*, 1959. 2.2.5, 7.1.1

[75] N. H. Abu-Hamdeh, A. I. Khdair, and R. C. Reeder, "A comparison of two methods used to evaluate thermal conductivity for some soils," *International Journal of Heat and Mass Transfer*, vol. 44, pp. 1073–1078, Mar. 2001. 2.2.5

[76] C. Festa and A. Rossi, "Apparatus for routine measurements of the thermal conductivity of ice cores," *Annals of Glaciology*, vol. 29, no. 1, pp. 151–154, 1999. 2.2.5

[77] Y. Nagasaka and A. Nagashima, "Absolute measurement of the thermal conductivity of electrically conducting liquids by the transient hot-wire method," *Journal of Physics E: Scientific Instruments*, vol. 14, no. 12, p. 1435, 1981. 2.2.5

[78] C. A. N. d. Castro, J. C. G. Calado, W. A. Wakeham, and M. Dix, "An apparatus to measure the thermal conductivity of liquids," *Journal of Physics E: Scientific Instruments*, vol. 9, no. 12, p. 1073, 1976. 2.2.5

[79] M. J. Assael, L. Karagiannidis, N. Malamataris, and W. A. Wakeham, "The Transient Hot-Wire Technique: A Numerical Approach," *International Journal of Thermophysics*, vol. 19, pp. 379–389, Mar. 1998. 2.2.5

[80] H. Xie, H. Lee, W. Youn, and M. Choi, "Nanofluids containing multiwalled carbon nanotubes and their enhanced thermal conductivities," *Journal of Applied Physics*, vol. 94, pp. 4967–4971, Sept. 2003. 2.2.5

[81] P. Krupa and S. Malinarič, "Using the Transient plane source method for measuring thermal parameters of electroceramics," *Int. J. Math., Comput., Statistical, Natural Phys. Eng*, vol. 8, pp. 733–738, 2014. 2.2.6

[82] D. Zhao, X. Qian, X. Gu, S. A. Jajja, and R. Yang, "Measurement techniques for thermal conductivity and interfacial thermal conductance of bulk and thin film materials," *Journal of Electronic Packaging*, vol. 138, no. 4, 2016. 2.2.6

[83] M. Gustavsson, E. Karawacki, and S. E. Gustafsson, "Thermal conductivity, thermal diffusivity, and specific heat of thin samples from transient measurements with hot disk sensors," *Review of Scientific Instruments*, vol. 65, pp. 3856–3859, Dec. 1994. 2.2.6

[84] Y. He, "Rapid thermal conductivity measurement with a hot disk sensor: Part 1. Theoretical considerations," *Thermochimica acta*, vol. 436, no. 1, pp. 122–129, 2005. 2.2.6

[85] W. M. Rohsenow, J. P. Hartnett, Y. I. Cho, and others, *Handbook of heat transfer*, vol. 3. McGraw-Hill New York, 1998. 3.1.1

[86] A. Jain and A. J. H. McGaughey, "Thermal transport by phonons and electrons in aluminum, silver, and gold from first principles," *Physical Review B*, vol. 93, Feb. 2016. 3.1.1, 3.2.1

[87] F. P. Incropera and F. P. Incropera, eds., *Fundamentals of heat and mass transfer*. Hoboken, NJ: John Wiley, 6th ed ed., 2007. OCLC: ocm62532755. 3.1.1, 3.1.3

[88] M. J. Latif, *Heat convection*. Second Edition, Berlin: Springer-Verlag, 2009. 3.1.2

[89] Tritt, Terry M, "Thermal conductivity : theory, properties, and applications." 3.2

[90] V. K. Goyal, *Thermal Characterization of Nanostructures and Advanced Engineered Materials*. PhD thesis, UC Riverside, 2011. 3.2, 3.2.2

[91] Kittel, C, *Introduction to solid state physics*. Fifth edition, Jan. 1976. 3.2.1, 3.2.1, 3.2.1

[92] Goran Grimvall, *The electron-phonon interaction in metals*. North Holland Publishing Company. 3.2.1

[93] P. B. Allen, "Theory of thermal relaxation of electrons in metals," *Physical Review Letters*, vol. 59, pp. 1460–1463, Sept. 1987. 3.2.1

[94] Z. Lin, L. V. Zhigilei, and V. Celli, "Electron-phonon coupling and electron heat capacity of metals under conditions of strong electron-phonon nonequilibrium," *Physical Review B*, vol. 77, Feb. 2008. 3.2.1

[95] L. Zhang, J.-T. Lü, J.-S. Wang, and B. Li, "Thermal transport across metal–insulator interface via electron–phonon interaction," *Journal of Physics: Condensed Matter*, vol. 25, no. 44, 2013. 3.2.1

[96] André Boden, *Copper graphite composite materials a novel way to engineer thermal conductivity and expansion*. PhD thesis, Freien Universität Berlin, Berlin, Sept. 2015. 3.2.1

[97] J. M. Ziman, *Electrons and Phonons: The Theory of Transport Phenomena in Solids (International Series of Monogrqaphs on Physics)*. Oxford at the Clarendon Press, first edition ed. 3.2.2

[98] C. Heinle, *Simulationsgestützte Entwicklung von Bauteilen aus wärmeleitenden Kunststoffen*. OCLC: 820421197. 3.2.3

[99] T. B. Lewis and L. E. Nielsen, "Dynamic mechanical properties of particulate-filled composites," *Journal of Applied Polymer Science*, vol. 14, no. 6, pp. 1449–1471, 1970. 3.2.3

[100] L. E. Nielsen, "Thermal conductivity of particulate-filled polymers," *Journal of applied polymer science*, vol. 17, no. 12, pp. 3819–3820, 1973. 3.2.3

[101] R. C. Progelhof, J. L. Throne, and R. R. Ruetsch, "Methods for predicting the thermal conductivity of composite systems: A review," *Polymer Engineering & Science*, vol. 16, no. 9, pp. 615–625, 1976. 3.2.3

[102] J. C. H. Affdl and J. L. Kardos, "The Halpin-Tsai equations: A review," *Polymer Engineering and Science*, vol. 16, pp. 344–352, May 1976. 3.2.3

[103] S. C. Cheng and R. I. Vachon, "The prediction of the thermal conductivity of two and three phase solid heterogeneous mixtures," *International Journal of Heat and Mass Transfer*, vol. 12, pp. 249–264, Mar. 1969. 3.2.3

[104] H. Hiroshi and T. Minoru, "Equivalent inclusion method for steady state heat conduction in composites," *International Journal of Engineering Science*, vol. 24, pp. 1159–1172, Jan. 1986. 3.2.3

[105] D. W. Sundstrom and Y.-D. Lee, "Thermal conductivity of polymers filled with particulate solids," *Journal of Applied Polymer Science*, vol. 16, no. 12, pp. 3159–3167, 1972. 3.2.3

[106] B. N. J. Persson, A. I. Volokitin, and H. Ueba, "Phononic heat transfer across an interface: thermal boundary resistance," *Journal of Physics: Condensed Matter*, vol. 23, no. 4, 2011. 4.1

[107] R. J. Linderman, T. Brunschwiler, U. Kloter, H. Toy, and B. Michel, "Hierarchical nested surface channels for reduced particle stacking and low-resistance thermal interfaces," in *Semiconductor Thermal Measurement and Management Symposium, 2007. SEMI-THERM 2007. Twenty Third Annual IEEE*, pp. 87–94, IEEE, 2007. 4.1

[108] R. Schacht, D. May, B. Wunderle, O. Wittler, A. Gollhardt, B. Michel, and H. Reichl, "Characterization of thermal interface materials to support thermal simulation," *arXiv preprint arXiv:0709.1849*, 2007. 4.1

[109] B. Wunderle, M. Abo Ras, M. Klein, R. Mrossko, G. Engelmann, D. May, O. Wittler, R. Schacht, L. Dietrich, H. Oppermann, and B. Michel, "Progress in thermal characterisation methods and thermal interface technology within the Nanopack

project," in *15th International Workshop on Thermal Investigations of ICs and Systems (THERMINIC)*, pp. 224–232, Oct. 2009. 4.1

[110] M. Abo Ras, D. May, R. Schacht, T. Winkler, S. Rzepka, B. Michel, and B. Wunderle, "Limitations and accuracy of steady state technique for thermal characterization of thermal interface materials and substrates," in *IEEE Intersociety Conference on Thermal and Thermomechanical Phenomena in Electronic Systems (ITherm)*, pp. 1285–1293, May 2014. 4.3.2

[111] M. Rencz, "The increasing importance of thermal test dies," *Electronics Cooling*, vol. 6, pp. 34–43, 2000. 4.4

[112] R. Young, C. Bailey, P. Cooper, M. Harrington, T. Starke, C. Stirling, N. Stockham, and C. Beck, "Developments and Trends in Thermal Management Technology - A Mission to the USA," *DTI Global Watch Missions, USA*, 2006. 4.4

[113] A. Claassen and H. Shaukatullah, "Comparison of diodes and resistors for measuring chip temperature during thermal characterization of electronic packages using thermal test chips," in *Thirteenth Annual IEEE Semiconductor Thermal Measurement and Management Symposium, 1997. SEMI-THERM XIII*, pp. 198–209, Jan. 1997. 4.4

[114] M. Abo Ras, G. Engelmann, D. May, M. Rothermund, R. Schacht, B. Wunderle, H. Oppermann, T. Winkler, S. Rzepka, and B. Michel, "Development and fabrication of a thin film thermo test chip and its integration into a test system for thermal interface characterization," in *19th International Workshop on Thermal Investigations of ICs and Systems (THERMINIC)*, pp. 67–72, Sept. 2013. 4.4.1, 4.4.2, 4.4.2

[115] D. May, B. Wunderle, R. Schacht, and B. Michel, "Transient thermal response as failure analytical tool-A comparison of different techniques," in *2013 14th International Conference on Thermal, Mechanical and Multi-Physics Simulation and Experiments in Microelectronics and Microsystems (EuroSimE)*, 2013. 4.4.3

[116] I. Sauciuc, R. Yamamoto, J. Culic-Viskota, T. Yoshikawa, S. Jain, M. Yajima, N. Labanok, and C. Amoah-Kusi, "Carbon based Thermal Interface Material for high performance cooling applications," in *2014 IEEE Intersociety Conference on Thermal and Thermomechanical Phenomena in Electronic Systems (ITherm)*, pp. 426–434, May 2014. 4.20, 4.5.1.1, 8

[117] Q. Mu, S. Feng, and G. Diao, "Thermal conductivity of silicone rubber filled with ZnO," *Polymer Composites*, vol. 28, pp. 125–130, Apr. 2007. 4.5.1.1

[118] H. Kristiansen, K. Redford, S. Helland, E. Kalland, N. H. H(/)glund, M. Abo Ras, C. Grosse, B. Hay, L. Ramiandrisoa, G. Davée, S. Gomès, and S. R. Pettersen, "Thermal conduction in novel isotropic conductive adhesive," in *2017 23rd International Workshop on Thermal Investigations of ICs and Systems (THERMINIC)*, Sept. 2017. 4.5.1.2

[119] "ASTM E1461-07, Standard Test Method for Thermal Diffusivity by the Flash Method, ASTM International, West Conshohocken, PA, 2007, www.astm.org." 4.5.2

[120] F. Steinhäußer, G. Sandulache, W. Fahrner, W. Hansal, A. Bittner, and U. Schmid, "Thermal Conductivity Measurements with Galvanic Metallization Lines on Porosified LTCC Applying the 3-Omega Technique," *Procedia Engineering*, vol. 87, pp. 104–107, Jan. 2014. 4.7

[121] K. Azar and J. E. Graebner, "Experimental determination of thermal conductivity of printed wiring boards," in *Twelfth Annual IEEE Semiconductor Thermal Measurement and Management Symposium. Proceedings*, pp. 169–182, Mar. 1996. 4.7

[122] F. Sarvar, N. J. Poole, and P. A. Witting, "PCB glass-fibre laminates: Thermal conductivity measurements and their effect on simulation," *Journal of Electronic Materials*, vol. 19, pp. 1345–1350, Dec. 1990. 4.7

[123] J. F. Shackelford, Y.-H. Han, S. Kim, and S.-H. Kwon, *CRC materials science and engineering handbook*. New York: Kluwer Academic / Plenum Publishers, New York 233 Spring Street, New York, New York 10013, 2004. 4.7

[124] B. Wunderle, D. May, J. Heilmann, J. Arnold, J. Hirscheider, Y. Li, J. Bauer, R. Schacht, and M. Abo Ras, "Accelerated Pump Out Testing for Thermal Greases," in *2019 20th International Conference on Thermal, Mechanical and Multi-Physics Simulation and Experiments in Microelectronics and Microsystems (EuroSimE)*, IEEE, 2019. 4.5.3

[125] A. Gowda, D. Esler, K. Nagarkar, and S. Tonapi, "reliability testing of thermal greases," *Electronics Cooling*, vol. 13, no. 4, p. 10, 2007. 4.5.3

[126] J. Due and A. J. Robinson, "Reliability of thermal interface materials: A review," *Applied Thermal Engineering*, vol. 50, pp. 455–463, Jan. 2013. 4.5.3

[127] M. Abo Ras, T. von Essen, J. Fortel, P. Panchal, L. Divay, A. Borta-Boyon, D. May, C. C. Darmawan, M. K. Samani, B. Wunderle, and A. Ziaei, "Design and realization of characterization demonstrator to investigate thermal performance of

vertically-aligned carbon nanotubes TIM for avionics and aerospace applications," in *2017 23rd International Workshop on Thermal Investigations of ICs and Systems (THERMINIC)*, Sept. 2017. 5.2

[128] Y. Ni, H. Le Khanh, Y. Chalopin, J. Bai, P. Lebarny, L. Divay, and S. Volz, "Highly efficient thermal glue for carbon nanotubes based on azide polymers," *Applied Physics Letters*, vol. 100, no. 19, 2012. 5.2.1

[129] E. Leveugle, L. Divay, H. L. Khanh, J. Daon, E. Chastaing, P. L. Barny, and A. Ziaei, "Free standing thermal interface material based on vertical arrays composites," in *19th International Workshop on Thermal Investigations of ICs and Systems (THERMINIC)*, pp. 244–247, Sept. 2013. 5.2.1

[130] G. S. Kumar, G. Prasad, and R. O. Pohl, "Experimental determinations of the Lorenz number," *Journal of materials science*, vol. 28, no. 16, pp. 4261–4272, 1993. 6.5.1, 6.5.1

[131] A. A. Wereszczak, D. J. Vuono, H. Wang, M. K. Ferber, and Z. Liang, "Properties of bulk sintered silver as a function of porosity," tech. rep., Oak Ridge National Laboratory (ORNL), 2012. 6.5.2

[132] A. J. Angström, "New method of determining the thermal conductibility of bodies," *The London, Edinburgh, and Dublin Philosophical Magazine and Journal of Science*, vol. 25, no. 166, pp. 130–142, 1863. 7.1

[133] A. Wolf, P. Pohl, and R. Brendel, "Thermophysical analysis of thin films by lock-in thermography," *Journal of Applied Physics*, vol. 96, pp. 6306–6312, Nov. 2004. 7.1.1, 7.3.1

[134] A. Muscio, P. G. Bison, S. Marinetti, and E. Grinzato, "Thermal diffusivity measurement in slabs using harmonic and one-dimensional propagation of thermal waves," *International Journal of Thermal Sciences*, vol. 43, pp. 453–463, May 2004. 7.1.1

[135] O. Breitenstein and M. Langenkamp, *Lock-in thermography: basics and use for functional diagnostics of electronic components*, vol. 10. Springer Science & Business Media, 2003. 7.1.2

[136] D. May, "Transiente Methoden der Infrarot-Thermografie zur zerstörungsfreien Fehleranalytik in der mikroelektronischen Aufbau- und Verbindungstechnik," Jan. 2015. 7.1.2

[137] H. R. Shanks, P. D. Maycock, P. H. Sidles, and G. C. Danielson, "Thermal Conductivity of Silicon from 300 to 1400k," *Physical Review*, vol. 130, pp. 1743–1748, June 1963. 7.3.2

# Versicherung

Hiermit versichere ich, dass ich die vorliegende Arbeit ohne unzulässige Hilfe Dritter und ohne Benutzung anderer als der angegebenen Hilfsmittel angefertigt habe; die aus fremden Quellen direkt oder indirekt übernommenen Gedanken sind als solche kenntlich gemacht. Bei der Auswahl und Auswertung des Materials sowie bei der Herstellung des Manuskripts habe ich keine Unterstützungsleistungen erhalten.

Die Hilfe eines Promotionsberaters habe ich nicht in Anspruch genommen. Weitere Personen haben von mir keine geldwerten Leistungen für Arbeiten erhalten, die im Zusammenhang mit dem Inhalt der vorgelegten Dissertation stehen.

Die Arbeit wurde bisher weder im Inland noch im Ausland in gleicher oder ähnlicher Form einer anderen Prüfungsbehörde vorgelegt.

## *Assurance*

*Herewith I assure that I have made the present work without inadmissible assistance third and without use of other than the indicated sources; the thoughts taken over directly or indirectly from strange sources are marked as such.*

*I did not receive any support in the selection and evaluation of the material or in the production of the manuscript.*

*I did not use the help of a promotion consultant. Other persons have not received any monetary benefits from me for work in connection with the content of the dissertation submitted.*

*The dissertation in the same or similar has either been submitted in Germany nor abroad to another examining authority*

Berlin, den 20.08.2019 Unterschrifft: . . . . . . . . . . . . . . . . . . . . . . . . . . . . . . .

# Theses

1. Thermal management becomes increasingly important in electronic industries due to miniaturization and rising of power dissipation.

2. Around 80% of the total thermal resistance of a standard electronic package mounted onto a heat sink is attributed to thermal interface materials.

3. The thermal interface resistance of two media with surface roughness of 2 µm can be decreased by a factor of 10 by filling the gap with a thermal interface material.

4. The measuring systems for thermal material characterization have to be designed and developed in such a way that they enable to take into account specific application conditions.

5. Accuracy of temperature measurement has the largest influence on the measurement error of test equipment based on steady-state technique.

6. ASTM standard D5470 can be extended by using a thermal test chip to characterize the TIM under real application condition.

7. A thermal test chip consisting of heater and temperature sensor can be fabricated using only one titanium layer and provides uniform temperature distribution and accurate temperature measurement.

8. Heat losses by convection and radiation along the reference bodies of the steady-state technique based on ASTM standard D-5470 is negligible for temperatures below 100 °C.

9. Commercial steady-state techniques based on ASTM standard D-5470 are limited to thermal resistance between $10\,\mathrm{mm}^2 \cdot \mathrm{K/W}$ and $1000\,\mathrm{mm}^2 \cdot \mathrm{K/W}$. However, the novel steady-state techniques based on ASTM standard D-5470 enable to measure thermal resistance down to $1\,\mathrm{mm}^2 \cdot \mathrm{K/W}$.

10. Filled thermal grease has size effect, its effective thermal conductivity increase at thickness below the triple diameter of the particles.

11. Increasing particle volume fraction in a particle-filled TIM leads usually to non-linear increase of thermal conductivity of the TIM.

12. Bulk thermal conductivity of a substrate can be measured by a modified steady-state technique based on ASTM standard D-5470, even if it exists in only one thickness.

13. Thermal conductivity of a single via in a substrate can be determined by a modified steady-state technique based on ASTM standard D-5470.

14. Thermal impedance technique can also be used for TIM characterization at material level by using thermal test chip as active device.

15. Thermal property of VACNT based TIM is strongly process dependent and must not be measured on material level.

16. The novel modifications of the steady-stated technique allows to measure thermal conductivity of highly thermal conductive materials, particularly of sintered silver.

17. Thermal and electrical conductivities of sintered silver are highly dependent on sinter parameters. Sinter pressure has more influence on thermal and electrical properties than sinter temperature.

18. There is a clear correlation between process, structure and property of sintered silver.

19. The Wiedemann-Franz law is valid not only for bulk metals but also for sintered mono metals.

20. Steady-state method and Ångström's method can be combined in one test procedure allowing simultaneous measurement of the thermal conductivity and diffusivity of the same samples.

21. Losses due to convection and radiation lead to underestimation of the calculated thermal diffusivity from the amplitude and overestimation of the one calculated from the phase. But this can be compensated.

22. The measurement procedures and test stands developed enable, in their entirety, the determination of thermal material data of almost all relevant materials in electronic packages in an appropriate, fast, easily applicable and accurate way.

# Curriculum Vitae

## PERSONAL DETAILS

| | |
|---|---|
| Name: | Mohamad ABO RAS |
| Contact: | aboras@nanotest.eu |
| Date of birth | $5^{th}$ May 1978 |

## EDUCATION

| | |
|---|---|
| 2007 − 2008 | **Master's degree** at University of Applied Sciences in Berlin in the academic program Applied Physics/ Medical Engineering. **Master Thesis:** Investigation of the possibility for application of the infrared thermography for the quality assurance of electrical vias in printed circuit boards |
| 2003 − 2007 | **Diploma** at University of Applied Sciences in Berlin in the academic program Applied Physics/ Medical Engineering. **Diploma Thesis:** Enhancement and optimization of a test stand for characterization of thermal interface materials |
| 2002 − 2003 | **Studienkolleg** at University of Applied Sciences in Kiel (Fachhochschule Kiel) |
| 2001 − 2002 | **German course** at Hartnackschule in Berlin |
| 1997 | **Abitur** in Aleppo, Syria |

## PROFESSIONAL EXPERIENCE

| | |
|---|---|
| Since 2017 | CEO of Berliner Nanotest und Design GmbH |
| 2011 − 2017 | Research assistant at Fraunhofer ENAS |
| 2010 − 2016 | CTO of Berliner Nanotest und Design GmbH |
| 2008 − 2010 | Project manager at Berliner Nanotest und Design GmbH |

| | |
|---|---|
| 2008 − 2011 | Research assistant at Fraunhofer IZM |
| 2006 − 2008 | Student research assistant at Fraunhofer IZM |

# RESEARCH PROJECTS

| | |
|---|---|
| 2007 − 2011 | **Sub-project leader** of EU funded project NANOPACK <br> **Topic:** Advanced characterization techniques for new technologies and materials aimed at low thermal resistance interfaces and electrical interconnects |
| 2011 − 2014 | **Sub-project leader** of EU funded project SMARTPOWER <br> **Topic:** Thermal and thermo-mechanical characterization of thermo-electric cooler modules |
| 2011 − 2014 | **Project coordinator** of BMBF funded project CharTIM <br> **Topic:** Development and integration of innovative test methods for characterization of thermal interface materials |
| 2012 − 2015 | **Sub-project leader** of EU funded project NANOTHERM <br> **Topic:** Thermal characterization for innovative nano and micro technologies for advanced thermal and mechanical interfaces |
| 2014 − 2016 | **Sub-project leader** of BMBF funded project Powerblock+ <br> **Topic:** Novel characterisation procedures for thermal behaviour of components and demonstrator of the high-power system |
| 2014 − 2016 | **Sub-project leader** of BMBF funded project EHLMOZ <br> **Topic:** Thermal characterization and evaluation of high power modules |
| 2014 − 2017 | **Sub-project leader** of EU funded project QUANTIHEAT <br> **Topic:** Development of characterization system for thermal characterization based on three omega method |
| 2016 − 2018 | **Sub-project leader** of EU funded project SMARTHERM <br> **Topic:** Development of characterization methods for Thermal characterization of VACNT based TIM |
| 2018 − 2020 | **Project coordinator** of EU funded project INLINETEST <br> **Topic:** Development of failure analysis systems for in-line quality control of electronic components |

# PUBLICATIONS

## Publications as Author

1. M. Abo Ras, T. von Essen, J. Fortel, P. Panchal, L. Divay, A. Borta-Boyon, D. May, C.C. Darmawan, M.K. Samani, B. Wunderle, A. Ziaei, "Design and realization of characterization demonstrator to investigate thermal performance of vertically-aligned carbon nanotubes TIM for avionics and aerospace applications" in 23rd International Workshop on Thermal Investigations of ICs and Systems (THERMI-NIC), Amsterdam, Netherlands 2017

2. M. Abo Ras, D. May, and B. Wunderle, "Novel test stand for thermal diffusivity measurement of bulk and thin films" in 22nd International Workshop on Thermal Investigations of ICs and Systems (THERMINIC), Budapest, Hungary 2016, pp. 243–249.

3. M. Abo Ras, D. May, J. Heilmann, S. Rzepka, B. Michel, and B. Wunderle, "Processing-structure-property correlations of sintered silver" in 15th IEEE Intersociety Conference on Thermal and Thermomechanical Phenomena in Electronic Systems (ITherm), Las Vegas, USA, 2016, pp. 1064–1071.

4. M. Abo Ras, D. May, R. Schacht, M. Bast, R. Eisele, B. Michel, T. Winkler, R. Rzepka and B. Wunderle "'LaTIMA' an innovative test stand for thermal and electrical characterization of highly conductive metals, die attach, and substrate materials" in 21st International Workshop on Thermal Investigations of ICs and Systems (THERMINIC), Paris, France, 2015 (Best Paper Award).

5. M. Abo Ras, B. Wunderle, D. May, R. Schacht, T. Winkler, R. Rzepka and B. Michel "Limitations and accuracy of steady state technique for thermal characterization of solid and composite materials" in 15th international conference on Thermal, mechanical and multi-physics simulation and experiments in microelectronics and microsystems (eurosime), Ghent, Belgium, 2014.

6. M. Abo Ras, D. May, T. Winkler, B. Michel, S. Rzepka, and B. Wunderle, "Thermal characterization of highly conductive die attach materials" in 20th International Workshop on Thermal Investigations of ICs and Systems (THERMINIC), London, UK, 2014.

7. M. Abo Ras, D. May, R. Schacht, T. Winkler, R. Rzepka, B. Michel and B. Wunderle "Limitations and accuracy of steady state technique for thermal characterization of thermal interface materials and substrates" in IEEE Intersociety Conference

on Thermal and Thermomechanical Phenomena in Electronic Systems (ITherm), Orlando, USA, 2014, pp. 1285–1293.

8. M. Abo Ras, G. Engelmann, D. May, M. Rothermund, R. Schacht, B. Wunderle, H. Oppermann, T. Winkler, S. Rzepka and B. Michel "Development and fabrication of a thin film thermo test chip and its integration into a test system for thermal interface characterization" in 19th International Workshop on Thermal Investigations of ICs and Systems (THERMINIC), Berlin, Germany, 2013, pp. 67–72.

9. M. Abo Ras, B. Michel, T. Winkler, J. Knüppel, and J. Keller, "Reliability and Safety Estimations for Micro- and Nanotechnology" in 1st Biotechnology World Congress, Dubai, UAE, 2012.

10. M. Abo Ras, R. Schacht, B. Wunderle, T. Winkler, and B. Michel, "Innovative Charakterisierungsplattform zur Bewertung von Thermischen Interface-Materialien (TIM)" in 11. Chemnitzer Fachtagung Mikrosystemtechnik -Mikromechanik und Mikroelektronik, Chemnitz, Germany, 2012.

11. M. Abo Ras, R. Haug, R. Schacht, C. Monory-Plantier, D. May, B. Wunderle, T. Winkler and B. Michel "Combined and accelerated in-situ measurement method for reliability and aging analyses of thermal interface materials" in 17th International Workshop on Thermal Investigations of ICs and Systems (THERMINIC) Paris, France, 2011.

12. M. Abo Ras, R. Haug, R. Schacht, C. Monory-Plantier, D. May, B. Wunderle, T. Winkler and B. Michel "Automated test system for in-situ testing of reliability and aging behaviour of thermal interface materials" in NSTI Nanotechnology Conference and Expo, Boston, USA, 2011, pp. 159–163.

13. M. Abo Ras, B. Wunderle, D. May, H. Oppermann, R. Schacht, and B. Michel, "Influences of technological processing and surface finishes on thermal behaviour of thermal interface materials" in 16th International Workshop on Thermal Investigations of ICs and Systems (THERMINIC), Barcelona, Spain, 2010.

14. M. Abo Ras, D. May, R. Schacht, B. Wunderle, and B. Michel, "IR-Thermographie zur Qualitätssicherung von elektrischen Durchkontaktierungen in Leiterplatten" in GMM-Fachbericht-Zuverlässigkeit und Entwurf, Wildbad Kreuth, Germany, 2010.

## Publications as co-Author

1. David Saums, Tim Jensen, Carol Gowans, Ron Hunadi, Mohamad Abo Ras, "Mechanical Cycling Reliability Testing of TIMs Developed Specifically for Semiconductor Test", Electronics Cooling® Spring 2020 Edition, P20-24

2. Wargulski, D.R., Nowak, T., Thiele, M., Dobbelstein, H., Dillkötter, D., Stoppok, J., Schacht, R., Abo Ras, M., 2019. "Quality management of laser cladding processes for additive manufacturing by new methods of visualisation and evaluation of thermographic data". Quantitative InfraRed Thermography Journal 0, 1–12. https://doi.org/10.1080/17686733.2019.1592392

3. B. Wunderle, D. May, J. Heilmann, J. Arnold, J. Hirscheider, Y. Li, J. Bauer, R. Schacht, M. Abo Ras, "Accelerated Pump Out Testing for Thermal Greases" in 20th International Conference on Thermal, Mechanical and Multi-Physics Simulation and Experiments in Microelectronics and Microsystems (EuroSimE), Hannover, Germany, 2019.

4. M. Schulz, R. Mroßko, B. Wunderle, M. Abo Ras, "Advanced Mixed-Mode Bending Test: Influence of the Surface Topography on the Fracture Behavior of an EMC to Copper Lead Frame Bi-Material Interface" in 20th International Conference on Thermal, Mechanical and Multi-Physics Simulation and Experiments in Microelectronics and Microsystems (EuroSimE), Hannover, Germany, 2019.

5. C. Grosse, M. Abo Ras, D. May, M. Wöhrmann, V. Bader, J. Bauer, B. Wunderle, "Glaschips zur Messung der Wärmeleitfähigkeit" in MikroSystemTechnik Kongress, Berlin, Germany, Oct. 28-30, 2019

6. D. R. Wargulski, B. Rabay, A. Stelzer, J. Rudzki, A. Hindel, M. Bast, D. Busse, E. Auerswald, M. Abo Ras, "Paving the way for the replacement of solder interconnections in power electronics by silver-sinter using pulsed infrared thermography" in 22nd Microelectronics and Packaging Conference (EMPC), Pisa, Italy, Sep. 16-19, 2019

7. D. R. Wargulski, D. May, F. Löffler, T. Nowak, J. Petrick, B. Wunderle, E. Boschman, M. Abo Ras, "An In-line Failure Analysis System based on IR Thermography ready for Production Line Integration" in 25rd International Workshop on Thermal Investigations of ICs and Systems (THERMINIC), Lecco, Italy Sep. 25-27, 2019

8. Grosse, C., Abo Ras, M., Varpula, A., Grigoras, K., May, D., Wunderle, B., Prunnila, M., 2018. "Thermal characterization of liquid and solid samples using a measurement platform for the bidirectional 3-omega method", in Nanoscale and Microscale Heat Transfer VI Eurotherm Seminar No 111, p. 197.

9. Wargulski, D., Nowak, T., Thiele, M., Dobbelstein, H., Schacht, R., Abo Ras, M. "Quality Management of Laser Cladding Processes for Additive Manufacturing by New Methods of Visualization and Evaluation of Thermographic Data" in International Conference on Quantitative InfraRed Thermography. Presented at the 2018 Quantitative InfraRed Thermography, QIRT Council.

10. C. Grosse, M. Abo Ras, K. Grigoras, D. May, A. Varpula, K. Elabshihy, B. Wunderle, M. Prunnila. "A novel sensor platform for thermal property measurements of thermosetting resins using the three-omega method" in Thermosetting Resins, Sept. 25-27 2018, Berlin, Germany, 2018

11. D.R. Wargulski, F. Löffler, D. May, J. Heilmann, B. Wunderle, A. Borta-Boyon, A. Ziaei, M. Abo Ras "Comparative die-attach failure analysis by thermoreflectance, lock-in infrared thermography and scanning acoustic microscopy" in 24rd International Workshop on Thermal Investigations of ICs and Systems (THERMINIC), Stockholm, Sweden, 2018

12. B. Völker, D. May, C. Grosse, M. Abo Ras, B. Wunderle, M. Krikunova, "Precision measurement of thermal diffusivity for thin layers by a customised Laser pulse method" in 24rd International Workshop on Thermal Investigations of ICs and Systems (THERMINIC), Stockholm, Sweden, 2018

13. A. Nylander, C. Darmawan, A. Borta Boyon, L. Divay, M. Kabiri Samani, M. Abo Ras, J. Fortel, Y. Fu, L. Ye, A. Ziaei, J. Liu, "Thermomechanical reliability study of polymer bonded Carbon nanotube based thermal interface materials" in 24rd International Workshop on Thermal Investigations of ICs and Systems (THERMINIC), Stockholm, Sweden, 2018.

14. Hakim, I., Schumacher, D., Sundar, V., Donaldson, S., Creuz, A., Schneider, R., Keller, J., Browning, C., May, D., Abo Ras, M., Meyendorf, N., "Volume imaging NDE and serial sectioning of carbon fiber composites". AIP Conference Proceedings 1949, 120003, 2018.

15. Grosse, C., Abo Ras, M., Varpula, A., Grigoras, K., May, D., Wunderle, B., Chapuis, P.-O., Gomès, S., Prunnila, M., "Microfabricated sensor platform with through-glass vias for bidirectional 3-omega thermal characterization of solid and liquid samples". Sensors and Actuators A: Physical 278, p. 33–42, 2018.

16. K. Grigoras, A. Varpula, C. Grosse, D. May, M. Abo Ras, and M. Prunnila, "Sensors for Thermal Characterization of Solid and Liquid Samples by 3-Omega Method," Proceedings Eurosensors 2018, vol. 2, no. 13, p. 883, 2018.

17. C. Grosse, M. Abo Ras, A. Varpula, K. Grigoras, D. May, M. Prunnila, B. Wunderle. "Thermal characterization of thermal interface materials using the three-omega method" 7th Electronics System-Integration Technology Conference (ESTC), Dresden, Germany, Sept. 18-21

18. P. Panchal, T. von Essen, M. Abo Ras, C. Grosse, D. May, B. Wunderle. "Accurate, versatile and compact transient measurement system for fast thermal package characterization and health monitoring" 7th ESTC, Dresden, Germany, Sept. 18-21, 2018

19. B. Wunderle, D. May, M. Abo Ras, C. Grosse, M. Wöhrmann, V. Bader, J. Keller "Spatially resolved, non-destructive in-situ detection of interface degradation by remote electrical readout of an on-chip thermal pixel (Thixel) matrix" 7th ESTC, Dresden, Germany, Sept. 18-21, 2018

20. Wunderle, B., May, D., Heilmann, J., Arnold, J., Hirscheider, J., Li, Y., Bauer, J., Abo Ras, M., "A Novel Concept for Accelerated Stress Testing of Thermal Greases and In-situ Observation of Thermal Contact Degradation" in 17th IEEE Intersociety Conference on Thermal and Thermomechanical Phenomena in Electronic Systems (ITherm)., 2018 pp. 1071–1080.

21. C. Grosse, M. Abo Ras, A. Varpula, K. Grigoras, D. May, M. Prunnila, B. Wunderle and S. Gomès. "Development, design and fabrication of a measurement chip for thermal material characterization based on the 3-omega method" in 23rd International Workshop on Thermal Investigations of ICs and Systems (THERMINIC), Amsterdam, Netherlands, 2017

22. D.R. Wargulski, M. Abo Ras, D. May and B. Wunderle, "TIMAwave an innovative test platform for thermal diffusivity measurements of solid materials at high temperature" in 23rd International Workshop on Thermal Investigations of ICs and Systems (THERMINIC), Amsterdam, Netherlands, 2017

23. B. Wunderle, J. Heilmann, D. May, J. Arnold, J. Hirscheider, J. Bauer, R. Schacht, J. Vogel and M. Abo Ras "Modelling and characterisation of a grease pump-out test stand and its use for accelerated stress testing of thermal greases" in 23rd International Workshop on Thermal Investigations of ICs and Systems (THERMINIC), Amsterdam, Netherlands, 2017

24. H. Kristiansen, K. Redford, S. Helland, E. Kalland, N.H. Hoglund, M. Abo Ras, C. Grosse, B. Hay, L. Ramiandrisoa, G. Davée, S. Gomès and S.R. Pettersen, "Thermal conduction in novel isotropic conductive adhesive" in 23rd International Workshop

on Thermal Investigations of ICs and Systems (THERMINIC), Amsterdam, Netherlands, 2017

25. J.S. de Sousa, P. Fulmek, M. Unger, P. Haumer, J. Nicolics, M. Abo Ras and D. May. "Enhanced In-Plane Heat Transport in Embedded Mini Heat Pipes PCB". International Symposium on Microelectronics, North Carolina, USA 2017

26. B. Wunderle, D. May, M. Abo Ras and J. Keller, "Non-destructive in-situ monitoring of delamination of buried interfaces by a thermal pixel (Thixel) chip," in 16th IEEE Intersociety Conference on Thermal and Thermomechanical Phenomena in Electronic Systems (ITherm), Orlando, USA, 2017, pp. 1238–1246 (Best Paper Award).

27. A. Otto, R. Dudek, S. Rzepka, M. Abo Ras, T. von Essen, M. Bast, A. Hindel, R. Eisele, U. Mueter and A. Lunding, "Reliability Investigation on SiC based Diode and MOSFET Modules Developed for High Power Conversion in Medical X-Ray Applications," in PCIM Europe 2017; International Exhibition and Conference for Power Electronics, Intelligent Motion, Renewable Energy and Energy Management, Nuremberg, Germany, 2017

28. B. Wunderle, D. May, M. Abo Ras, M. Schulz, M. Wöhrmann, J. Bauer and J. Keller "In-situ monitoring of interface delamination by local thermal transducers exemplified for a flip-chip package" in 22nd International Workshop on Thermal Investigations of ICs and Systems (THERMINIC), Budapest, Hungary, 2016, pp. 230–235.

29. J. Ordonez-Miranda, M. Hermens, I. Nikitin, V. G. Kouznetsova, O. van der Sluis, M. Abo Ras and C. S. Torres "Measurement and modeling of the effective thermal conductivity of sintered silver pastes" International Journal of Thermal Sciences, vol. 108, pp. 185–194, Oktober 2016.

30. J. Ordonez-Miranda, M. Abo Ras, B. Wunderle and S. Volz, "Modelling and measurement of the thermal conductivity of composites with silver particles," in 22nd International Workshop on Thermal Investigations of ICs and Systems (THERMINIC), Budapest, Hungary, 2016, pp. 121–124.

31. I. Hakim, D. May, M. Abo Ras, N. Meyendorf, and S. Donaldson, "Quantifying voids effecting delamination in carbon/epoxy composites: static and fatigue fracture behavior" 2016.

32. T. von Essen, M. Abo Ras, S. Stegmeier and G. Mitic, "Investigation of the Influence of Ageing Processes on Thermal Characteristics of an IGBT Power Module by Means

of Transient Thermal Analysis" in PCIM Europe 2016, International Exhibition and Conference for Power Electronics, Intelligent Motion, Renewable Energy and Energy Management, Nuremberg, Germany, 2016.

33. M. Springborn, B. Wunderle, D. May, R. Mrossko, C.-A. Manier, M. Abo Ras, H. Oppermann, T. Xhonneux, T. Caroff and R. Mitova "Transient thermal management by using double-sided assembling, thermo-electric cooling and phase-change based thermal buffer structures: Design, technology and application" in 21st International Workshop on Thermal Investigations of ICs and Systems (THERMINIC), Paris, France, 2015.

34. R. Schlag, M. Abo Ras, V. Arlt, D. May, T. Winkler and B. Wunderle, "Precision determination of thermoreflectance coefficients for localised thermometry" in 21st International Workshop on Thermal Investigations of ICs and Systems (THERMINIC), Paris, France, 2015.

35. E. Merten, T. von Essen, F. Luczack, A. Otto, A. Lunding, P. Lürkens M. Bast, M. Abo Ras and S. Rzepka "Reliability investigation and design of high power rectifier modules based on material characterization, simulation and experimental verification" in 16th International Conference on Thermal, Mechanical and Multi-Physics Simulation and Experiments in Microelectronics and Microsystems (EuroSimE), Budapest, Hungary, 2015.

36. B. Wunderle, M. Springborn, D. May, R. Mrossko, M. Abo Ras, C.-A. Manier, H. Oppermann and R. Mitova "Phase change based thermal buffering of transient loads for power converter" in 20th International Workshop on Thermal Investigations of ICs and Systems (THERMINIC), London, UK, 2014.

37. B. Wunderle, M. Springborn, D. May, C.-A. Manier, M. Abo Ras, R. Mrossko, H. Oppermann, T. Xhonneux, T. Caroff, W. Maurer and R. Mitova "Double-sided cooling and transient thermo-electrical management of Silicon on DCB assemblies for power converter modules: Design, technology and test" in IEEE Intersociety Conference on Thermal and Thermomechanical Phenomena in Electronic Systems (ITherm), Orlando, USA 2014, pp. 851–861.

38. M. Springborn, B. Wunderle, M. Springborn, D. May, R. Mrossko, C.-A. Manier, H. Oppermann, M. Abo Ras and R. Mitova "Thermal management of electrical overload cases using thermo-electric modules and phase change buffer techniques: Simulation, technology and testing" in 15th international conference on Thermal, mechanical and multi-physics simulation and experiments in microelectronics and microsystems (eurosime), Ghent, Belgium, 2014.

39. B. Wunderle, C.-A. Manier, M. Abo Ras, M. Springborn, D. May, H. Oppermann, M. Toepper, R. Mrossko, T. Xhonneux, T. Caroff and R. Mitova "Double-sided cooling and thermo-electrical management of power transients for silicon chips on DCB-substrates for converter applications: Design, technology and test" in 19th International Workshop on Thermal Investigations of ICs and Systems (THERMI-NIC), Berlin, Germany, 2013, pp. 253–261.

40. E. Merten, M. Abo Ras, T. von Essen, R. Schacht, D. May, T. Winkler and B. Michel "Combined method for thermal characterization of high power semiconductors" in 19th International Workshop on Thermal Investigations of ICs and Systems (THERMINIC), Berlin, Germany, 2013, pp. 341–343.

41. B. Wunderle, M. Abo Ras, M. Springborn, D. May, J. Kleff, H. Oppermann, M. Töpper, T. Caroff, R. Schacht and R. Mitova "Modelling and characterisation of smart power devices" in 18th International Workshop on Thermal Investigations of ICs and Systems (THERMINIC), Budapest, Hungary, 2012.

42. T. Nowak, R.Schacht, H. Walter, B. Wunderle, M.Abo Ras, D. May, O. Wittler and K. D. Lang "Experimental and numerical reinvestigation for lifetime-estimation of plated through holes in printed circuit boards" in 17th International Workshop on Thermal Investigations of ICs and Systems (THERMINIC), Paris, France, 2011.

43. B. Wunderle, M. Klein, L. Dietrich, M. Abo Ras, R. Mrossko, D. May, R. Schacht, H. Oppermann, B. Michel and H. Reichl "Advances in thermal interface technology: mono-metal interconnect formation, processing and characterisation" in 12th IEEE Intersociety Conference on Thermal and Thermomechanical Phenomena in Electronic Systems (ITherm), Las Vegas, USA, 2010.

44. B. Wunderle, M. Abo Ras, M. Klein, R. Mrossko, G. Engelmann, D. May, O. Wittler, R. Schacht, L. Dietrich, H. Oppermann and B. Michel "Progress in thermal characterisation methods and thermal interface technology within the Nanopack project" in 15th International Workshop on Thermal Investigations of ICs and Systems (THERMINIC), Leuven, Belgium, 2009, pp. 224–232.

45. R. Schacht, M. Abo Ras, D. May, B. Wunderle, and B. Michel, "Non-Destructive Tests for Via Structures in Organic Multi Layer PCBs" presented at the Smart Systems Integration, Brussels, Belgium, 2009.

46. B. Wunderle, J. Kleff, R. Mrossko, M. Abo Ras, D. May, R. Schacht, H. Oppermann, J. Keller and B. Michel "In-situ measurement of various thin bond-line-thickness

thermal interface materials with correlation to structural features" in 14th International Workshop on Thermal Inveatigation of ICs and Systems (THERMINIC), Rome, Italy, 2008, pp. 112–117.

47. R. Schacht, B. Wunderle, D. May, M. Abo Ras, W. Faust, B. Michel and H.Reichl "Effective thermal modelling evaluation and non-destructive tests for thermal via-structures in organic multi layer PCBs" in 2nd Electronics System-Integration Technology Conference (ESTC), London, 2008, pp. 999–1008.

48. D. May, B. Wunderle, M. Abo Ras, W. Faust, A. Gollhard, R. Schacht and B. Michel "Material characterization and non-destructive failure analysis by transient pulse generation and IR-thermography" in 14th International Workshop on Thermal Inveatigation of ICs and Systems (THERMINIC), Rome, Italy, 2008, pp. 47–51.

# PATENTS

1. M. Abo Ras, R. Haug, D. May, C. Monory-Plantier, R. Schacht, and B. Wunderle, "Verfahren und Messanordnung zur Charakterisierung eines thermischen Interface-Materials Procedures and measuring system for characterization of a thermal interface material," DE102011003862 A1, 09-Aug-2012.